

**FATIGUE CRACK THRESHOLD AND GROWTH
BEHAVIOUR IN A NEAR FULLY-LAMELLAR
GAMMA BASED TITANIUM ALUMINIDES**

by

SHIYUAN WANG

A thesis submitted to the University of Birmingham for the degree of
DOCTOR OF PHILOSOPHY

School of Materials and Metallurgy
University of Birmingham
Edgbaston
Birmingham
B15 2TT

January 2015

UNIVERSITY OF
BIRMINGHAM

University of Birmingham Research Archive

e-theses repository

This unpublished thesis/dissertation is copyright of the author and/or third parties. The intellectual property rights of the author or third parties in respect of this work are as defined by The Copyright Designs and Patents Act 1988 or as modified by any successor legislation.

Any use made of information contained in this thesis/dissertation must be in accordance with that legislation and must be properly acknowledged. Further distribution or reproduction in any format is prohibited without the permission of the copyright holder.

Abstract

Fatigue crack threshold (ΔK_{th}) and fatigue crack growth behaviour of a near fully-lamellar γ -TiAl alloy (Ti-4522XD alloy) have been investigated in air at five temperatures (room temperature, 400, 650, 700 and 750 °C) and at three R ratios (0.1, 0.5 and 0.8) in this study. Studies were carried out on both corner-cracked specimens and smooth specimens.

A combination of a ΔK - increasing loading method and growing a crack from notch were applied throughout the tests to minimise crack wake effects on ΔK_{th} values. As a consequence of consistent material microstructure, use of standardized testing procedure and a sufficient number of tests, for the first time trends in fatigue threshold and crack growth behaviour have been established in a 'single' microstructure in TiAl. Such trends include: lack of dependence of ΔK_{th} values on test temperature; average ΔK_{th} values decrease with increasing R ratio; a strong dependence of crack growth rate on K_{max} values at RT; a reduced dependence of crack growth rate on K_{max} values and increased plasticity at elevated temperatures; crack blunting causes a reduction of fatigue crack growth rate at R=0.8 and at elevated temperatures; and little effect of test temperature on 'fracture toughness' values.

Above all, the origins of naturally initiated cracks under cyclic loading are often found to be centered on up to four colonies which have failed by interlamellar fracture. However, continuous crack growth requires further translamellar crack growth and such transitions can be characterised by the values of the threshold fatigue stress intensity factor (ΔK_{th}) calculated experimentally. Fracture surfaces produced under cyclic loading and catastrophic failures are closely similar.

Dedicated to

My Parents and Husband

Acknowledgements

Immeasurable appreciation and deepest gratitude for the help and support are extended to the following persons who in one way or another have contributed in making this study possible.

Prof. P. Bowen, for his specialist supervision, advice, guidance, encouragements, support throughout this research and patience for helping improve my study.

Dr. H. Y. Li, for her supervision, advice, sharing her knowledge and endless help with all aspects of my research.

EPSRC and Rolls-Royce Plc. (Derby, UK), for full sponsorship of my research.

School of Material and Metallurgy, for providing testing facilities and equipment.

Dr. T. Doel, for his valuable comments in science discussions and his precious time for reading my thesis.

Mr. D. Price, for his technical training and indispensable friendship.

Finally, my special thanks go to my beloved parents and husband for their love and support-both spiritually and materially. I also would like to give many thanks to my friends and colleagues for giving me friendship, kindness and support all these years.

Contents

1. Introduction	1
1.1 Background of the project	1
1.2 Challenge of Titanium Aluminides	3
1.3 Aims and objectives	4
2. Fracture Mechanics	7
2.1 Introduction	7
2.2 Linear elastic fracture mechanics	7
2.2.1 Griffith theory of fracture and Irwin's work	7
2.2.2 Stress intensity approach	10
2.2.3 Crack tip plasticity	12
2.3 Elastic-Plastic fracture mechanics	14
2.3.1 The J -integral	15
2.3.2 The R-curve	16
2.3.3 The crack tip opening displacement (CTOD) approach	18
3. Fatigue	29
3.1 Introduction of fatigue	29
3.2 Different approaches to fatigue	30
3.2.1 Total-life approaches	30
3.2.2 Damage-tolerance approach	31
3.3 Fatigue crack growth resistance curve (da/dN vs. ΔK curve)	32
3.4 Factors affecting fatigue crack threshold and growth	34
3.4.1 Effect of mean load	34
3.4.2 Temperature	35
3.4.3 Microstructure	36
3.5 Crack closure mechanisms and other retardation mechanisms	37
3.5.1 Concepts of crack closure	37
3.5.2 Different crack closure mechanisms	39
3.5.3 Other retardation mechanisms	40
3.6 The small crack behaviour	41
3.6.1 Definition of small crack	42
3.6.2 Effect of small crack on fatigue threshold and crack propagation	42
4. Gamma Titanium Aluminides	48
4.1 Overview	48
4.1.1 Titanium Aluminides and related phases	48
4.1.2 Microstructure of Gamma Titanium Aluminides	50
4.2 Alloying additions	51
4.2.1 Niobium	51
4.2.2 Manganese	52

4.2.3 Boron.....	52
4.2.4 Other elements	53
4.3 Mechanical properties	54
4.3.1 Microstructure and Deformation.....	54
4.3.2 Ductility and tensile properties	55
4.3.3 Fracture toughness	58
4.4 Fractographic characteristics	60
4.5 Fatigue threshold and fatigue crack propagation in γ -TiAls	61
4.5.1 High-cycle fatigue.....	61
4.5.2 Fatigue crack growth resistance curve of γ -TiAl	63
4.6 Extrinsic and intrinsic fatigue resistance in γ -TiAls	64
4.6.1 Introduction.....	65
4.6.2 Extrinsic toughening mechanisms in γ -TiAls – bridging mechanisms	65
4.6.3 Extrinsic toughening mechanisms in γ -TiAls – crack closure	67
4.6.4 Extrinsic toughening mechanisms in γ -TiAls – crack deflection.....	68
4.6.5 Extrinsic toughening mechanisms in γ -TiAls – small cracks	69
4.6.6 Intrinsic mechanisms in γ -TiAls	71
4.7 Effects of temperature on fatigue threshold and fatigue crack propagation ..	71
4.8 Effect of stress ratio on fatigue threshold and fatigue crack propagation.....	74
4.9 Effect of environment on fatigue threshold and fatigue crack propagation...	76
4.10 Creep resistance in γ -TiAl alloys	78
4.10.1 Creep resistance	78
4.10.2 Interaction between creep and fatigue on crack growth	79
5. Experimental Work	110
5.1 Material and specimen	110
5.2 Fatigue tests	110
5.2.1 Specimens for fatigue and fracture toughness tests	110
5.2.2 Test condition and method of fatigue tests on corner-cracked specimens	111
5.2.3 Pre-crack procedure	112
5.2.4 Fatigue threshold and crack growth tests procedure on CC specimens	113
5.2.5 Heat-tint	114
5.2.6 Results processing.....	114
5.2.7 Interrupted tests.....	114
5.2.8 Fatigue test on smooth specimen	115
5.3 Fracture toughness tests on corner-crack specimen.....	115
5.3.1 Pre-crack	115
5.3.2 Fracture toughness test.....	116
5.4 Microstructural analysis.....	117
5.4.1 Sample preparation	117
5.4.2 Colony size measurement	117

5.4.3 Measurement of other microstructural parameters	117
5.5 Fractographic analysis	118
5.6 Fracture surface roughness assessment.....	118
6. Results	129
6.1 Microstructure.....	129
6.2 Fracture toughness tests	129
6.2.1 Fracture toughness at different temperatures	129
6.2.2 Fractography	130
6.3 Fatigue crack threshold results of Ti-4522XD alloy.....	130
6.3.1 Effect of test temperature on ΔK_{th} values	130
6.3.2 Effect of R ratio on ΔK_{th} values.....	132
6.4 Fatigue crack growth resistance curves of Ti-4522XD alloy.....	133
6.4.1 General features of fatigue crack growth resistance curves.....	133
6.4.2 Effect of test temperature on fatigue crack growth.....	133
6.4.3 Effect of R ratio on fatigue crack growth	134
6.5 Fractography	135
6.5.1 Effect of test temperature on fracture surfaces	135
6.5.2 Effect of test temperature on fatigue crack path	137
6.5.3 Effect of R ratio on fracture surface	137
6.5.4 Fracture surface roughness measurement	138
6.6 Potential effects of other factors on fatigue crack growth	138
6.6.1 Effects of notch depth on fatigue crack growth	138
6.6.2 Crack growth from a notch or from a pre-crack	139
6.6.3 Effects of surface condition on fatigue crack growth	139
6.6.4 Effects of equiaxed γ grain clusters on fatigue crack growth	140
6.7 High cycle fatigue (HCF) tests	140
6.7.1 HCF at RT	141
6.7.2 HCF at 650 °C.....	142
6.8 Creep crack growth.....	144
6.8.1 Specimens failing in creep manner	144
6.8.2 Fractography of specimen failed in creep manner	145
7. Discussion	216
7.1 Introduction.....	216
7.2 Fatigue crack threshold and near threshold behaviour	216
7.2.1 Effects of microstructure and test temperature on ΔK_{th} values.....	217
7.2.2 Effect of test temperature on fatigue crack growth in the near-threshold region	218
7.2.3 Effect of R ratio on ΔK_{th} values.....	220
7.3 Fatigue crack growth behaviour in near-lamellar TiAls	220
7.3.1 Effect of temperature and environment at R=0.1 and 0.5:.....	221
7.3.2 Effect of temperature on extrinsic mechanisms.....	222
7.3.3 Effect of temperature at R=0.8.....	223

7.3.4 Effect of R ratio on stable fatigue crack growth	224
7.4 Fracture toughness	225
7.5 Small fatigue crack considerations in near fully lamellar γ -TiAl alloys.....	226
7.5.1 Natural-initiated small fatigue cracks	226
7.5.2 Small fatigue cracks behaviour	228
7.5.3 Practical concerns of small cracks in near fully-lamellar γ -TiAl alloys	229
7.6 General discussion	230
8. Conclusions	240
9. Future work	243
References	244

1. Introduction

1.1 Background of the project

Modern aircraft engines are required to be able to stand high temperature, corrosion, oxidation and all kinds of mechanical damage. In recent decades a lot of effort has been put into developing the durability, reliability and performance of aircraft engines. The increase of engine performance is closely related to the development of improved materials.

Aircraft engines are composed of many components, such as a fan, compressor, combustor, turbines and shafts. Thus, the physical and mechanical property requirements of structural materials may vary according to where they are employed. For example, turbine blades and discs are the most critical components of an engine. The operating temperature for turbine blades can exceed 1200 °C which is higher than any other rotating components within a turbine engine. The high spin velocities (~30,000 rpm) at the airfoil result in large centrifugal loads on the blade airfoil [1]. Hence the materials must be able to withstand a number of failure modes including fatigue, creep rupture, ballistic damage and environmental impacts. Beside these damage modes, the materials used for blades also need to withstand very high temperature gradients during transient conditions and fretting wear with turbine discs. All the requirements are interpreted into material properties for material design including tensile and fatigue strengths, thermal expansion, elastic modulus, corrosion resistance, toughness, ductility and damage tolerance. The further interpretation of these parameters is to verify the composition and microstructure of materials to achieve the required properties.

The three most important structural materials used in aircraft engines are nickel-based superalloys for gas turbines, titanium alloys for fan blades and disks as well as high

strength steels for shafts. Although the current materials can meet the demands for aircraft engines and realise good performance, new materials are required for more efficient aircraft engines in the future. The material technology is also required to provide economic and environmental benefit. Since most materials used in aircraft have reached a plateau, the efficiency and performance improvements greatly depend on the introductions of more potential materials with both good high temperature properties and lower density for weight saving at the same time.

Intermetallics have been studied for many decades. Recently, they have received increasing attention as potential candidates for gas turbine applications because of their improved properties, such as high melting point, good oxidation resistance and low density, over more the conventional superalloys [2, 3]. An intermetallic compound is a type of ordered alloy phase consisting of two or more different kinds of metal atoms. Below a certain critical temperature (T_c), the compound is an ordered phase. Unlike metals, the atomic bonding between the different types of atoms is partly ionic and directional. Therefore the intermetallics often present mechanical properties between ceramics and metals. Among intermetallic compounds, several aluminides have been studied for possible applications in engines, such as FeAl, Fe₃Al, Ni₃Al, TiAl or their orthorhombic alloys, for example Ti₂AlNb [2-4]. Beside the satisfaction of most basic requirements for craft engines, high aluminum content is the key aspect that makes them not only significantly lighter but also more resistant to oxidation than other intermetallics (the relative atomic weight of Al is only about 27). Titanium aluminides are even more popular than other aluminides in the aerospace and automotive market. Recently, TiAl-based alloys has been introduced for the application of turbocharger turbine wheels in automotive engines [5]. Moreover, very recently the successful implementation of gamma TiAl alloy has been announced in low pressure turbine blades of aircraft engines by General Electric Company [6]. However, the larger-scale aeronautical applications of TiAl or other intermetallics are still impeded by a number

of technical barriers in material manufacture and property development.

1.2 Challenge of Titanium Aluminides

Titanium aluminides are a class of intermetallics targeted for the use in high-temperature applications, such as aerospace engines, automotive engines, and nuclear plants. The three major phases have been identified for titanium aluminides: γ -TiAl, α_2 -Ti₃Al and TiAl₃, of which γ -TiAl and its alloys have attracted most attention [3]. The main reasons why they are so attractive in many industries are their high-temperature capability, good oxidation and creep resistance and especially their low density which is nearly half that of Ni-based superalloys. However, based on their properties the possible applications for TiAl-based alloys are not that extensive, only including some components of the high-pressure compressor and low-pressure turbines. How to break through the limitations to broaden their scope of application is the challenge of titanium aluminides [2].

Titanium aluminides have drawbacks in common with other intermetallics, which are a direct result of their structures. Brittleness is a common characteristic of intermetallic compounds and is also the origin of a series of restricts on their introduction [2, 3]. Even though the ductility could be increased at elevated temperature (the brittle-ductile transition temperature of TiAl is in a range around 650-800 °C), the improvement is still not widely applicable for aerospace engines. The brittleness causes lower fracture toughness and fatigue crack resistance at low or even medium temperature. Moreover, the brittleness also increases the difficulties for manufacturing since processes, such as forging and machining, introduction of deformation or flaws. And the cost for processing can be increased as a consequence of these difficulties. In addition, it is less possible to use strain hardening strengthening.

In spite of these difficulties, titanium aluminides are still the most competitive

structural materials for aerospace or other high-temperature associated industries since they have numbers of advantages. Much effort has been devoted to the research and development on titanium aluminides over more than twenty years and significant advances have been achieved in understanding the deformation mechanisms as well as developing new TiAl-based alloys. The mechanical properties of dual-phase titanium aluminides ($\gamma+\alpha_2$) exhibit a good combination of tensile strength, ductility and fracture toughness. Of these microstructures, the duplex and fully lamellar are the two categories that have received most attention since they can offer a range of mechanical properties adapted to industrial requirements. Because of the relatively fine grain size, duplex microstructures present better ductility and tensile strength at lower temperature but are less resistant to creep and fatigue. Fully lamellar microstructures usually have relatively larger colony size and thus lower ductility, but excellent creep and fatigue crack growth resistance [7]. A new class of TiAl alloys with high niobium content (5%-10%) is known as TNB alloys and TNM alloys. Due to the addition of Nb, these types of TiAl alloys exhibit significant improvement in strength as well as creep and oxidation resistance [8]. Other nonmetallic elements such as C and B are also added in TiAl alloys to increase their strength as a result of precipitation hardening [5]. More than the advances for alloys design, manufacturing techniques are gradually maturing as well. Some traditional techniques like investment casting, ingot metallurgy and powder metallurgy are widely used for producing TiAl components. New techniques, such as laser melting for producing complex-shaped components and directional rolling for sheet materials, have been well investigated with favourable results and a good prospect [8].

1.3 Aims and objectives

It needs to be noted that the understanding of deformation mechanisms and microstructure associated properties in TiAl-based alloys is nearly integrated, and the implementation of some TiAl-based alloys has also achieved success. However, some

problems still need to be solved in order to get more development on enhancing mechanical properties, processability and reducing costs. Among many of these questions, the fundamental understanding of fatigue behaviour of TiAl-based alloys is especially important for alloy design. Although many theories on fatigue failure mechanisms of γ TiAl-based alloys have been proposed and studied in the past, there is no systematic explanation about the fatigue threshold and near threshold behaviour under different test conditions, such as temperatures, stress ratios and environments. To minimise the risk of using relatively new alloys in aerospace engines, it is necessary to understand how such behaviour of these materials changes with different test conditions.

Ti-45Al-2Mn-2Nb-1B (at.%) (Ti4522XD) is a γ -TiAl which is under consideration as a potential substitutive material to be used in Trent-XWB low pressure turbines by Rolls-Royce plc. High tensile strength, good fatigue crack and creep resistance as well as low density are the main advantages that make it attractive for aero-engine [9].

Aims:

The main aims of this project to be achieved in the Ti4522XD alloy and other similar near-fully lamellar γ -TiAl alloys are: (1) establishing reliable testing method for measuring the fatigue threshold and crack growth behaviour; (2) understanding the effect of temperature, environment and cyclic loading condition on the fatigue threshold and crack growth; (3) acquiring the design stress ranges of different conditions for practical applications.

Objectives:

To achieve these aims, objectives were designed and completed as follows:

(1) Repeated fatigue threshold and crack growth tests were performed with three different stress ratios (0.1, 0.5 and 0.8) at three main test temperatures (RT, 400 °C and

650 °C);

(2) Limited number of tests was also conducted at 700 °C and 750 °C to examine the high-temperature fatigue properties and the alloy's working temperature capability;

(3) Changes were designed on the crack size and specimen geometry (corner-cracked specimens and cylindrical smooth specimens) to study the effect of crack size and morphology, as well as naturally-initiated short cracks in Ti4522XD alloy;

(4) Fractographic characterisations were carried out to study the failure mechanisms at different temperatures and stress ratios.

2. Fracture Mechanics

2.1 Introduction

Failures occur for many reasons, including defects in material, corrosion, fracture, environmental damage, inadequate design and extreme loading conditions. For the design of structural or machining component, a vital issue is to identify the most likely mode of failure and the application of a suitable failure criterion. During a fracture process, there are diverse factors, such as crack nucleation, growth and coalescence of cracks, which makes the study of the fracture in solids more complex. From the standpoint of engineering application, the theories are established macroscopically based on the notions of continuum solid mechanics and classical thermodynamics. Studies about defect geometry and applied stress on fracture behaviour are important for the development of fracture mechanics. The term “fracture mechanics” is a branch of solid mechanics which refers to a vital specialisation of the relationship between the crack length, the material’s inhere resistance to crack propagation, and the stress to cause the final rupture. It provides quantitative working tools to solve the fracture criterions for the applications in engineering components where failure may result in the loss of life.

2.2 Linear elastic fracture mechanics

2.2.1 Griffith theory of fracture and Irwin’s work

When discussing the fracture mechanics, A. Griffith [10] must be mentioned as the pioneer of the advent of fracture mechanics. It was noticed that there was two orders of magnitude difference between theoretical strength and laboratory results in glass, and it was believed to be caused by microcracks in the glass that could propagate under a load level smaller than the theoretical strength. Rather than focusing on the crack-tip stresses like what Inglis solution works for calculating the stress concentration around elliptical

holes, Griffith adopted the energy balance approach to predict fracture strength in the solids with cracks, which has become one of the most widely accepted and used theories in materials science [11-14].

The basic concept of Griffith's theory was that, solids have surface energy, and in order to propagate a crack, the corresponding surface energy (or increase its surface area), must be equal to the total energy of the externally added and internally released energy [13]. The schematic diagram of the concept of fracture energy balance is shown in Figure 2.1. As shown in Figure 2.1, the total energy associated with the crack length is the sum of positive surface energy (S) absorbed to generate the new surfaces, plus the negative strain energy (U) released due to unloading near the crack flanks.

The strain energy per unit volume ($\frac{1}{V}$) of material under stresses (σ) is:

$$U^* = \frac{1}{V} \int f dx = \int \frac{f}{A} \frac{dx}{L} = \int \sigma d\epsilon \quad \dots 2.1$$

If the material is elastic, according to Hooke's Law ($\sigma = E\epsilon$, ϵ is the strain of material and E is Young's Modulus of the material), then the strain energy per unit volume is:

$$U^* = \int E\epsilon d\epsilon = \frac{E\epsilon^2}{2} = \frac{\sigma^2}{2E} \quad \dots 2.2$$

As shown in Figure 2.2, for a solid with a crack length of a , a region adjacent to the crack flanks can be considered as unloaded, and therefore the strain energy is released in this region. In a completely unloaded region with a height of βa (β is a parameter can be selected, for the plane stress loading $\beta = \pi$) and width of crack length (a), Griffith used Inglis solution to calculate that the total strain energy U released is as follows:

$$U = -\frac{\sigma^2}{2E} \cdot \pi a^2 \quad \dots 2.3$$

The surface energy (S) associated with a crack length of a is:

$$S = 2\gamma a \quad \dots 2.4$$

in which γ is the surface energy density.

As the crack length (a) length increase, the U strain energy becomes dominant on the total energy since it is a quadratic function of a . The crack can only grow if the stress is increased until it reaches a critical crack length (a_c). Beyond this point the crack can grow until final fracture occurs. This critical value can be solved by making the derivative of the total energy equal to zero, so [11]:

$$\frac{\partial(S + U)}{\partial a} = \frac{\partial(-\frac{\sigma_f^2}{2E} \cdot \pi a^2 + 2\gamma a)}{\partial a} = 2\gamma - \frac{\sigma_f^2}{2E} \cdot \pi a = 0 \quad \dots 2.5$$

By solving this equation, the result of the fracture stress (σ_f) is:

$$\sigma_f = \sqrt{\frac{2E\gamma}{\pi a}} \quad \dots 2.6$$

In the case of plane stress, the fracture stress can be expressed as:

$$\sigma_f = \sqrt{\frac{2E\gamma}{\pi(1 - \nu^2)a}} \quad \dots 2.7$$

where ν is Poisson' ratio, in the case of plane strain.

The energy released dU for a crack extension of da can be interpreted as the “strain energy release rate per crack tip” (G) as:

$$dU = G da \quad \dots 2.8$$

Thus for the plane strain:

$$G = \frac{dU}{da} = \frac{\pi a \sigma^2 (a - \nu^2)}{2E} \quad \dots 2.9$$

And for the plane stress:

$$= \frac{\pi a \sigma^2}{2E} \quad \dots 2.10$$

Then the instability condition can be considered as $G \geq 2\gamma$, and when $G = 2\gamma$, the value of G is the fracture toughness or the crack-resistant force of the material.

However, Griffith's work was only focused on brittle materials, such as glass. The released energy rate obtained by this theory was found to be much smaller than the experimental data since most materials are not completely brittle and there is always

some plasticity around the crack tip. This deficiency was modified by Irwin and Orowan [11, 13] later. They proposed that in actual fracture process in ductile materials, the released strain energy was depleted by plastic flow near the crack tip rather than by creating new surfaces. Therefore, they concluded that the plastic work γ_p must be applied with the surface energy in Griffith's model as $\gamma + \gamma_p$. Orowan [13] also estimated that for typical metals, the value of γ_p is about 3 orders of magnitude of γ . Irwin and Orowan use \mathcal{G}_c to denote the critical strain energy released during fracture ($\gamma + \gamma_p$). Then the Griffith formula was written in the form as:

$$\sigma_f = \sqrt{\frac{E\mathcal{G}_c}{\pi a}} = \sqrt{\frac{E(2\gamma_e + \gamma_p)}{\pi a}} \quad \dots 2.11$$

in which, γ_e is the elastic surface energy of the material and γ_p is the energy of plastic work absorbed during the fracture. Hence, the high fracture strength of metals was explained by Irwin and Orowan's work.

2.2.2 Stress intensity approach

When the crack in a solid is subjected to externals, there will be relative displacement of the two crack flanks. The relative displacement is not simply a two dimensional movement, but usually varies with the direction of loading axes. To describe this kind of movement between the crack flanks, a local Cartesian coordinate system (x,y,z) with a zero point at the crack front has been introduced, in which the x-axis and y-axis are perpendicular to the crack front and crack plane respectively, and the z-axis is along the crack front. Irwin [13] also identified three modes of crack movement, termed as mode I, II, and III as shown in Figure 2.3.

Mode I (opening mode): The crack surfaces move directly and symmetrically apart along the y axis (perpendicular to the xz plane.)

Mode II (sliding mode): The crack surfaces slide over one another in a direction

perpendicular to the leading edge of the crack along x axis (parallel to xz plane).

Mode III (tearing mode): The crack surfaces tear over each other and parallel to the leading edge of the crack along z axis.

The crack can move by either of the three basic modes, or the combinations of any two or three modes. Among the three modes, mode I loading is the most damaging mode to materials, thus most analyses are carried out to solve the stress-crack relationship under this loading mode. According to the semi-inverse method developed by Westergaard[15], Irwin [11] point out that, the opening-mode stresses in the vicinity of the crack tip of a crack with a length of $2a$ in terms of K_I can be expressed as and schematically shown in Figure 2.4:

$$\begin{aligned}\sigma_x &= \frac{K_I}{\sqrt{2\pi r}} \cos \frac{\theta}{2} \left(1 - \sin \frac{\theta}{2} \sin \frac{3\theta}{2} \right) \\ \sigma_y &= \frac{K_I}{\sqrt{2\pi r}} \cos \frac{\theta}{2} \left(1 + \sin \frac{\theta}{2} \sin \frac{3\theta}{2} \right) \\ \tau_{xy} &= \frac{K_I}{\sqrt{2\pi r}} \cos \frac{\theta}{2} \cos \frac{3\theta}{2} \sin \frac{\theta}{2}\end{aligned} \quad \dots 2.12$$

In this equation, the r and θ are the polar coordinates of a point to the crack tip, respectively. At the crack tip, $r=0$, thus the stress tends to infinity. The K_I is known as the stress intensity factor, which defines the magnitude of the elastic stresses around the crack tip, and the 'I' subscript represent for the mode I. This K_I factor depends on applied stress, the size, shape of the crack and the geometric boundaries. Originally, this factor was expressed as:

$$K_I = \sigma\sqrt{\pi a} \quad \dots 2.13$$

However, it is not useful in practical situations where specimens have a finite width. The width of specimens must be considered for the practical case. Therefore, this factor was recomposed as a function of crack length-width ratio:

$$K_I = \sigma\sqrt{\pi a} f\left(\frac{a}{w}\right) \quad \dots 2.14$$

in which, $f\left(\frac{a}{w}\right)$ is a function depending on specimen and crack geometry and w is the specimen width. The stress intensity factors for some common geometries are given in

Table 2.1. This function provides a very accurate way to calculate the stresses around the crack tip and so to design against failures. There is a critical value of stress intensity, K_{IC} , beyond which the crack growth is unstable and reaches the rupture very fast. By knowing the value of this factor and the applied stress, the critical crack length can be easily worked out for engineering design purpose. The failure stress can also be expressed as a function related to crack length a and the fracture toughness value as:

$$\sigma_f = \frac{K_{IC}}{Y\sqrt{\pi a}} \quad \dots 2.15$$

where Y is equal to $f\left(\frac{a}{w}\right)$ in the equation 2.14. This equation provides a useful tool for engineering designs by working out any of the parameters if the other two are known. By comparing equation 2.15 with equation 2.11, the K_{IC} value can be related to the viewpoints of energy for plane stress situation as:

$$\sigma_f = \frac{K_{IC}}{Y\sqrt{\pi a}} = \sqrt{\frac{EG_c}{\pi a}} \rightarrow K_{IC}^2 = YEG_c \quad \dots 2.16$$

For the plane strain:

$$K_{IC}^2 = YEG_c(1 - \nu^2) \quad \dots 2.17$$

2.2.3 Crack tip plasticity

As mentioned in equation 2.12, in the linear elastic theory, the stresses in the vicinity of a crack tip can be expressed generally as:

$$\sigma_{ij} = \frac{K}{\sqrt{2\pi r}} f_{ij}(\theta) + \dots \quad \dots 2.18$$

According to equation 2.18, when r approaches zero, the stresses become infinite at the crack tip. However, in reality, the stresses near the crack tip can be relaxed by inelastic deformation, such as plasticity in metallic materials. The plastic strains in most solid materials are developed when the stress around the crack tip exceeds material's yield strength. Hence, the linear elastic fracture mechanics (LEFM) gets less applicative in this inelastic deformed region.

The size of the plastic zone is restricted by the surrounding material and loading conditions. Irwin [16] considered a circular plastic zone with a diameter of $2r_y$ (as shown Figure 2.5). The scope of the plastic zone (r_y) then can be calculated by letting the $\sigma_y = \sigma_{ys}$, then:

$$r_y = \frac{1}{2\pi} \left(\frac{K}{\sigma_{ys}} \right)^2 \quad \dots 2.19$$

However, Irwin [16] also observed that the occurrence of plasticity caused the crack show larger displacements and lower stiffness than in the elastic cases. Because the crack displacements became larger and the stiffness was lower than in the elastic case. This observation led him to put forward a concept of notional crack tip by a ‘plastic zone correction’ to the crack length, which is at the center of the circular plastic zone as shown in Figure 2.5. Moreover, beyond the plastic zone, the elastic stress distribution should be calculated by the notional crack size.

In the case of a through-thickness crack in a non-infinite specimen, if the thickness is small and $\sigma_z = 0$, but the strain is not zero on the free surfaces, thus the stresses normal to the free surfaces are absent. Nevertheless, towards the center of the crack front, the stress becomes triaxial, and the plane strain is present. Hence, the plastic zone at the tip will vary in the thickness direction along the crack front from plane stress at the side surface to plane strain in the center (shown in Figure 2.6). For the plane strain condition, the plastic zone is restrained by the triaxial stress field, thus for a small plastic zone radius under plane strain condition, the estimated r_y is as follows [16]:

$$r_y = \frac{1}{2\pi} \left(\frac{K}{C\sigma_{ys}} \right)^2 \quad \dots 2.20$$

Dugdale model [17] is another commonly used model for estimating the size of the yield zone ahead of a Mode I crack. In the Dugdale model, the plastic region is assumed as a narrow strip zone with zero height along the crack tip extending a distance r each side, and loaded at a yield stress of σ_{ys} . There is an internal crack with a crack length $2a$ that tends to grow to a length $2c$ ($r = c - a$), and internal stresses tend to close this crack in the region $|a| < |x| < |c|$ (see Figure 2.7). As shown in Figure 2.7, all plastic

deformation in crack plane ($\theta = 0$; $r > 0$), the applied stress intensity factor can be expressed as:

$$K_I(\sigma) = \sigma\sqrt{\pi(a+r)} \quad \dots 2.21$$

and the stress intensity factor due to yielding ahead of the crack tip can be expressed as:

$$K_I(\sigma_{ys}) = -\frac{2\sigma_{ys}}{\pi}\sqrt{\pi(a+r)}\arccos\left(\frac{x}{a+r}\right) \quad \dots 2.22$$

Assume that stress singularities are zero, then $K_I(\sigma) = -K_I(\sigma_{ys})$, and simplified equation takes the form as:

$$\frac{\pi\sigma}{2\sigma_{ys}} = \arccos\frac{x}{a+r} \rightarrow \frac{x}{a+r} = \frac{a}{c} = \cos\left(\frac{\pi\sigma}{2\sigma_{ys}}\right) \quad \dots 2.23$$

Let $y = \cos\left(\frac{\pi\sigma}{2\sigma_{ys}}\right)$, then

$$\frac{x}{a+r} = \cos y \rightarrow r = a(\sec y - 1) \quad \dots 2.24$$

The trigonometric function can be expanded as:

$$\sec y = 1 + \frac{y^2}{2!} + \frac{y^4}{4!} + \frac{y^6}{6!} + \dots \simeq 1 + \frac{y^2}{2!} \quad \dots 2.25$$

For $\sigma \ll \sigma_{ys}$, the higher order terms can be neglected, then the plastic zone size can be expressed as:

$$r = \frac{ay^2}{2} = \frac{\pi^2 a^2}{8\sigma_{ys}^2} \quad \dots 2.26$$

Comparing Irwin's and Dugdale's models for estimating the plastic zone size under plane stress conditions, the difference between the two approaches can be derived:

$$r(\text{Irwin}) = \frac{8}{\pi^2}r(\text{Dugdale}) = 0.81r(\text{Dugdale}) \quad \dots 2.27$$

The difference becomes significant as $\sigma/\sigma_{ys} \rightarrow 1$, but similarities also exist at $0 < \sigma/\sigma_{ys} \lesssim 0.2$. Therefore, care needs to be taken when about selecting which approximation method to be used at high stress ratios.

2.3 Elastic-Plastic fracture mechanics

The linear elastic fracture mechanics is only applicable for limited crack tip plasticity conditions that the plastic zone must be smaller than the crack size and the cracked

body remains nearly elastic. When the nonlinear deformation of material is confined to a small region near the crack tip, it is necessary to use Elastic-Plastic Fracture mechanics (EPFM) to solve these problems. Although the EPFM is not as well developed as LEFM theories, it contributes a great extent of solutions in analysing fracture beyond the elastic scale.

2.3.1 The J -integral

The crack-path independent J integral, as presented by Rice [12], is a line integral used as a parameter to describes the intensity of the near-tip stress and deformation fields which is similar to the way that the stress intensity factor represent the stress and strain in linear elastic materials. Consider a cracked linear body subjected to a monotonic load as shown in Figure 2.8, all stresses σ_{ij} are only dependent on two Cartesian coordinates (x,y), the strain-energy density (W) can be expressed as:

$$W = W(x, y) = W(\epsilon) = \int_0^\epsilon \sigma_{ij} \partial \epsilon_{ij} \quad \dots 2.28$$

and the J integral along any contour (Γ) encircling the crack tip can be defined as:

$$J = \int_{\Gamma} (W \partial y - T \frac{\partial u}{\partial x} \partial s) \quad \dots 2.29$$

where u is the displacement vector, y is the distance along the direction normal to the plane of the crack, ds is an incremental length along the path Γ , and T is the components of the vectors of traction [13, 18]. J also can be thought of as the energy flow into the crack tip. Therefore, in the case of elastic-plastic fracture behaviour, J provides a way of measuring the singularity strength at the crack tip. It is worth noting that the path Γ of J integral is evaluated counterclockwise starting from the lower surface and ending at the upper surface of the crack [13]. Rice showed that the stress energy release rate (G) in a linear elastic material for small-scale yielding is equivalent to the rate of change of potential energy for a nonlinear elastic solid (J). Hence, the stress intensity factor can be defined by G as follows:

$$G = \frac{K_I^2}{E^*} \quad \dots 2.30$$

$$J = G = \frac{K_I^2}{E^*} \quad \dots 2.31$$

$$\rightarrow K_I = \sqrt{JE^*} \quad \dots 2.32$$

where $E^* = \frac{E}{1-\nu^2}$ for the plane strain condition and $E^* = E$ for the plane stress condition. Similar to the stress intensity factor in LEFM, it is reasonable to assume there is also a critical value of J as J_{IC} can allow the crack to extend. It was found that J is equal to the energy release rate $G_{IC} = 2\gamma_s$, therefore, $J_{IC} = G_{IC} = 2\gamma_s$.

For nonlinear elastic solid, Hutchinson and Rice and Rosengren [18] found the so called HRR singular behaviour of strength, strains and displacements around the crack tip and showed that the strength of the near-fields is the J -integral. Although the J -integral concept has limitation in the plastic zone near the crack tip because unloading occurs there as a crack grows, it would be useful in the case of plane strain, predicting a reasonable energy release rate and the crack driving force in certain elastic-plastic fracture problems [13].

2.3.2 The R-curve

The crack extension resistance curve (R-curve) approach was also established by Irwin, which attempts to examine the processes of slow stable crack growth and unstable fracture in terms of the relationship between the crack size and the total energy dissipation rate. The fracture resistance can be represented in terms of energy (G_R , R or J_R) or sometimes stress intensity factor (K_R) [13].

In many high toughness materials, the failure does not occur at a certain value of J or crack tip opening displacement (CTOD), but these two parameters increase with crack growth showing a rising R curve behaviour. The rising R curve is normally caused by

the growth and coalescence of microvoids around the crack tip. A schematic diagram of a typical J resistance curve for a ductile material is shown in Figure 2.9. As indicated in the diagram, the crack extension is not prompt because of crack blunting, while the J increases dramatically. When the J is high enough, the crack tip becomes sharper somewhere as the crack advances and propagates faster. The slope of J resistance curves reveal the stability of the crack growth, a steep R curve is probably associated with unstable crack propagation. The slope is usually expressed by a dimensionless tearing modulus:

$$T_R = \frac{E}{\sigma_o^2} \frac{dJ_R}{da} \quad \dots 2.33$$

where J_R is a value of J on the resistance curve. Unstable crack growth appears when the driving force curve is tangent to the R curve. The R -curve behaviours are different between load control condition and displacement control conditions. As shown in Figure 2.10, under the load control condition, the crack growth is less stable than the displacement control. The driving force can be also expressed as the same R -curve slope by an applied tearing modulus:

$$T_{app} = \frac{E}{\sigma_o^2} \left(\frac{dJ}{da} \right)_{\Delta_T} \quad \dots 2.34$$

where Δ_T is the total remote displacement defined as:

$$\Delta_T = \Delta + C_m P \quad \dots 2.35$$

and C_m is the system compliance. For a stable crack growth, there is condition tenable as:

$$J = J_R \text{ and } T_{app} \leq T_R \quad \dots 2.36$$

and when $T_{app} \geq T_R$, unstable crack growth occurs.

In small-scale yielding, there is a J -dominated zone as long as the crack tip and plastic zone do not reach the specimen surfaces, which is only dependent on the real-time load and crack size. The J -controlled crack growth condition is shown in Figure 2.11. To meet the J -controlled condition, the elastic unloading and nonproportional plastic loading zones must be within the J -dominated zone [19]. Three distinct stages can be

identified in crack growth resistance curves as presented in Figure 2.12. As mentioned above, the crack growth during the initial stage exhibits a finite slope because of crack tip blunting which also has a continuous influence on the crack-tip stresses and strain at stage 2. At the stage 2, the slope becomes steeper as a result of fracture initiation [19, 20]. When the crack propagates far away from the initial stage, the slope of the R curve decreases and approaches a steady-state condition, where the local stresses and strains no longer depend on the extent of crack growth [19].

2.3.3 The crack tip opening displacement (CTOD) approach

Although the J-integral and R-curve concepts can provide some solutions in characterising the elastic-plastic fracture mechanics, they all have limited scope of applications. For instance, the R-curve concept is not applicable if the plastic zone intersects with the specimen boundaries, and the J-integral is only practicable for stationary cracks. It is necessary to have an approach to describe the near-tip crack profile [12]. Wells [21] introduced the crack tip opening displacement (CTOD) approach as a measurement for fracture toughness where finite strain deformation is dominant. The schematic definition of CTOD is shown in Figure 2.13. The opening displacement of the original crack tip is defined as δ , which can be analysed using Dugdales strip yield model. This displacement is the distance between two intersection points of a 90° vertex with the upper and lower crack faces. The Wells modeling approach can be expressed in terms of K as:

$$\delta = \frac{4}{\pi} \frac{K_I^2}{\sigma_{ys}^* E^*} \quad \dots 2.37$$

where $E^* = E$ and $\sigma_{ys}^* = \sigma_{ys}$ for plane stress, and $E^* = E/(1 - \nu^2)$ and $\sigma_{ys}^* = \sigma_{ys}/(1 - 2\nu)$ for plane strain [12]. Alternatively, CTOD can also be related to the energy release rate (\mathcal{G}) for small-scale yielding as [19]:

$$\delta = \frac{4}{\pi} \frac{\mathcal{G}}{\sigma_{ys}} \quad \dots 2.38$$

Dugdale [19] latterly conducted a strip-yield model as an alternate method to analyse CTOD. The CTOD is defined as the crack opening displacement at the end of the strip-yield zone, as shown in Figure 2.14. The material in this strip is assumed as having a perfect plastic manner. This model provides a solution for a center Mode I crack in an infinite plate under a remote tensile stress as:

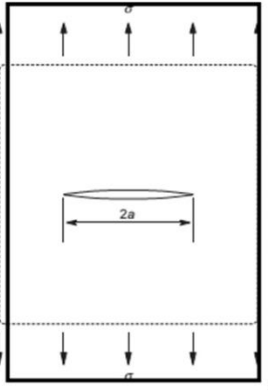
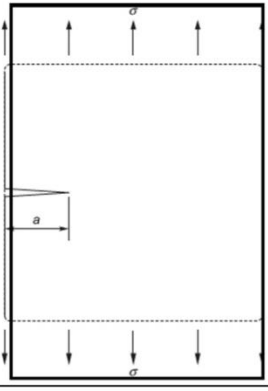
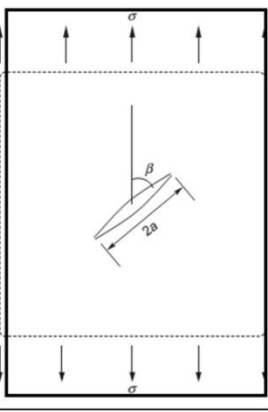
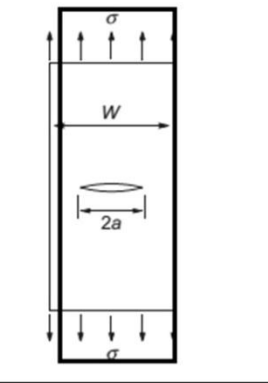
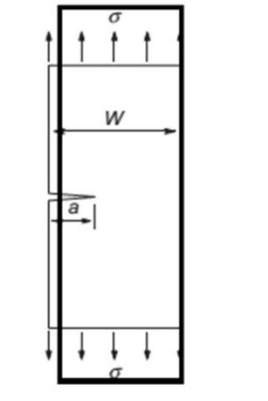
$$\delta = \frac{8\sigma_{ys}a}{\pi E} \ln \sec\left(\frac{\pi}{2} \frac{\sigma}{\sigma_{ys}}\right) \quad \dots 2.39$$

In small-scale yielding for linear elastic materials, the J-integral and the CTOD have a relationship, that is:

$$J = \mathcal{G} = \frac{K^2}{E} = m\sigma_{ys}\delta \quad \dots 2.40$$

where m is a dimensionless constant which depends on the stress state and material properties [19]. For plane stress condition and non-hardening materials, m=1, and m=2 for plane strain condition [22].

Table 2.1. The stress intensity factors of some common geometries [17]

	<p>Center-Crack, length $2a$, infinite plate, Tension</p> $K_I = \sigma\sqrt{\pi a}$	 <p>Single-Edge- Cracked, length a, semi-infinite body, Tension</p> $K_I = 1.12\sigma\sqrt{\pi a}$
	<p>Single Inclined Crack, length $2a$, infinite plate, Tension</p> $K_I = \sigma\sqrt{\pi a} \sin^2 \beta$ $K_{II} = \sigma\sqrt{\pi a} \sin \beta \cos \beta$	
	<p>Center-Cracked, Length a, plate of width W, Tension</p>	$K_I = \sigma\sqrt{\pi a}F(\alpha), \quad \alpha = 2a/W$ $F(\alpha) = \sqrt{\sec(\pi\alpha/2)}$ <p>Accuracy: 0.3% for $\alpha \leq 0.7$</p> $F(\alpha) = 1 + 0.128\alpha - 0.288\alpha^2 + 1.525\alpha^3$ <p>Accuracy: 0.5% for $\alpha \leq 0.7$</p> $F(\alpha) = (1 - 0.5\alpha + 0.37\alpha^2 - 0.044\alpha^3) / \sqrt{1 - \alpha}$ <p>Accuracy: 0.3% for any α</p>
	<p>Single-Edge- Cracked, Length a, plate of width W, Tension</p>	$K_I = \sigma\sqrt{\pi a}F(\alpha), \quad \alpha = a/W$ $F(\alpha) = 1.122 - 0.231\alpha + 10.55\alpha^2 - 21.71\alpha^3 + 30.38\alpha^4$ <p>Accuracy: 0.5% for $\alpha \leq 0.6$</p> $F(\alpha) = \sqrt{\frac{2}{\pi\alpha} \tan \frac{\pi\alpha}{2}} \left[0.752 + 2.02\alpha + 0.37 \left(1 - \sin \frac{\pi\alpha}{2} \right)^3 \right] / \cos \frac{\pi\alpha}{2}$ <p>Accuracy: 0.5% for any α</p>

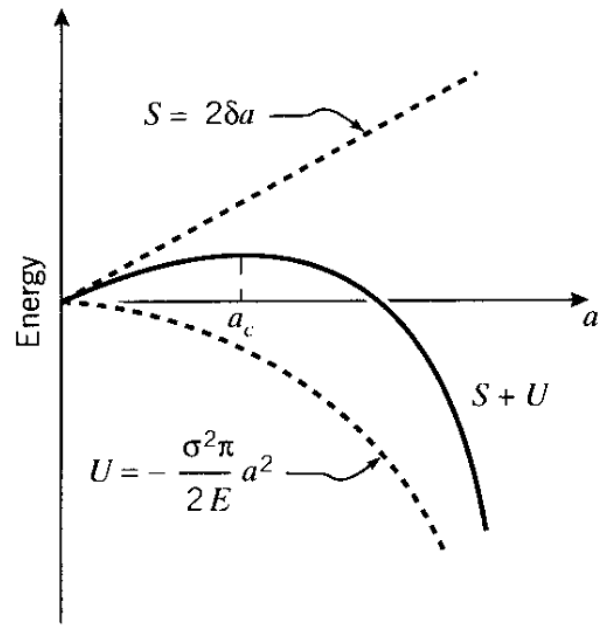


Figure 2.1. Schematic diagram of the fracture energy balance theory. S is the surface energy, U is the strain energy released per unit thickness of specimen, a is the crack length [11]

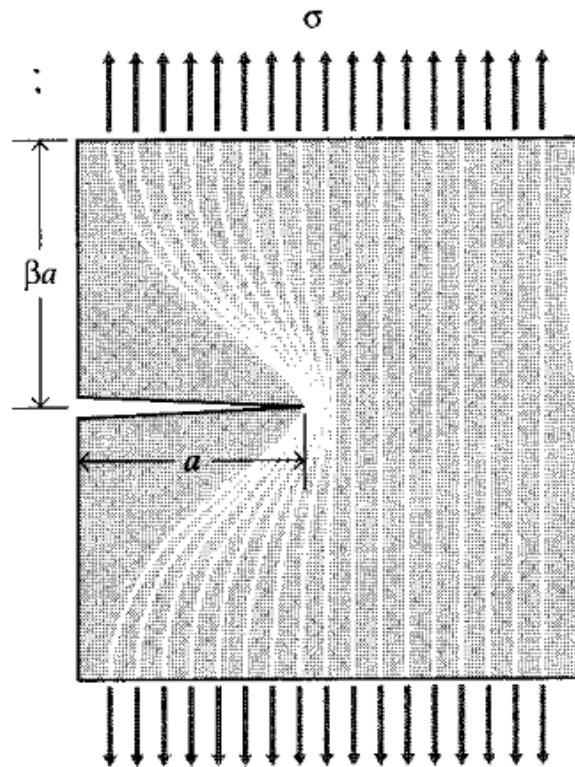


Figure 2.2. Idealisation of unloaded region in a solid near the free surface [11]

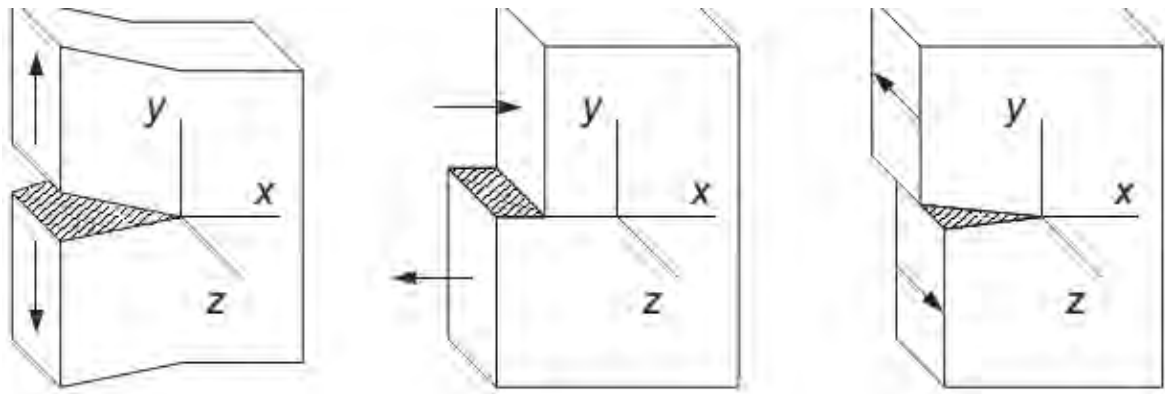


Figure 2.3. Three modes of crack fracture [12]

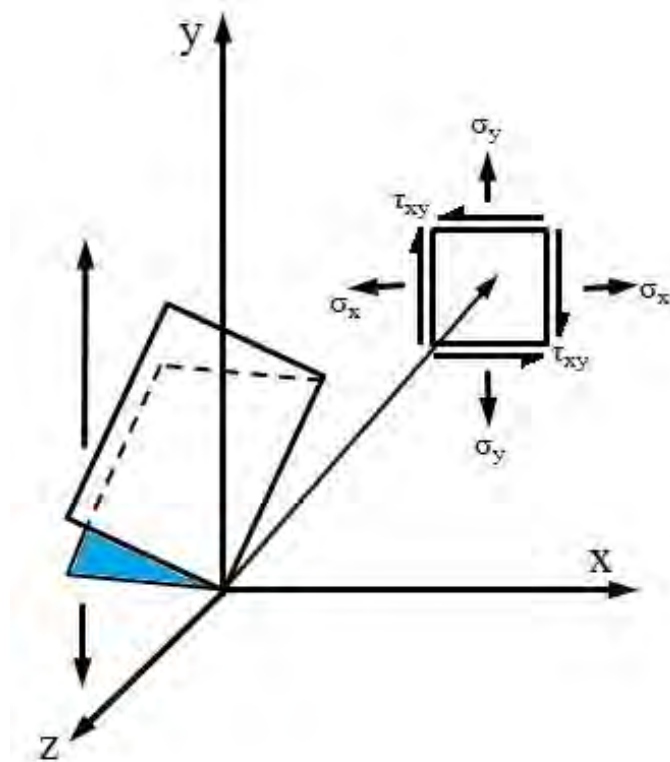


Figure 2.4. Distribution of stresses in vicinity of crack tip under mode I loading condition

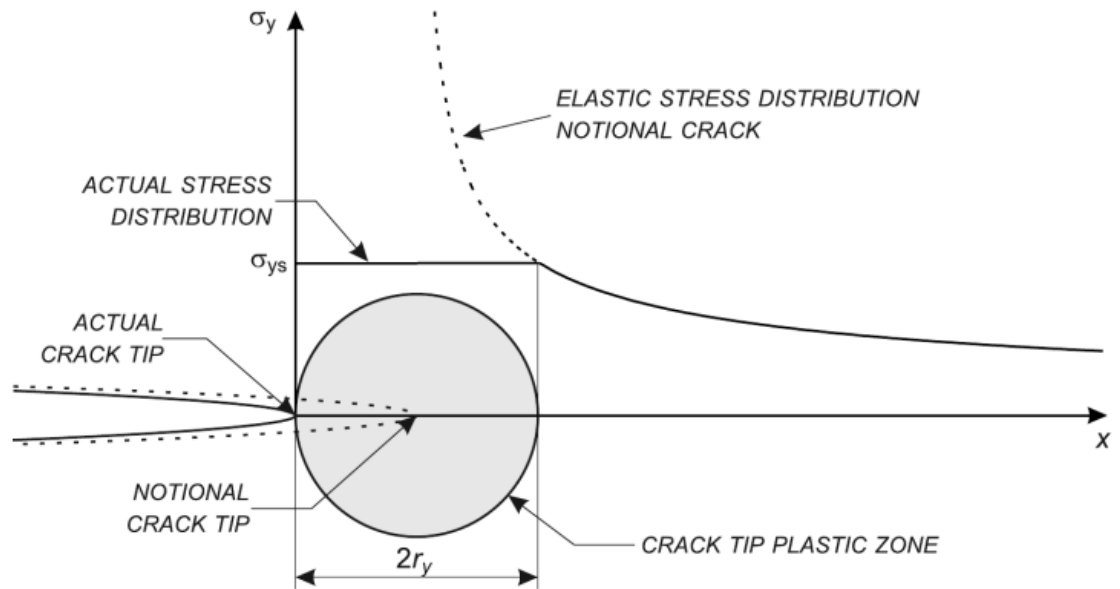


Figure 2.5. The crack tip plastic zone proposed by Irwin [16]

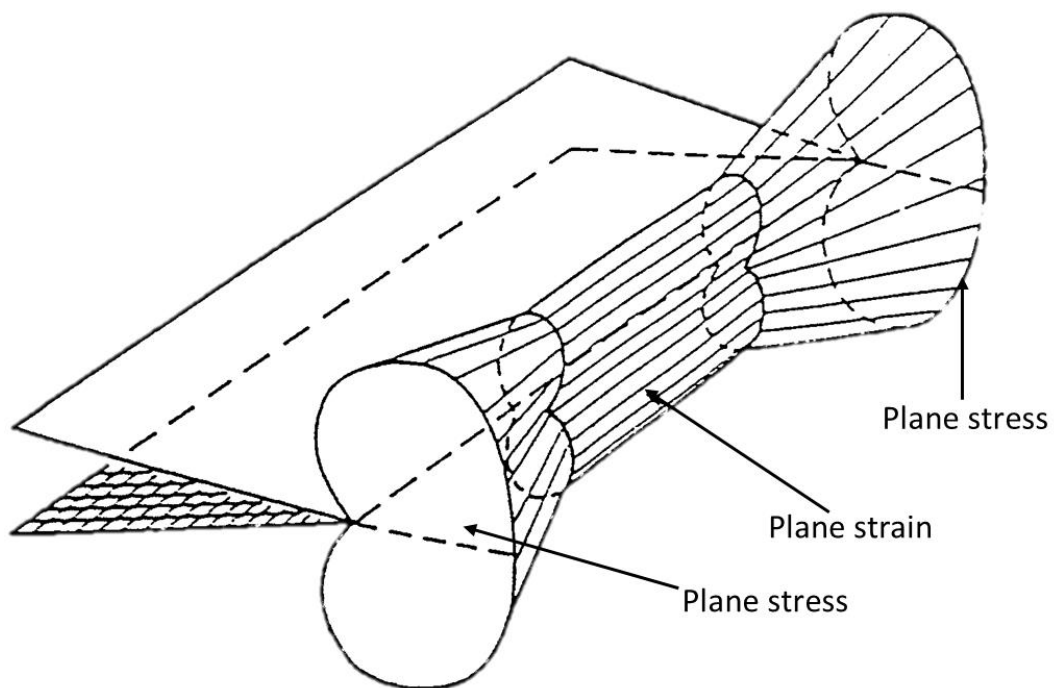


Figure 2.6. Variation of plastic zone of through-thickness crack in non-infinite specimen

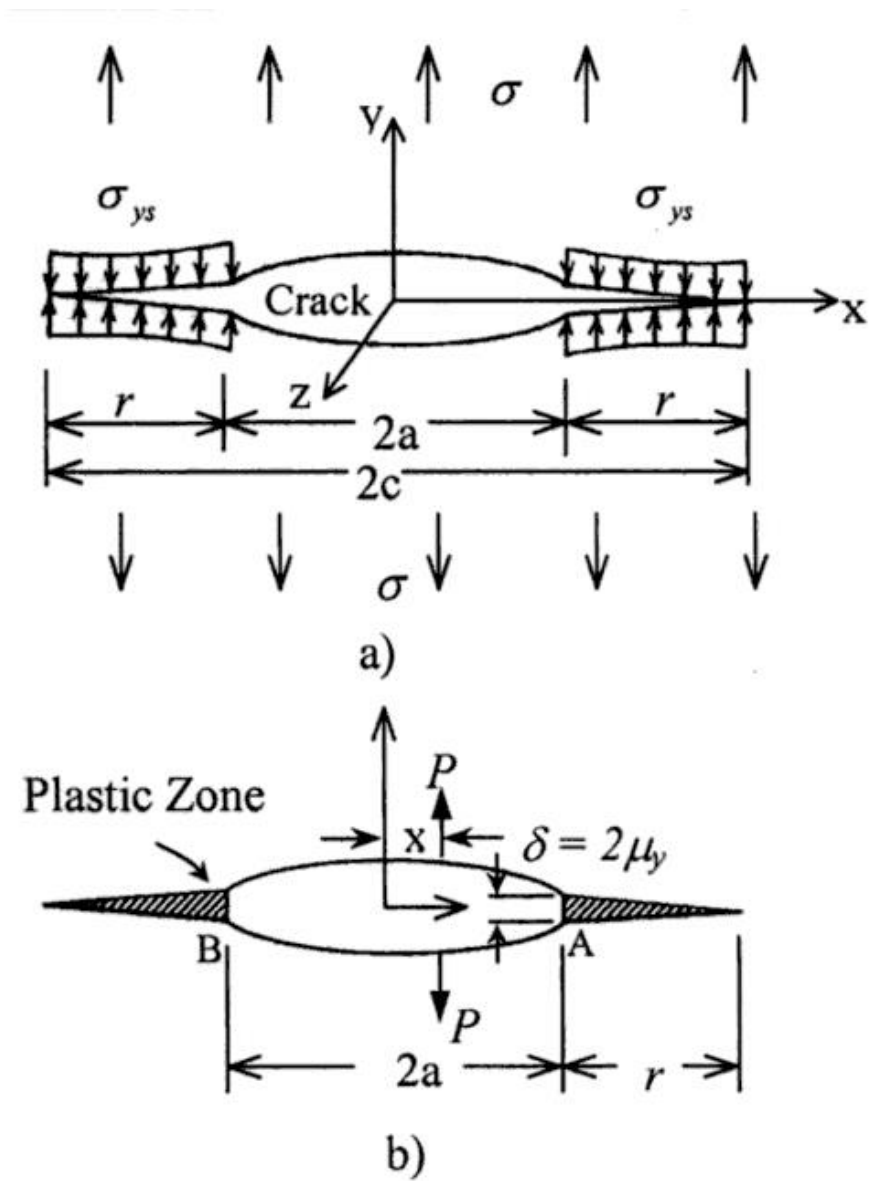


Figure 2.7. Dugdale plastic zone strip model for non-strain hardening plastic solid (subjected to plane stress deformation): (a) Dugdale crack and (b) wedge crack [14]

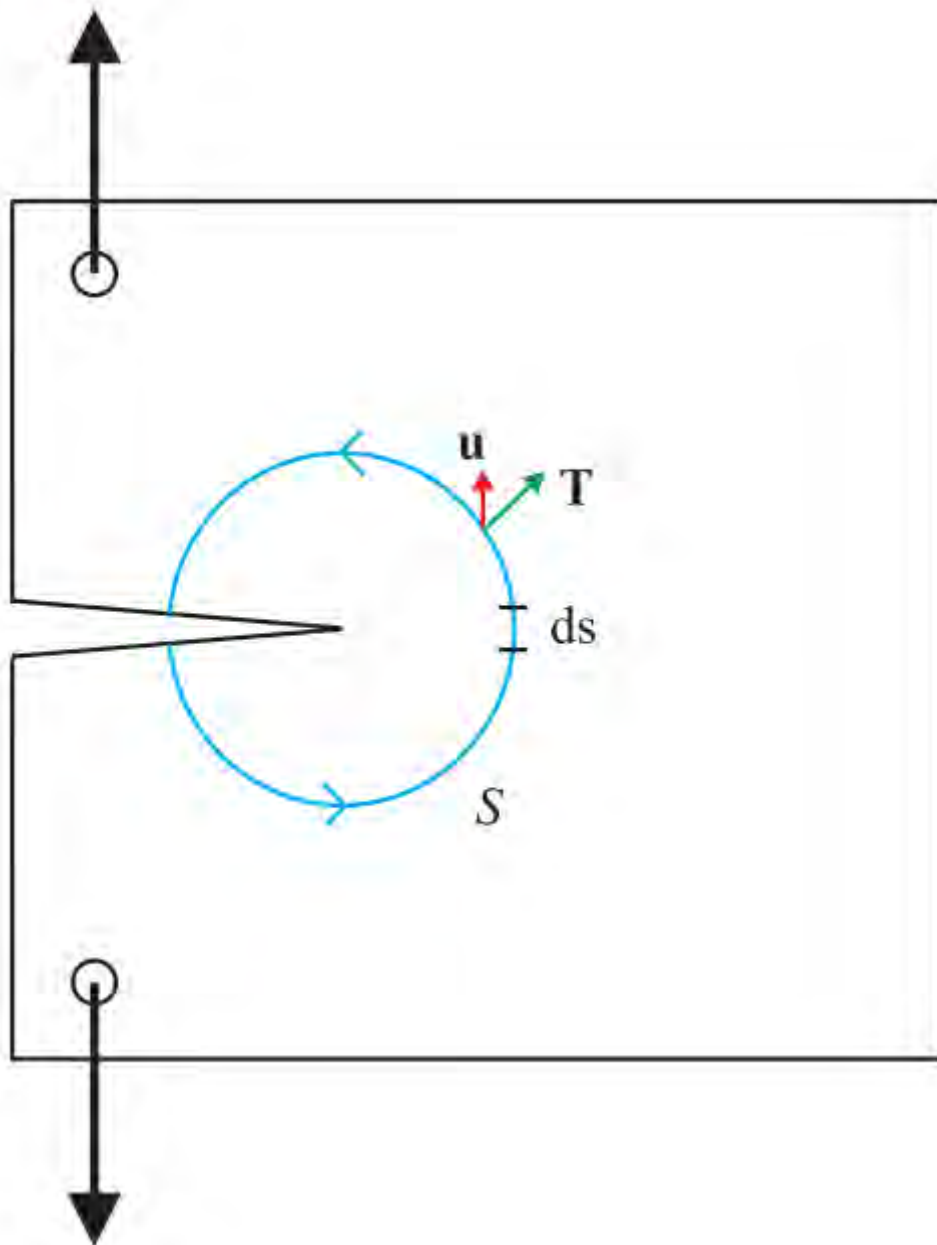


Figure 2.8. A typical line integral contour around a crack tip used for defining the J integral [18]

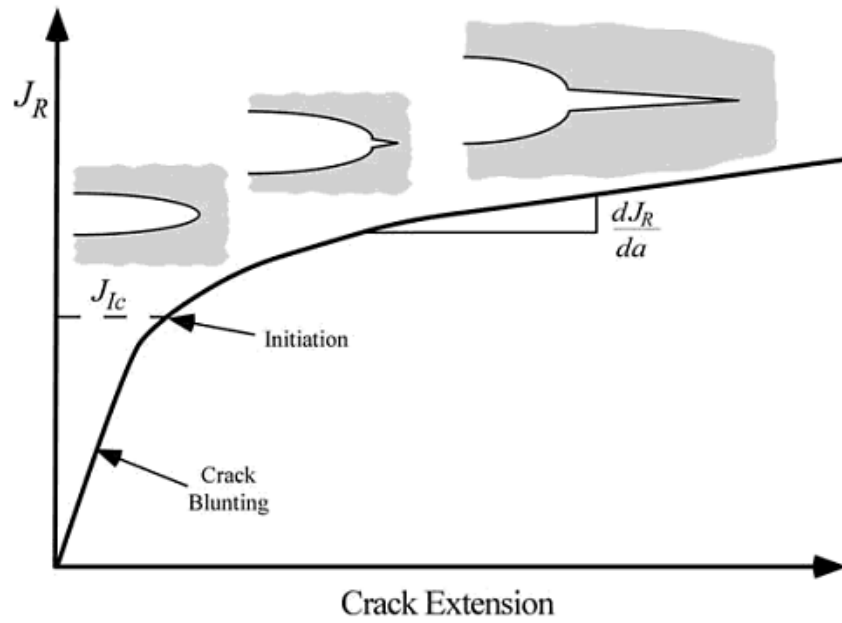


Figure 2.9. Schematic diagram showing a typical J resistance curve for a ductile material [19].

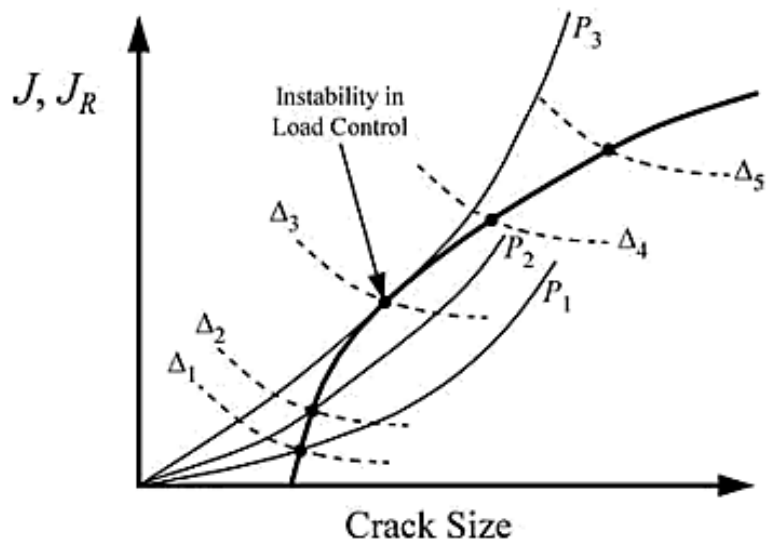


Figure 2.10. J driving force/R curve diagram showing the comparison of load control and displacement control [19]

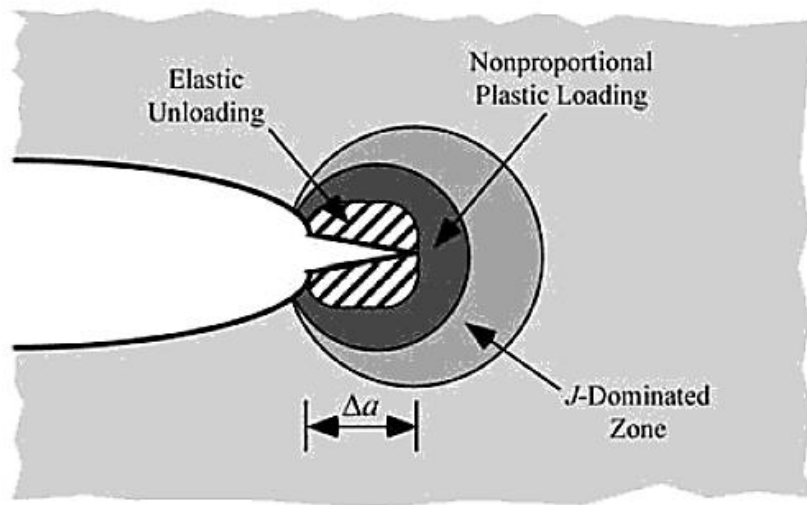


Figure 2.11. crack growth under J-controlled condition [19]

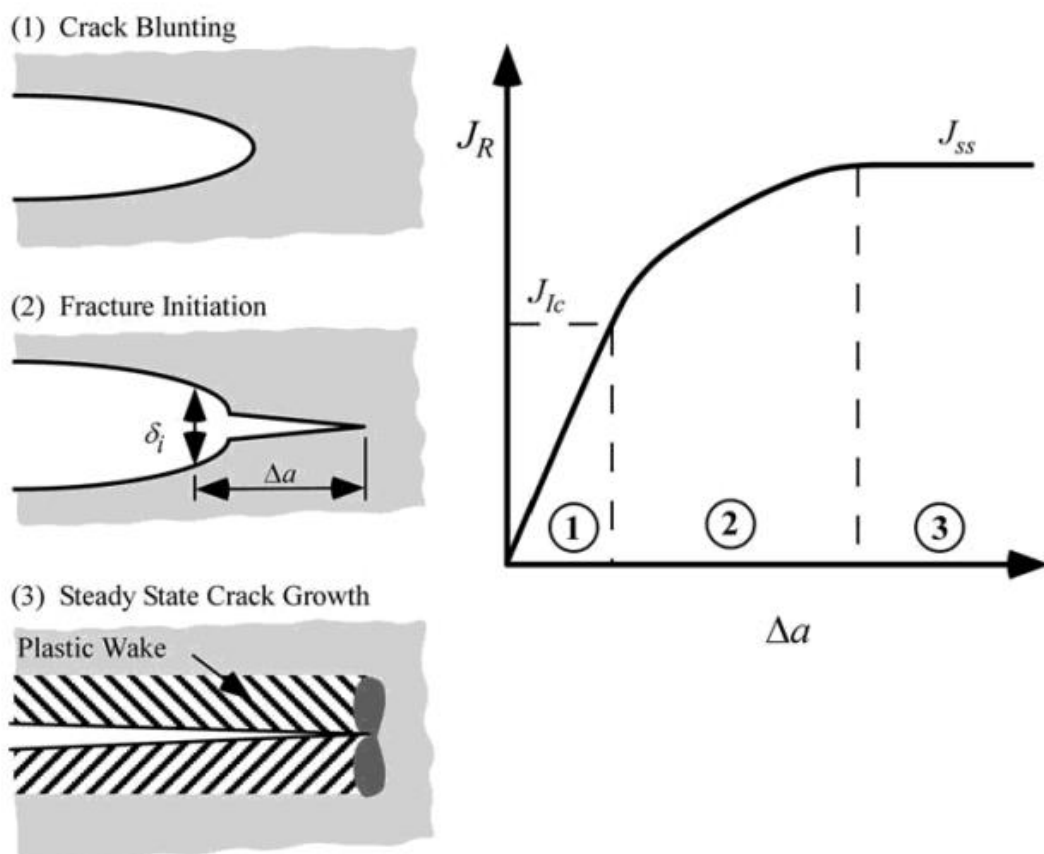


Figure 2.12. The three distinct stages in a crack growth resistance curve in an infinite body [19]

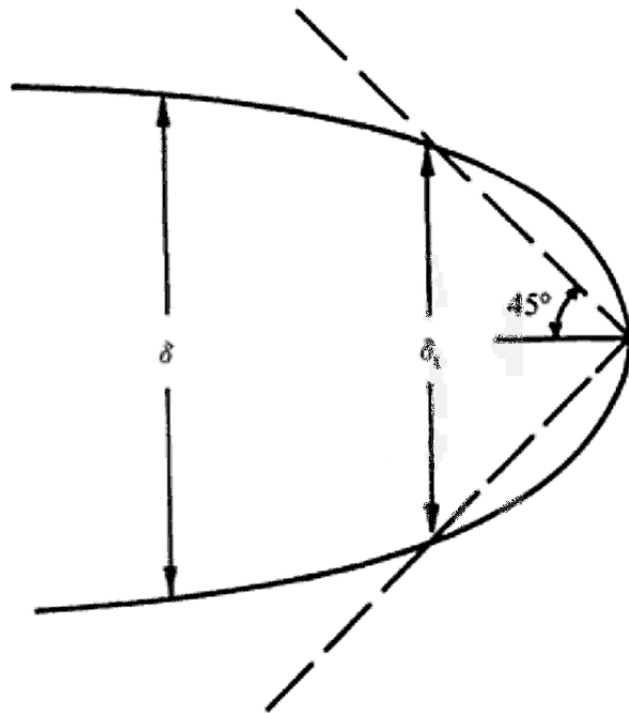


Figure 2.13. Definition of crack tip opening displacement (CTOD), δ [18]

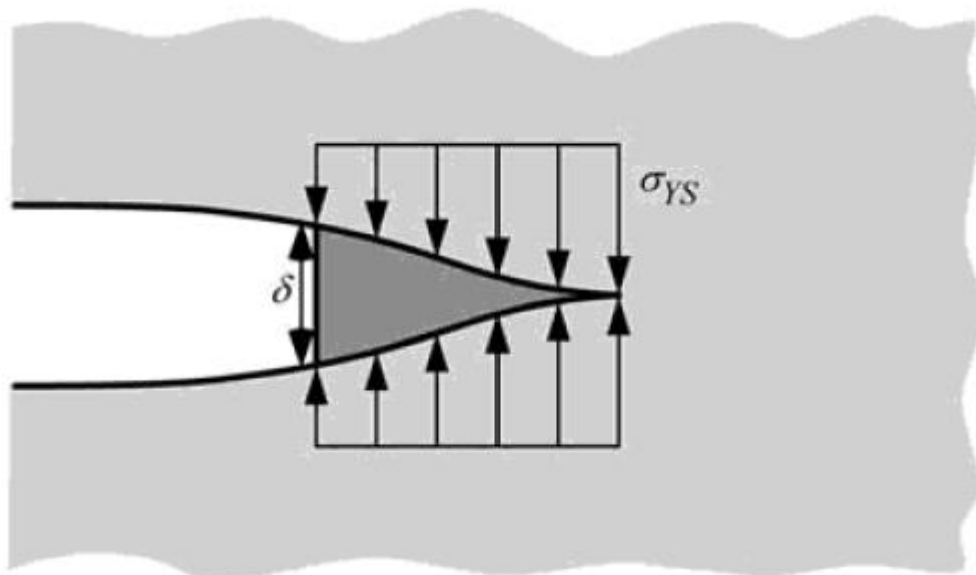


Figure 2.14. Dugdale type of strip-yield zone for estimation of CTOD [19]

3. Fatigue

3.1 Introduction of fatigue

Fatigue is the process which causes local cracking due to cyclic loading. It involves the initiation and evolution of cracks at loads that are far below the static strength of a material. Fatigue cracks can initiate very slow but their propagation rate increases dramatically with the increasing crack length. 90% of all mechanical failures have been reported to have occurred as a consequence of fatigue [23]. Therefore, fatigue of structural material is regarded as a crucial problem for engineering design.

In terms of metals, the fatigue process starts at an internal or surface defect where the stresses are concentrated, and continuously develops due to shear flow along slip planes. After a number of cycles, slip steps will be created due to cyclic slip, and begin to resemble a crack [11]. As soon as fresh material surface created, it will be immediately covered by an oxide layer in most environments [23]. The fatigue process usually cannot be fully reversible for two reasons. First, the oxide layers cannot be easily removed and thereby arrests some slip at the fresh crack surface. Secondly, strain hardening in the slip band is not fully reversible. Thus, the reversed slip can only occur on adjacent parallel slip planes instead of the original slip plane [23]. On a typical fatigue fracture surface, the clamshell region which contains concentric “beach marks” can be observed, and each clamshell marking may represent hundreds or thousands of cycles. The final fracture region is usually very rough [11].

There are some basic factors that are used to characterise a fatigue process as shown in Figure 3.1. These are: (1) Maximum stress (σ_{max}) and Minimum stress (σ_{min}); (2) Mean stress (σ_m): $\sigma_m = \frac{\sigma_{max} + \sigma_{min}}{2}$; (3) Load/stress ratio, (R): $R = \frac{\sigma_{min}}{\sigma_{max}} = \frac{K_{min}}{K_{max}}$; (4) stress amplitude ($\Delta\sigma$): $\Delta\sigma = \frac{\sigma_{max} - \sigma_{min}}{2}$; (5) Frequency of loading cycle (f); and (6) the loading waveform. In addition, there are a host of other variables, such as temperature,

temperature variation, corrosion, oxidation, surface finish, coatings and microstructure. These variables can be considered by using a number of empirical laws and different testing methods. According to the variables listed above, the fatigue conditions can be classified into two regimes: high-cycle fatigue and low-cycle fatigue.

High-cycle fatigue (HCF): Low amplitude stresses result in primarily elastic strains and so that fatigue life is long, i.e. ($N > 10^5$ cycles). HCF data is usually presented by S-N curves (see in section 3.2.1) [24].

Low-cycle fatigue (LCF): usually low frequency, in the case of gas turbines due to engine start/stop or throttle cycles. Significant plastic deformation during cyclic loading, and the fatigue life is relatively short ($N < 10^4$ cycles). LCF data are often presented by plotting the plastic strain range, $\Delta\epsilon_p$, against cycles to failure, N , which can be described by the Coffin-Manson equation [24]:

$$\frac{\Delta\epsilon_p}{2} = \epsilon'_f (2N)^c \quad \dots 3.1$$

where ϵ'_f is a constant named fatigue ductility coefficient, and c is an empirical constant known as the fatigue ductility exponent of which the range is about -0.5 to -0.7 for common metal materials.

3.2 Different approaches to fatigue

3.2.1 Total-life approaches

This approach focuses on predicting the fatigue life i.e. total cycles to failure (N) in order to retire a component before fatigue cracks cause final rupture. S-N curve is usually used to characterise the total fatigue life for HCF where the stress range is low and the stresses are theoretically elastic. For LCF, the stresses are much higher than HCF and so that plastic strain may be extensive. Thus strain range can be used as a reference for fatigue total life.

The S-N curve is the most important concept to characterise HCF, in which the constant cyclic stress amplitude (S) is plotted as a function of the total number of loading cycles (N). In some materials, usually ferrous alloys, there is a fatigue limit below which failure does not occur no matter how many loading cycles are applied and the S-N curve becomes flat after a certain number of cycles [24]. However, for other materials, such as aluminum, no fatigue limit exists. Hence the lifetime of a component should be designed to be less than the failure point on the S-N curve of the material for the most severe condition.

3.2.2 Damage-tolerance approach

For a structure with inherent flaws, it is necessary to know the crack growth rate and crack size to ensure that flaws will not grow to a critical size and cause catastrophic failure. The damage-tolerance approach was adopted by the U.S. Air Force in order to predict an accurate fatigue life of a structure with initially existing flaws. A damage tolerance approach aims to solve two questions for an initially cracked structure: the critical crack length under a certain fracture stress and the length of time for a crack to grow to the critical size leading to the final fracture at the given stress [25].

The use of linear elastic fracture mechanics enables the prediction of critical crack size by knowing the applied stress and the critical stress intensity factor, K_{IC} . Therefore, nominally elastic behaviour is required for the analysis, but small amounts of crack-tip plasticity are allowed [25]. For purposes of determining the initial crack size, Non-Destructive Testing (NDT) techniques, such as X-ray, ultrasonic, dye penetrant or eddy current are often used. The crack growth rate is exponential in nature, and when it is plotted versus the corresponding crack length, i.e. the fatigue crack resistance curve, the fatigue behaviour of a material can be revealed [18].

3.3 Fatigue crack growth resistance curve (da/dN vs. ΔK curve)

The fatigue crack growth tests are mostly carried out under constant load amplitude test condition with a sharp mode I crack. The fatigue crack growth rate is usually expressed by a log-log plot of da/dN versus ΔK curve, i.e. fatigue crack growth resistance curve (FCGRC). The fatigue crack growth rate, da/dN , is the instantaneous slope of an a - N curve at a particular crack length. The corresponding applied stress intensity factor range, ΔK , can be calculated by knowing the crack length (a), applied stress range ($\Delta\sigma$), and the stress intensity factor solution, as given by the following equations:

$$\Delta\sigma = \sigma_{max} - \sigma_{min} \quad \dots 3.2$$

$$\Delta K = K_{max} - K_{min} = Y\Delta\sigma\sqrt{\pi a} \quad \dots 3.3$$

In equation 3.2, the σ_{max} and σ_{min} are the maximum and minimum stresses of cyclic fatigue loading, respectively. In equation 3.3, the K_{max} and K_{min} are the maximum and minimum stress intensity factors of cyclic fatigue loading, respectively. Y is dimensionless geometry parameter.

A typical sigmoidal FCGRC for normal engineering materials has been found to have three regimes as shown in Figure 3.1. The three regimes exhibit different fatigue crack growth behaviours, behind which the failure mechanisms are various as well.

Regime I: This is the near threshold region. There is a fatigue threshold value, ΔK_{th} , below which the fatigue crack cannot propagate. Once a crack is initiated, it prefers to propagate along the maximum shear stress planes (45° to the loading axis). The naturally-initiate cracks are likely to occur within microstructural units, such as grain boundaries, lamellar interfaces, thus often shows short crack growth behaviours. Grain boundaries, inclusions, precipitates can act as microstructural barriers to decelerate the crack propagation. Hence, at this regime the crack growth is extremely sensitive to the microstructure since the ΔK value is low. Grain refinement and surface treatments are effective ways to increase microstructural barriers at this regime to restrict crack

initiation and propagation [26]. Load ratio also has strong influences on the fatigue crack initiation, which is associated with effective stress intensity factor range, ΔK_{eff} . The influence of load ratio on ΔK_{eff} is associated with crack closure shielding mechanism which can increase the effective minimum stress intensity in a fatigue cycle [27]. The concepts mentioned above are usually applied for long fatigue cracks. Short fatigue cracks often exhibit difference fatigue behaviour in this regime, and the reasons will be given in section 3.6.

Regime II: This regime is also called “Paris Law” regime, where the slope of the $\log da/dN$ vs. ΔK curve is approximately linear and can be described by the Paris Law equation, which was proposed in the early 1960s as follows [18]:

$$\frac{da}{dN} = C(\Delta K)^m \quad \dots 3.4$$

where C and m are material constants. The value of m is the slope of the liner relationship, and it is usually used as a parameter to examine and describe the increasing speed of fatigue crack growth.

Because the stress intensity becomes higher as a consequence of crack growth, the plastic zone around the crack tip is able to cover more grains. Therefore, the crack growth begins to involve more slip planes initiating regime II. Appearance of visible “striations” on the surface is an important sign of this stage. However, not all engineering materials exhibit striations, they are mostly found in ductile materials [26]. The possible reason to explain the formation of striations is that the successive blunting and re-sharpening of the crack tip [26].

Regime III: The crack growth rate increases dramatically to unstable status as K_{max} approaches K_{IC} . At this stage, the crack growth is mainly dominated by static fracture and is sensitive to the microstructure and stress ratio. On the fracture surface, there are two distinct fatigue fracture regions – stable fatigue crack growth region and unstable

fatigue crack growth region. The former has a relative smooth fracture surface while the fractographic feature of the latter is similar to that of monotonic load caused fracture [26]. The Paris Law relationship can be modified to estimate the FCGR by considering the R related mean stress level and fracture toughness (K_Q) of the material[28]:

$$\frac{da}{dN} = \frac{C(\Delta K)^m}{(1 - R)K_Q - \Delta K} \quad \dots 3.5$$

3.4 Factors affecting fatigue crack threshold and growth

3.4.1 Effect of mean load

The mean load has been found to have a strong influence on fatigue crack growth rates. The mean load can be indicated by the R ratio which has been defined above. Increasing the R ratio means increasing the mean stress, thus the FCGR tends to be increased although the increase of region II may be small. In addition, the fatigue life may be reduced by higher mean stress as well. As mean stress has significant influence on the fatigue crack growth, a number of mathematical models have been established in order to predict the effects of mean stress on stress amplitude from fully reversed-bending data [24]. The Goodman diagram is the most common method to solve this problem, shown in Figure 3.3 [11]. This diagram can be mathematically described as follows:

$$\frac{\sigma_a}{\sigma_e} + \frac{\sigma_m}{\sigma_f} = 1 \quad \dots 3.6$$

where σ_a is the alternating stress, σ_m is the mean stress, σ_e is the fatigue limit for completely reverse loading, and σ_f is the ultimate tensile stress [11]. This diagram can be used to predict the safe cyclic loading condition: stress conditions that fall under the line means that the material should not fail for the given stresses (mean stress and applied stress), and no failure at stresses in the area above the line. If knowing the ratio of σ_e to σ_a , by drawing a line from the origin with a slope equal to that ratio, the intersection point at the lifeline indicates the effective endurance limit for the

combination of σ_e and σ_f [29].

3.4.2 Temperature

At low temperature (around Room Temperature), the fatigue process involves crack initiation through intercrystalline slip on the surface, followed by transcrystalline propagation [30]. The fatigue mechanisms and macroscopic modes of failure in brittle materials are similar to those caused by monotonic loading. Because of bridging stresses and frictional contact between the pull-push grains and the crack faces, R-curve behaviour is more significant at low temperature than elevated temperature, especially in brittle materials [18].

At elevated temperatures ($\geq 0.5T_m$), grain boundary sliding and diffusion, and environmental interaction, such as stress corrosion cracking, oxidation, and hydrogen embrittlement, significantly affect the fatigue crack threshold and propagation [18]. On one hand, oxidation can lessen the slip reversibility and cause embrittlement of the material due to diffusion of oxygen so that the result is higher fatigue crack growth rates. On the other hand, oxidation can also improve fatigue crack growth resistance by reducing the crack opening displacement and thereby reducing the ΔK_{eff} , which is called oxidation-induced crack closure (see section 3.5.2).

In high temperature fatigue, there is a transition from fatigue failure to creep failure as the temperature increase, and the creep becomes dominant at high temperatures and high stresses. Creep-fatigue interaction is common during cyclic loading at elevated temperatures, which occurs when the cyclic stress or strain amplitude is large compared to the mean stress. For creep-fatigue alternate loading tests, the total failure time can be predicted by combination of Palmgren-Miner (P-M) rule for fatigue life with Robinson's (R) rule for creep life as:

$$\sum \frac{N_i}{N_{fi}} + \sum \frac{t_i}{t_{fi}} = 1 \quad \dots 3.7$$

where the two terms represent the portion of life time for pure fatigue and pure creep, respectively [31]. Both fatigue and creep failures are time-dependent. More time-dependent processes, such as increasing temperature, reducing the frequency and other environmental interactions, can greatly affect the fatigue life. It has been reported that temperature increase or frequency decrease causing fatigue life reduction is usually accompanied with a change of fracture mode from transgranular to intergranular [31].

3.4.3 Microstructure

As mentioned above, microstructure has a strong influence on fatigue crack growth behaviour in stage I and III, i.e. the crack initiation/near threshold region and unstable crack growth region. The material microstructure can affect the fatigue crack growth in several ways:

1. Grain size: A number of studies have been carried out on different materials to investigate the effect of grain size on fatigue crack growth. Fine grain structures have been shown to generally provide better fatigue resistance than coarse grains, except at elevated temperatures where creep-fatigue interaction exists. However, coarse grain is superior to fine grain in certain creep regimes [24]. Fine grains can also enhance fatigue crack growth resistance in two ways: reducing localised strains along the slip bands and the amount of irreversible slip; more grain boundaries can assist transcrystalline crack arrest and deflection, thus continuous crack propagation becomes more difficult [32]. Other grain size effects are associated with small/short crack behaviour and crack closure effects which will be discussed below.
2. Anisotropy: In polycrystalline materials, mechanical properties, such as Young's Modulus, fracture toughness and fatigue properties vary with texture orientation which is called material anisotropy. The anisotropy is usually produced by

manufacturing processes like casting, rolling, forging, and extrusion [33]. There are so-called “hard orientation” and “soft orientation” where crystallographic orientations that are favourable for fatigue crack growth of grains are near-parallel and near-perpendicular to the loading direction, respectively. Higher fatigue crack growth resistance is always found in grains that have a ‘hard orientation’. Therefore, when fatigue cracks reach hard-orientated grains, they may change the propagation path by deflection or renucleation in other “softer” grains, unless the driving force is high enough to allow them to grow transgranularly.

3. Inclusions, voids and porosity: The presence of defects in metallic materials, such as inclusions, voids and porosity, is usually due to impurity of raw material, oxidation during solidification, gas evolution, or incomplete sintering during consolidation. They can affect the fatigue properties of material in three ways: (1) act as stress concentration sites, (2) reduce the stress/strain required for crack nucleation (usually short cracks which may exhibit short crack behaviour), and (3) reduce total fatigue life. NDT techniques are often used to identify those defects before putting a component into service. Moreover, the damage-tolerance and total-life approaches can be used to calculate the critical defect size and predict fatigue life to failures.

3.5 Crack closure mechanisms and other retardation mechanisms

3.5.1 Concepts of crack closure

Most fracture mechanics concepts applied to fatigue crack growth considering the crack surfaces to be smooth, and the crack is zero-width. In practice, there is always crack surface contact with each other during fatigue loading. Elber firstly emphasised the importance of fatigue crack closure under a tensile load, and provided a quantitative method for its analysis [34]. After the discovery of “plasticity” induced crack closure,

several other closure mechanisms, such as roughness induced crack closure, oxidation induced crack closure, have been identified by Suresh, Ritchie et al. [18]. More types of crack closure mechanisms are presented in Figure 3.4. By introducing the crack closure concept, more types of fatigue crack growth behaviours have been able to be explained.

Due to the crack closure mechanism, the fatigue crack growth is retarded during fatigue cycling and is no longer simply dependent on K_{max} - K_{min} , but is decided by the effective stress intensity factor range which can be expressed as following relationship:

$$\Delta K_{eff} = K_{max} - K_{op} \quad \dots 3.7$$

where K_{op} refers to the lowest stress intensity factor for fully crack opening. Sometimes, the K_{op} can be replaced by K_{cl} which is the stress intensity at which the crack faces come into contact, i.e. close a crack. When $K_{min} < K_{op}$, the ΔK_{eff} can be written as equation 3.7. If $K_{min} > K_{op}$, $\Delta K_{eff} = K_{max} - K_{min}$.

One parameter used to define the effect of crack closure is the closure ratio [35]:

$$U = \frac{\Delta S_{eff}}{\Delta S} = \frac{S_{max} - S_{op}}{S_{max} - S_{min}} = \frac{\Delta K_{eff}}{\Delta K} = \frac{(1 - K_{op}/K_{max})}{(1 - R)} \quad \dots 3.8$$

where S represents stress. If there is little or no crack closure, the value of U approaches 1, and if the loading conditions show extensive crack closure, the value of U is small. According to LEFM, the fatigue crack growth rates can be characterised by this closure ratio as:

$$\frac{da}{dN} = C(\Delta K_{eff})^m = C(U\Delta K)^m \quad \dots 3.9$$

Most studies of crack closure effects on fatigue crack growth focus on regime I (threshold region) because: (1) crack closure is most significant since the K_{min} is lower than K_{op} ; (2) More influential factors are involved, such as environment, microstructure and stress ratio, which also have a direct influence on the crack closure mechanisms.

3.5.2 Different crack closure mechanisms

Plasticity-induced crack closure (PICC): Elber [18] proposed a hypothesis that crack closure is induced by the existence of residual strain left in the crack wake. This was obtained from the observation that crack surfaces remain in contact while the specimen as a whole is under a tensile load. This type of closure arises from residual compressive stress introduced by the elastic and plastic deformation during unloading in the plastic wake zone. During a new cycle, the crack tip remains closed until the applied load is high enough to overcome this compressive residual stress. Therefore, the fatigue crack growth rate is not only dependent on the stress field ahead of the crack tip, but also affected by the nature of crack face contact which is associated with factors such as the loading history, crack length and stress state. As the stress intensity factor increases, the size of the plastic zone ahead of crack tip becomes larger and so forms an envelope of plastic zone around the crack wake (as shown in Figure 3.5) [18].

Roughness-induced crack closure (RICC): This kind of closure is caused by the crack wedging effect of asperities and other protrusions on the crack surface. A small Mode II deflection occurs due to crack path deviation [24]. This deviation is caused by transcrystalline facets since cracks propagate at favorable orientations [36]. This concept provides explanation for many anomalous fatigue crack growth behaviour caused by microstructure, especially in the near-threshold regime which is particularly sensitive to microstructure variation [18]. Gary et al. [37] studied the grain size effect on the RICC in steel, and found that coarse grain samples were superior to fine grain samples in near-threshold crack growth rate at low R ratios ($R=0.1$), but this difference nearly disappeared at high R ratio ($R=0.7$). This suggested that roughness-induced crack closure is less significant at high R ratios due to Mode II displacement. However, the relationship between RICC mechanism and grain size has not been fully understood. There are several factors that can enhance RICC: (1) low stress intensity factor regime as grain size is greater or comparable to the plastic zone size; (2) small crack tip

opening displacements of which size is comparable or smaller than the average height of the fracture surface asperities; (3) microstructures containing highly planar, crystallographic slip (such as coarse grain, shearable and coherent precipitates); (4) crack deflections caused by microstructural incoherence and multiphase; (5) enhance slip irreversibility [18].

Oxidation-induced crack closure (OICC): The formation of oxide and corrosion debris on the crack wake has been confirmed as the reason for OICC. OICC has been noticed to have significant effect on near-threshold fatigue crack growth and such effects are associated with the oxide thickness. Moist atmospheres readily cause oxide films to develop as a result of “fretting oxidation” at low R ratio, i.e. a repeated process of breaking and reforming oxide scale on the crack wake due to crack surface “smashing” caused by PICC. This closure mechanism is less effective in a dry and oxygen-free atmosphere and high R ratio loading condition where the high K_{max} values are high and thereby weaken the PICC mechanism. However, this environmental associated closure mechanism is only applicable to near the threshold regime where the thickness of oxide layer is the same order of magnitude as the CTOD [36-38].

3.5.3 Other retardation mechanisms

Crack bridging effect: This mechanism is usually found in a composite material with unidirectional, continuous fibre reinforcements, but is also available in some metallic alloys with a lamellar structure or reinforced fibers, such as lamellar γ -TiAl and SiC fiber-reinforced Ti alloys. Studies have shown that ductile alloys reinforced with brittle fibres have better near-threshold fatigue crack growth behaviour than unreinforced alloys if fatigue failure occurs predominantly within the ductile matrix. The reinforcing phase itself ahead of crack front can play a role of trapping the crack front. In addition, the fatigue resistance also can be improved through limiting the effective CTOD by

unbroken brittle fibres forming bridging ligaments [18]. For brittle alloys, such as γ -TiAl alloy, a ductile phase, for instance TiNb fibres, provides significant bridging toughening effect which improves fatigue crack resistance of the alloy [4]. However, if the particles debond from the matrix, the interfacial debonding site can act as a crack initiation site and so reduce fatigue crack growth resistance of the alloy. Moreover, the bridging toughening mechanism depends on the size, shape, distribution of reinforcing phases and their toughness compared with the matrix [18].

Crack deflection: During fatigue crack propagation, the crack front tends to seek the easiest path, such as soft-oriented grains, grain boundaries, and the maximum loading direction, thus cracks deflect from the nominal growth plane. Crack deflection has been shown to enhance the fatigue crack resistance in both brittle and ductile materials. It has been reported that even small amounts of deflection in the growth path can reduce fatigue crack growth rate by several orders of magnitude, especially in the near-threshold regime. The reasons why crack deflection can promote fatigue crack growth resistance are summarised by Suresh [18] from three points of view:

- (1) If the crack deflects from Mode I growth direction, the required driving force is apparently larger than it for a straight crack path.
- (2) For the same effective driving force, a deflected crack propagates at a slower rate than a straight crack since the crack path is longer than a straight line from one point to the other point.
- (3) During the closing portion of a cycle, a small mismatch between the mating crack faces can cause premature contact, and thereby leads to crack closure which further amplifies the apparent driving force required for the crack growth.

3.6 The small crack behaviour

Most studies based on LEFM focus on crack size beyond a critical value, but for short cracks, which practically exist in a number of engineering components, the LEFM

meets its limitation since short fatigue cracks behave differently from long cracks. Lots of efforts have been made to reveal the mechanisms of the so-called anomalous growth of “small/short” fatigue cracks compared to those “large/long” ones. There are several questions needed to be answered for short cracks: (1) How to define short cracks? (2) What are the differences in fatigue behaviour between short and long cracks? (3) Why short cracks exhibit anomalous fatigue crack growth behaviour?

3.6.1 Definition of small crack

According to several crack size dependent fatigue crack growth behaviours, possible definitions of short cracks were proposed by Suresh & Ritchie [18]:

- (1) The length of the fatigue crack is smaller or comparable to some controlling microstructural dimensions, such as the grain size, where the crack growth can be retarded or arrested by localised microstructural “barriers”, such as grain boundaries or other interfaces [18, 39, 40].
- (2) For smooth specimens, the crack length is small comparable to the near-tip plasticity, where the stress intensity K is inapplicable for small-scale yielding.
- (3) Fatigue crack size is significantly larger than the microstructural units and scale of local plasticity, but is still small physically (i.e. crack length less than about 1 or 2mm) [18]. This kind of small cracks can reduce the role of shielding and result in a higher local driving force than the large fatigue crack for a same value of stress intensity [39].

3.6.2 Effect of small crack on fatigue threshold and crack propagation

The two main characteristics of small cracks in terms of fatigue behaviour are: (1) the small cracks can grow at values of ΔK lower than that of the threshold for long cracks; and (2) the crack growth rates of small cracks are higher than a long crack for the same

value of ΔK [18, 41]. The schematic diagram showing the difference of fatigue behaviour between short and long cracks is presented in Figure 3.6.

In the study of McEvily [27], the reasons for faster fatigue crack growth rate of short crack than long cracks were summarised as:

- (1) The plastic zone size around the short crack tip is relatively larger than the crack length, and thus LEFM is no longer applicable.
- (2) The applied stress level may be even higher than the yield strength of material which should be considered as small scale yielding condition. Cracks can naturally initiate at stress or strain amplitudes above the fatigue limit and yield stress. Although the normal stress may be below the yield strength of entire specimen, localised resolved shear strength can be in excess of the critical resolved stress required to activate the primary slip system.
- (3) The crack closure effect varies with crack length from a short to a long crack. When the crack just initiates, the closure level is zero and then it increases with increasing crack length to the level associated with a long crack. Moreover, the higher closure level is the lower ΔK_{eff} if the K_{cl} is greater than K_{min} , and a greater driving force is required to grow a short crack compared to a long crack at the same ΔK level.

Among these theories, crack closure has been mostly used to explain the cause of short crack behaviour in different materials [40, 42-44]. It was found that roughness- and plasticity-induced closure plays a dominant role on the early stage of fatigue crack growth [45]. The closure level varies with crystallographic orientation which results in the changes of the crack growth path and model [44, 45]. The other factor that alters closure level is the angle between the slip planes in different grains. Short cracks usually retard at microstructural interfaces which explain the decrease of growth rate as shown in Figure 3.6. There are two possible reasons to explain this interface retardation for short cracks: (1) it is difficult for slip to occur across an interface and so cause an

incubation period which is dependent on the angle between interfaces; and (2) Crack closure level at the interface may be increased due to non-continuum crack tip plasticity which is caused by slope extending to the next interface [45].

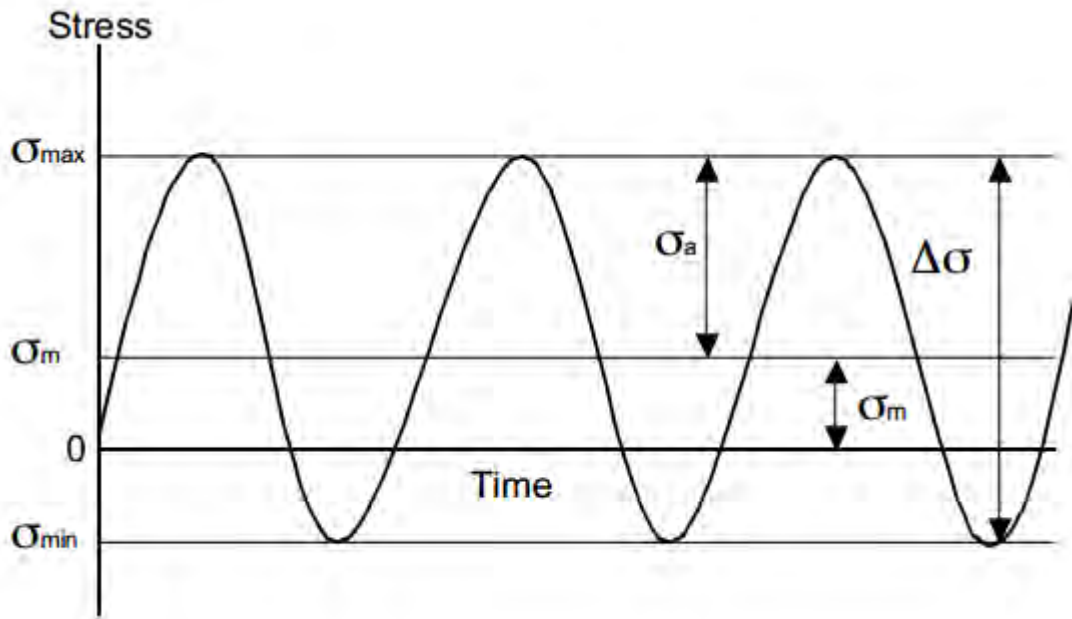


Figure 3.1. The diagram to show the fatigue loading and relative parameters

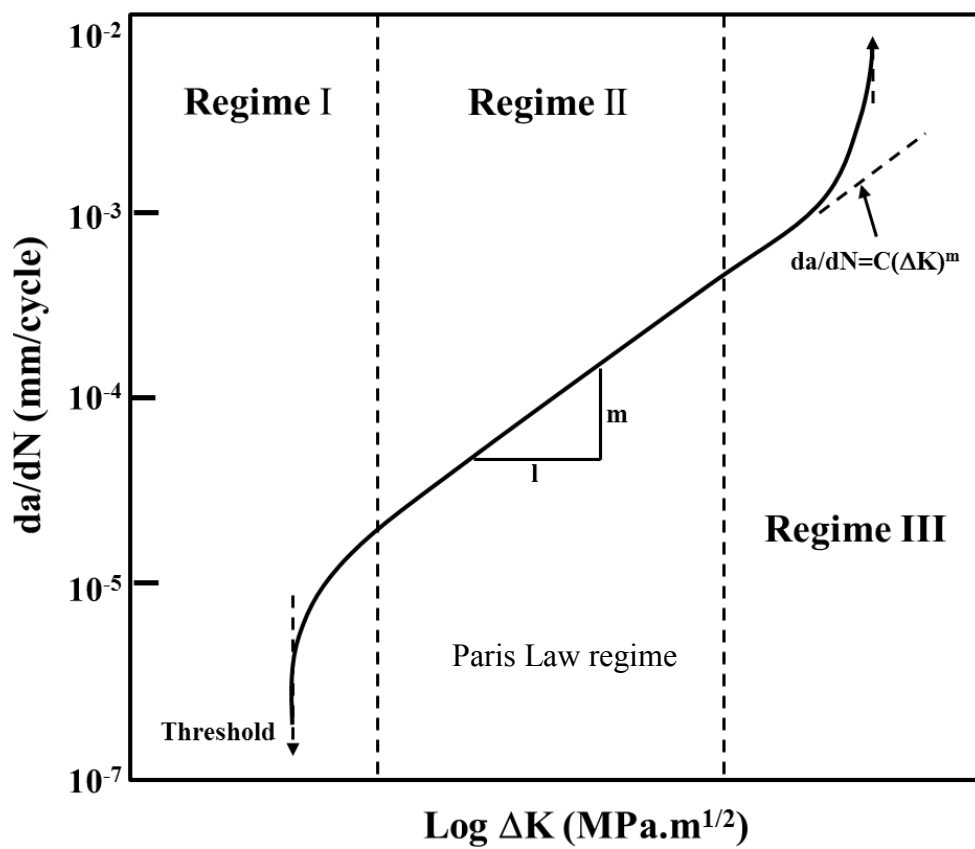


Figure 3.2. a typical fatigue crack growth resistance curve for engineering materials.

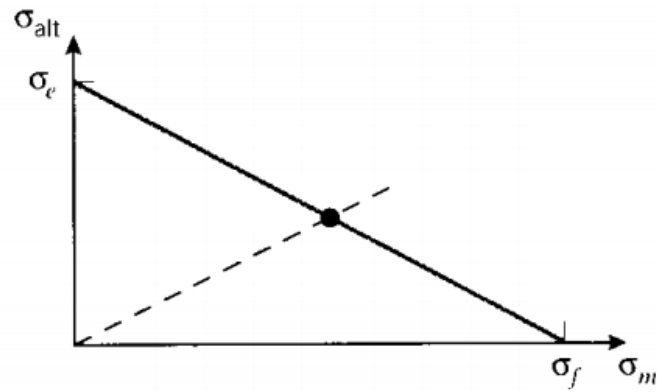


Figure 3.3. The Goodman diagram to solve effect of mean stress on fatigue life [11]

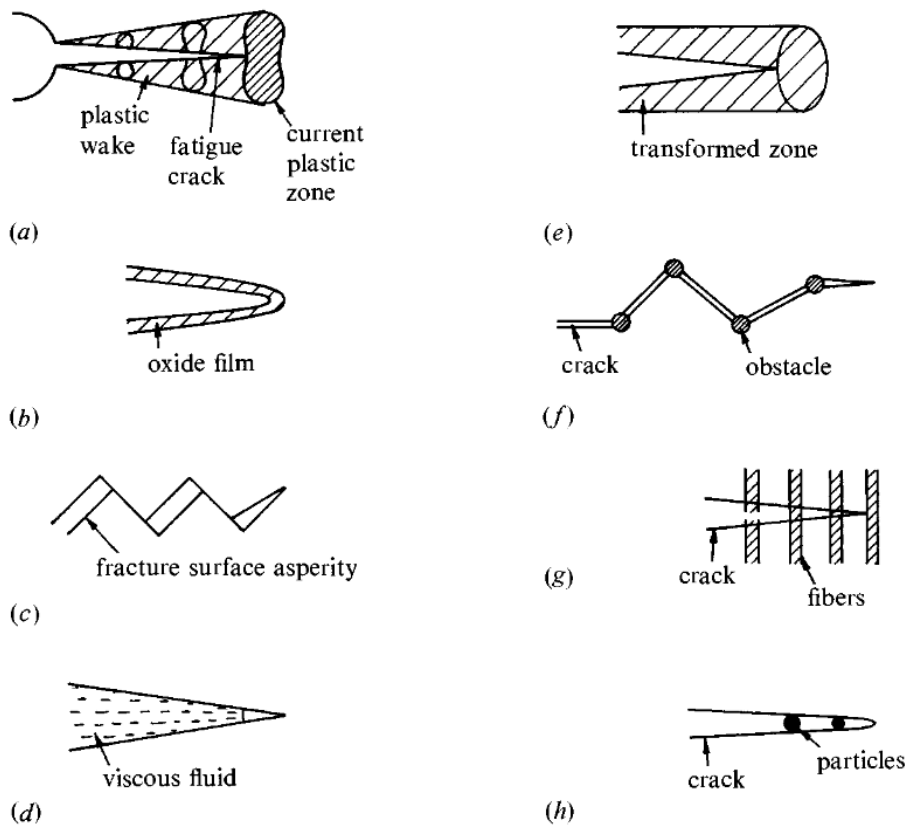


Figure 3.4. Different types of crack closure mechanisms: (a) plasticity-induced crack closure; (b) oxide-induced crack closure; (c) roughness-induced crack closure; (d) fluid-induced crack closure; (e) transformation-induced crack closure; (f) crack deflection; (g) crack-bridging by fibers and (h) crack-bridging (trapping) by particles[18].

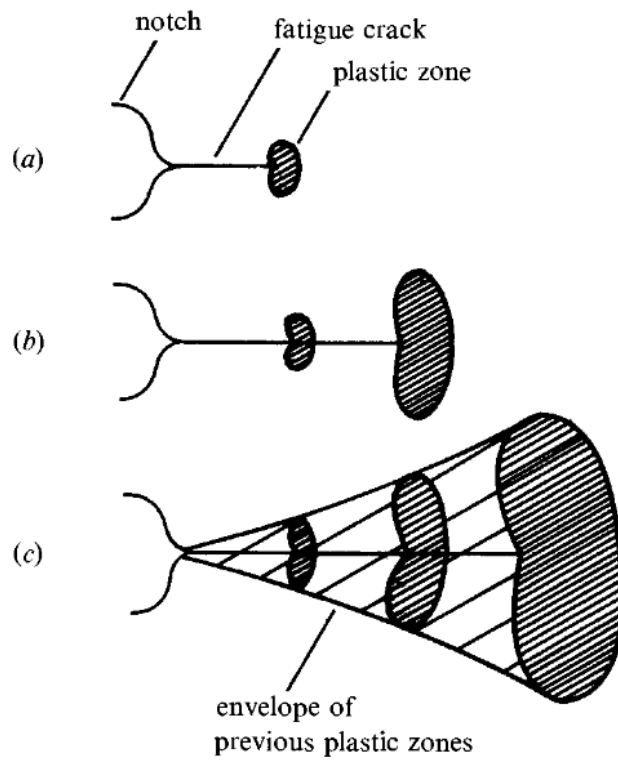


Figure 3.5. Schematic diagram showing the develop of an envelope of plastic zones around the wake of crack advance [18].

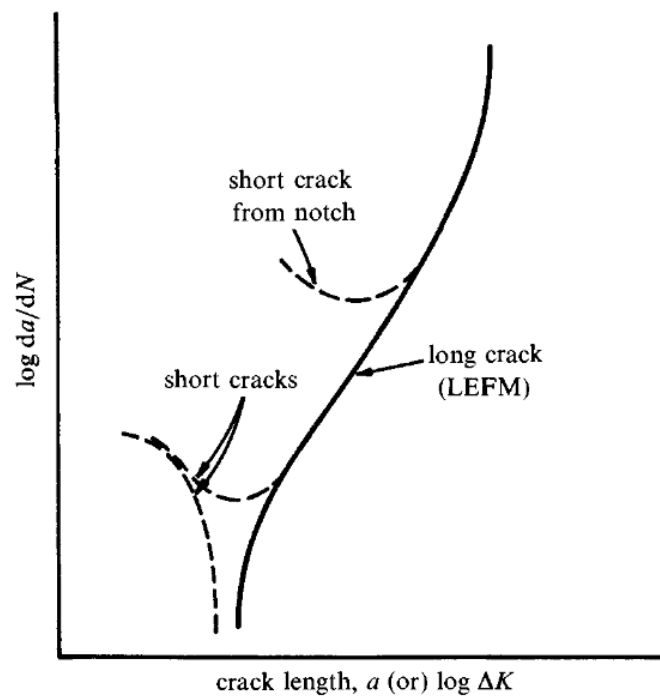


Figure 3.6. A schematic diagram showing the difference of fatigue behaviour between short and long cracks as a function of ΔK values [18].

4. Gamma Titanium Aluminides

4.1 Overview

4.1.1 Titanium Aluminides and related phases

Titanium aluminides (TiAl) are a class of intermetallic compound. Three major intermetallic phases have been identified in the TiAl alloys, α_2 -Ti₃Al, γ -TiAl and TiAl₃ [3]. Among these three phases, the γ -TiAl and α_2 -Ti₃Al phases have been found to be of engineering significance in high-temperature applications. The Ti-Al phase diagram is given in Figure 4.1. Ti-Al phase diagram [8]. The properties of Ti₃Al-based alloys and TiAl-based alloys are compared and shown in Table 4.1.

Ti₃Al (α_2)

The content of aluminum in the Ti₃Al phase (usually called α_2 phase) is in a range of 22-39 at.%. The α_2 phase has a hexagonal ordered D0₁₉ structure as shown in Figure 4.2(a). The ratio of the lattice parameters c and a is about 0.8. The fracture strength remains at approximately 600 MPa up to 600 °C. At temperatures below 400 °C, this phase is brittle with nearly no deformability (such as microcracking). Due to the limited number of slip systems, there is and no stress-relieving twinning in this hexagonal structure, cleavage fracture usually initiates at grain boundaries. Moreover, high rates of oxygen and hydrogen absorption makes this phase even more brittle at high temperatures [3, 8]. The addition of Nb has been reported to improve the mechanical properties although not creep resistance. Other alloying elements such like Cr, Ta and Mo can also improve the strength of α_2 phase, and the Mo additionally benefits the creep strength.

TiAl₃

This phase is of less concern for aero-engines than the other two phases. It has a

tetragonal $D0_{22}$ structure which makes the dislocation mobility low so that twinning is a main deformation mode in this phase. As a consequence of this, there is nearly no ductility at temperatures below 620 °C. However, it is still quite useful, for instance, its density is only 3.3 g/cm³ which is suitable for lightweight structural applications and its oxidation resistance is superior to the α_2 phase and γ phases. Hence it is being considered as a coating material [3].

TiAl (γ)

The TiAl phase has an ordered face –centered tetragonal $L1_0$ structure as shown in Figure 4.2 (b), with a wide range of Al content (49-66 at.%) . The range of Al content that is of practical use is about 44-49%. The ratio of the lattice parameter c and a is 1.02 and increases with increasing Al content up to 1.03 [46]. There is nearly no deformability below about 700 °C, thus it is brittle at low and medium temperatures. Above this temperature, the phase softens and more plasticity leads to a yield strength below its fracture strength [3]. The micromechanisms of deformation and associated mechanical properties have been studied by many researchers previously [47-50]. The plasticity in this phase is caused by single dislocations and superdislocations. However, the mobility of dislocations is low which is responsible for its brittleness. Twinning is the other important deformation mechanism. At high temperature, its kinematic irreversibility results in fast crack growth rates in the Paris regime and high ΔK regime [3, 47]. Various elements have been alloyed in TiAl in order to optimise its mechanical properties, for instance, Nb, Ta and W can improve its oxidation resistance and V, Cr and Mn offer the benefit for increasing ductility. However, these elements cannot give both benefits at the same time [46]. The solubility of oxygen in TiAl is lower than in Ti_3Al . As with other titanium aluminides, it also has the problem of environmental embrittlement which depends on several factors such as temperature, strain rate, microstructure and phase distribution [3].

4.1.2 Microstructure of Gamma Titanium Aluminides

Although a lot of research has been carried out in improving mechanical properties, especially ductility of the three titanium aluminide phases using grain refinement or alloying, no complete solution for the problem has been worked out. But dual phase alloys of titanium aluminides which can be obtained with an Al content between 53.2-62.1wt.% exhibit better performance [8, 51].

The microstructures of two-phase gamma titanium aluminides have been widely classified into four categories which are (1) near-gamma, (2) duplex (DP), (3) nearly-lamellar (NL) and (4) fully lamellar (FL). More microstructures of gamma TiAl-based alloys are schematically shown in Figure 4.3. These microstructures can be obtained through different heat-treatments, and can vary in volume fraction of lamellar colonies and in colony size, such as refined fully lamellar, refined duplex, and coarse lamellar [8, 52]. Among these microstructures, duplex and fully lamellar microstructures have received most attention because their mechanical properties are suitable for aero-engine applications. As shown in Figure 4.4, a duplex microstructure consisting of equiaxed γ single phase grains and lamellar colonies can be obtained using heat-treatment in the $\alpha+\gamma$ phase field at a temperature (T_3) around 1200 °C [5, 8]. A lamellar microstructure consists of colonies containing alternating γ and α_2 plates[53]. The fully lamellar microstructure is generated by heat-treatment at temperature (T_1) in the pure α phase field while a nearly-lamellar microstructure forms at a temperature (T_2) between that of fully lamellar and duplex microstructures [8]. Due to fine grain size and homogeneousness, duplex microstructures have better ductility and strength at room temperature and are more resistant to crack initiation than a fully lamellar structure. The lamellar microstructures exhibit poor ductility, but are superior to the duplex structure in high-temperature creep, fatigue resistance and fracture toughness [5, 7, 54].

Even for the same microstructure type, the mechanical properties can vary because of

microstructural parameters, such as colony/grain size, lamellar spacing, and colony orientations. Kim [12] measured and compared the tensile properties of γ -based TiAl alloys with different microstructures, grain size and lamellar spacing against temperature (shown in Figure 4.5). As can be seen, the UTS of duplex structures remained at a quite high level up to 800 °C, while a slight drop in yield strength is found over a similar temperature range. Even though a coarse fully-lamellar alloy exhibited lower strength than a duplex microstructure at room and medium temperatures, the retention of its strength at high temperatures is more preferable, which is only less than 25% reduction at 950 °C compared to RT. The fine fully-lamellar microstructure also showed good high temperature retention, but has higher yield strength and UTS than the large-colony lamellar alloy. The fully lamellar structures appear to have higher brittle-ductile transition temperatures than duplex structures [54].

4.2 Alloying additions

4.2.1 Niobium

Niobium (Nb) is one of the most frequently used additions to titanium aluminides. Its functions are similar to those mentioned above for Ti_3Al phase. The enhancement of oxidation and creep resistance is the uppermost reasons for its addition. It is reported by Tsuyama et al. that additions of Nb over 1at.% result in greatly improved oxidation resistance [55]. Moreover, TiAl-based alloys can still retain a fully-lamellar structure even with additions of Nb as high as 10 at.% [5]. Appel et al. [56] summarised the reasons for the good balance of mechanical properties in the Ti-45Al-(5-10)Nb alloys which are common in Nb-bearing alloys: (1) structural refinement, (2) reduction of the stacking-fault energy and (3) reduction of diffusivity because Nb is a slow diffuser in γ -TiAl.

4.2.2 Manganese

It is reported that the addition of manganese (Mn) can improve ductility of TiAl alloys for a number of reasons. These include increased slip activity [46], increased deformation induced twin activity [57], and the reduction in lattice tetragonality [46, 57, 58]. Because it reduces the stacking fault energy, Mn is able to increase the propensity of twinning [8]. However, it has also been reported that the addition of Mn results in a reduction in high temperature properties like oxidation resistance [55]. However, other research suggests that Mn can combine with other elements like Ta and W to give oxidation-resistant alloys [59].

4.2.3 Boron

It has been reported that a reduction in colony size can significantly improve the ductility of lamellar microstructures at room temperature. Currently, the most effective and economic method for colony refinement in TiAl alloys is by addition of boron which is well known as XDTM technology [60, 61]. The XDTM process was developed by Martin Marietta Company. It involves an exothermic reaction resulting in the in-situ formation of discontinuous particles (usually TiB₂ in γ -based alloys) in the matrix, and is applicable for either ingot metallurgy or powder metallurgy [62]. The mechanism of refinement is believed to result from grain/colony boundary pinning and prevention of excessive grain growth via precipitation of borides during solidification. Additionally, the presence of particulates in titanium aluminides can also strongly influence the kinetics of phase transformation, which makes them critical for mechanical property enhancement [62].

Although the reinforcing boride phase can have a large volume fraction in the matrix metal (up to about 10 vol.% by investment casting and 60 vol.% by powder metallurgy

processing), the effect on grain refinement is not unbounded. There is a minimum boron level below which no grain refinement occurs at all. It has also been commented by Larsen et al that maximum grain refinement was achieved at 1 vol.% TiB₂ and there is no prominent reduction in grain size with further additions of boron[60, 63].

Comparisons have been made of the creep resistance between titanium aluminides with and without TiB₂. The results suggest that the mechanisms of creep deformation are independent of processing methods and the presence of TiB₂ particulates. However, since the creep resistance can increase with decreasing matrix grain size, the alloy with particulates did show an improvement on creep resistance by grain refinement [62].

Tensile tests carried out by Hu et al. [61] showed that borides morphology can also affect crack initiation. Some long titanium boride ribbons (up to 200 µm) were observed in cast high-alloyed alloys, such as Ti-(44-46) Al-8 (Nb, Hf)-xB. These alloys showed poor ductility of less than 0.3% due to debonding of the long boride ribbons causing cracks.

4.2.4 Other elements

The research on enhancing mechanical properties by alloying has never stopped. Beside the elements mentioned above, there are a number of elements which are advantageous for improving mechanical properties of TiAl alloys. A summary of other elements offering enhancement of mechanical properties of TiAl alloys is shown in Table 4.2. Effect of selected alloying elements on mechanical properties of TiAlThe basic principle of alloying is to optimise the mechanical properties, oxidation resistance, corrosion resistance and working temperatures of TiAl alloys without significant sacrifice of its advantages and rise in cost. For example, Ta can increase oxidation and creep resistance of γ -TiAl alloys, but its density is about 16.7g/cm³ and the price is

much higher than that of Ti, Nb and other alloy elements. Therefore, the addition of too much Ta is neither beneficial for weight saving nor economical.

4.3 Mechanical properties

4.3.1 Microstructure and Deformation

The lamellar structure contains γ phase and α_2 phase lamellae. The orientation relationship between the two phases is $\{111\}_{\gamma} // (0001)_{\alpha_2}$ and $\langle 1\bar{1}0 \rangle_{\gamma} // \langle 11\bar{2}0 \rangle_{\alpha_2}$ [64].

The three $\langle 11\bar{2}0 \rangle$ directions in α_2 phase are all equivalent to each other, while the $[\bar{1}10]$ direction and the $[10\bar{1}]$ and $[0\bar{1}1]$ directions in the γ phase are not equivalent to each other due to the tetragonal $L1_0$ structure. Thus there are six different variants in the γ phase with respect to the $\langle 11\bar{2}0 \rangle$ direction in α_2 phase [5, 64].

It has been confirmed that the main deformation mode in γ -TiAl are slip and twinning which both occur on the $\{111\}$ planes. Because the $L1_0$ structure is similar to the face-centered cubic (fcc) structure, slip occurs in γ phase on the close packed $\{111\}$ plane. Because of the slight tetragonality and the ordered nature, there are two types of dislocations with $1/2\langle 110 \rangle$ type Burgers vector on $\{111\}$ planes. The ordinary dislocation is $1/2 \langle 110 \rangle$, and the superdislocation is $1/2 \langle 101 \rangle$. These superdislocations consist of pairs of dislocations creating anti-phase boundaries (APB) in order to minimise the degree of disorder [8]. The possible slip plane and Burgers vectors are shown in Figure 4.6 [46]. The deformation mechanisms are different for single phase γ -TiAl and dual phase TiAl. At low temperatures, single phase alloys deform by movement of $\langle 101 \rangle$ superdislocations, while twinning and gliding of ordinary $1/2\langle 110 \rangle$ dislocations are the dominant deformation modes in dual phase lamellar γ -TiAl alloys. At elevated temperatures in single phase alloys, the ordinary dislocations become glissile. These ordinary dislocations and twinning are the primary deformation modes.

Beside the active dislocations at low temperatures, some superdislocations also appear in dual phase alloys. At room temperature, the mobility of superdislocations is limited due to the covalent nature of the Ti-Ti and Ti-Al bonds. Therefore, the low ductility at room temperature in single phase γ -TiAl alloy can be explained [65].

4.3.2 Ductility and tensile properties

The influence of microstructure

As mentioned above, the ductility and tensile properties of two-phase γ -based alloys show rather complex microstructural dependence. As shown in Figure 4.8, the small strain range of a fully lamellar structure indicates that they have poor ductility at room temperature, due to a lack of slip and twinning activity, deformation anisotropy and relative large grain size [66]. Duplex structures often show better ductility and higher yield strength compared to fully lamellar structures because of small grain size, as well as yield point behavior [66].

It also can be deduced from Figure 4.9 that the yield strength increases with decreasing grain size for the same type of microstructure. The same trend is also found in ductility both for duplex and fully lamellar TiAl alloys as shown in Figure 4.10. If the grain size is greater than 50 μm , the elongation of lamellar alloys can be well predicted using an initiation toughness (K_{IC}) model developed by Kim et al. [66]. The crack nucleation model is more applicable for alloys with small grain size. This effect of grain size on ductility is limited by microcracks caused by strain incompatibility of which size is comparable to the grain size [66].

For the lamellar structures, lamellar spacing (LS) is the other important parameter factor influencing tensile and ductility properties. After taking anisotropy into consideration, Kim [66] modified the Hall-Petch relationship for fully-lamellar

material as:

$$\begin{aligned}\sigma_y &= \sigma_o + k_{FL}d^{-1/2} \\ k_{FL} &= \alpha k_d (k_d \sim 1 \text{ MPa} \sqrt{m}) \\ \alpha &= f(\tau_H^*/\tau_S^*) = f(\lambda, \alpha_2/\gamma) \\ \sigma_o^l &= f(2\lambda, D) \quad \dots 4.1\end{aligned}$$

Where τ_H^* and τ_S^* are the resolved shear stress on the hard and soft orientation, respectively. α is a measure of the anisotropy of strength of the lamellar grains which is a function of lamellar spacing (λ) and the α_2/γ volume ratio. The Hall-Petch constant (k_y) value was corrected from $\sim 2.5 \text{ MPa.m}^{1/2}$ for ultrafine LS and to $\sim 1 \text{ MPa.m}^{1/2}$ for coarse LS. According to this function, it was reported that yield strength increase with decreasing grain size as well as LS. The yield strength is usually high for fine grains and fine LS, and the intrinsic strength (σ_o) increases with decreasing LS [66].

The mechanical properties of lamellar structures are quite sensitive to the lamellar orientation. Either ductility or tensile properties are strongly dependent on the angle (ϕ) between the lamellar boundaries and loading axis. A schematic defining the relationship of angles (ϕ and ψ) between lamellar boundaries and loading axis is given in Figure 4.10. It was reported that the tensile properties of polysynthetically twinned (PST) crystals are more dependent on the angle ϕ than the angle ψ . The macroscopic deformation of PST crystals in general is shown in Figure 4.11. When $\phi = 90^\circ$ or 0° , shear deformation occurs in the γ lamellae on the $\{111\}$ planes intersecting with the lamellar boundaries, and thereby interacts with the lamellar boundaries and the α_2 lamellae (deformation in hard mode). The highest strength was found when $\phi = 90^\circ$, at which the tensile ductility is nearly zero. The optimal balance between ductility and strength was obtained at $\phi = 0^\circ$. Although the tensile strength is slightly weakened, the room-temperature ductility can be as large as 10% at $\phi = 0^\circ$. When $\phi = 30^\circ - 60^\circ$, shear deformation occurs parallel to the lamellar boundaries without any interaction with lamellar boundaries (deformation in the soft mode). Thus the yield stress is much

lower but the elongation is much higher compared to $\phi = 0^\circ$ or 90° [5].

The influence of alloy composition

Aluminum content is also reported to significantly affect the mechanical properties and fracture mode of TiAl alloys. The microstructure varies with the Al content and so does the resulting deformation mechanisms as shown in Figure 4.12. Among the alloys with Al content of 46-48 at.%, the Ti-48.22 at.% Al alloy, with an α_2 - γ lamellar structure showed the best tensile strength and fracture toughness, since the critical strength level for lamellar grain boundary cracking increases with increasing Al content within this range.

Impurities such as oxygen and carbon can also affect the ductility of γ -TiAl alloys. Kim et al. [46] did tests on a two-phase Ti-48Al alloy. It was found that the tensile elongation slightly increased by 0.6% when the oxygen level decreased from 0.08% to 0.03%. It was also found that the addition of vanadium, chromium or manganese can reduce the grain size of gamma alloys. Grain size refinement appears to improve the ductility of two-phase gamma alloys [46].

The influence of temperature

The brittle-ductile transition (BDT) occurs in the range of 700 – 900 °C for γ -TiAl alloys. The ductility usually increases with increasing test temperatures. About the BDT temperature, ductility increases even more rapidly with temperature, approaching 100% at 1,000 °C. Generally, increased RT ductility results in a lower BDT temperature. The variations of yield strength and tensile ductility with temperature are shown in Figure 4.13. Above the BDT temperature, there is a dramatic increase in tensile elongation as well as good strength retention [46].

4.3.3 Fracture toughness

Similar to ductility and tensile properties, the fracture toughness of γ -TiAl alloys is also dependent on microstructure. The fracture toughness for a fine-grained duplex structure is in the range of 10-16 MPa.m^{1/2}, while fully-lamellar structures exhibit remarkable improvement in fracture toughness values (usually as high as approximately 30MPa.m^{1/2}). The RT fracture resistance behavior was studied by Kim et al. [54, 66], and the results were plotted as R – curves (or K-resistance curves) as shown in Figure 4.14. It was specified that the R-resistance curves can be divided into crack initiation or initiation toughness (K_{IC}) and resistance to crack growth. As shown in Figure 4.14, a duplex structure shows little plastic strain near the onset of crack extension and no resistance to crack propagation, whereas a fully-lamellar structure not only yields and has large plastic strains but also increased resistance as crack propagation [54]. Campbell et al [7] did further investigation with more different types of microstructure, and showed similar conclusions as the previous studies. The R-curves obtained by Campbell et al are presented in Figure 4.15. The higher fracture toughness of lamellar structures can be explained by the occurrence of uncracked ligaments, crack deflection and microcrack shielding [7, 54, 67]. For the same reasons, the negligible R-curve behaviour in duplex microstructures and low fracture toughness are as results of uncracked ligament bridges in the duplex microstructure.

By comparing the microstructural details and mechanical properties of the γ -TiAl alloys used in the study carried out by Campbell [7] (shown in Table 4.3 (a) and (b)), it can be seen that the grain size can also influence the fracture toughness of γ -TiAl alloys. It was suggested that refinement of the lamellar microstructure, especially the colony size, leads to lower toughness. However, although the colony size of G7 coarse lamellar ($D = 1-2$ mm) is much greater than that of the finer MD (named in terms of material source) fully lamellar structure ($D = 145$ μ m), as seen in the figure, the fracture resistance of the finer MD lamellar ($K_{ss} \sim 32$ MPa.m^{1/2}, K_{ss} is the maximum

crack-growth toughness) is only slightly lower than that of the G7 alloy ($K_{ss} \sim 32 - 39 \text{ MPa.m}^{1/2}$). Even the XD nearly-lamellar structure which has a colony size as small as the MD fully lamellar material exhibits about 5% lower R-curve toughness [7]. The complex dependence of toughness on colony size was earlier explained by Kim et al. The steady-state toughness in various lamellar γ -TiAl alloys was found to increase with increasing colony size. However, when the colony size is comparable to or exceeds the crack tip plastic zone size (r_y), only one or part of a colony can be encompassed in front of the crack tip. Therefore, the steady-state toughness is closely related to the intrinsic ductility of the lamellar structure, i.e. it is dominated by the lamellar spacing and lamellae orientation within a colony [7, 54].

The research carried out by Chan and Kim [54, 68] suggest that the fracture toughness values increase with $\lambda^{-1/2}$, i.e. decrease with increasing lamellar spacing, in a similar manner to the Hall-Petch relation. However, Chan et al [69] also note that K_i (crack-initiation toughness) and K_{ss} (maximum crack-growth toughness) are independent of λ , when the lamellar spacing is sufficiently small, e.g. $\lambda < \sim 1 \text{ }\mu\text{m}$. The effect of lamellar spacing was explained through experimental work by Chan and Kim as well. It was found that the lamellar spacing can influence the K_i/K_{IC} and K_{ss} values by affecting translamellar microcracking and the size of the shear ligaments. A small lamellar spacing is not wide enough for the formation of translamellar microcracking, which means linkage of the main crack with interlamellar microcracks become difficult, thus a larger ligament size can be obtained, which results in a higher ligament toughening for the lamellar TiAl alloys. On the contrary, a large lamellar spacing enables more translamellar microcracks to form so that the linkage of the main crack with these microcracks becomes easier, leading to relatively smaller ligament size and so causes lower ligament toughening [69].

The presence of equiaxed γ grains also has a significant influence on toughness in

lamellar TiAl alloys, especially on the formation of bridging ligaments. Based on results obtained by Campbell et al [7], it was observed that an XD nearly lamellar structure showed about 50 percent lower R – curve toughness than a MD fully lamellar material, even though they had nearly the same small colony size (see in Figure 4.16). The XD nearly lamellar structure has ~ 30% equiaxed γ grains which was much greater compared to the other γ alloys tested (less than 5%). The equiaxed γ grains are associated with reduction of ligament bridging. In Figure 4.16, it can be seen that the equiaxed γ grains degrades both the initiation and R-curve toughness. Since duplex and single-phase γ microstructures have more than 90% equiaxed γ grains, there is only little or even no R-curve behaviour in these microstructures due to a lack of the ligament bridging effect [7, 70].

4.4 Fractographic characteristics

Crack advance in duplex and lamellar microstructures shows different natures of fracture. Balsone et al. [71] did a comparison of the fractography between these microstructures in Ti-46.5Al-3Nb-2Cr-0.2W (at. %). They found that the crack advance in a duplex microstructure is predominantly by transgranular cleavage or microcleavage. Because of the fine grain size, the fracture surface in a duplex microstructure was relatively flat for all the ΔK levels and temperatures analysed. At room temperature, the crack advance in a duplex microstructure was quite sensitive to the ΔK level due to alloy's brittleness, whereas less dependent on ΔK level at 600 °C and above due to more plasticity involved. However, higher plasticity at elevated temperatures leads to increasing amount of intergranular fracture, especially at high stress levels.

In a lamellar structure, there are three distinct types of fracture which are translamellar, interlamellar and intralamellar, among which translamellar and interlamellar are the two most common. Translamellar fracture is where a crack propagates through the

lamellae, while interlamellar fracture propagates along the lamellar interfaces leaving a flat cleavage. The schematic diagram of translamellar and interlamellar fractures are shown in Figure 4.17. Intralamellar fracture where a crack grows through a single lamella is rarely studied, as it is not a common fracture mode in lamellar γ -TiAl alloys[72]. The crack direction and mode in a lamellar microstructure depend on the orientation of colonies in front of the advancing crack. Generally, a tortuous fatigue crack path can be observed at room temperature and high stress levels. On the contrary, at elevated temperatures and low stress levels crack advance occurs primarily by translamellar fracture and is less dependent on the surrounding colony orientation. Relatively smooth fracture surfaces can be observed in typical isotropic materials [71]. Chan et al. defined three types of fracture features according to the relationship between crack advance and colony orientations which are crack divider, interface delamination and crack arrestor orientations, and their features are shown in Figure 4.18 [68].

4.5 Fatigue threshold and fatigue crack propagation in γ -TiAls

4.5.1 High-cycle fatigue

Dimiduk compared the high-cycle fatigue behaviour of γ -TiAl based alloys with nickel and titanium alloys (see in Figure 4.19) [73]. The fatigue resistance of γ -TiAl based alloys was beyond that of nickel and titanium alloys for a normalised ratio of the maximum stress over their ultimate tensile strength (UTS). This result indicates that the intrinsic fatigue capability or resistance to crack initiation via intrinsic processes of gamma based alloys is relatively high. However, the failure strengths of TiAl based alloys could be less superior to the other alloys, and they are evidently affected by the environment such as water-vapour or hydrogen.

An early study on the fatigue behaviour of a lamellar alloy (Ti-36.5 Al wt.%) at

different temperatures was carried out by Sastry and Lipsitt [74]. As seen in Figure 4.20, the S-N curves are relatively flat compared to other Ti alloys no matter what the test temperature is. This indicates that a slight change in stress amplitude can result in a significant difference in the number of cycles to failure. The observation has been proved by lots of studies [75-77]. Sastry and Lipsitt also found a good retention of fatigue resistance in this alloy up to 600 °C as shown in Figure 4.21. The ratio of fatigue strength determined at 10^6 cycles over the UTS was plotted versus temperature. This ratio only drops slightly at 800 °C by about 0.25. The high-cycle fatigue behaviour of γ -TiAl alloys is also influenced by the microstructure. The same type of graph as in Figure 4.22 was plotted for several different type of microstructure. Most of the microstructures were achieved from K5 alloy which are classified as coarse lamellar, refined lamellar, and duplex. KD-CBS is an alloy modified from K5 using carbon-boron-silicon for grain refinement. The other two lamellar TiAl alloys which are 3-95 alloy (Ti-46Al-2Cr-2Nb-1Mo-0.2B) and 47XDTM were also considered. From Figure 4.22, it can be deduced that the S-N curve is strongly dependent on the microstructure, and the peak load of fatigue limit at 10^7 cycles is always higher than 75% of the UTS. This means that, even at low stress ratios, the maximum stress is higher than the initial yield stress of the material during fatigue loading. [78].

Influence of surface finish and defects on fatigue resistance

A number of previous studies found surface finish and defects can affect the fatigue resistance of γ -TiAl alloys [2, 75, 79-81]. An early study carried out by Vaidya et al. as shown in Figure 4.23, suggests that a machined surface and a single deep scratch do not cause an obvious loss of fatigue strength compared with an electropolished surface [82]. However, Sharman et al. [75] found that different surface finishing result in variation of fatigue strength as shown in Figure 4.24. S-N curves for turned, ECM (electro-chemical machining) and EDT (electro-discharge texturing) specimens (EDT-L and EDT-H mean low operating energy and high operating energy respectively)

[75]. They measured the surface integrity data of specimens with four different surface finish conditions as shown in Table 4.4. After a comprehensive analysis on fatigue strength and surface integrity data, they came to the conclusion that the presence of cracks penetrating into the testpieces and tensile residual stresses results in a substantially reduced fatigue life of the EDT specimens. In addition, deeper cracks in combination with higher tensile residual stresses caused the lowest fatigue life of EDT-H. Moreover, a highly compressive residual stress is beneficial for counterbalancing the deleterious effect of surface crack or defects [75]. This observation is consistent with the results found by Bentley et al. in their earlier studies [81]. Nazmy et al. [80] by studying different crack size (0.04 to 0.8 mm), found that when crack size is close to or smaller than the average size of the relevant microstructural unit, no crack propagation occurs and hence do not influence HCF life. In the studies by Trail [83], it was pointed out that the fatigue life can be improved with a ground and polished surface as a result of a combination of improved surface finish and reduced tensile residual stress.

Although it has been proved by Trail and Paul [83] that the fatigue strength of notched specimens is reduced significantly by the introduction of a notch, the fatigue performance of these notched specimens was greater than which is predicted using the theoretical K_t (stress concentration factor) value. This is associated with a “notch strengthening effect” which increases with increasing K_t value. The “notch strengthening” can be explained by the influence of local plasticity and work hardening around the notch root [83].

4.5.2 Fatigue crack growth resistance curve of γ -TiAl

Due to limited ductility and toughness of γ -TiAl based alloys as well as other intermetallics, one obvious feature of fatigue crack resistance curves is that they are

extraordinary steep and there are not three distinct fatigue regimes as observed for ductile materials. The Paris law exponent (m) for γ -TiAl based alloys is about 9-22, which is much higher than for ductile materials [84]. Therefore, their crack-propagation lives are inevitably very short and strongly dependent on the applied stress-intensity range for all application temperatures, so that it is vitally important to characterise the fatigue crack initiation i.e. fatigue threshold of γ -TiAl based alloys in order to avoid crack growth in implemented components [53].

Henaff et al. investigated the fatigue crack growth behaviour of a quaternary Ti-48Al-2Mn-2Nb gamma alloy in air and vacuum at room temperature [85]. Three types of notches were introduced with respect to the orientation as described in the Figure 4.18. The fatigue crack resistance curves of the specimen tested in air with a crack-arrester oriented notch is presented in Figure 4.25, and the results of the other two tests conducted in vacuum with notches in a crack divider orientation are shown in Figure 4.26. The fatigue crack resistance curves show discontinuous crack growth and dormant segments during several cycles. This is explained by the observation of discontinuous fatigue crack advance which resulted from a diffuse damage process encompassing a large region ahead of the crack tip and the crack wake. It was also noticed that the propagation rate was high once the crack initiated from the notch and there was no crack closure at the very beginning during the propagation.

The low-cycle fatigue threshold and fatigue crack growth behaviour are influenced by a number of factors, such as microstructure, stress ratio, test temperature and environment. All of these aspects will be discussed in sections 4.6-4.9.

4.6 Extrinsic and intrinsic fatigue resistance in γ -TiAls

4.6.1 Introduction

Microstructure, temperature and environment have significant influence on the fatigue properties of γ -TiAl based alloys, and a number of mechanisms are responsible for these effects. The mechanisms have been classified into extrinsic and intrinsic mechanisms by Ritchie [4]. The intrinsic mechanisms determine the inherent resistance of a material against fatigue crack propagation, such as crack advance by cyclic blunting and reshaping in ductile materials and fatigue crack propagation predominated by a degradation of crack tip shielding. In intermetallic materials, intrinsic mechanisms (intrinsic damage mechanisms) usually involve processes which cause microcracks or voids, for example, by dislocation pile-ups between lamellar interfaces or colony boundaries, leading to interface debonding or intergranular cracking. Extrinsic mechanisms cause a local reduction in the crack driving force at the crack tip, such as unbroken ligaments induced bridging effect in lamellar γ -TiAl alloys. Extrinsic mechanisms (extrinsic shielding mechanisms) enhance the fatigue resistance by forming inelastic zones surrounding the crack wake or physical contact between the crack surfaces to degrade the crack propagation energy. A schematic diagram of intrinsic and extrinsic mechanisms is shown in Figure 4.27, and different types of extrinsic toughening are shown in Figure 4.28. The fatigue crack propagation is a result of competition between intrinsic damage mechanisms and extrinsic shielding mechanisms.

4.6.2 Extrinsic toughening mechanisms in γ -TiAls – bridging mechanisms

It is well accepted that the fracture toughness and fatigue resistance of lamellar TiAl alloys are enhanced from extrinsic toughening by intact ligaments in the crack wake [4, 85-87]. A good example of ligament bridging effects in γ -TiAl alloys is the reinforcement with a small fraction of ductile Nb or TiNb. The extensive crack bridging

by the uncracked ductile phase delays the failure of the matrix alloy [88]. The lamellar structure itself can also provide bridging by unbroken lamellae. Chan et al summarised three means of forming crack-wake ligaments in lamellar TiAl alloys: (1) interface decohesion within a colony; (2) interface delamination in a neighbouring colony; and (3) cracking at colony boundaries. Fracture of the ligaments can be caused by shear, tension, or a combination of bending and shear [86]. The toughness of ligaments is influenced by the way they form. Yamaguchi et al. [89] measured the fracture toughness along the “crack delamination” “crack divider” and “crack arrestor” orientations in lamellar and PST crystals. The fracture toughness value obtained at crack delamination orientation which causes interlamellar fractures was $4 \text{ MPa.m}^{1/2}$, while the other two orientations which cause translamellar fractures were $15 \text{ MPa.m}^{1/2}$ (crack divider orientation) and $20 \text{ MPa.m}^{1/2}$ (crack arrestor orientation). Hence, the ligaments formed by crack delamination orientation are much weaker than those formed via translamellar fracture.

Pippan et al. [87] found if the crack extension was below $10 \text{ }\mu\text{m}$ ($\Delta K \leq 3 \text{ MPa.m}^{1/2}$) the microstructure did not have a significant influence on the toughening effect (R-curve effect) at the threshold. Although both duplex and lamellar microstructures both exhibit an R-curve behaviour for the threshold, the R-curve is much steeper for the fully lamellar microstructure for long cracks (shown in Figure 4.29). Both microstructures show a steep rising R-curve of the threshold at the beginning. The possible reasons for this are explained by several extrinsic toughening mechanisms, which are: (1) building up of plasticity induced crack closure; (2) roughness induced crack closure on the fracture facets and (3) formation of a cloud of nanocracks in the vicinity of the main crack, or the formation of nanobridges.

4.6.3 Extrinsic toughening mechanisms in γ -TiAls – crack closure

Because of highly planar slip, the fracture surface of titanium aluminides is crystallographically faceted and the crack path is tortuous, which results in crack closure during crack propagation under cyclic loading. Elber firstly observed crack closure which involves the premature contact and consequent wedging in the crack wake before complete unloading, and as such causes crack-tip shielding [27, 90]. The possible mechanisms of crack closure are schematically illustrated in Figure 4.30. In TiAl alloys, crack closure is believed to arise from (1) crack wedging by oxide-induced closure; (2) roughness-induced closure and (3) residual compressive stress developed during unloading of a plastically deformed material [91] .

In the study of Mercer et al. [47], oxide-induced crack closure was proved and explained in a lamellar TiAl alloy. It was found that oxide-induced crack closure is more significant at 700 °C compared to 450 °C. On the fracture surface, a rougher translamellar fracture mode observed at 700 °C suggested that higher levels of plastic deformation occurred during the cyclic loading compared to room temperature. Similar observations of oxide-induced crack closure have been also found in a duplex microstructure in their previous studies. Henaff et al. [85] also did an in-depth study on crack closure in a nearly fully lamellar TiAl alloy. They found crack closure affects fatigue crack propagation in air and in vacuum. Experimental procedure seems to have an effect on the closure evolution especially for crack initiation and precracking. Gloanec et al. found that there was no crack closure when the load ratio was above $R=0.45$ for the cast alloy (nearly fully lamellar microstructure) and above $R=0.4$ for a PM alloy (fine equiaxed γ grains) [92]. Some investigations have attempted to avoid the influence of crack closure by testing at high R ratio or using specialised techniques[27].

In addition, Sadananda et al. [91] claim that the actual closure contribution is only 20% of K_{cl} value. They also analysed the crack closure in terms of dislocation theory. For

every dislocation that comes out of the crack tip to form a plastic zone which is the source of crack closure, there is a negative part of the loop which forms ledges at the crack tip to keep the crack open. Since the opening displacement from negative dislocations is always greater than closing displacements, plasticity at crack tip has no effect on the crack closure. It was also concluded from their experimental works that crack closure is not necessary to account for the load ratio dependence. Based on all the analysis above, Sadananda et al. argue that closure is either non-existent or negligible in terms of plasticity-induced closure.

Roughness induced or asperity-induced crack closure are found in titanium alloys, steels with lamellar microstructures, nickel based superalloys, aluminum alloys and titanium aluminides with lamellar and duplex microstructures [93]. According to a simulation carried out by Garcia and Sehitoglu, the crack opening stress is a function of both the height of asperities and the density of asperities and is governed by a competition between crack opening displacement and surface profile [93]. Gnanamoorthy et al. [94] observed microscopically tortuous crack paths in both lamellar and duplex microstructures. Contacts and interlocks between crack surfaces were also observed for both microstructures which is believed to introduce crack closure during testing.

4.6.4 Extrinsic toughening mechanisms in γ -TiAls – crack deflection

Crack deflection generally occurs in TiAl based alloys [87, 94-96]. By examining furnace-cooled fully-lamellar specimens, Mine et al. reported that the specimens with a tortuous crack path including crack deflection, branching and/or bridging exhibit higher fatigue crack growth resistance compared to the specimens having a relatively straight crack path in the mode I crack growth direction [95]. It was observed when interlamellar cracking away from the mode I crack growth direction, it results in crack

deflection, branching and ligament bridging. Gloanec et al. also claimed that higher crack growth resistance of a cast lamellar TiAl alloy in the high growth rate regime is caused by extrinsic toughening mechanisms such as crack deflection, crack branching along lamellar interfaces, microcracking and crack bridging [92]. The crack branching or deflection usually occurs on grain boundaries and lamellar interfaces as shown in Figure 4.31.

4.6.5 Extrinsic toughening mechanisms in γ -TiAls – small cracks

As it is a common concern, small-crack behaviour of TiAl based alloys has been investigated by a number of researchers [39, 43, 53, 97, 98]. It has been shown in the previous studies [40, 53, 97] that a small crack can have a higher growth rate at the same ΔK and lower fatigue threshold than those of large cracks. The size of a small crack is usually comparable with microstructural size scales, the extent of local inelasticity and the extent of crack-tip shielding, as shown in Figure 4.32. Due to their brittle nature, TiAl alloys have a low tolerance of flaws. Therefore, design must be based on the concept of threshold for TiAl based alloys.

It is well documented that microstructure influences the small-crack effect in TiAl based alloys. Campbell and Kruzic compared the fatigue behaviour of small-crack and large-cracks in a Ti-47Al-2Nb-2Cr-0.3B (at.%) alloy for both lamellar and duplex microstructures [53, 97]. As shown by the results in Figure 4.33, for a given ΔK value, growth rates are up to five orders of magnitude slower and the fatigue thresholds much higher in lamellar microstructure than those of duplex microstructure. At the same ΔK level, the growth rates of the small cracks are faster than those of corresponding long crack for both microstructures and the data is far more scattered than for long-cracks. Moreover, small cracks in both microstructures also exhibited lower ΔK_{th} values than long-crack thresholds. All the small-crack effects are less significant in the duplex microstructure. After correcting the ΔK values of long-crack results from crack

bridging and crack closure, the large crack and small crack data agree with the duplex microstructure as shown in Figure 4.34. This indicates that the small-crack effect is primarily attributed to the role of crack-tip shielding principally from uncracked ligament bridging and crack closure in long cracks. This bridging and crack closure is significantly greater in lamellar microstructures than in duplex microstructures. Because the crack sizes are comparable to the scale of the coarser lamellar colony sizes (continuum limitation), the crack front of the elliptical flaw is only encompassed by a few colonies, the crack growth rates are easily affected by those colony orientations. Hence, the small-crack and long-crack data were less normalised even after correction in lamellar microstructures [39, 53, 97].

In the study carried out by Chan and Shih [99], the long and small crack fatigue data obtained at 25 °C for fine-grained TiAl alloy (Ti-47Al-2Nb-2Cr-0.2B) was compared with the long crack data for two coarse-grained, fully lamellar TiAl alloys, Ti-48Al-2Nb-2Cr and Ti-47Al-2.6Nb-2(Cr+V), the results are shown in Figure 4.35. The small crack fatigue crack growth rate in the fine-grain fully-lamellar TiAl alloy was agreed with the extrapolation of the large crack data at equivalent ΔK levels from the power-law regime to lower stress intensity ranges [99]. This is different from what was observed of small cracks in the coarse-grain lamellar alloys as mentioned above. It was also noted that individual small fatigue cracks exhibit difficulties to propagating across grain boundaries due to the incapacity to spread slip into adjacent grains. Hence, a small crack may arrest at grain boundaries leading to slower growth rates. When the small cracks arrested at grain boundaries, they prefer to nucleate in the other close-by colonies, and this process repeated itself until the critical size was reached and resulted in final failure [99].

4.6.6 Intrinsic mechanisms in γ -TiAls

Unlike ceramics and conventional metallics, the TiAl alloys can be toughened both extrinsically and intrinsically, although the latter is far more difficult. Contrary to extrinsic mechanisms which suffer cyclic degradation, intrinsic mechanisms, such as the activation of additional slip systems, do not degrade under cyclic loading [39]. Intrinsic toughening mechanisms in TiAl alloys usually occur via crack renucleation across the metal phase. β -TiNb is a useful reinforcement phase for intrinsically toughening γ -TiAl. As shown in Figure 4.36, the fatigue-crack growth resistance is achieved from intrinsic toughening by crack renucleation across the Nb layer, which increases the crack-initiation toughness and remains equally potent under cyclic loading [4, 100].

A lamellar microstructure can generate intrinsic toughening by interlamellar microcracking at crack-arrest orientations. The unbroken lamellae themselves also play a role of bridging toughening as an extrinsic toughening mechanism. By comparing the measured near-tip strain field against that computed from the applied load, Chan et al. [27, 86] studied the intrinsic fracture resistance in lamellar TiAl alloys. They found the intrinsic fracture toughness of an interlamellar cracking is about $3 \text{ MPa}\cdot\text{m}^{1/2}$ in single-colony thick specimens. There are one or more shielding mechanisms at the crack tip indicated by the near-tip strain distribution, which play important roles on intrinsic toughening such as reducing the crack driving force and increase the fracture resistance.

4.7 Effects of temperature on fatigue threshold and fatigue crack propagation

The influence of temperatures on fatigue crack growth in TiAl alloys is extremely controversial. The “anomalous temperature effect” was observed by Balsone et al. [71] by studying the influence of temperature on fatigue crack growth of a TiAl alloy for

both duplex and lamellar microstructures at room temperature, 600 °C and 800 °C. In both microstructural conditions, the fatigue crack growth resistance in the low ΔK regime was found to be worst at 600 °C and best at 800 °C. This is explained as, below the DBTT, there is combination of some degree of environmental embrittlement at the crack tip and the inherent low ductility and toughness of this alloy. The properties at room temperature are intermediate [71].

This observation was also found by Mckelvey et al. [70] in an XD-processed TiAl alloy at the same test temperatures with R ratio of 0.1 and 0.5. As shown in Figure 4.37, the lowest thresholds were found at 600 °C and highest at 800 °C at both R ratios. Although Larsen and co-workers reported that the fatigue threshold values generally increase with increasing temperature and the lower thresholds at 600 °C and 650 °C are caused by environmental embrittlement. Mckelvey argued that the fatigue threshold decreases with temperature in the absence of prominent environmental effects, while the 800 °C data are anomalous due to oxidation-induced crack closure at this high temperature. Moreover, according to the calculated transition time, the hypothesis of creep was supported at 800 °C which leads to crack-tip blunting and the subsequent reduction in the near-tip stress field, thus results in further enhancement of threshold at this temperature [101, 102].

Mercer et al. [47] selected the other two other test temperatures (450 °C and 700 °C) as well as room temperature (25 °C) to investigate the effects of temperature on the fatigue crack growth behaviour of a cast lamellar Ti-48Al-2Cr-2Nb alloy. According to the results as presented in Figure 4.38, the lowest and highest fatigue threshold was found at 450 °C ($\sim 6.5 \text{ MPa.m}^{1/2}$) and 700 °C ($\sim 10.0 \text{ MPa.m}^{1/2}$) respectively. The fatigue threshold at 25 °C is comparable to that at 700 °C ($\sim 9.0 \text{ MPa.m}^{1/2}$). The fatigue crack growth rates are significantly lower at 700 °C than at 450 and 25 °C. However, the Paris exponent value was also highest at 700 °C ($m= 6.9$), which is much higher than the

results obtained at 600 °C and 800 °C ($m \approx 3.2-3.6$) by Balsone et al.) [71] in a lamellar TiAl alloy (Ti-46.5Al-3Nb-2Cr-0.2W at.%). The reasons for these trends observed by Mercer et al. [47] are explained by differences in fracture modes and crack-tip deformation mechanisms under cyclic loading at different temperatures, and it is believed there is significant oxidation-induced crack closure at 700 °C. The author expounded the crack-tip deformation mechanisms as (1) Slip appears to be the predominant deformation mechanism at 25 °C; (2) Duplex mode of micro-twinning and conventional slip at 450 °C leads to high fatigue crack growth rates as the micro-twinning component is irreversible; (3) Although both micro-twinning and slip are active at 700 °C, slip may play a more dominant role in crack-tip plasticity.

Contrary to all these authors above, Mabru et al. [103] reported that temperature has only a slight influence on the global fatigue crack growth resistance. As shown in Figure 4.39 (a) and (b), even after normalising the ΔK values with Young's modulus (E), the threshold values are similar for all temperatures, and the fatigue crack growth rates are also almost identical at the three temperatures, except for a slight reduction at 750 °C above 10^{-8} m/cycle. It was noted that the intrinsic behaviour of Ti-48Al-2Mn-2Nb alloy is slightly improved with increasing temperature. However, this is denied by the author to have a relationship with fracture mode when crossing the DBTT since the fracture surfaces exhibited little difference. By comparing with other authors' opinions, Mabru concluded that toughness improvement at high temperature induces a higher fatigue crack propagation resistance in the high crack growth rates regime. In addition, it was found that at 850 °C, the intrinsic behaviour of the alloy is very similar to the intrinsic resistance of conventional ductile alloys, the comparative results are shown in Figure 4.40. Therefore, the fatigue crack propagation mechanism is the same as for conventional ductile alloys [103].

Even though results at elevated temperatures vary in different studies due to various

testing approaches and alloy composition, most of the authors mentioned the oxidation-induced crack closure at elevated temperatures. Mercer et al. [47] determined the compositional nature of the oxidation layer at 700 °C on the fracture surface using X-ray diffraction (XRD). The analysis shows that the oxide layer was predominantly alumina (Al_2O_3) and no rutile (TiO_2) as detected on the fracture surface. However, Auger spectroscopy could detect low levels of TiO_2 in the oxide. No discernible oxide layers were detected on the fracture surface of the specimens tested at 25 and 450 °C. Approximately 3 μm of excess oxide thickness was comparable to the minimum crack-tip opening displacements in the near-threshold regime, which is sufficiently thick to promote oxide-induced crack closure in the near-threshold regime as well as possibly to reduce the crack growth rates at 700 °C.

A unique investigation on the effect of temperature and orientation dependence of cyclic deformation, fatigue life and fracture behaviour in PST TiAl alloy was carried out by Umakoshi et al [104]. Two orientations of $\phi=0$ and 45 ° were selected, where ϕ is the angle between the loading axis and the lamellar planes along a $\langle 1\bar{1}0 \rangle$ zone in the γ phase. It was observed that the deformation mode in this PST TiAl alloy depended on the loading axis, type of domain and temperature. Moreover, fatigue strength monotonically decreased with increasing temperature at $\phi=45$ °, while a high stress level can be maintained up to 400 °C. And then fatigue life drops rapidly above 600 °C at $\phi=0$ ° [104].

4.8 Effect of stress ratio on fatigue threshold and fatigue crack propagation

The influence of stress ratio on fatigue crack growth and thresholds in TiAl alloys has been studied by a few researchers. Mckelvey et al. [101] found that the ΔK_{th} of a XD-processed alloy decreased with increasing load ratio at a given temperature as shown in Figure 4.42 . Similar results were obtained in a duplex TiAl alloy by Zhu et al.

[105]. Such behaviour has been seen in many metallic materials up to a critical R value, above which the effect of crack closure is assumed to be minimal [101]. As seen in Figure 4.43, in many brittle materials such as ceramics, the effect of stress ratio can be normalised by characterising fatigue-crack growth rates as a function of K_{\max} . On the contrary, in metals where the ΔK term is dominant, normalisation of stress ratio is achieved in terms of ΔK . However, in intermetallics, the stress ratio dependence cannot be scaled solely in terms of either ΔK or K_{\max} [4]. A modified Paris law relationship can be used to estimate the dependence of crack growth rate, da/dN as a function of both ΔK and K_{\max} , which is:

$$da/dN = C'(\Delta K)^p(K_{\max})^n \quad \dots 4.3$$

where C' is a scaling constant (independent of K_{\max} and ΔK) and p and n are experimentally determined crack growth exponents. Since $K_{\max} = \Delta K / (1-R)$, $m = p + n$ and $C = C' (1-R)^n$ [101, 105]. As shown in Figure 4.43, in metal where $p \gg n$, an intrinsic mechanism at crack advance is responsible for fatigue-crack growth, while in ceramics where $p \ll n$, the crack-advance mechanism is identical to that under static loading so that K_{\max} dependent crack growth is normal. The intermetallics represented by TiAl alloy, appear to exhibit intermediate behaviour between ductile and brittle materials [4, 101, 105]. The p and n values measured by Mckelvey et al. [101] are shown in Table 4.5. From the values of p and n , it can be concluded that (1) at room temperature, K_{\max} -controlled mechanisms are dominant as $n > p$; (2) at 800 °C, ΔK -controlled mechanisms are dominant as $n < p$, while (3) at 600 °C, $n \approx p$, the influence of K_{\max} and ΔK are nearly equivalent.

Zhu et al. characterised the influence of stress ratio on a lamellar TiAlNb alloy via observation of subtle differences between fracture surfaces generated at different stress ratios and stress intensity ranges. It was found in the low ΔK regime at low stress ratios ($R=0.1$ and 0.3), translamellar crack growth is the dominant fracture mode, while in the intermediate ΔK regime of $R=0.3$ and almost the whole stress intensity range of ΔK at

$R=0.5$, colony-boundary cracking is predominant [105].

Additionally, a study carried out by Mabru et al. investigated the influence of load ratio on fatigue crack closure in a fully-lamellar TiAl using a constant K_{\max} -increasing load ratio method [103]. In this method, the K_{\max} value was fixed and the crack was allowed to grow over at least 0.1 mm before increasing the K_{\min} value. The crack growth rates were then plotted as a function of the load ratio as presented in Figure 4.41. According to the equation 3.7 in section 3.5.1, the K_{eff} is constant as long as the K_{\min} value is less than the K_{op} value whatever R ratio is, and the crack growth rates should also be identical as ΔK_{eff} is constant. Once the K_{\min} value exceeds the K_{cl} value, the crack growth rates should decrease with decreasing ΔK_{eff} . It was found when $R=0.1$, $K_{\text{cl}}=3.9 \text{ MPa.m}^{1/2}$ which was nearly consistent with the estimated K_{op} value. When $R \geq 0.4$, no crack closure can be detected [103]. Similar results were also obtained by Gloanec et al.. They found no crack closure at load ratios of 0.45 and 0.4 in cast TiAl alloy and PM alloy, respectively [92].

4.9 Effect of environment on fatigue threshold and fatigue crack propagation

An early study conducted by Liu [106] on moisture-induced environmental embrittlement in a duplex γ -TiAl alloy showed that the lowest ductility and highest room-temperature ductility were found in air and in oxygen respectively as shown in Table 4.6. It was proposed that aluminides appear to be prone to environmental embrittlement due to a reaction with moisture in air at ambient temperatures. However, Chan and Kim reported that the tensile properties of a nearly-lamellar γ -TiAl alloy are not affected by testing environment, i.e. in air or in vacuum, at room temperature [107]. Two reasons were suggested for the lack of clear environmental effect: (1) the environmental effect may be masked by other embrittlement mechanisms; (2) the effect of environment was too small to be detected [106]. On the other hand, Oh et al. [108]

found that the tensile ductility of PST crystals of TiAl is sensitive to test environment. It was higher in vacuum or in dry air than in air or in hydrogen gas at room temperature. The environmental embrittlement of this alloy was interpreted in terms of hydrogen embrittlement caused by a decohesion mechanism at lamellar interface and colony boundaries as in many intermetallics.

In a study carried out by James and Bowen [85, 109], little environmental effect in nominal fatigue crack growth rates or fractography was observed in a Ti-48Al-2Mn-2Nb alloy, and the crack growth rate was even slightly higher in vacuum. However, all the fatigue-crack growth data were not corrected with crack closure. Henaff et al. compared the fatigue crack growth behaviour of a lamellar γ -TiAl alloy in air and vacuum after a closure correction. As shown in Figure 4.44, the crack growth rates in air are nearly more than two orders of magnitude higher than it in vacuum, and this difference seems independent on the lamellae orientation [85]. In a latter article also from Henaff, more mechanisms about environmentally-assisted fatigue crack propagation (EAFCP) have been analysed [110]. Petit et al. [111] proposed two main EAFCP mechanisms in conventional metallic alloys:

1. Adsorption of water vapour can reduce the surface energy, therefore, enhance the crack growth.
2. The crack-tip embrittlement caused by hydrogen atoms released from the absorbed water vapour in air and then intruded by the cyclical loading at the crack tip [110].

As shown in Figure 4.45 (b), the fatigue-crack resistance curves obtained in intermediate atmospheres fall in a narrow band. The boundaries of this band are the marginal curves obtained in air and vacuum at RT and 500 °C (see in Figure 4.45 (a)). It can be deduced that the enhancement of fatigue crack growth is mainly controlled by the amount of water vapour and independent on the amount of oxygen in the test

atmosphere [110]. Therefore, the EAFCP mechanisms in TiAl alloys is schematically exhibited as in Figure 4.46.

Mabru et al.[112] found that the fracture surfaces showed little difference in a lamellar microstructure of samples tested in air and in vacuum at 750 °C. Therefore, it was believed that the environment did not affect the basic fracture mode significantly by just promoted fatigue damage accumulation at the crack tip. This is consistent with the fractographic observation of Rosenberger. However, the fracture surface roughness measurement conducted also for a lamellar microstructure shows a much rougher surface near K_Q region in ultra high vacuum (UHV) than in laboratory air, that suggests changes in the fracture mode [112, 113].

4.10 Creep resistance in γ -TiAl alloys

4.10.1 Creep resistance

The creep resistance in two-phase TiAls is mainly dependent on the microstructure and aluminum content. A coarse-grain fully lamellar microstructure exhibits better creep resistance than a fine-grained duplex microstructure. Duplex microstructures show higher creep-rupture strength up to 650 °C, above which lamellar microstructures become superior to duplex microstructure for rupture strength [8, 114]. Two-phase TiAl alloys with serrated grain boundaries are effective for delaying propagation of creep deformation. This is because the serrated grain boundaries can reduce the stress concentration at triple points and extend the intergranular crack path compared with straight grain boundaries [55].

Significant microstructural changes in lamellar TiAl alloys during creep have been observed in a few studies, that result in a serious degradation of mechanical properties[115, 116]. By using TEM, Appel et al. [115] found the structural changes

start with the formation of multiple-height ledges perpendicular to the interfacial plane. These interfacial ledges are often associated with misfit dislocations having a Burgers vector component perpendicular to the interfacial plane. In order to achieve a phase equilibrium, which was unbalanced by a difference in the density of ledges between α_2/γ and γ/γ interfaces, climb of those dislocations and propagation of the ledges leads to a lateral migration of the interfaces. This process finally results in the formation of new γ grains and a complex conversion of lamellar morphology to a fine spheroidised microstructure. This interface related process might be the explanation why the recrystallisation is relatively easy in this ordered structures [115].

The other characteristic feature of the microstructure of crept TiAl alloys is the presence of precipitates (as shown in Figure 4.47). Most of the precipitates are located at isolated dislocations, the mismatched structures of subgrain boundaries and lamellar interfaces. According to the well-established knowledge of TiAl alloys that α_2 phase has much higher solubility limit for oxygen, carbon and nitrogen than γ phase, the precipitates might be as a consequence of the $\alpha_2 \rightarrow \gamma$ phase transformation [115].

4.10.2 Interaction between creep and fatigue on crack growth

Several authors have discussed issues related to creep-fatigue interactions during crack growth in γ -TiAl alloys [105, 110, 117, 118]. Mall et al. found that crack growth in a Ti₃Al alloy at elevated temperature can be cycle dependent, time dependent or a combination of these two [117]. At elevated temperatures, the yield strength can be decreased which leads to increased plasticity and thereby reduces the crack growth rates. If the applied stress intensity factor is above the crack growth threshold stress intensity, creep resulted in crack tip blunting which could retard crack growth [117]. Nichols et al. [117, 119] found in Inconel 718 that the creep crack growth rate following a fatigue cycle is dependent on the amplitude and frequency of the fatigue cycles. If the

creep growth is ahead of a fatigue cycle, the fatigue crack growth rate is usually reduced because no “steady state” condition before the fatigue cycle achieved. The creep-fatigue crack growth (CFCG) behaviour can be described by an equation including both cyclic and time-dependent damage as follows:

$$\left(\frac{da}{dN}\right)_{CFCG} = \left(\frac{da}{dN}\right)_{FCG} + (T - T_c) \times \left(\frac{da}{dN}\right)_{TDCG} \quad \dots 4.4$$

for $T > T_c$

where $\left(\frac{da}{dN}\right)_{FCG}$ and $\left(\frac{da}{dN}\right)_{TDCG}$ represent the fatigue crack growth (FCG) and the time-dependent crack growth (TDCG) rate, respectively. And T is the load period and T_c critical value of the period above which the CFCG rates are proportional to the period T [110]. After identifying the T and T_c values by plotting the CFCG rates as a function of the loading period for selected K_{max} values, the TDCG and creep-crack growth (CCG) rates can be calculated by equation 4.4, to determine a crack-growth model and how the models affect the crack-growth behaviour under a creep-fatigue interaction situation.

Zhu et al. reported that the high-temperature fatigue crack growth rates in the higher crack growth rate regime is different from it at room temperature due to creep-introduced crack-tip blunting at an R ratio of 0.5 [105].

Table 4.1. Properties of Titanium alloys, Titanium Aluminides and Superalloys [52]

Property	Ti-based	Ti ₃ Al-based	TiAl-base	Superalloys
Structure	Hcp/bcc	D0 ₁₉	L1 ₀	Fcc/L1 ₂
Density (g/cm ³)	4.5	4.1-4.7	3.7-3.9	7.9-8.5
Modulus (GPa)	95-115	110-145	160-180	206
Yield Strength (MPa)	380-1,150	700-900	350-600	800-1,200
Tensile Strength (MPa)	480-1,200	800-1,140	440-700	1,250-1,450
Room-Temp. Ductility (%/°C)	10-25	2-10	1-4	3-25
High-Temp. Ductility (%/°C)	12-50	10-20/660	10-600/870	20-80/870
Room-Temp. Fracture Toughness (MPa√m)	12-50	13-30	12-35	30-100
Creep Limit (°C)	600	750	750-950	800-1,090
Oxidation (°C)	600	650	800-950	870-1,090

Table 4.2. Effect of selected alloying elements on mechanical properties of TiAl [8]

Element	Effect
Nb	Increases oxidation and creep resistance in small amounts, also increases high temperature strength if added between 5% and 10%
Ta	Increases oxidation and creep resistance and tendency for hot cracking
V	Increases ductility
W	Oxidation and creep resistance
B	Grain refiner
C	Increases creep and oxidation resistance
Cr	Increases ductility if added in small amounts; increases oxidation resistance if added in the range of 8%
Mn	Increases ductility
Mo	Increases strength, and creep and oxidation resistance.

Table 4.3. (a) microstructure and (b) mechanical properties of γ -TiAl alloys obtained at room temperature [7]

(a) Microstructure of γ -TiAl alloys

Microstructure/Composition (At. Pct)	Lamellar Colony Size, D	Lamellar Spacing, λ^*	Equiaxed γ Phase	γ Grain Size
XD nearly lamellar/ Ti-47.7Al-2.0Nb-0.8Mn + 1 vol pct TiB ₂	120 μm	2.0 μm	~30 pct	~23 μm
MD fully lamellar/ Ti-47Al-2Nb-2Cr-0.2B	145 μm	1.3 μm	~4 pct	5 to 20 μm
MD duplex/ Ti-47Al-2Nb-2Cr-0.2B	—	—	90 pct	17 μm
P/M lamellar/ Ti-47Al-2Nb-2Cr	65 μm	0.2 μm	<5 pct	~1 μm
G7 coarse lamellar/ Ti-47.3Al-2.3Nb-1.5Cr-0.4V**	1 to 2 mm	1.3 μm	<5 pct	10 to 40 μm
G7 duplex/ Ti-47.3Al-2.3Nb-1.5Cr-0.4V**	—	—	90 to 95 pct	15 to 40 μm

*Center-to-center spacing of the α_2 phase.
**From Ref. [6].

(b) Mechanical properties of γ -TiAl alloys

Microstructure/Composition (At. Pct)	Yield Strength (MPa)	Fracture Strength (MPa)	Elongation (Pct)	Fracture Toughness* (MPa $\sqrt{\text{m}}$)
XD nearly lamellar**/ Ti-47.7Al-2.0Nb-0.8Mn + 1 vol pct TiB ₂	546	588	0.7	12 to 16
MD fully lamellar/ Ti-47Al-2Nb-2Cr-0.2B	426	541	0.8	18 to 32
MD duplex/ Ti-47Al-2Nb-2Cr-0.2B	384	489	0.9	—
P/M lamellar/ Ti-47Al-2Nb-2Cr	975	1010	1.0	18 to 22
G7 coarse lamellar/ Ti-47.3Al-2.3Nb-1.5Cr-0.4V	450	525	1.0	18 to 39
G7 duplex/ Ti-47.3Al-2.3Nb-1.5Cr-0.4V	450	590	4.0	11

*A range in values indicates R -curve behavior; the first value corresponds to the crack-initiation toughness, K_{Ii} ; the second to the steady-state toughness or maximum measured crack-growth resistance, K_{Im} .
**Tensile data are taken from a material of similar composition and microstructure.^[24]

Table 4.4. Surface integrity data for the fatigue specimens made from a grain-refined γ -TiAl alloy (Ti-45 Al-2Mn-2Nb+0.8B at.%) [75]

Machining procedure	Max. crack depth (μm)	Ra (μm)	Residual stress
Turning	5	0.84	Highly compressive
ECM	0	1.43	Neutral
EDT-L	10	1.32	Tensile
EDT-H	40	3.98	Tensile

Table 4.5. Modified Paris-Law parameters revealing dependencies of a XD TiAl alloy to ΔK and K_{\max} [101]

Temperature	C' , m/cycle	$p; (\Delta K)^P$, MPa $\sqrt{\text{m}}$	$n; (K_{\max})^n$, MPa $\sqrt{\text{m}}$
25 °C	2.85×10^{-23}	10.3	5.6
600 °C	4.48×10^{-13}	2.8	2.4
800 °C	1.81×10^{-23}	2.2	10.8

Table 4.6. Effect of test environment on tensile properties of Ti-47.5Al-2.5Nb-2Cr-0.5Mn-0.5Si (at.%) tested with an loading rate of $3.3 \times 10^{-3} \text{s}^{-1}$ [106]

Test environment	Plastic strain to fracture (%)	Yield strength (MPa)	Ultimate tensile strength (MPa)
Air ^a	0.2	497	497
Vacuum ^b	0.5	494	502
Oxygen ^c	1.2	496	516

^aLaboratory air with a relative humidity of 55%.

^bVacuum = 4×10^{-4} Pa.

^cOxygen pressure = 66 kPa.

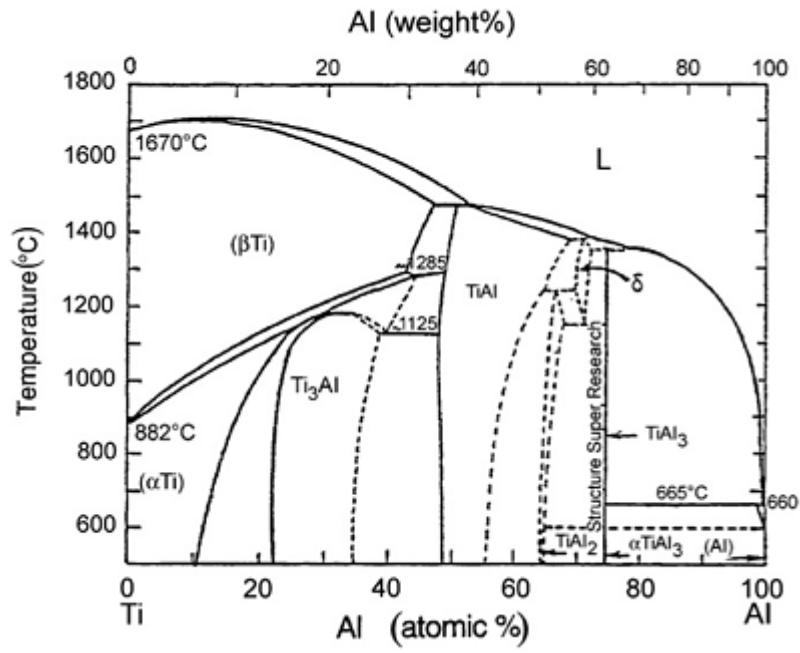
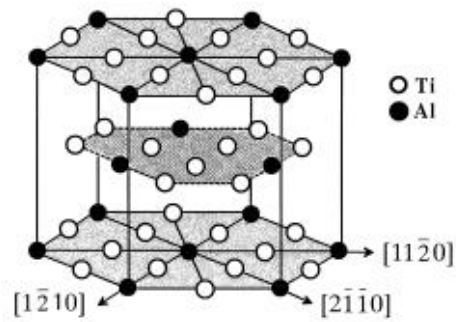
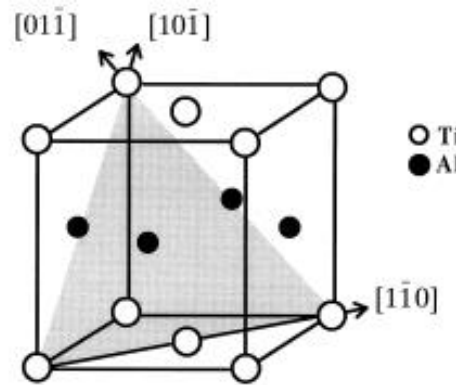


Figure 4.1. Ti-Al phase diagram [8]



(a)

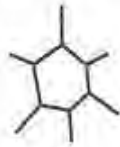


(b)

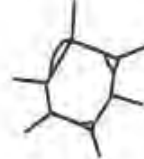
Figure 4.2. Crystal structure of (a) α₂-Ti₃Al (D0₁₉) and (b) γ-TiAl (L1₀) [5]

Microstructural Types in Gamma-Base Alloys

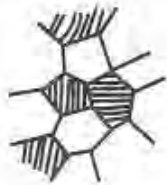
(a) single phase



(d) super solvus



(b) duplex structure



(e) sub-transus



(c) fully transformed



(f) dual-phase equiaxed

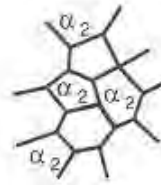


Figure 4.3. Schematic of microstructure categories in gamma TiAl-based alloys

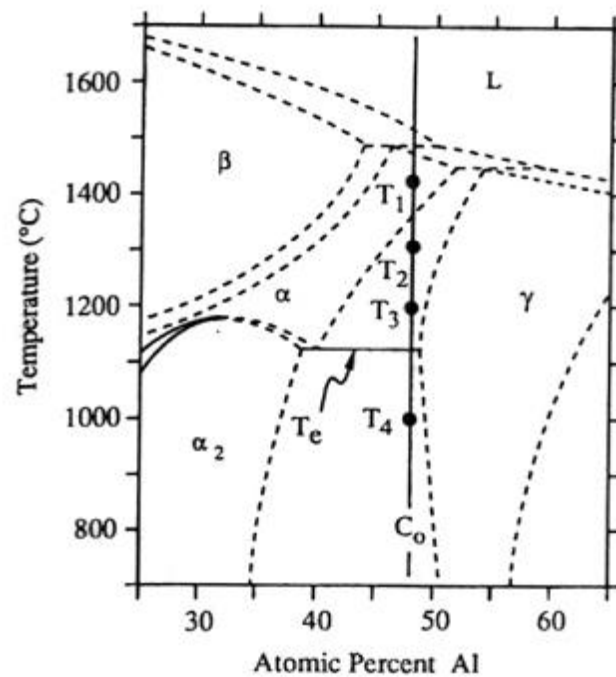


Figure 4.4. Central portion of the Ti-Al phase diagram [120]

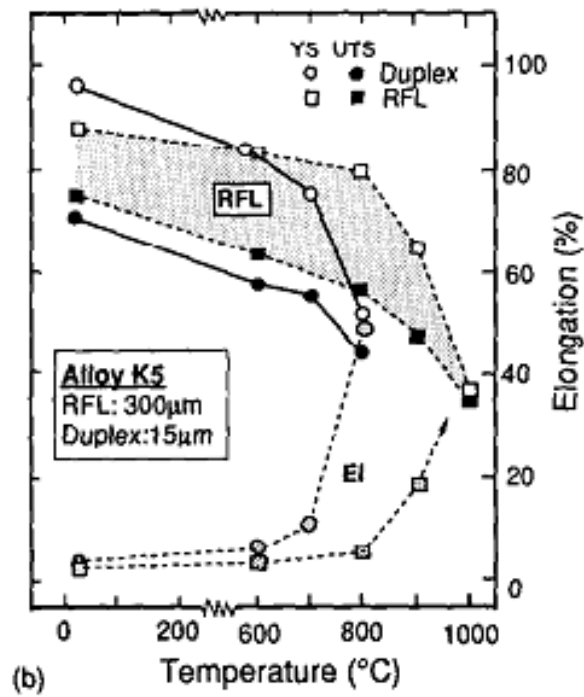
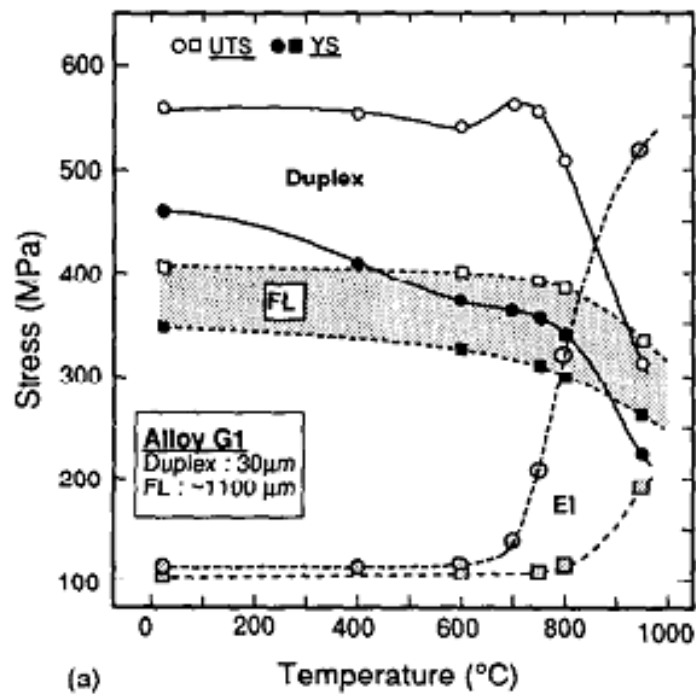


Figure 4.5. Tensile properties vs. test temperature in γ -based TiAl alloys with duplex (DP), fully-lamellar (FL) and refined fully-lamellar (RFL) microstructures [54]

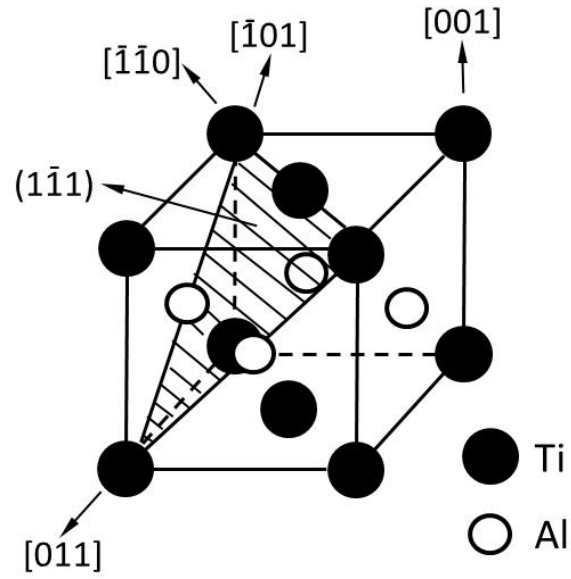


Figure 4.6. Possible dislocations slip directions and planes in γ phase [46]

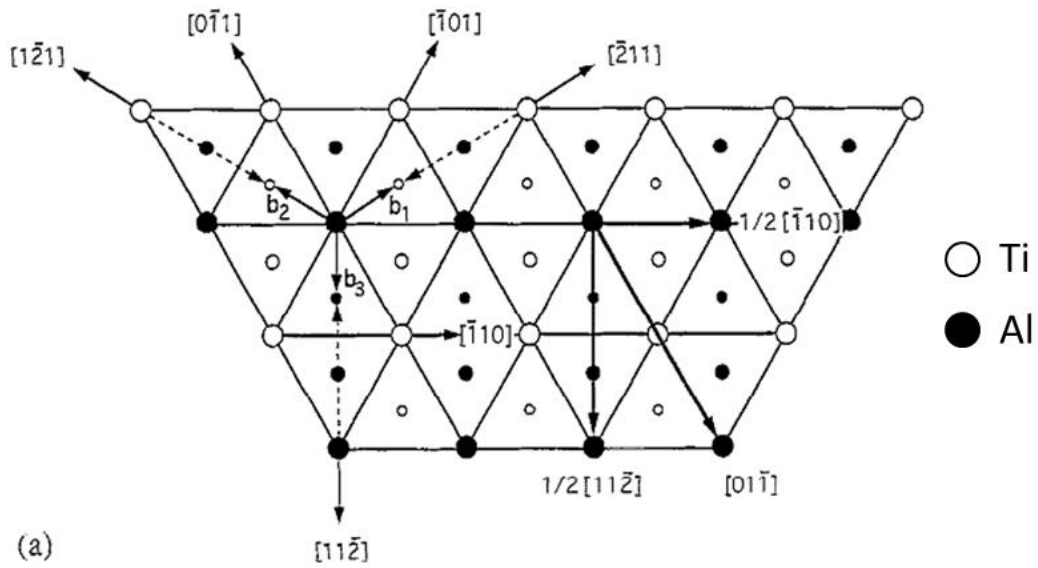


Figure 4.7. Potential slip and twinning systems of the $L1_0$ structure showing three-layer sequence of atomic stacking on the $\{111\}$ planes distinguished by small, medium and larger circles. $b_1=1/6[211]$, $b_2=1/6[121]$ and $b_3=1/6[112]$ are the burgers vectors of partial dislocations [67]

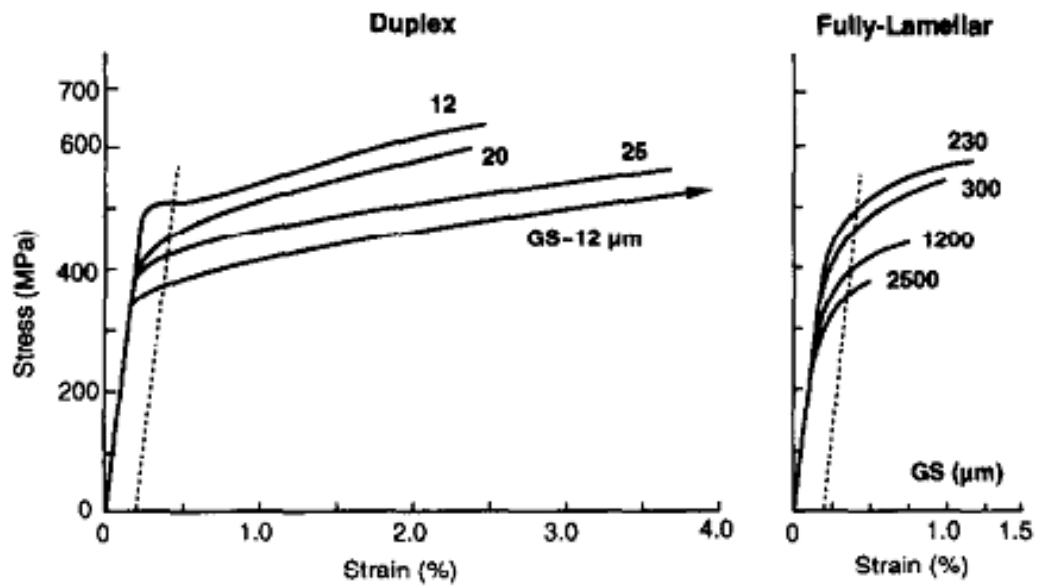


Figure 4.8. Tensile properties of two typical microstructures of TiAl alloys (duplex and fully lamellar structures) varied with grain size at room temperature[66]

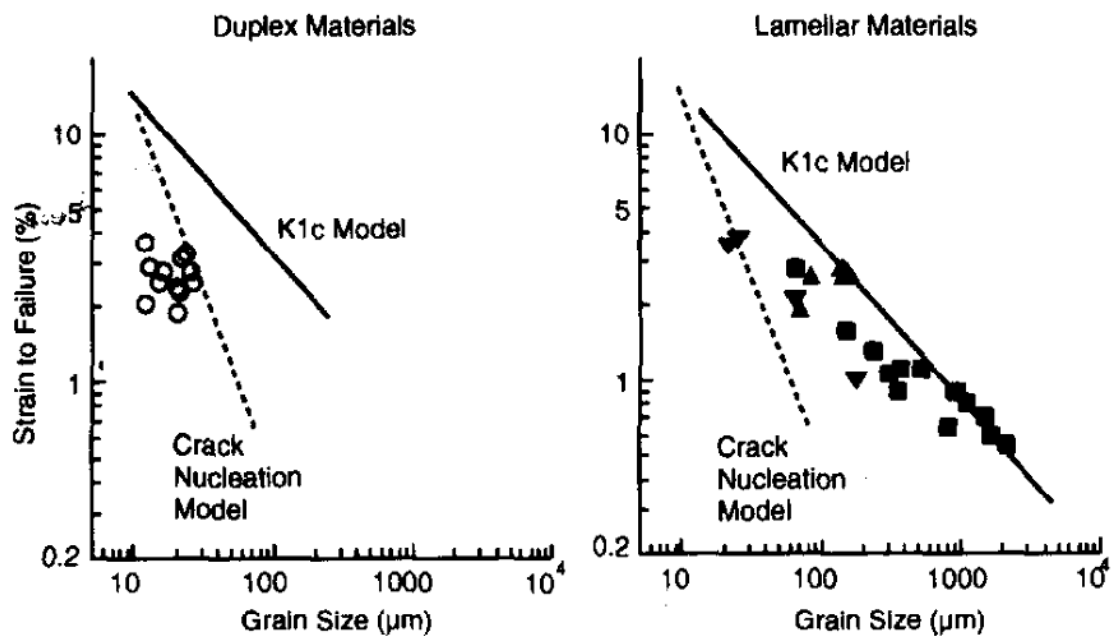


Figure 4.9. Strain-to-failure values vs. grain size for duplex and fully-lamellar microstructures. The elongation was predicted by K_{IC} model and crack nucleation model [66].

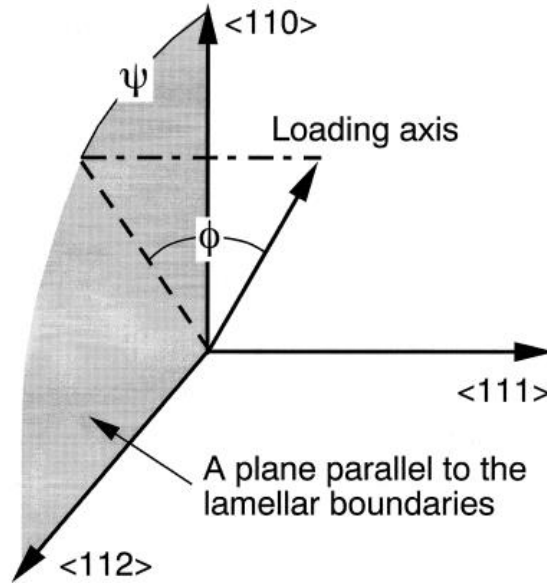


Figure 4.10. The relationship of loading axis orientation and lamellar boundary orientation in PST crystals. Since γ lamellar consists of domains of six orientation variants, a loading axis orientation given by a set of ϕ and ψ is equivalent to that given by a set of ϕ and $\pm\psi$ with an integral multiple of 60° [5].

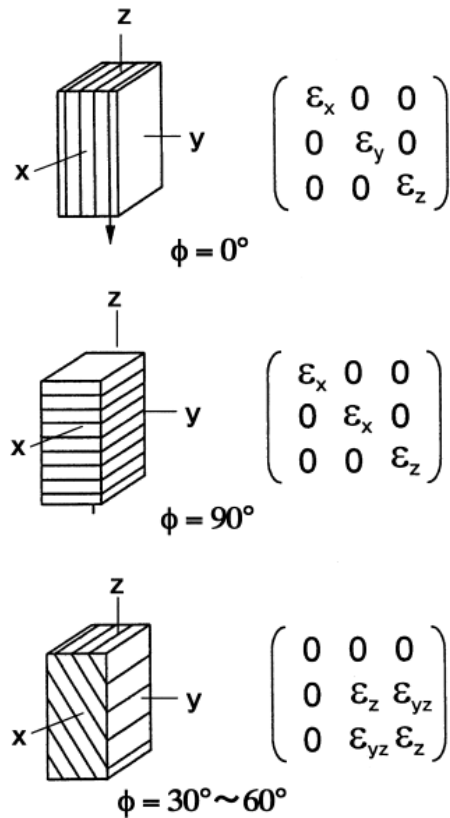


Figure 4.11. Macroscopic deformation of PST crystals [5].

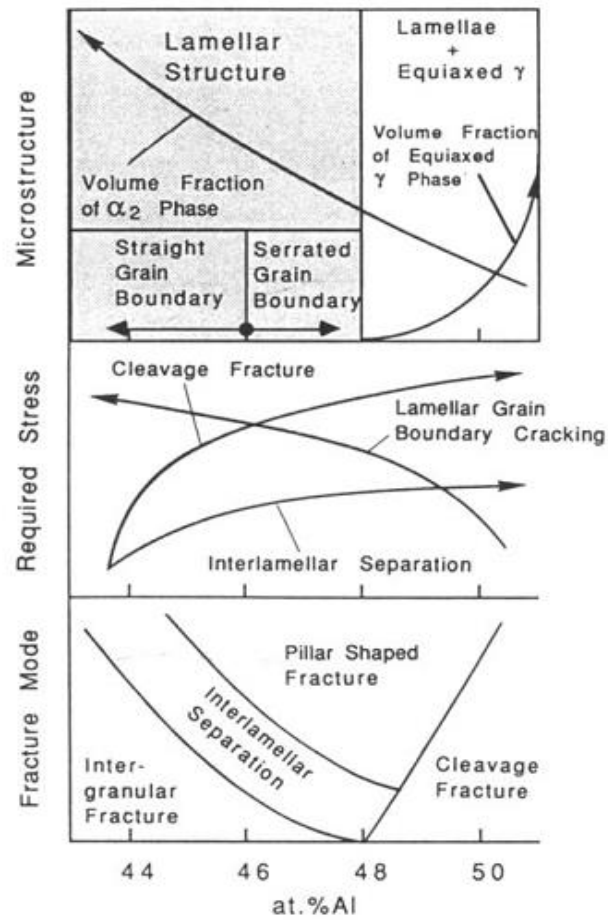


Figure 4.12. Diagram of fracture modes of binary TiAl alloys varying with content of Al at room temperature [121]

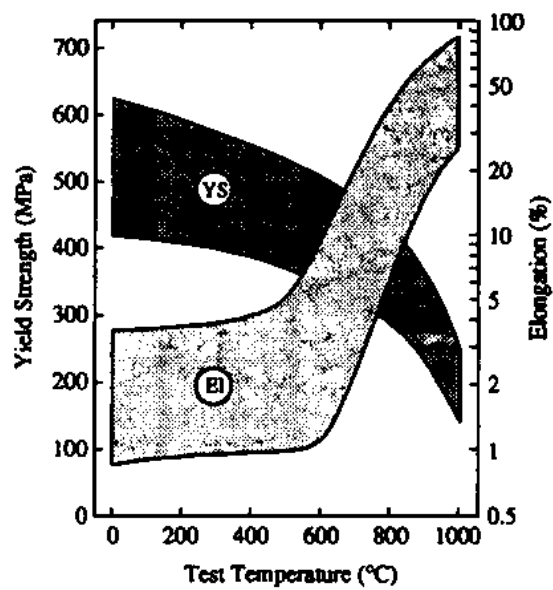


Figure 4.13. Change of yield strength and tensile elongation of gamma alloys against test temperature [46].

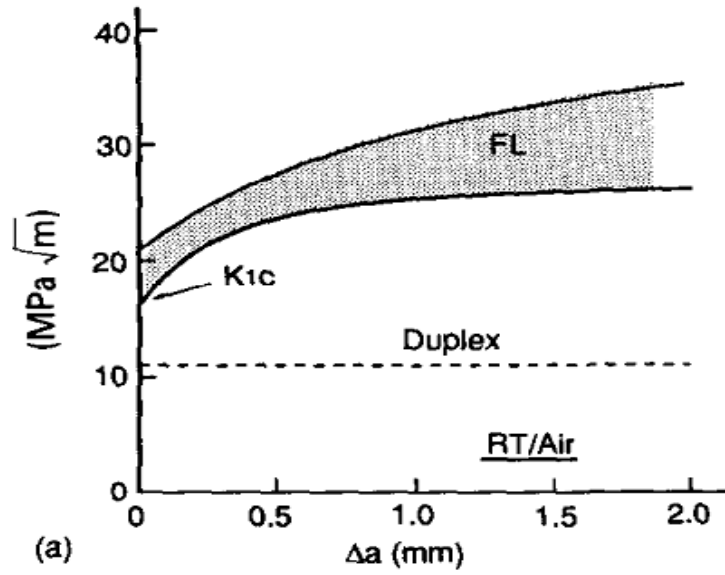


Figure 4.14. Fracture behaviour of alloy Ti-47Al-1Cr-1V-2.5Nb (at.%) at RT in duplex and fully-lamellar structures: (a) R-resistance curves and (b) effective strains vs. radial distance r [54].

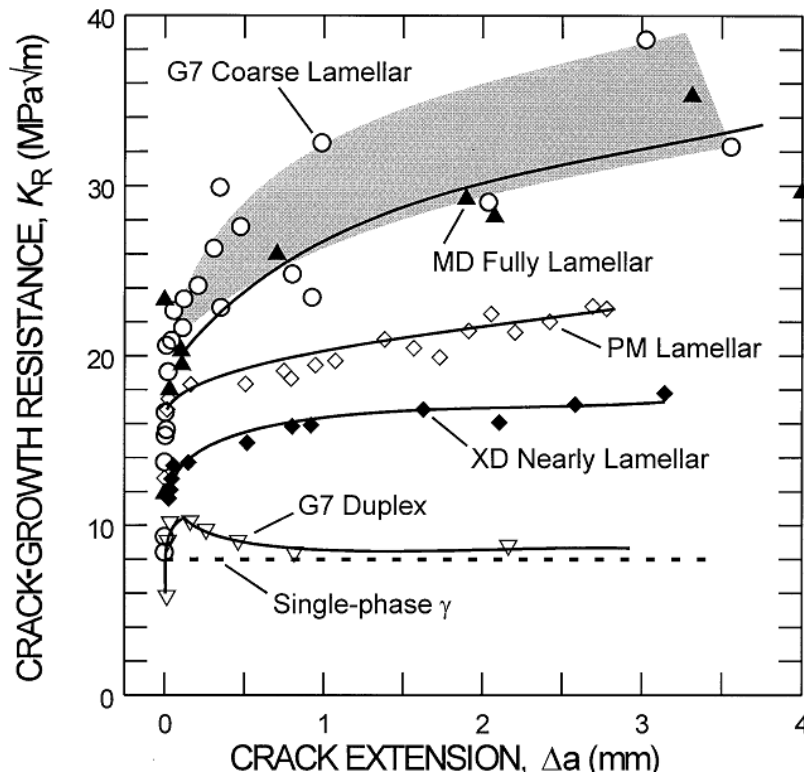


Figure 4.15. R- curves for MD fully lamellar, P/M lamellar, and XD nearly lamellar microstructures, compared to the fracture toughenss behaviour of G7 coarse lamellar, G7 duplex, and single-phase γ microstructures [7].

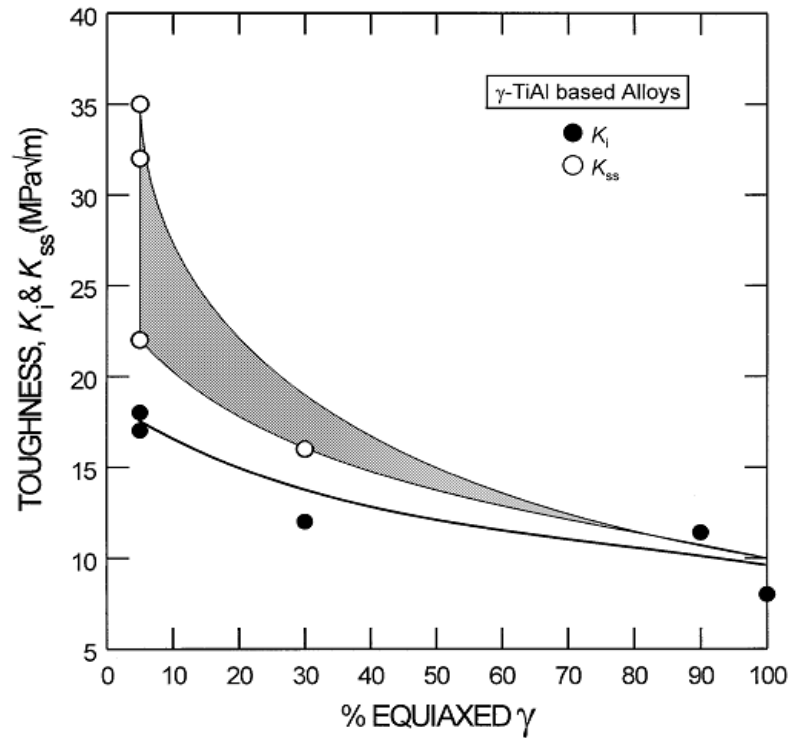


Figure 4.16. Crack initial toughness (K_I) and resistance toughness (K_{SS}) vs. volume fraction of equiaxed γ grains for several microstructures: MD fully lamellar, XD nearly lamellar, P/M lamellar, G7 coarse lamellar, G7 duplex, and single-phase [7]

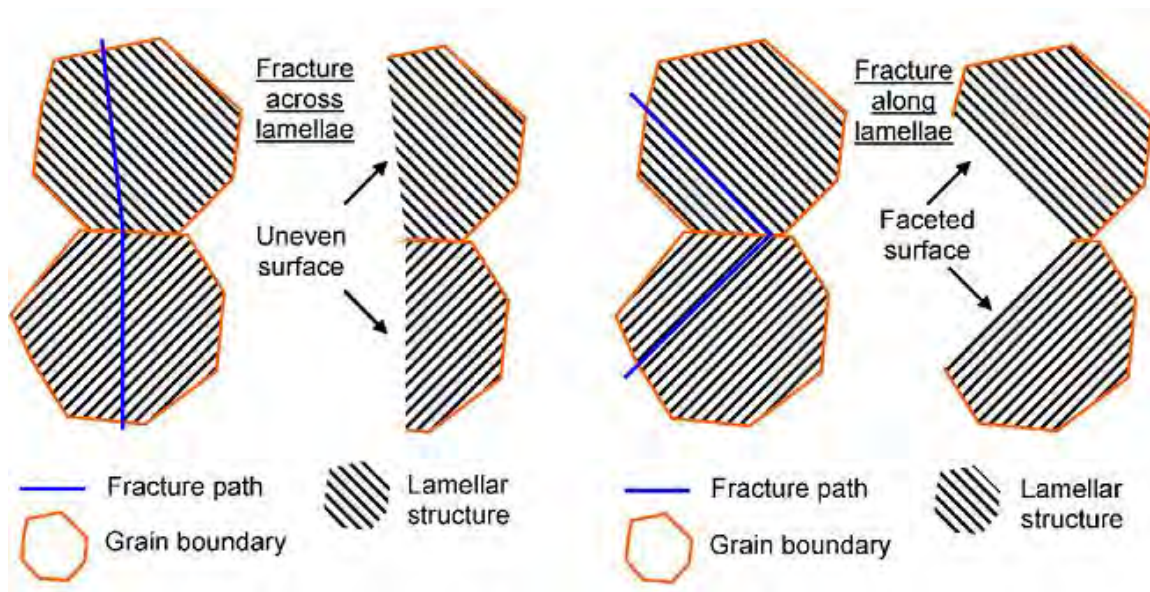


Figure 4.17. The schematic diagram of translamellar fracture and interlamellar fracture in a lamellar γ -TiAl alloy [122]

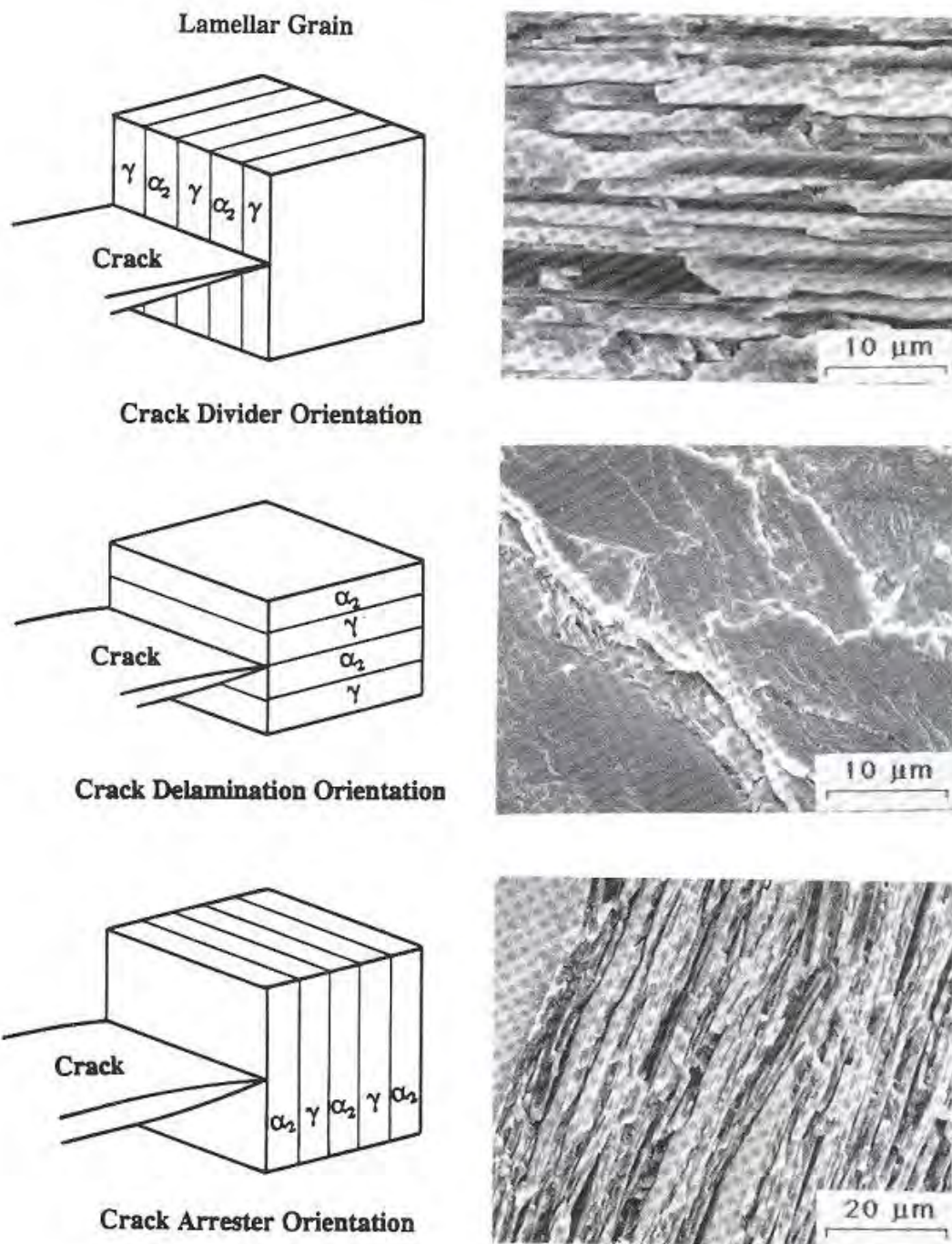


Figure 4.18. The three type of fractographic features observed in a lamellar microstructure [123].

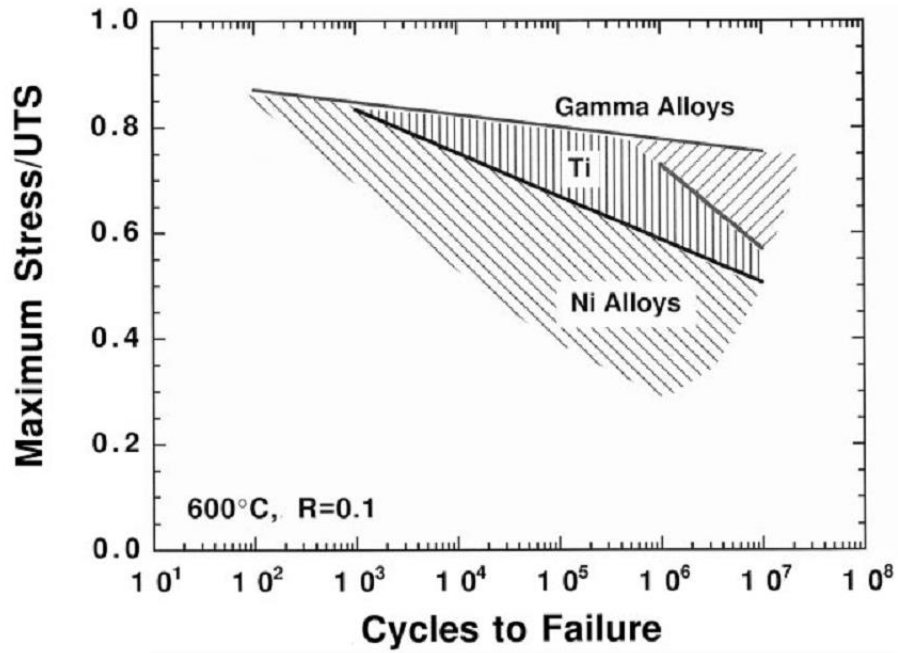


Figure 4.19. The comparison of high-cycle fatigue behaviour of nickel, titanium and γ -TiAl alloys at 600 °C. The maximum cyclic stress is normalised by ultimate tensile strength to show alloys' intrinsic fatigue capability [73]

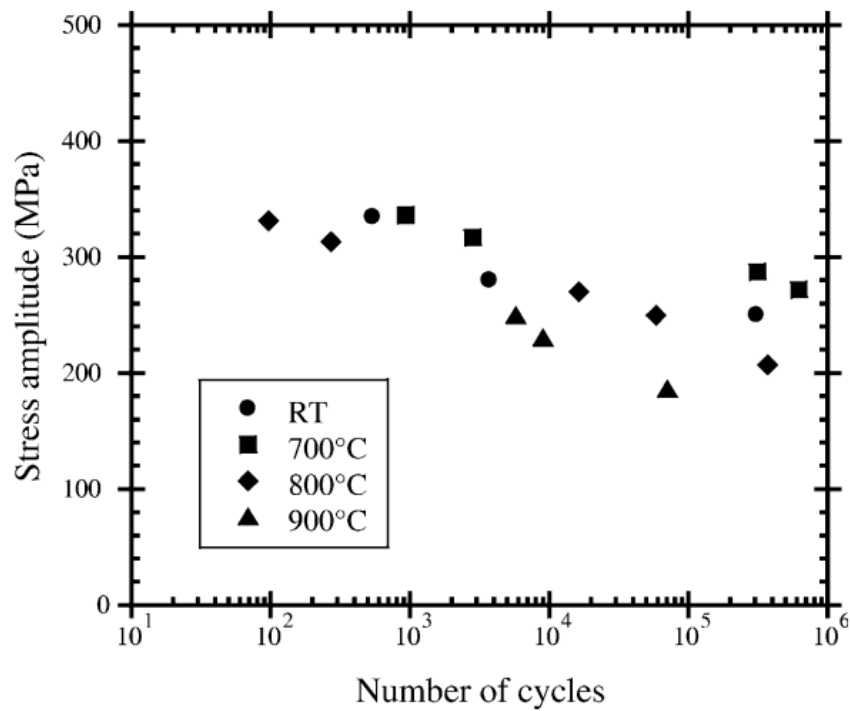


Figure 4.20. S-N curves of a lamellar TiAl alloy (Ti-36.5Al wt.%) at various temperatures [74]

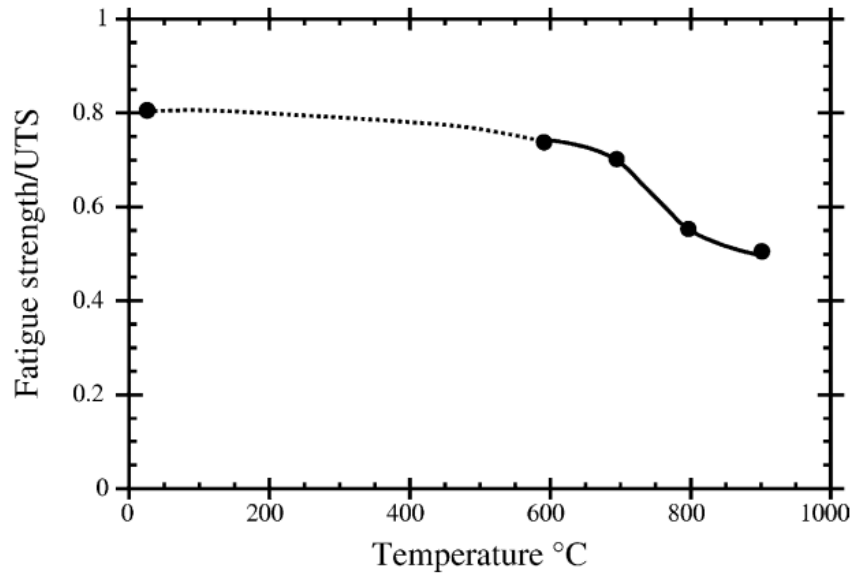


Figure 4.21. Influence of temperature on the high-cycle fatigue resistance of a lamellar TiAl alloy (Ti-36.5Al wt.%) [74]

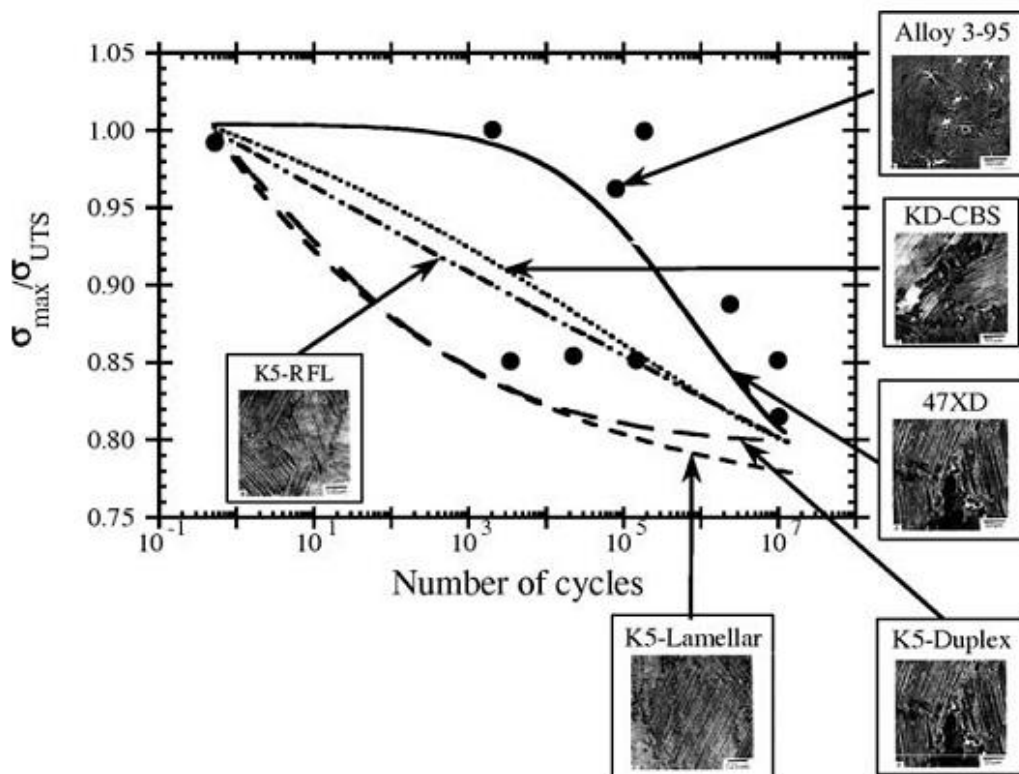


Figure 4.22. Influence of microstructure on fatigue resistance at room temperature. K5-RFL is refined fully lamellar structure, K5-lamellar is coarse lamellar structure, K5-duplex is duplex structure and KD-CBS is a carbon-boron-silicon modified K5 alloy. The compositions of 47XD and alloy 3-95 are Ti-48Al-2Nb-2Mn-0.2W and Ti-46Al-2Cr-2Nb-1Mo-0.2B, respectively [70].

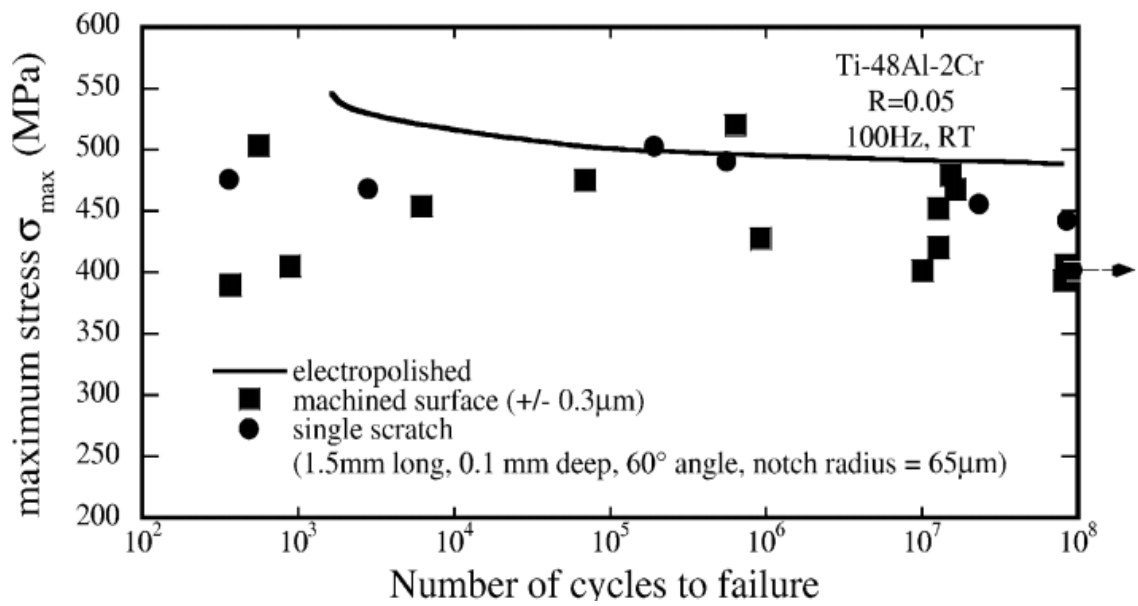


Figure 4.23. Influence of surface finishing on fatigue strength of a γ -TiAl alloy [82]

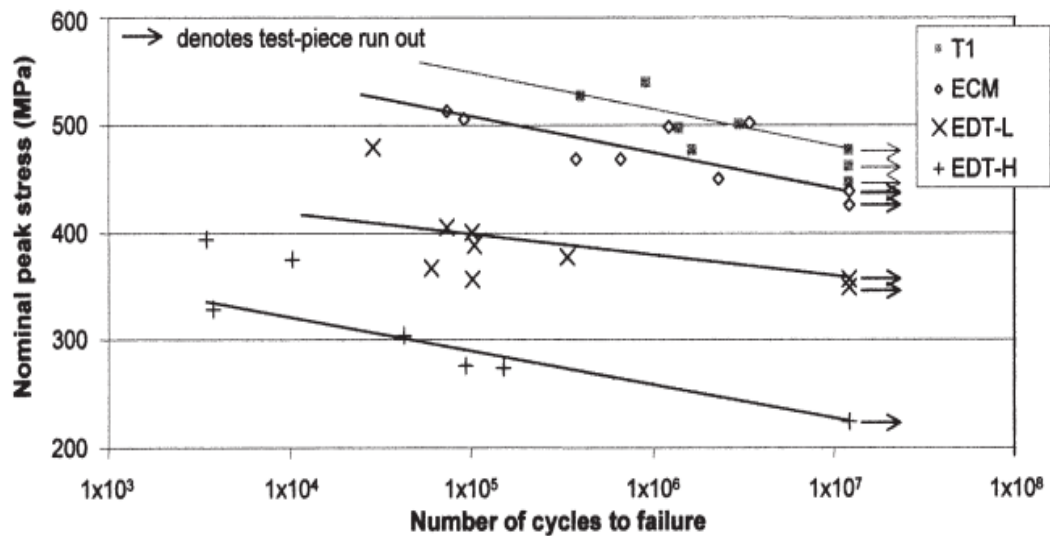


Figure 4.24. S-N curves for turned, ECM (electro-chemical machining) and EDT (electro-discharge texturing) specimens (EDT-L and EDT-H mean low operating energy and high operating energy respectively) [75].

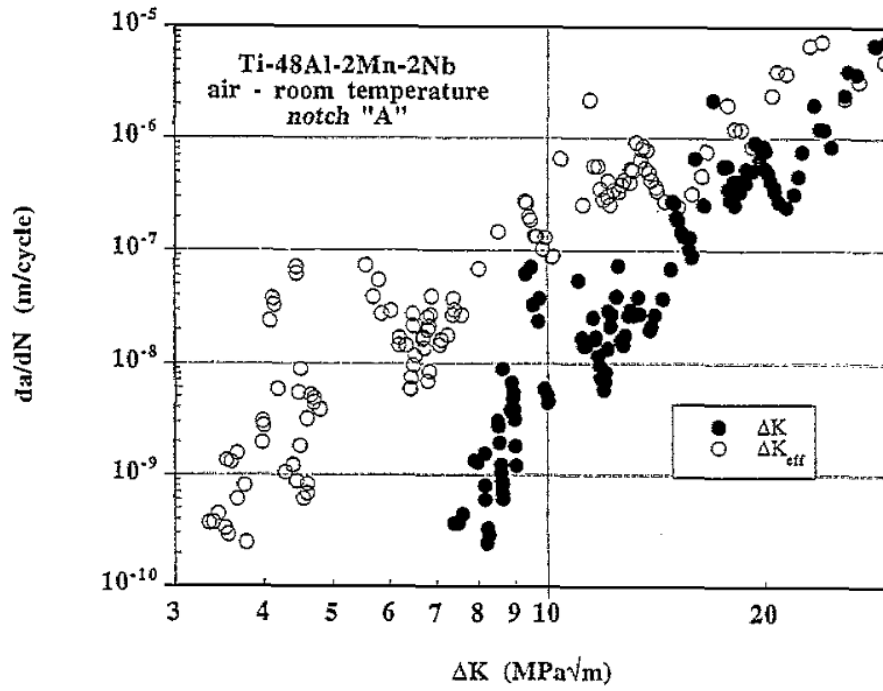


Figure 4.25. Fatigue crack resistance curve by plotting the fatigue crack growth rates as a function of ΔK and ΔK_{eff} in air at RT for the crack-arrester orientation [85]

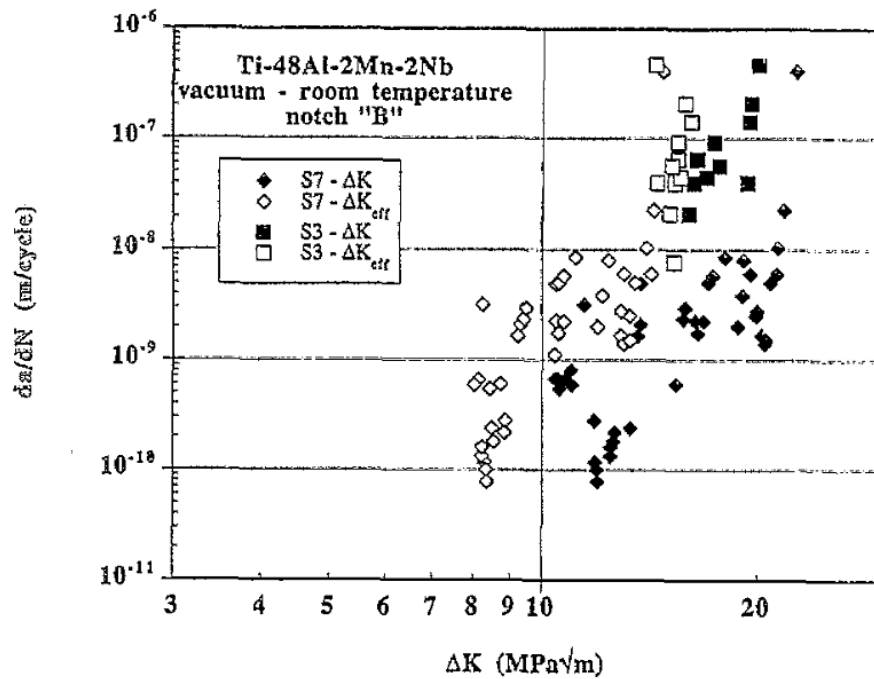


Figure 4.26. Fatigue crack resistance curves by plotting fatigue crack growth rates as a function of ΔK and ΔK_{eff} in vacuum at RT for the crack divider orientation [85]

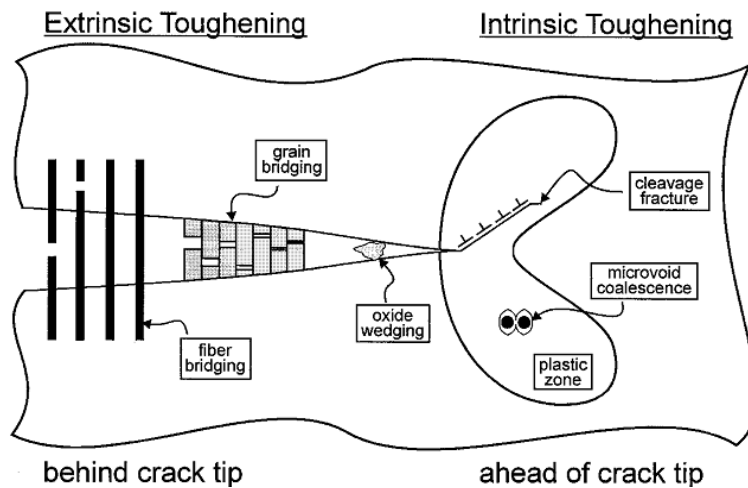


Figure 4.27. Schematic illustration of intrinsic and extrinsic mechanisms in a material[4]

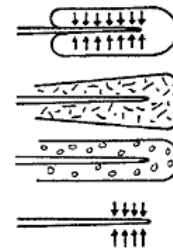
EXTRINSIC TOUGHENING MECHANISMS

1. CRACK DEFLECTION AND MEANDERING



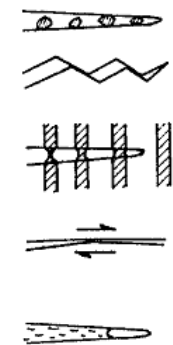
2. ZONE SHIELDING

- transformation toughening
- microcrack toughening
- crack wake plasticity
- crack field void formation
- residual stress fields
- crack tip dislocation shielding



3. CONTACT SHIELDING

- wedging:
 - corrosion debris-induced crack closure
 - crack surface roughness-induced closure
- bridging:
 - ligament or fiber toughening
- sliding:
 - sliding crack surface interference
- wedging + bridging:
 - fluid pressure-induced crack closure



4. COMBINED ZONE AND CONTACT SHIELDING

- plasticity-induced crack closure
- phase transformation-induced closure

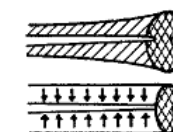


Figure 4.28. Schematic illustration of different types of extrinsic toughening [4]

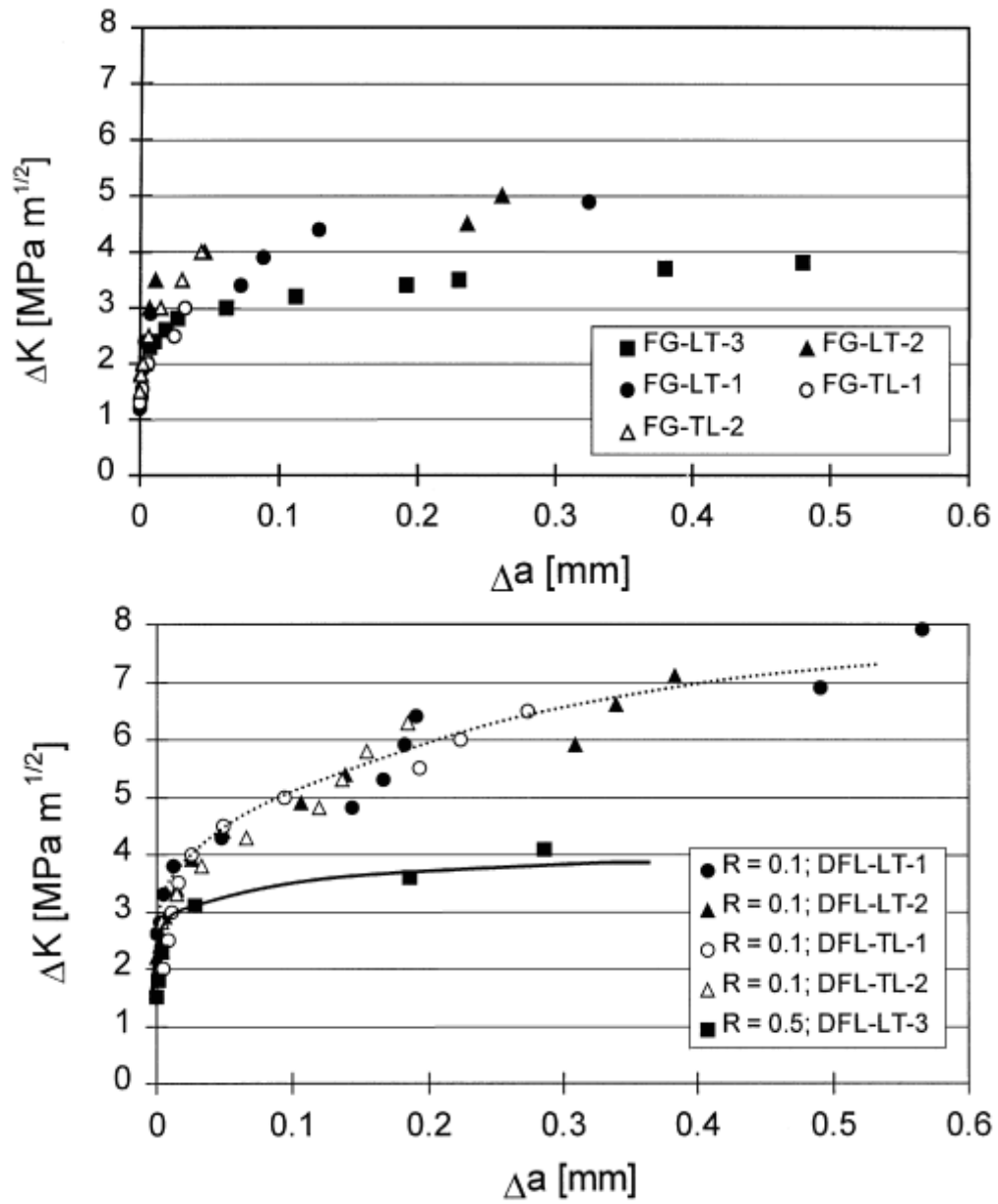


Figure 4.29. Stress intensity range vs. crack extension where the crack stops the propagation for both microstructures: (a) fine-grained near γ (FG) and (b) designed fully lamellar (DFL) microstructure. The specimens were machined from loading axis in rolling direction (LT) and perpendicular to the rolling direction (TL)

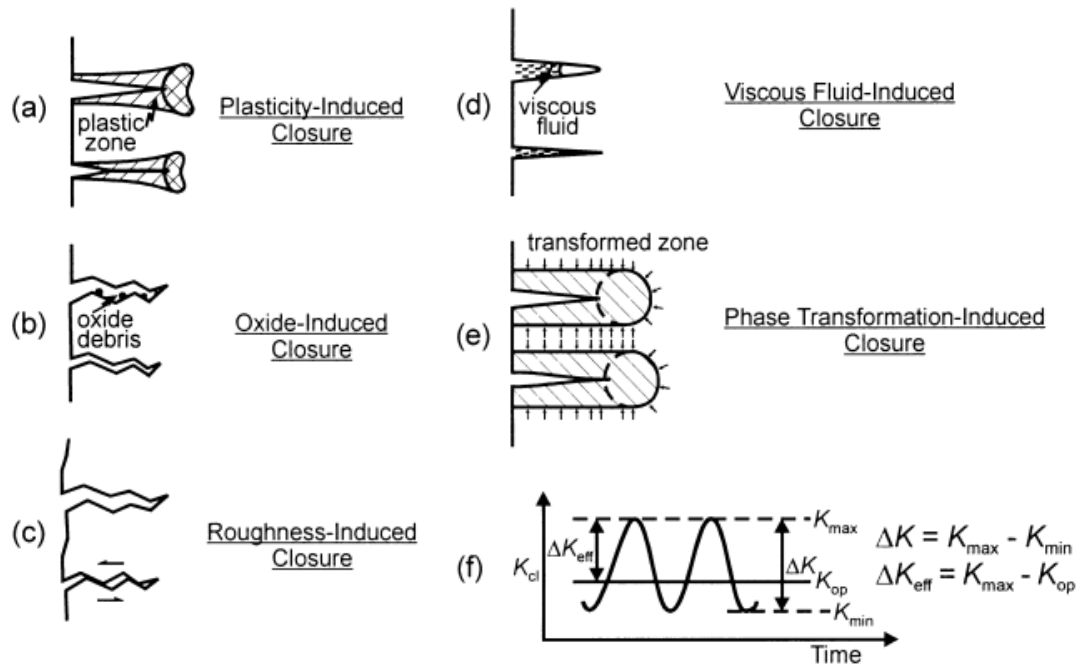


Figure 4.30. The possible mechanisms of crack closure

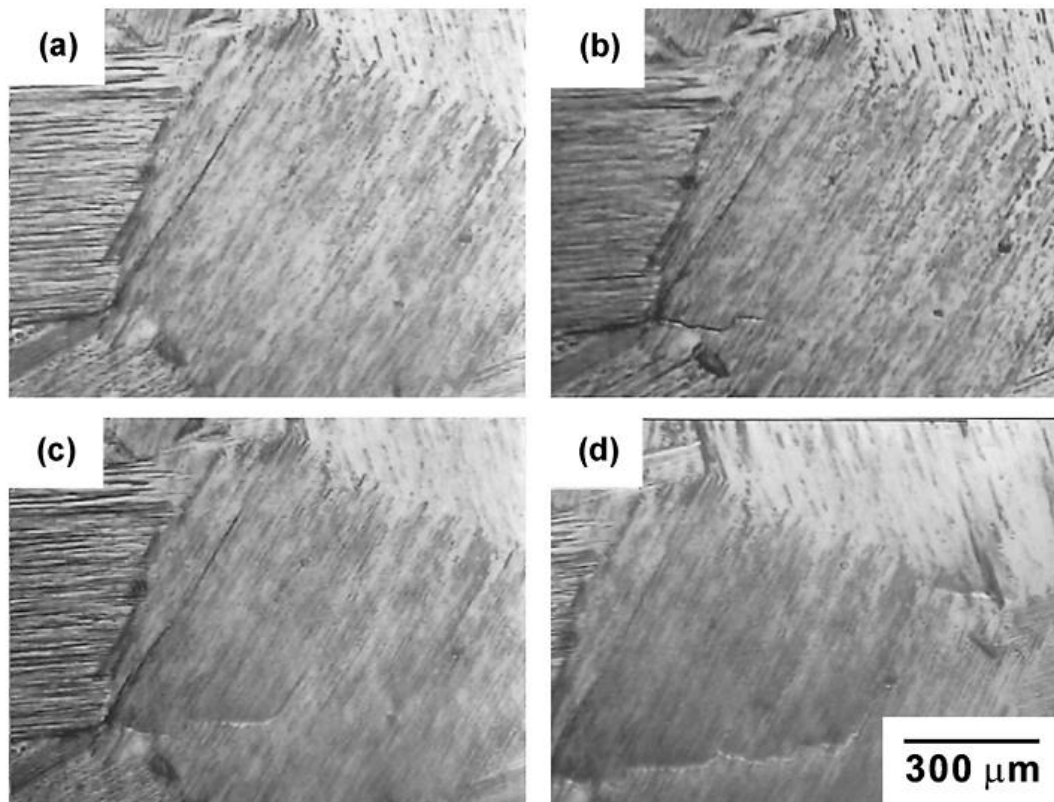
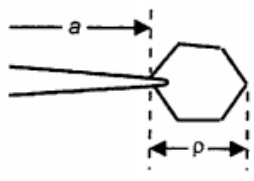
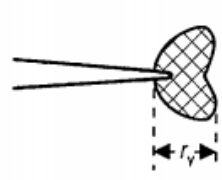
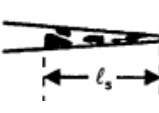


Figure 4.31. An example crack extension concurrent with crack deflection and branching in a furnace-cooled lamellar TiAl alloy (Ti-4822). The crack growth direction is from left to right

Major Classes of Small Cracks

- MICROSTRUCTURALLY SMALL:**


$a \sim \rho$ (microstructural dimension)
 continuum limitation
 statistical sampling of microstructure
 need to use probabilistic approach
- MECHANICALLY SMALL:**


$a \sim r_y$ (plastic zone size)
 LEFM/driving force limitation
K-field inappropriate
 need to use inelastic analysis, e.g., ΔJ
- PHYSICALLY SMALL:**


$a \sim \ell_s$ (size of crack-tip shielding zone)
 similitude limitation
 local driving force inappropriate
 need to correct for closure/shielding

Figure 4.32. Schematic illustration of the three major classes of small fatigue cracks[39].

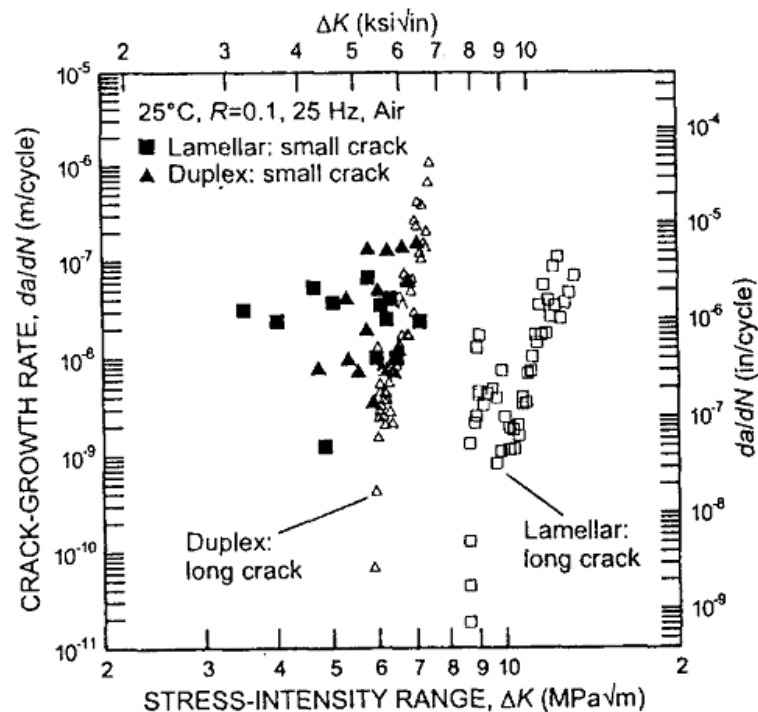


Figure 4.33. Fatigue crack-growth rates for through-thickness long cracks ($a > 5$ mm) and small surface cracks ($c \sim 35$ – 275 μm) in the lamellar and duplex microstructure of Ti-47Al-2Nb-2Cr-0.2B [97].

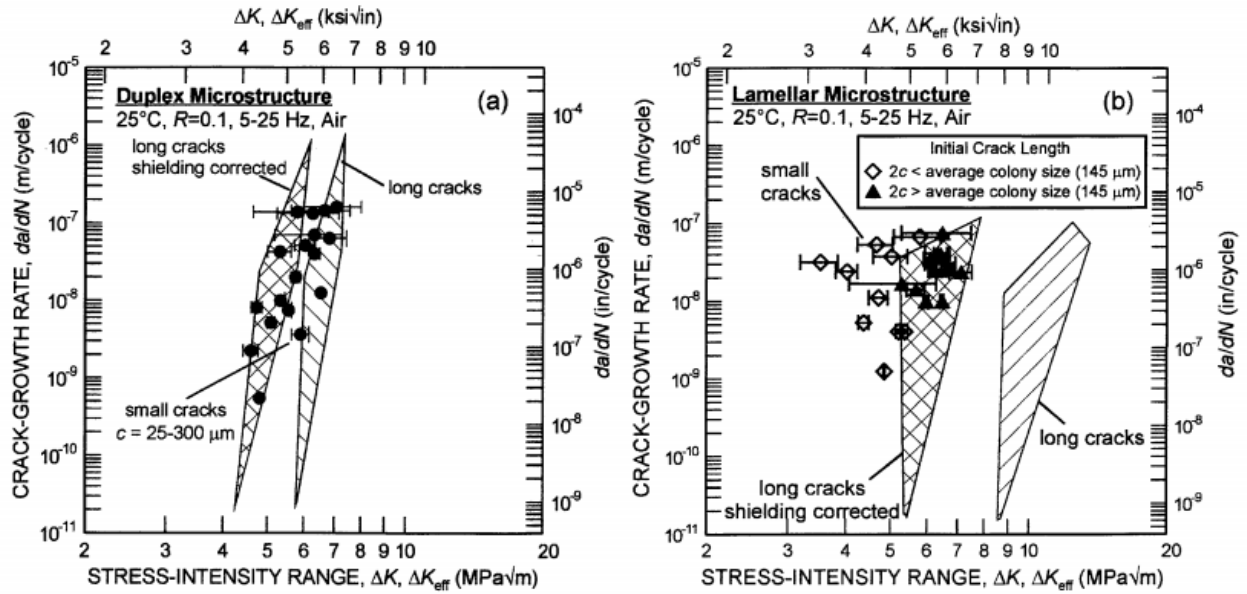


Figure 4.34. Comparison of the crack-growth rates of small surface cracks and through-thickness long cracks in (a) duplex and (b) lamellar microstructures. The long-crack data ΔK were corrected for both crack bridging (ΔK_{br}) and crack closure (ΔK_{cl}). The effective stress intensity, $\Delta K_{eff} = (K_{max} - K_{br}) - K_{cl}$ [39]

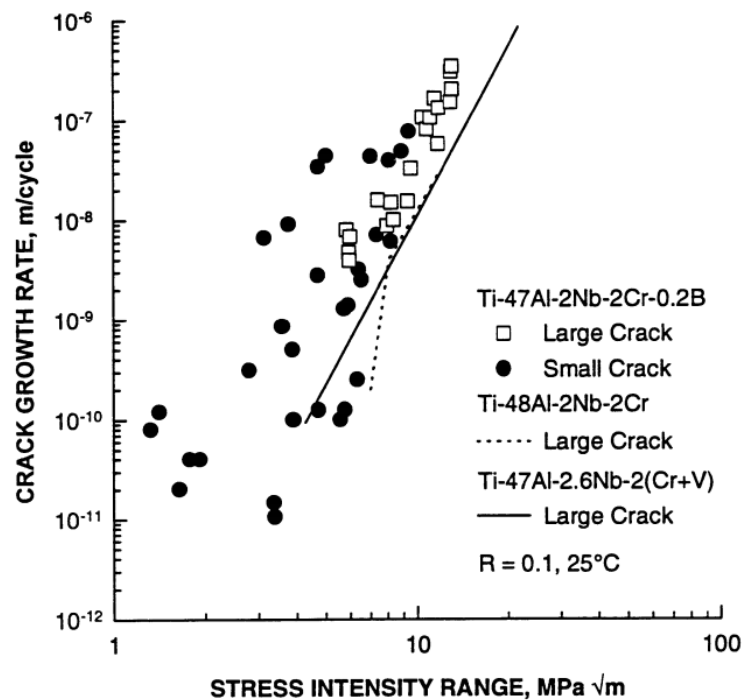


Figure 4.35. Summary of fatigue crack growth data of large and small cracks in fine-grained, fully lamellar Ti-47Al-2Nb-2Cr-0.2B and comparison with large crack data for two coarse-grained lamellar alloys, Ti-47Al-2.6Nb-2(Cr+V) and Ti-48Al-2Nb-2Cr [99].

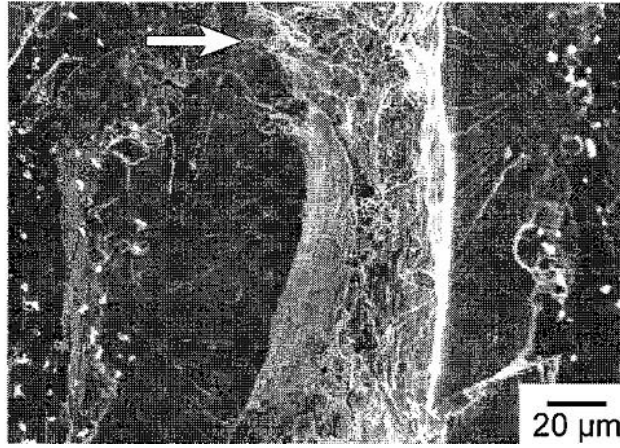


Figure 4.36. Intrinsic toughening via crack renucleation across the Nb layer [4]

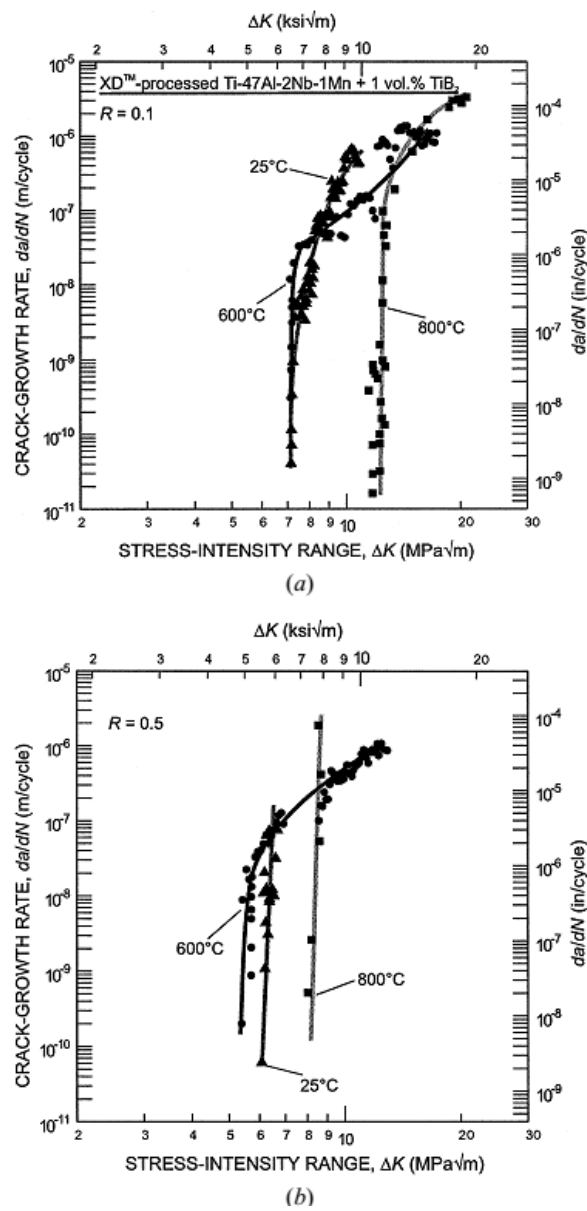


Figure 4.37. Fatigue crack resistance curves obtained at 25 °C, 600 °C and 800 °C at (a) $R=0.1$ and (b) $R=0.5$ in the XD-processed Ti-47Al-1.9Nb-0.9Mn (at.%) [101].

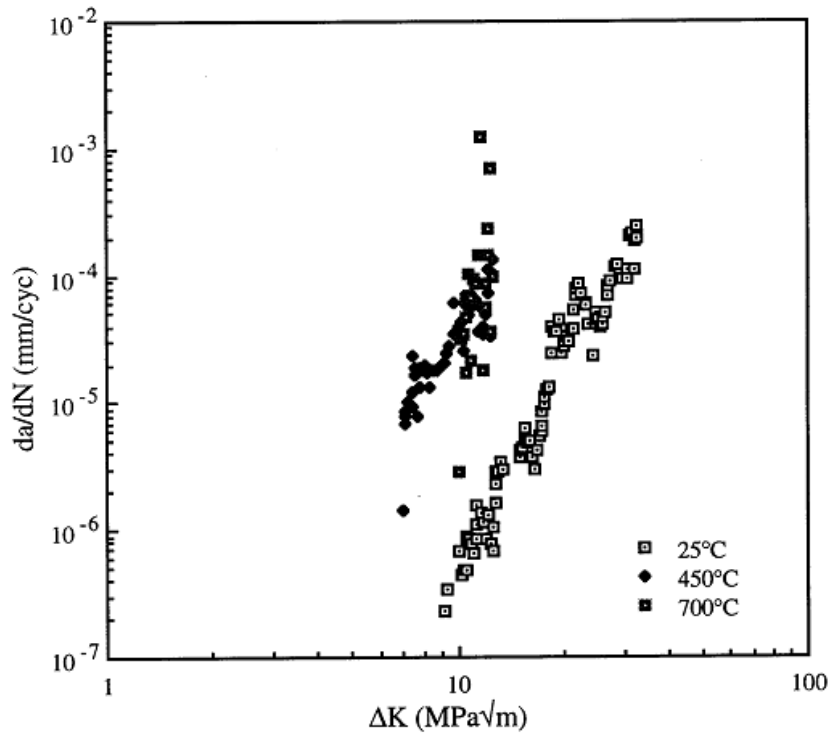


Figure 4.38. Fatigue crack resistance curves of Ti-48Al-2Cr-2Nb alloy tested at 25 °C, 450 °C and 700 °C [47]

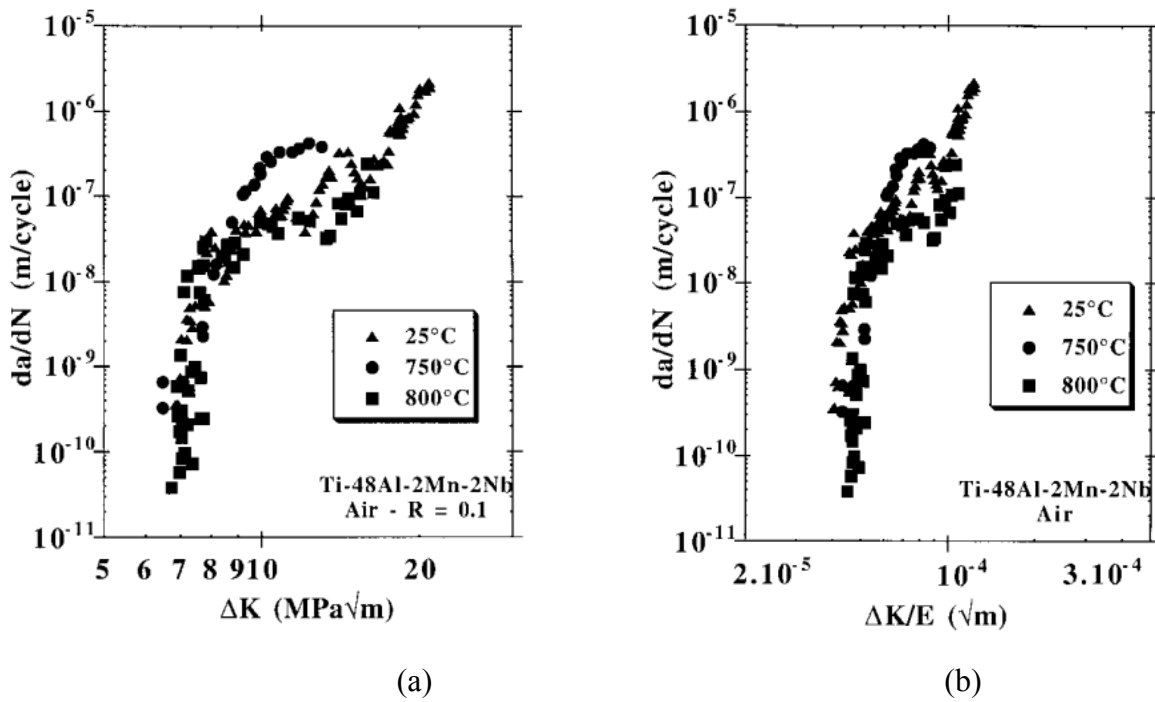


Figure 4.39. Fatigue crack growth rates in air vs. (a) ΔK and (b) $\Delta K/E$ as a function of temperature in a lamellar Ti-48Al-2Mn-2Nb alloy [103]

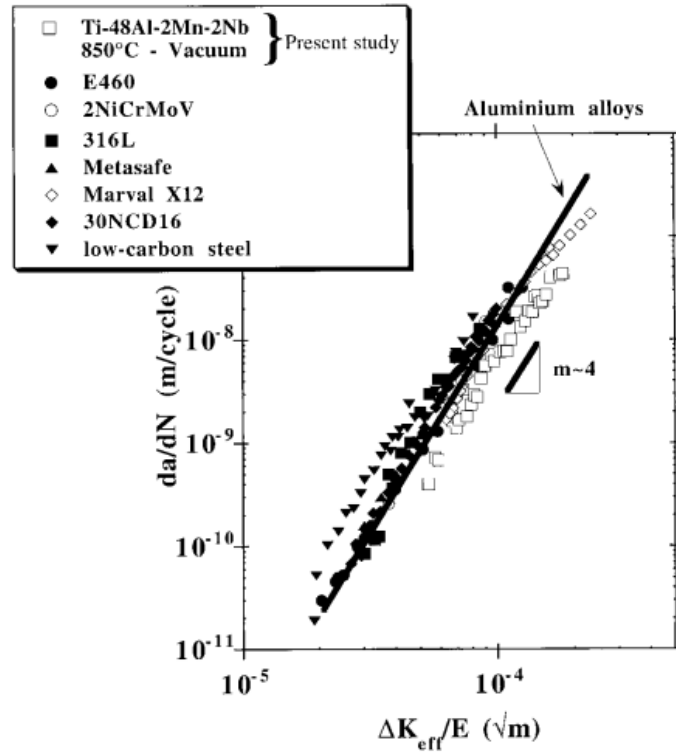


Figure 4.40. The comparison of intrinsic crack growth resistance of Ti-48Al-2Mn-2Nb and conventional ductile alloys at 850 °C [103].

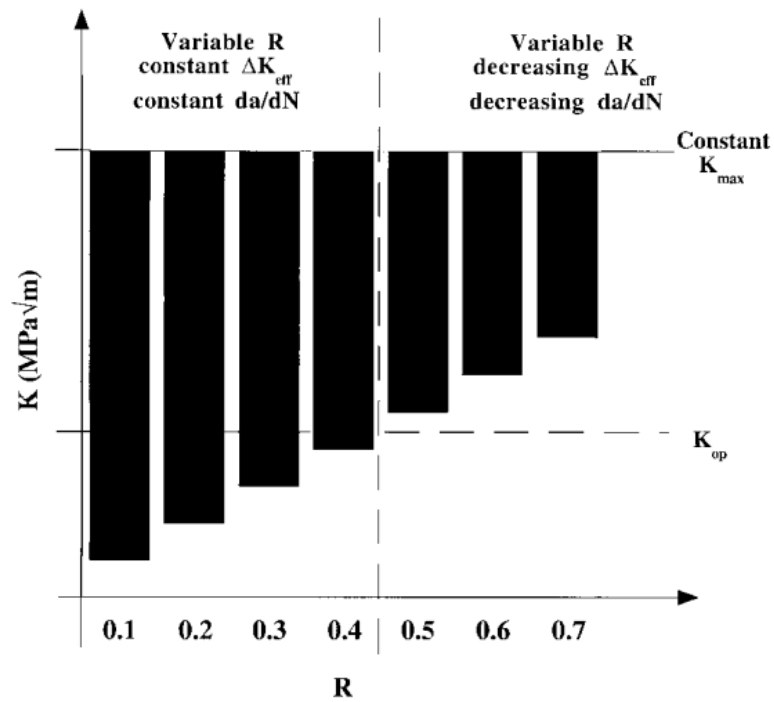
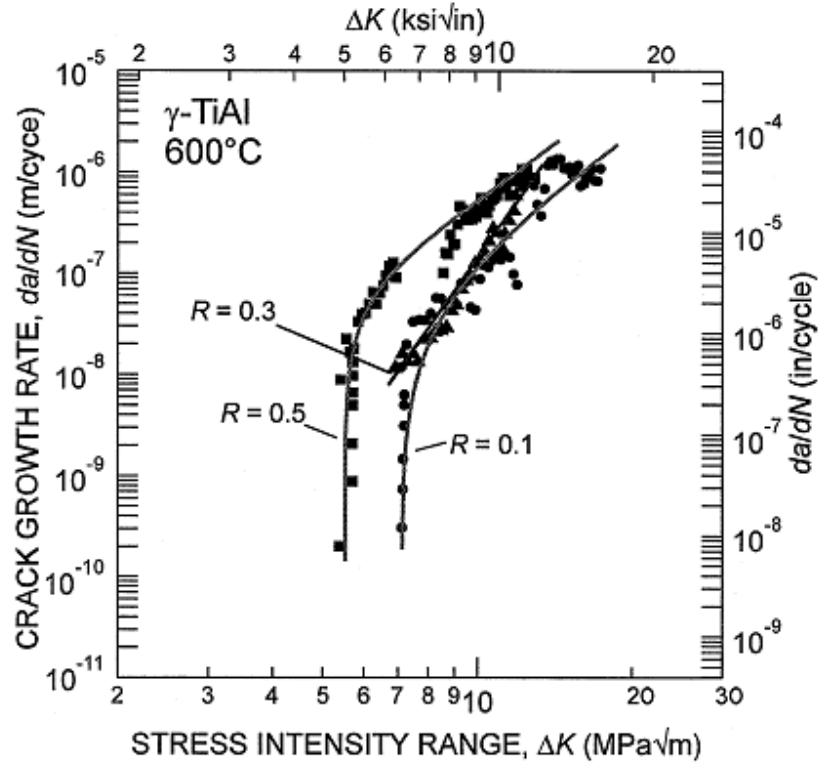
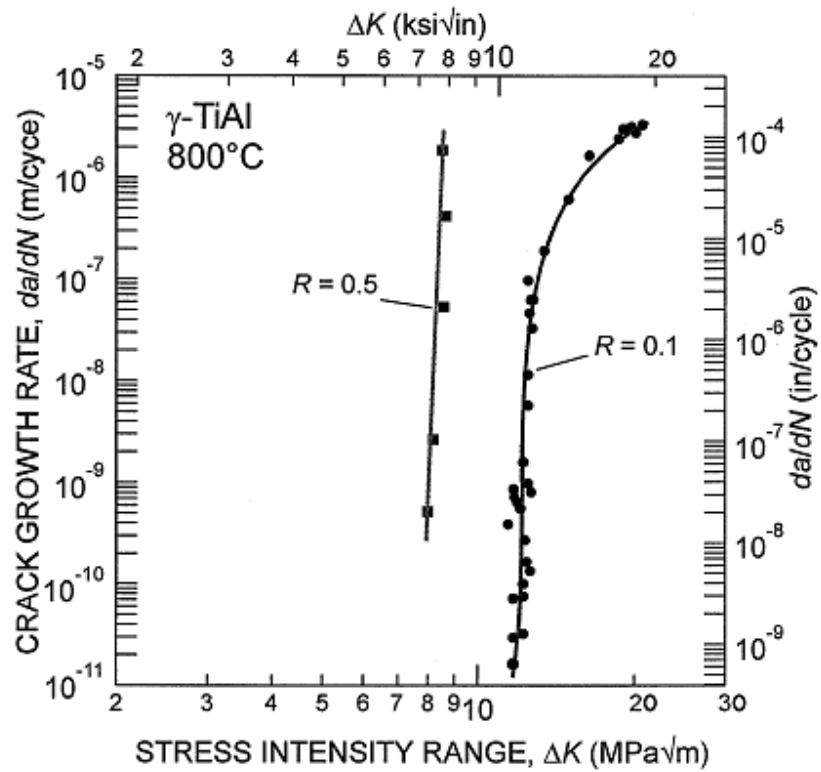


Figure 4.41. Constant K_{\max} -increasing R procedure in a fully-lamellar alloy (Ti-48Al-2Mn-2Nb) [103]



(a)



(b)

Figure 4.42. Effect of load ratio on the fatigue-crack growth rates, da/dN , at (a) 600 °C and (b) 800 °C in the XD-processed Ti-47.Al-1.9Nb-0.9Mn (at.%) alloy [101].

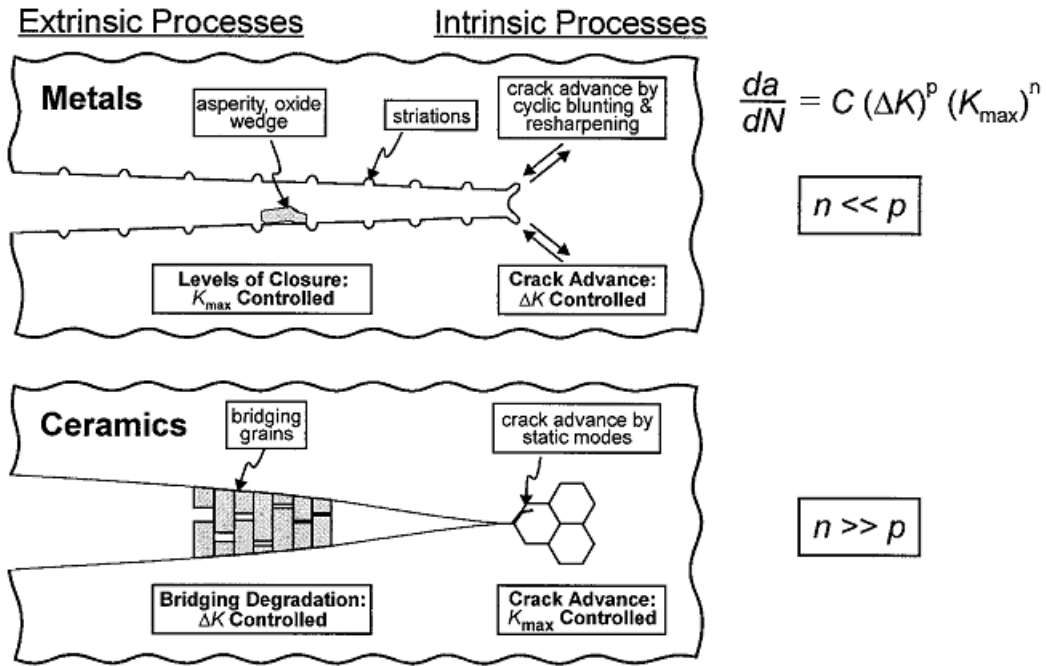


Figure 4.43. Schematic illustration of the intrinsic and extrinsic mechanisms involved in cyclic fatigue-crack growth in (a) metals and (b) ceramics, showing the relative dependencies of growth rates, da/dN , on the alternating, ΔK , and maximum, K_{\max} , stress intensities [4].

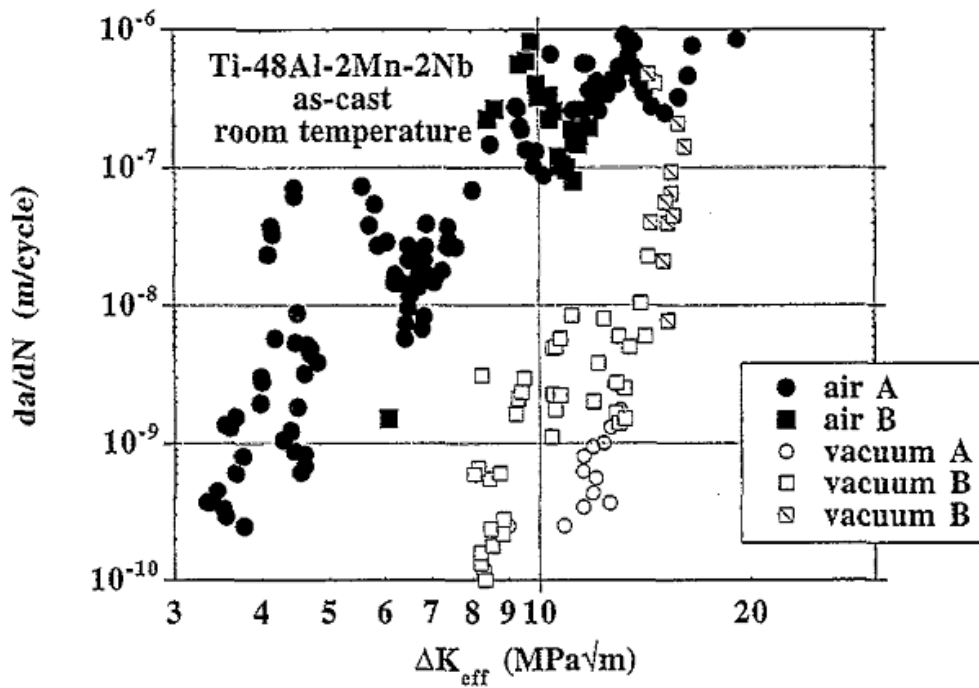


Figure 4.44. Comparison of effective stress intensity range in air and vacuum for a Ti-48Al-2Mn-2Nb alloy [85]

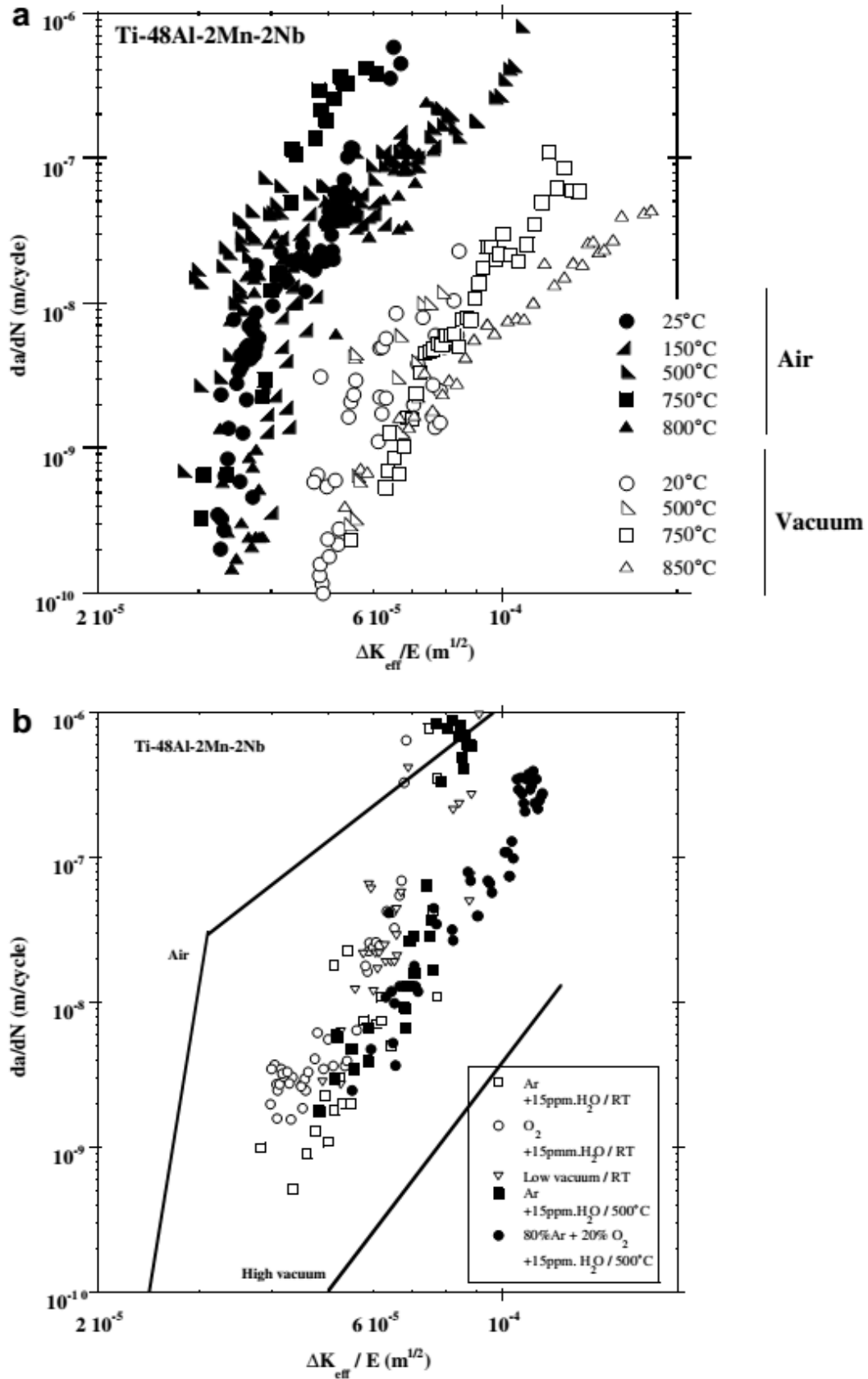


Figure 4.45. Influence of environment on fatigue crack growth in the Ti-48Al-2Mn-2Nb alloy in (a) air and vacuum, (b) intermediated atmospheres [110]

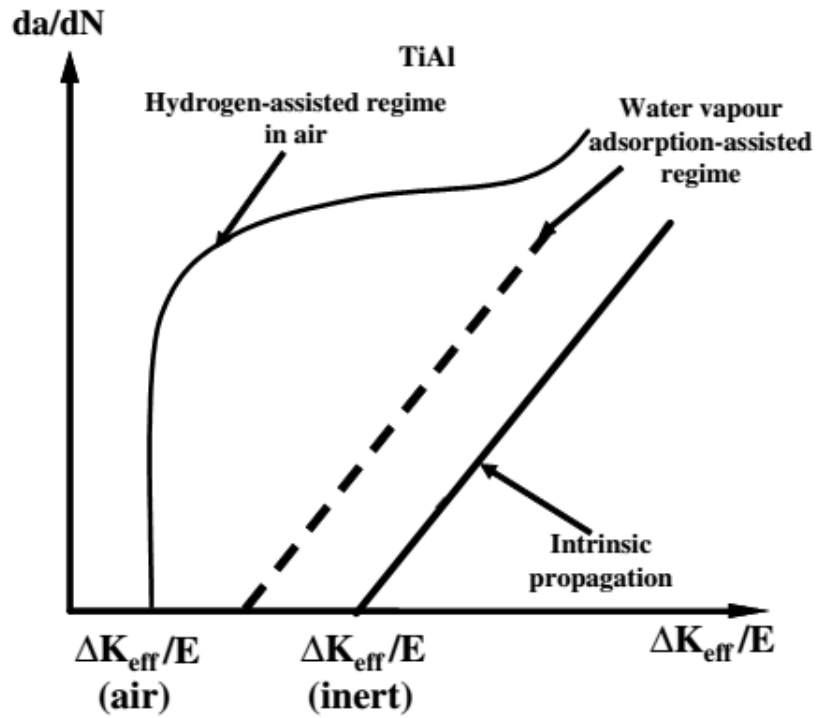


Figure 4.46. Schematic diagram showing mechanisms of environmentally-assisted fatigue crack growth in TiAl alloys [110]



Figure 4.47. Heterogeneous nucleation of precipitates in a sample (Ti-48Al-2Cr) crept at 700 °C, $\sigma_a=110$ MPa, $t=13,400$ h to strain $\varepsilon=0.46\%$ [115]

5. Experimental Work

5.1 Material and specimen

The materials were supplied by Rolls-Royce Plc. (RR) in different batches. The material was manufactured by different companies: GfE (GfE Metalle & Materialien GmbH), IMR (Institute of Metal Research, China) and TIMET (Titanium Metal corporation) and machined down to fatigue test pieces by GTG company.

The nominal composition of material used in this study is Ti-45Al-2Mn-2Nb-1B at. % (Ti-4522XD). The material was obtained by centrifugal casting, hipped at 1260 °C/150MPa/4h and aged at 1000 °C/8h. XDTM process was applied to form borides. The resulting microstructure is a near fully lamellar microstructure with small amount of equiaxed γ grains among colony boundaries (Figure 5.1). The lamellar colony consists of γ lath (dark phase) and α_2 lath (light phase). Needlelike TiB₂ particles homogeneously distributed in the order of 5-10 μm in length.

5.2 Fatigue tests

5.2.1 Specimens for fatigue and fracture toughness tests

The corner-crack (CC) specimens used for fatigue test were machined according to the Rolls-Royce drawing-RLH5325 or drawing modified based on it. The two kinds of geometries used for corner-crack specimens are shown in Figure 5.2 and Figure 5.3. The major differences between these two geometries are the total length of specimen and the diameter of threads. All of the cross sections containing notches are 5×5 mm² to make sure that the value of C in Equation 3.4 is consistent for all calculations. The notches were introduced by using electrical discharge machine (EDM) in the middle of gauge length on one corner. The notch width is about 30 μm for all corner-crack test pieces. The depth of notch varied from 0.1 mm to 0.7 mm according to testing purposes.

Most notches were about 0.5 mm in depth.

Four cylindrical gauge specimens were tested for the purposes of investigating naturally initiated crack and establishment of testing methodology. The geometry and dimension of cylindrical specimens is shown in Figure 5.4. All of the specimens mentioned above were machined from raw material blanks by EDM, ground to produce uniform surface condition.

5.2.2 Test condition and method of fatigue tests on CC specimens

Fatigue crack threshold stress intensity factor (ΔK_{th}) and crack growth resistance tests were designed and carried out based on Rolls-Royce standard test procedure document (MMM31002) and British Standard BS 6835-1:1998. Servo-hydraulic machines (ESH and Phoenix) were used for HCF tests with a sinusoidal loading waveform of 10 Hz (specimens from GfE batch 1 were tested with an frequency of 12 Hz). In order to evaluate ΔK_{th} and fatigue crack growth rate (FCPR) at multiple conditions, tests were performed at different temperatures (room temperature, 400 °C, 650 °C, 700 °C and 750 °C) and stress ratios (0.1, 0.5 and 0.8). The test conditions were chosen from combination of every temperature and stress ratio. A summary of test conditions and material sources are given in Table 5.1. During testing, crack length was monitored by Direct Current Potential Difference (DCPD) technique. In this approach, a stabilised DC was applied through specimen by two attached leads. Two PD wires were spot welded on either side of the notch as close as possible to edge of corner and notch (shown in Figure 5.5). Based on the function $V=IR$, for a constant current, the voltage increases with resistance of conductor. The reduction in cross section due to crack growth leads to the increase of resistance. As the resistance increasing, the output PD also increases. The output of potential difference was recorded by a chart recorder as a function of time. The recoded voltage was converted to crack length by calibrated in-house function according to specimen geometry. The whole set-up of facilities and

circuits are shown in Figure 5.6. The relationship among potential drop, specimen geometry and crack length for CC specimens can be expressed by following equation:

$$\frac{a}{W} = -0.0001818\left(\frac{V}{V_0}\right)^3 - 0.000528\left(\frac{V}{V_0}\right)^2 + 0.109103\left(\frac{V}{V_0}\right) - 0.008636 \quad \dots 5.1$$

where V is the potential drop across a specimen with crack length a and V_0 is the reference potential drop for a specified value of a . W is the thickness of specimen. After testing, the crack length is calibrated with the actual crack length by a liner relationship which was worked out by in-house study:

$$a = \frac{a}{W} \times \frac{(W + B)}{2} \quad \dots 5.2$$

$$a_{corrected} = a + \frac{a - a_0}{(a_f - a_0) \times (a'_f - a_f)} \quad \dots 5.3$$

where a_f is the calculated final crack length, a_0 and a'_f are the measured initial crack length and final crack length, respectively.

5.2.3 Pre-crack procedure

As earlier single-edged notch bending (SENB) tests [124] show that pre-cracking does not have an influence on fatigue threshold of Ti-4522XD alloy, and in order not to introduce loading history, all specimens for fatigue threshold and FCPR tests were tested without being pre-cracked for the tests at R=0.1 and 0.5. However, at R=0.8, specimens were pre-cracked to provide sharp crack front in order to promote the initiation of crack. Because of geometry restriction and limited crack width, fatigue pre-crack by compression-compression loading method, which had been reported successfully work on SENB specimens, is not applicable on the CC specimens. Therefore, specimens were fatigue pre-crack in tension-tension at temperatures of room temperature (RT), 400 °C and 650 °C with R ratios of 0.1. Limited number of pre-cracks was introduced with an R ratio of 0.5 for a limited number of tests. An increasing load method was applied for pre-cracking. The peak load was started approximately 10% lower than the experimental fatigue threshold of this alloy, and then

increased by 0.2kN every step until crack growing continuously, but controlled below the level for the average ΔK_{th} value of tests at $R=0.8$. The crack was allowed to grow by about 450 μm ($\sim 150 \mu V$) before stopping it. Several specimens were also pre-cracked for tests at $R=0.1$ and 0.5 in order to study whether pre-crack has influence on the fatigue threshold of corner-crack specimens. The method of introducing a pre-crack was as same as at $R=0.8$ except the fatigue condition which is at RT or 400 °C with $R=0.1$. The pre-crack length was around 100 μm ($\sim 30 \mu V$) that is just long enough to provide a sharp crack front while not introduce too much loading history.

5.2.4 Loading procedure for tests on CC specimens

According to previous studies [2], a decreasing load procedure can result in higher threshold values due to crack wake associated crack closure effect or loading history related shielding. Hence, the fatigue threshold and crack propagation tests were also conducted by load increasing method. The tests were started under a load range corresponding to a ΔK value that is lower than experimental ΔK_{th} of this alloy. There are different notch depth, the starting loads varies to provide similar starting ΔK value for the same test condition. The starting ΔK values under different test conditions are given in Table 5.3. The specimen was then cyclically loaded at this load range long enough (about 2 hours) to see if there was any crack growth. If there was no continuous crack growth, the peak load then increased by 0.2 kN to gain a higher ΔK level. This procedure was repeated until the crack grew (PD increases) continuously and steadily. The load then was kept constant at this level, and the crack growth rate was monitored by the chart recorder at same time. When the crack growth rate became rapid or unstable, such as the crack growth rate greater than about 5×10^{-4} mm/cycle, the cycling were stopped. RT or two-condition tests require heat-tint before open the specimens. After heat tint, samples were fatigued at room temperature until fracture.

5.2.5 Heat-tint

The purpose to do heat-tint is for making a mark of the final crack position. The heat tint procedures were verified according to different testing conditions. For tests conducted at stress ratios of 0.1 and 0.5, there was no requirement of pre-cracking. Hence, when the testing temperature is 650 °C or above, the crack can just be held at this temperature for 30 minutes and then air cool to room temperature to make a mark. Samples tested at room temperature and 400 °C were heated up to 500 °C in order to produce a clear brown colour as shown in Figure 5.7 (a). In an attempt to differentiate a pre-crack region and test region, heat-tint was applied at a temperature about 100 °C higher than the testing temperature after the test as seen in Figure 5.7(b).

5.2.6 Results processing

The actual initial and final crack lengths were obtained from the fracture surface by using Axiovision software to measure the images taken from an optical microscope. The crack length was measured from the notch tip to the final boundary along 7 angles as shown in Figure 5.8. The crack length was the average value of 7 lengths.

The crack growth rate was calculated by the corrected crack length versus corresponding number of cycles to grow this length. A five point secant method (shown in Table 5.2) was applied to smooth the da/dN curves. The stress intensity factor range was determined according to the solution developed by Pickard [125].

5.2.7 Interrupted tests

In order to relate the fracture surface features with microstructural units, three interrupted tests were conducted at a same stress ratio of 0.1 and at RT, 400 °C and 650 °C respectively. The testing procedure was exactly the same as fatigue threshold

testing and no pre-cracks were introduced. After noticing unstable crack growth, i.e. when the PD can increase at least about 10 $\mu\text{V}/\text{min}$, the tests were terminated without breaking the specimens. After the tests, the unbroken specimens were taken out carefully from the test machine followed by sectioning. A segment containing the crack was cut off from the whole specimen, and then sectioned along a line about 1 mm away and parallel to the diagonal of the cross-section. The method of sectioning is shown in the Figure 5.9. Subsequently, the thicker half was mounted in conductive Bakelite and polished to the near diagonal position.

5.2.8 Fatigue test on smooth specimen

Four cylindrical specimens and one square cross-section specimen (same geometry as shown in Figure 5.3) were tested without artificial defects or notches. The tests were performed in tension-tension at a stress ratio of 0.1 in air using an electro-mechanical fatigue machine with a load cell of 20 kN. Two of the four cylindrical specimens were tested at room temperature and the other two, in addition to one square cross-sectional specimen were tested at 650 °C. The edges of the square cross-section specimen were ground to be blunt in order to reduce the stress concentration around the sharp edges.

All tests were started with a peak stress far below its yield stress and left for more than 10^7 cycles at each stress level. If the specimen didn't fail at the stress, higher stresses would be applied until the final failure occurred.

5.3 Fracture toughness tests on corner-crack specimen

5.3.1 Pre-crack

Four CC samples (notch depth of 0.7 mm) were fatigue pre-cracked at $R=0.1$ and at 400 °C in tension-tension using a 10 Hz sine waveform load in air. The size of pre-cracks were calculated and monitored by DC difference, for the purposes of

ensuring the final peak stress was below the yield stress. The pre-cracks were introduced by using increase loading procedure. Unlike other pre-cracking, the K_{max} value was controlled 50% lower than the estimated fracture toughness values of this alloy. Since the K_{max} value increased with the increasing crack growth, the maximum load was reduced by 0.4 kN when the K_{max} was close to the limitation until the target crack length achieved. After pre-cracking, the specimen was heat tinted at 500 °C to mark the crack length which was regarded as the final crack length used for the calculation of fracture toughness (K_C) values.

5.3.2 Fracture toughness test

The pre-cracked specimens were tested in tension using a servo hydraulic machine (Phoenix) in air at RT, 400 °C, 650 °C and 750 °C. The cross-head speed of 0.16 mm/min and 0.05mm/min were applied for the room-temperature test and the other tests at elevated temperatures, respectively. A slower ramping rate at elevated temperatures was designed to see if there was any environmental influence. Load and displacement data were collected by Labview software during the tests. At the same time, the crack could propagate a little bit, thus the growth of crack was monitored by PD using a chart recorder. At the moment of final failure, the computer could catch the maximum load automatically and that load was noted down to determine the K_{IC} value.

Some fracture toughness values were also generated from specimens which have been used for fatigue crack threshold and growth tests under different conditions. The pre-existing fatigue cracks were regarded as pre-cracks for these fracture toughness tests, and their final crack lengths were used for the calculation of K_{IC} values.

5.4 Microstructural analysis

5.4.1 Sample preparation

Specimens from different batches were sectioned at different positions to observe the microstructure as shown in Figure 5.10. The cut-off parts were mounted in conductive bakelite and then ground and polished according to Struer's instruction for titanium and titanium alloys. The samples were examined by optical microscope and SEMs (JEOL 6060 and JEOL 7000). Since the samples were polished by active solution (oxide polishing suspension solution with Nitric acid), a light etching effect had been added to the polished surface. Hence, there is no need of etching for optical observations.

5.4.2 Colony size measurement

Firstly, five SEM images with a magnification of $\times 200$ were taken from each SEM sample. The locations of these images were randomly selected over the whole the surface of SEM samples. The colony size was obtained by following steps: (1) outline every complete colony in a SEM image with a calibrated scale in the AxioVision software; (2) after outlining all of the colonies, the software can produce a list of area (A) for each colony; (3) regarding the colonies as a circular shape, and using Equation 5.1 to calculate the diameter (d) which is defined as the colony size of this alloy.

$$A = \pi \left(\frac{d}{2}\right)^2 \Rightarrow d = \sqrt{\frac{4A^2}{\pi}} \quad \dots 5.1$$

Both individual colony size and average colony size were calculated.

5.4.3 Measurement of other microstructural parameters

The volume fraction of borides was measured by Image J. Since TiB_2 is the lightest phase on SEM images, by adjusting the image contrast, borides can be differentiated

from other phases. Then its area can be worked out by the software. Therefore, the volume fraction of borides was calculated based on 2-dimensional area fraction.

The volume fraction of equiaxed γ grains was also obtained by outlining the total γ grains on images using AxioVision, which was based on area fraction as well.

5.5 Fractographic analysis

After testing, the fracture surfaces were firstly examined and photos were taken by an optical microscope. The fracture surfaces were also observed using SEMs (JEOL 6060, JEOL 7000 and Hitachi S4000). Mostly, the accelerating voltage was 20 kV. The images mainly focus on the fatigue crack initiation areas i.e. along the notch front and axial directions of fatigue crack growth.

5.6 Fracture surface roughness assessment

The fracture surface roughness obtained from different testing conditions was measured by a Confocal laser microscope. The positions were selected corresponding to the stress intensity factor values. Some measurements were carried out on an area around $0.3\text{mm} \times 0.4\text{ mm}$ started from the middle of the notch front. The schematic diagram showing the measured areas are presented in Figure 5.11. Line roughness and area roughness was also measured on specimens tested at different conditions for areas approximately under a same ΔK value. R_a value was chosen and measured for evaluation of fracture surface roughness, where R_a is defined as the mean roughness which is the arithmetic average of the absolute values of roughness profile ordinates.

Table 5.1. Summary of test condition and specimen batches for tests. All of specimens were tested with a frequency of 10 Hz, except those were from GfE batch 1 which were tested at 12 Hz.

Test Temperature	Specimen ID		
	R=0.1	R=0.5	R=0.8
RT	CC602	CC608	CC610
	CC801	CC807	CC612
	CC802	CC808	CC814
	CC002	CC008	
	2D1		
	5A2		
	11-6-1		
	CC002		
	CC003		
400 ° C	CC603	CC609	CC604
	CC604	CC610	CC715
	CC703	CC710	CC816
	CC715	CC809	CC011
	CC803	CC810	
	CC814	CC007	
	CC816		
	CC011		
	CC003		
650 ° C	CC605	CC611	CC817
	CC615	CC612	CC818
	CC806	CC711	
	CC817	CC811	
	CC818	CC812	
	CC005	CC009	
	1D1		
	1C1		
	1D2		
	2D1		
	5A1		
	11-6-11		
	11-9-3		
700 ° C	CC006	CC617	CC006
	CC011	CC001	CC007
	CC012	CC002	CC008
750 ° C	CC714	CC003	CC009
	CC718	CC004	
	CC001	CC005	

Colour code
Corner Crack assessment trial
Corner Crack, GfE Batch 1
Corner Crack, IMR Batch 5
Corner Crack, GfE Batch 2
Corner Crack, GfE Batch 3
Corner Crack, Timet batch 1
Machined from SEBN sample left by Po-sri's research
Corner Crack, Timet batch 2
Corner Crack, Timet batch 3

Table 5.2. The five point secant method for smoothing the da/dN curves

Crack length, a (mm)	Number of cycle	da/dN (mm/cycle)
a_1	N_1	$(a_2 - a_1)/(N_2 - N_1)$
a_2	N_2	$(a_3 - a_1)/(N_3 - N_1)$
a_3	N_3	$(a_5 - a_1)/(N_5 - N_1)$
a_4	N_4	$(a_6 - a_2)/(N_6 - N_2)$
\vdots	\vdots	$(a_{x+2} - a_{x-2})/(N_{x+2} - N_{x-2})$
a_{n-2}	N_{n-2}	$(a_n - a_{n-4})/(N_n - N_{n-4})$
a_{n-1}	N_{n-1}	$(a_n - a_{n-2})/(N_n - N_{n-2})$
a_n	N_n	$(a_n - a_{n-1})/(N_n - N_{n-1})$

Table 5.3. Starting ΔK values at different test conditions for fatigue threshold and crack growth tests on CC specimens

R ratio	Test Temperature (°C)	Average Starting ΔK (MPa.m ^{1/2})
0.1	RT	4.5
	400	4.0
	650	4.0
	700	4.0
	750	4.0
0.5	RT	3.5
	400	3.0
	650	3.0
	700	3.0
	750	3.0
0.8	RT	2.0
	400	1.8
	650	1.8
	700	1.8
	750	1.8

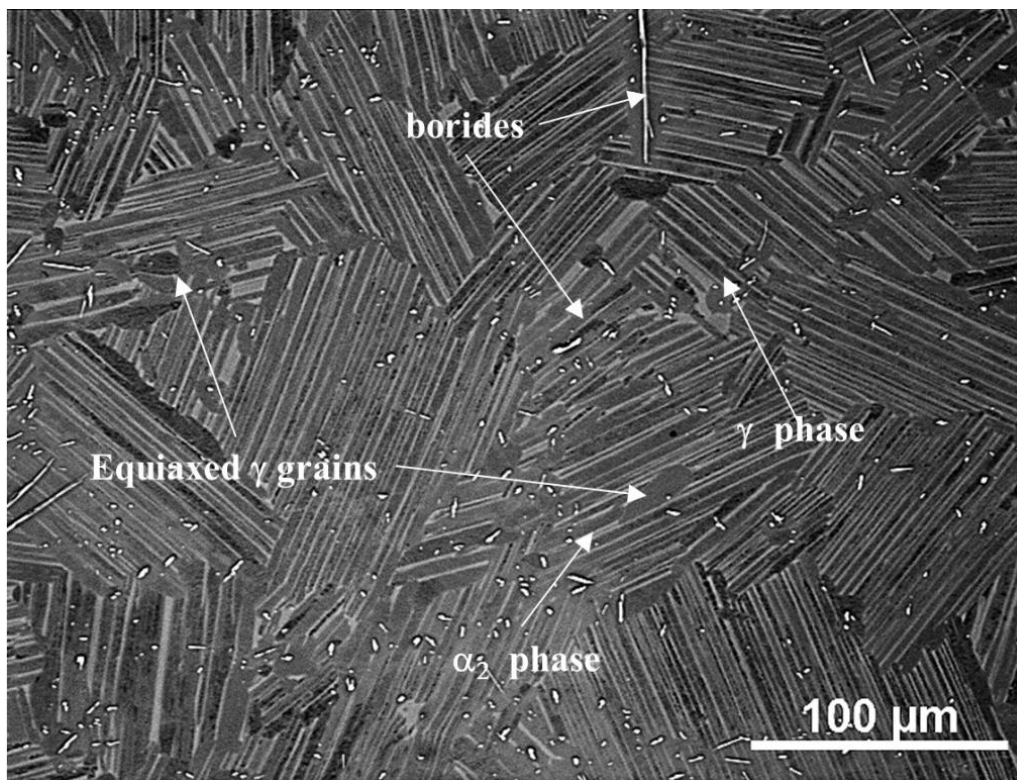


Figure 5.1. Microstructure of Ti-4522XD alloy

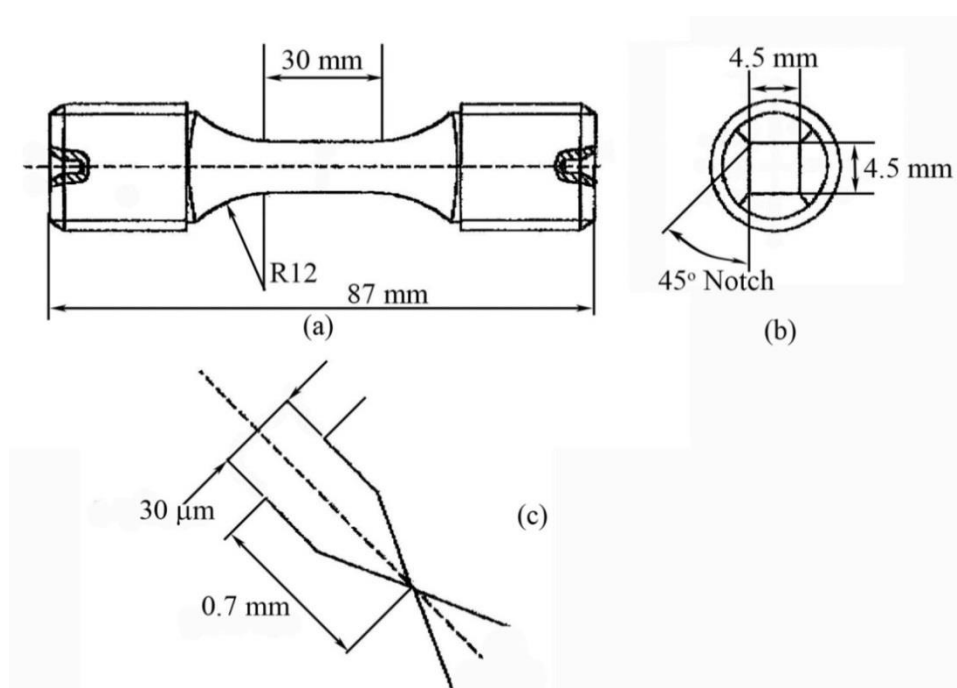


Figure 5.2. Geometry of corner-crack specimen used for fatigue threshold and crack propagation test based on RR drawing RLH5325.

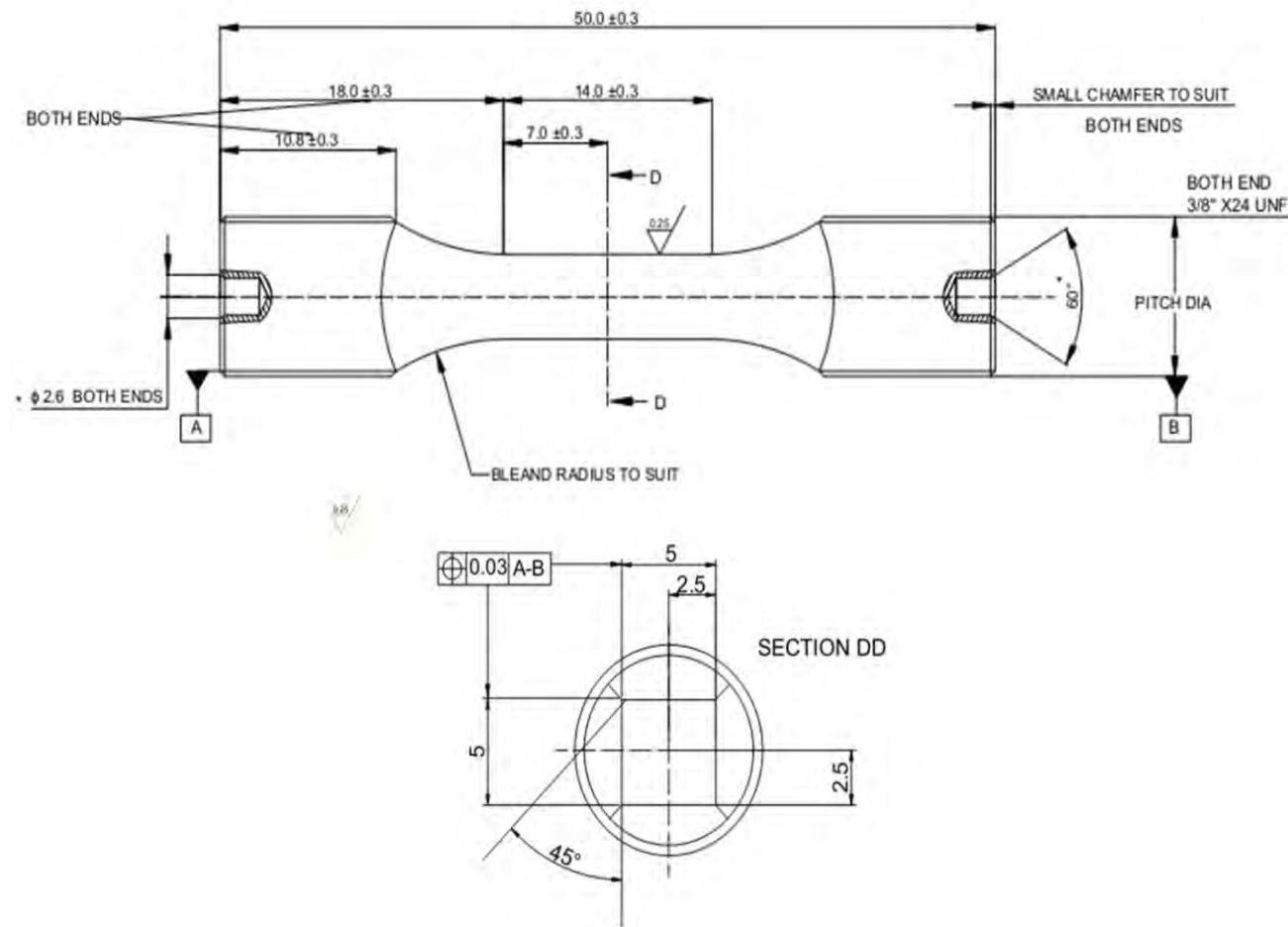


Figure 5.3. Geometry of corner-crack specimen used for fatigue threshold and crack propagation test modified according to RR drawing RLH5325.

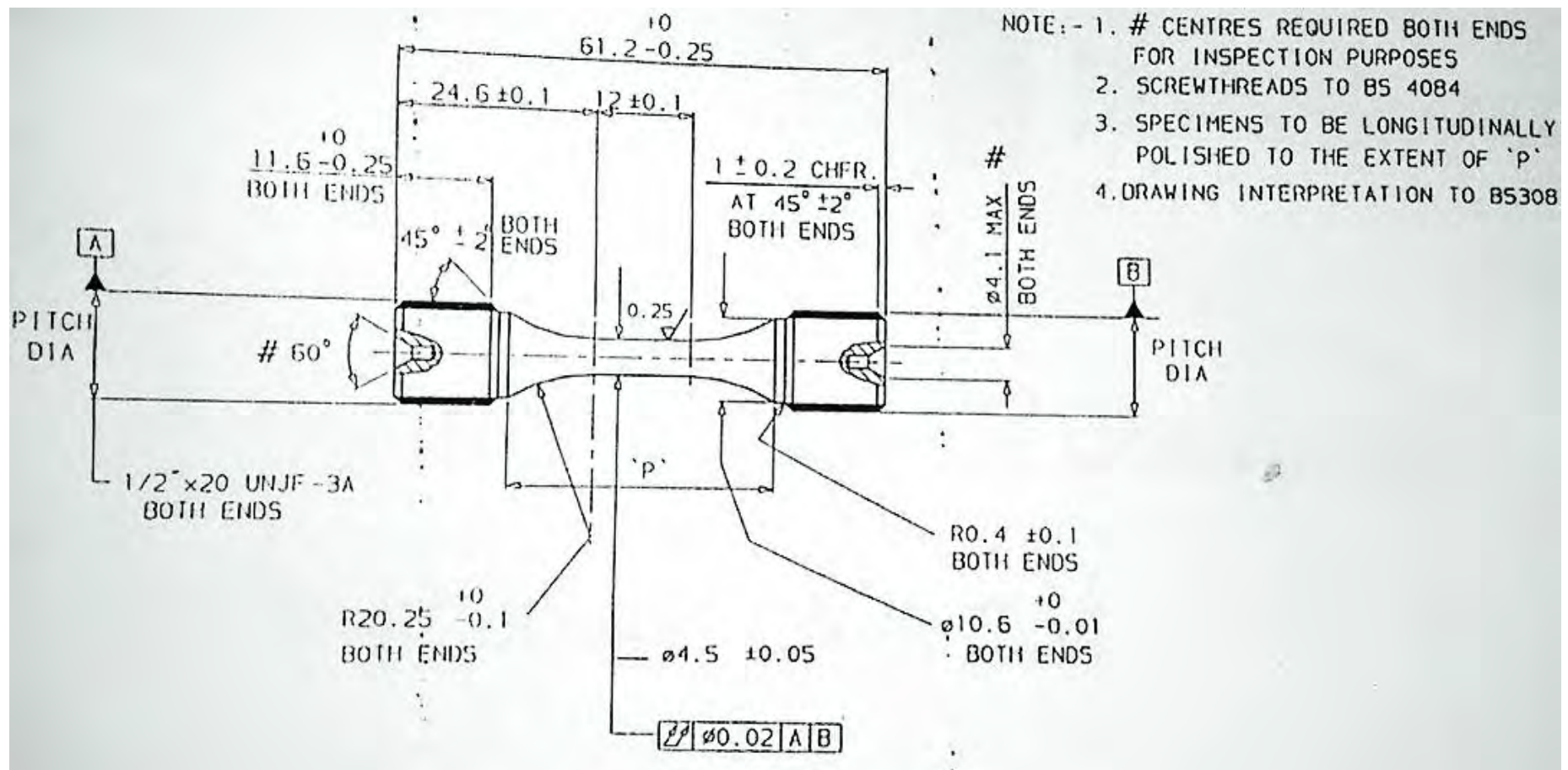


Figure 5.4. Geometry of cylindrical specimens used for high cycle fatigue tests based on RR drawing RLH 10007

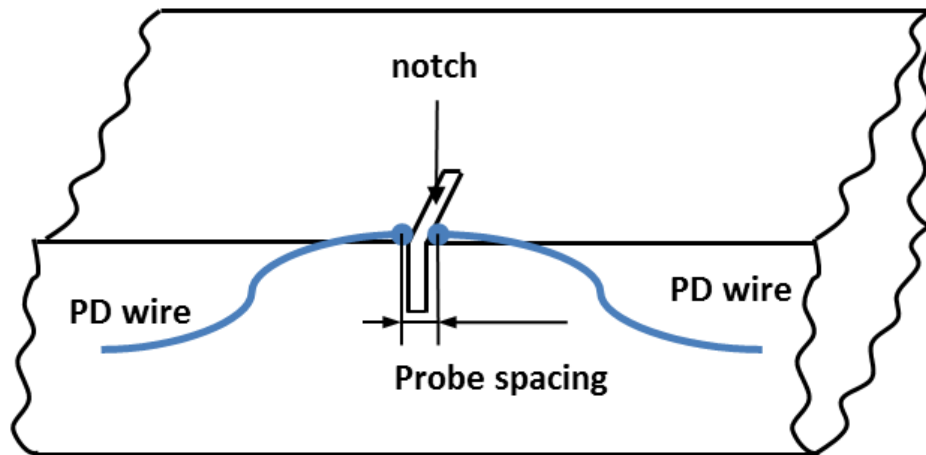


Figure 5.5. Schematic diagram of spots welding for PD wire

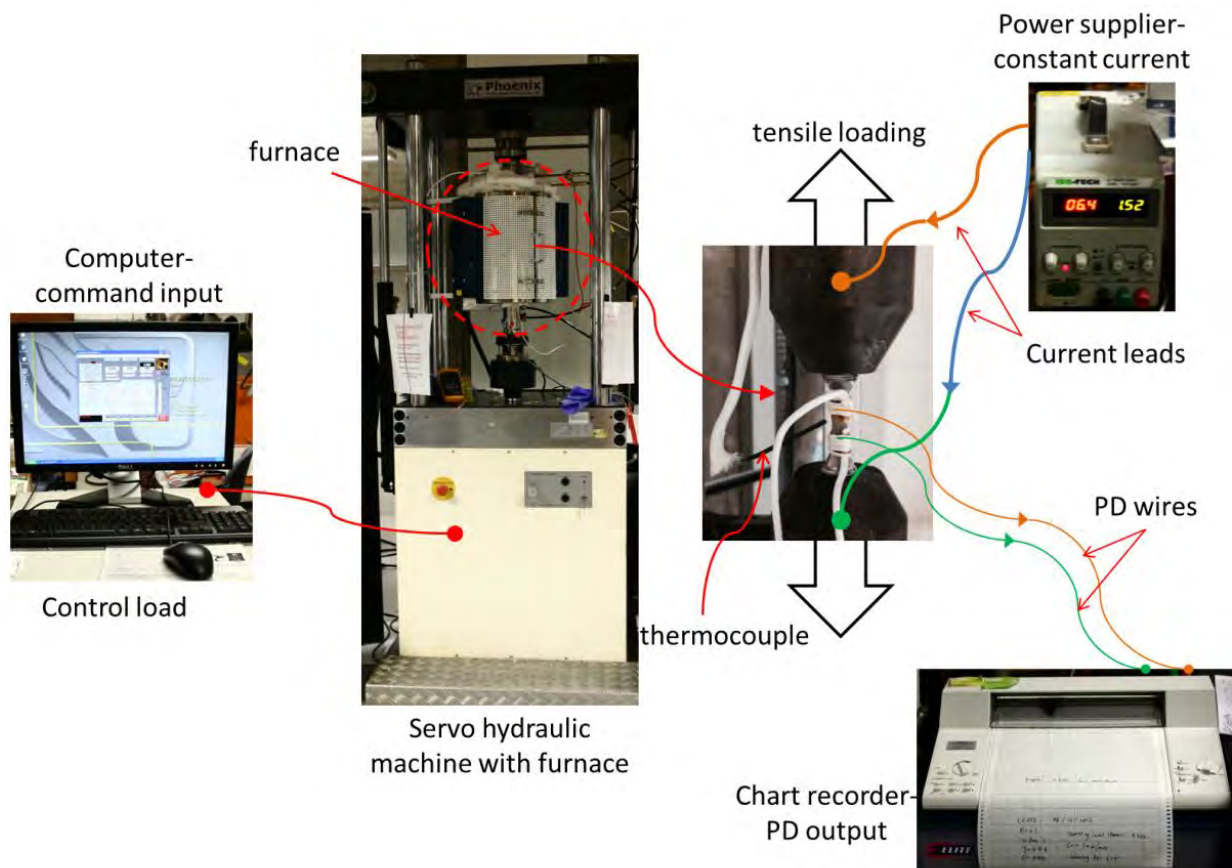
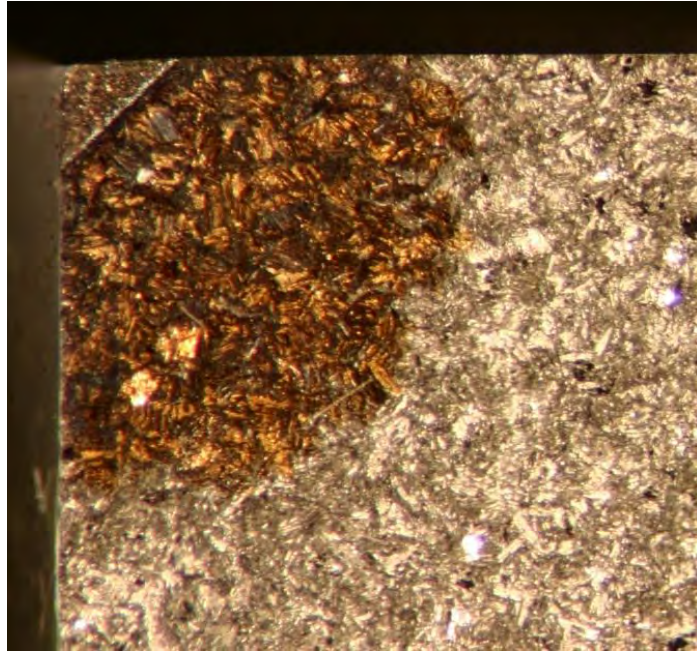
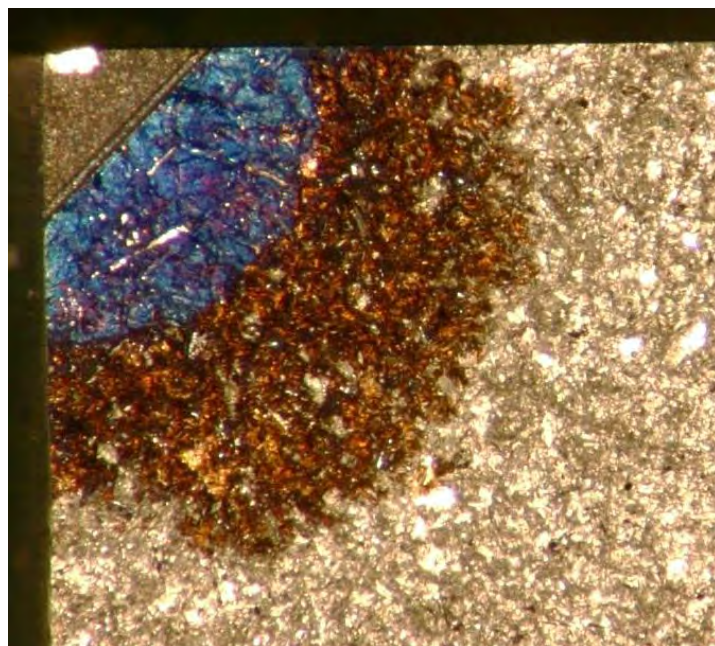


Figure 5.6. All facilities and circuits for fatigue testing as well as monitoring and recording crack growth by DCPD method.



(a)



(b)

Figure 5.7. Heat tint effects of tests started (a) straightly from notch and (b) from pre-cracked

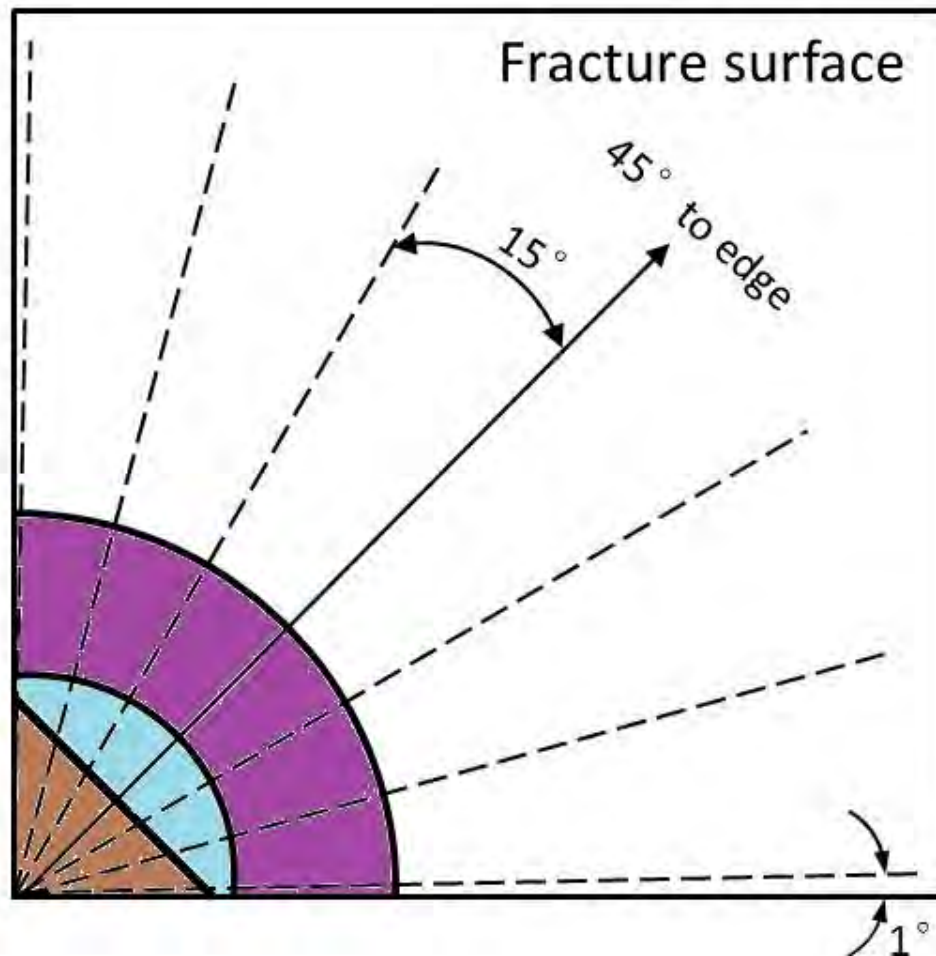


Figure 5.8. Schematic diagram of 7-points methodology used for measuring the actual crack length

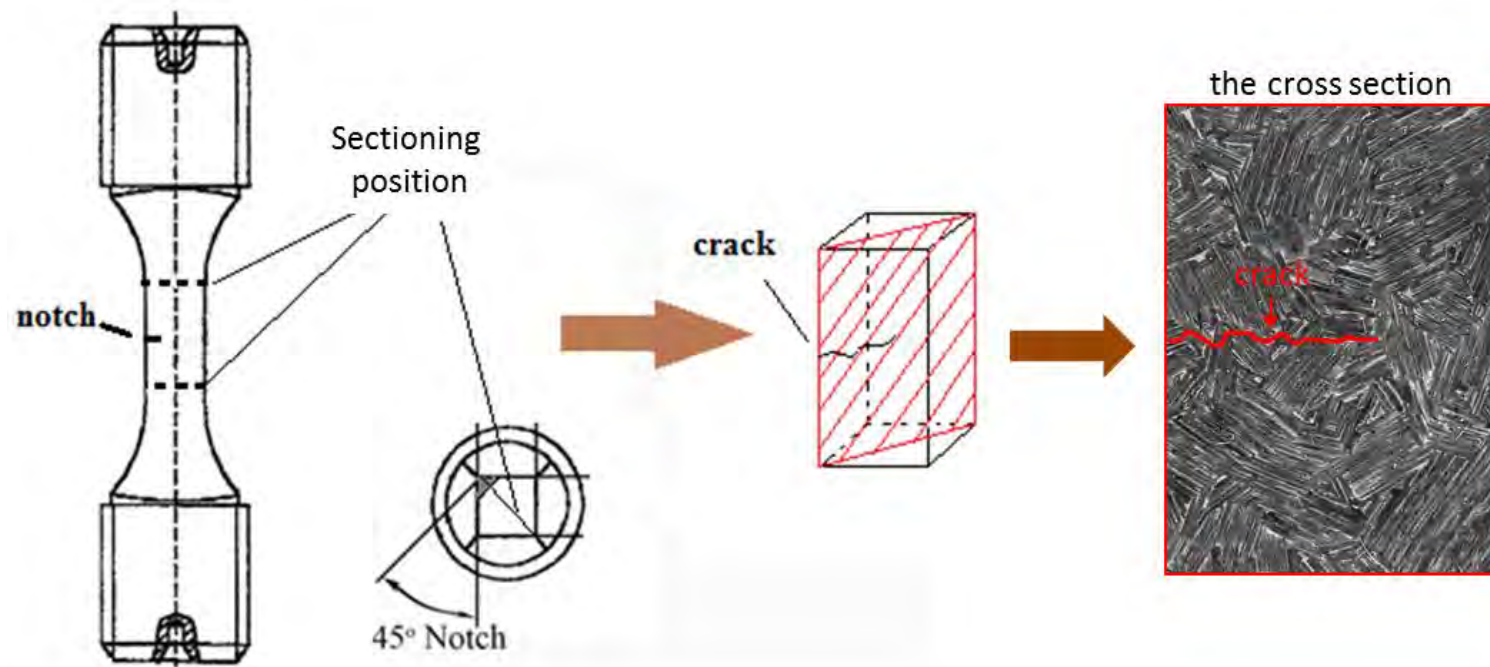


Figure 5.9. Schematic diagram showing the sectioning of specimens obtained from the interrupted tests

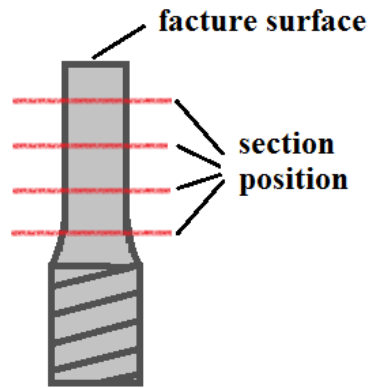
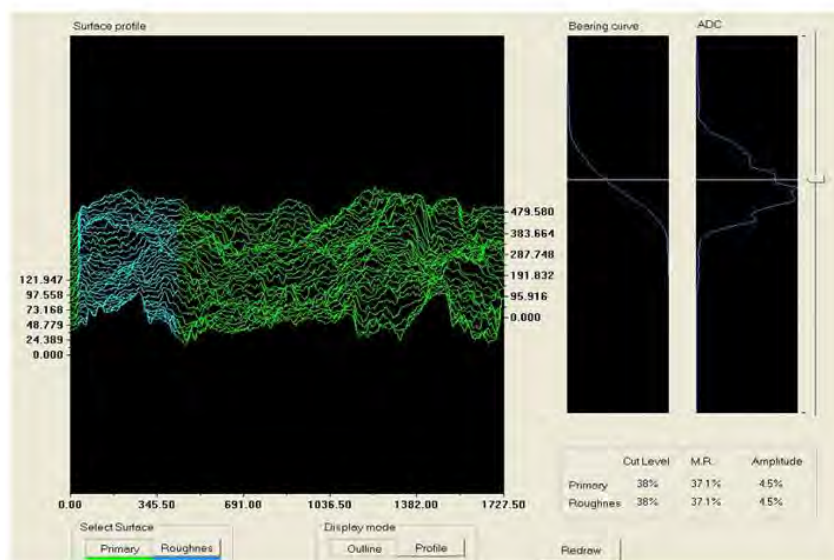
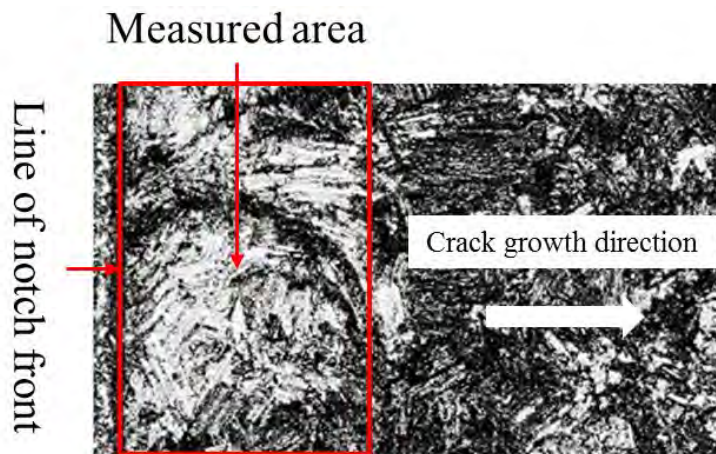


Figure 5.10. Schematic diagram showing the section positions in specimens after tests for the purpose of microstructural examinations



Surface profile

Figure 5.11. Fracture surface roughness measurement in an area behind the notch front and surface profile produced by con-focal laser microscope

6. Results

6.1 Microstructure

Although material came from different sources, the microstructure did not show a significant difference among the batches. The general microstructure of the different batches is near fully lamellar (shown in Figure 6.1). The lamellar colonies were randomly oriented throughout the images. The average colony size range was about 78 μm and in the range of approximately 40-130 μm . The average volume fraction of borides is about 0.8-1%. In general, a small amount of equiaxed γ grains about 11.3% (volume fraction) were found either among colony boundaries or dispersed within lamellar colonies. The grain size of the equiaxed γ grains is about 5-10 μm . However, clusters of equiaxed γ grains were also observed and one example is given in the Figure 6.2. Since the appearance of equiaxed γ grain clusters are not anticipated, no sectioning though the raw blanks was carried out to investigate the distribution and batch difference of equiaxed γ grain clusters, which could be of interesting for the future work.

EDS analysis confirmed that the needle like borides particles are titanium borides and the volume fraction was around 1.9%. The average colony size was about 80 μm , but some large lamellar colonies were found as well. The distribution of colony size is shown in the Figure 6.3.

6.2 Fracture toughness tests

6.2.1 Fracture toughness at different temperatures

All of the fracture toughness tests were carried out without a clip gauge to measure the crack opening displacement during tests. Therefore, fracture toughness values were simply determined using the pre-crack length and the maximum load when the

specimens failed. A summary of the test results is shown in Table 6.1. The overall variation of fracture toughness values (K_{IC}) is not significant at different temperatures. The highest average K_{IC} value was obtained at 400 °C around $20.3 \text{ MPa.m}^{1/2}$. The K_{IC} values at the other test temperatures show little variation (the maximum difference is $\sim 0.4 \text{ MPa.m}^{1/2}$). The difference between the highest K_{IC} value ($20.3 \text{ MPa.m}^{1/2}$) and the lowest K_{IC} value ($17.8 \text{ MPa.m}^{1/2}$) is only about $2.5 \text{ MPa.m}^{1/2}$. To show comparison of K_{IC} values among different temperatures visually, K_{IC} values were plotted in terms of temperature as presented in Figure 6.5. In Figure 6.4, the load was plotted against the relative change of stroke. Since the change of the stroke was associated with the entire set of fixtures and specimen, it cannot be used as a specimen displacement or any calculation for the strain.

6.2.2 Fractography

The fracture surfaces of specimens used for fracture toughness tests at RT and elevated temperatures are shown in Figure 6.6. In all cases the fracture surfaces exhibit a brittle failure mechanism mainly via translamellar and interlamellar fractures. The fracture surfaces are all rough, and there are no significant distinctions among these fracture surfaces. This observation is constant with their similar K_{IC} values.

6.3 Fatigue crack threshold results of Ti-4522XD alloy

6.3.1 Effect of test temperature on ΔK_{th} values

In the tests carried out at RT, the PD could increase initially for a short period after a higher load range was applied indicating that there was a small amount of crack growth. The increment of PD was usually about 3-5 μV (which equals to less than 0.018 mm in crack length), and there was no further crack growth even after leaving the specimen at that load for more than 12 hours. The crack could not start to grow again unless a higher load was applied. This procedure was repeated several times until a load range was

applied that enables continuous crack growth. Therefore, the ΔK value at which the cracks could grow continuously is defined as fatigue threshold in this study. However, this “start-and-stop” fatigue crack growth phenomenon at the threshold regime was rarely found at elevated temperatures.

The fatigue threshold results for all tests on CC specimens are summarised in Table 6.2. At both R ratios of 0.1 and 0.5, the highest and lowest average ΔK_{th} values are found at 750 °C and 400 °C, respectively. At R=0.1, there are little differences of average ΔK_{th} values among tests at RT, 700 °C and 750 °C (which are 6.6 MPa.m^{1/2}, 6.5MPa.m^{1/2} and 6.8 MPa.m^{1/2}, respectively). At R=0.5, the average ΔK_{th} values at RT, 650 °C and 700 °C are nearly the same, which are 4.2 MPa.m^{1/2}, 4.4MPa.m^{1/2} and 4.6MPa.m^{1/2}, respectively. At an R ratio of 0.8, there are no remarkable differences of average ΔK_{th} value at all temperatures. The average ΔK_{th} values at RT, 400 °C and 650°C are all 3.3MPa.m^{1/2}. The average ΔK_{th} value (2.9 MPa.m^{1/2}) at 700 °C is slightly lower than the average ΔK_{th} values of the other three temperatures. At an R ratio of 0.8 at 750 °C, there are no valid results of ΔK_{th} value as well as fatigue crack growth resistance curves (FCGRCs) because of the change of failure mechanism. More details will be shown in section 6.8.

In order to show the trends of ΔK_{th} values at different temperatures directly, the ΔK_{th} values are plotted against test temperatures for each R ratio as shown in Figure 6.7. A dotted line is drawn in every graph to show the average ΔK_{th} value at each R ratio. As seen in the graphs, the ΔK_{th} values at all temperatures have similar variation around the average ΔK_{th} value of each R ratio.

A statistical analysis is given in Table 6.3 to show the effect of temperature on ΔK_{th} values numerically. For a given R ratio, the differences between the average ΔK_{th} values at each temperature and their average ΔK_{th} value are all less than 1MPa.m^{1/2}, which are practically not significant compared to the total ΔK scale. Test conditions

showing larger standard deviation also have larger number of tests. For most of test conditions, the number of tests is no more than 3, which are not applicable to judge the divergence. No direct evidence that the scatter of ΔK_{th} value is caused by testing temperature.

From above observations, it can be implied that test temperature does not have a remarkable influence on the ΔK_{th} values of this near fully-lamellar TiAl alloy at all R ratios. The variations of ΔK_{th} values are associated with the number of tests, and are not caused by test temperatures.

6.3.2 Effect of R ratio on ΔK_{th} values

Figure 6.8 directly shows the trend of ΔK_{th} values with R ratios for a fixed test temperature. As seen, for a fixed temperature, the average ΔK_{th} values decrease with increasing R ratio, and almost follow a linear declining relationship as indicated by the black line in each graph. However, the K_{max} values at fatigue threshold increase as R ratio increases. It is worth noting that the K_{max} values at fatigue threshold are relatively high which are comparable to the K_C values (see in Table 6.1). Although the relationship between ΔK_{th} values and R follows the trend seen in traditional titanium alloys (e.g. Ti-6Al-4V), a smaller influence of R is noticed.

At RT, 400 °C and 650 °C, the ΔK_{th} values at an R ratio of 0.1 are more scattered than those at R=0.5 and R=0.8. However, there are also more data points at R=0.1 than at the other two R ratios. In addition, this dispersion at R=0.1 becomes less at 700 °C and 750 °C as the number of data points reduces to only 3. Therefore, there is no direct effect of R ratio on the variation of ΔK_{th} values at all temperatures.

6.4 Fatigue crack growth resistance curves of Ti-4522XD alloy

6.4.1 General features of fatigue crack growth resistance curves

All FCGRCs (da/dN vs. ΔK) of every single test condition are shown in Figure 6.9 to Figure 6.22. All Paris exponent (m) and coefficient (C) values of CC specimens were calculated according to equation 3.4 and are summarised in Table 6.4. Black dotted lines are drawn in Figure 6.9 to Figure 6.18 to show the average Paris law regime for each test condition. Although FCGRCs are slightly scattered at some test conditions of $R=0.1$ and 0.5 , especially in the fatigue threshold regime and unstable crack growth regime which are microstructure-dependent regimes, the general trend of FCGRCs for a fixed test condition is consistent, and the dispersion is not significant compared to the total ΔK range. At $R=0.8$, the FCGRCs are also consistent for a fixed temperature, except at $650\text{ }^{\circ}\text{C}$. Therefore, except for the tests at $R=0.8$ at $650\text{ }^{\circ}\text{C}$, the results can be regarded as reproducible. For this reason, the following results to show the effects of temperature and R ratio on fatigue crack growth are shown by the most representative curves selected from each test condition in order to present the comparisons clearly. The basic principle of data selection is which curve covers the largest range of ΔK values and its m and C values are close to the average values of that test condition.

6.4.2 Effect of test temperature on fatigue crack growth

Figure 6.23, Figure 6.24 and Figure 6.25 show comparisons of FCGRCs at different test temperatures for R ratios of 0.1 , 0.5 and 0.8 , respectively.

In Figure 6.23, at $R=0.1$ the steepest FCGRC is found at RT which can also be deduced from the highest average m values (7.2). There are no distinct fatigue regimes identifiable from the FCGRCs at RT. Although the test conducted at $400\text{ }^{\circ}\text{C}$ shows the most moderate slope, the average m value (3.6) is similar to that of tests at $650\text{ }^{\circ}\text{C}$ (3.7). The fatigue resistance curves at $650\text{ }^{\circ}\text{C}$, $700\text{ }^{\circ}\text{C}$ and 750°C nearly overlap with each

other. In the Paris Law regime, for a given ΔK value the crack growth rates are higher at 650 – 750 °C than at RT and 400 °C.

At $R=0.5$, the FCGRCs show similar trends to those observed at an R ratio of 0.1. At RT, the FCGRC become even steeper as revealed by m values (8.6), and intersected with those curves obtained at higher temperatures in the Paris Law regime. The FCGRCs of tests at and above 650 °C are also nearly consistent in the Paris Law regime. The average m value is slightly higher at 750 °C (5.8) compared with those at 400-700 °C which are 3.0, 3.8 and 4.8, respectively.

At $R=0.8$, generally for a given ΔK value the highest and lowest fatigue crack growth rate are found at RT and 650 °C, respectively. Both tests at 650 and 700 °C show a dramatic drop of crack growth rate after the cracks start to grow. Because there are no distinct fatigue regimes in FCGRCs at these two temperatures, no Paris constants are quoted here.

As mentioned above, at 650 °C there are two distinct fatigue crack growth behaviours as shown in Figure 6.21. The FCGRC of CC817 shows similar behaviour as the curves of tests at 700 °C (see in Figure 6.22), while CC818 shows a decreasing trend of fatigue growth rate and lower fatigue crack growth rate compared to CC817. For CC817, there was some crack propagation at an applied load (8.8 kN) which was lower than the final applied load at fatigue threshold (9.4 kN), but the crack growth rate was less than 10^7 mm/cycle. Nevertheless, no obvious crack propagation was observed in CC818 before the load at threshold. It seems that lower applied load at threshold can give more chance for crack blunt at 650 °C and thereby results in slow fatigue crack growth rates.

6.4.3 Effect of R ratio on fatigue crack growth

The comparisons of FCGRCs for different R ratios at RT, 400 °C, 650 °C, 700 °C and

750 °C are shown in Figure 6.26, Figure 6.27, Figure 6.28, Figure 6.29 and Figure 6.30, respectively.

As seen in Figure 6.26, at RT, it is clear that fatigue crack growth rate is highest at an R ratio of 0.8 and lowest at R ratio of 0.1 for a given ΔK value. The fatigue crack growth rate at R=0.5 is also about 2 order of magnitudes higher than at R=0.1 for the same ΔK value. The fatigue growth crack resistance curves are steep at all test temperatures.

As seen in Figure 6.27, at 400 °C, for a given ΔK value the highest crack growth rate is also found at R=0.8, whereas the crack growth rates of R=0.1 and 0.5 show little difference in the Paris Law regime. The tests at R=0.5 have slightly higher crack growth rates than at R=0.1 at both ends of the FCGRCs.

At 650 °C and 700 °C (see in Figure 6.28 and Figure 6.29), for the same ΔK value the fatigue crack growth rates of tests at R=0.5 becomes the highest, while the tests carried out at R=0.8 exhibit the lowest fatigue crack growth rates. At and above 650°C, the difference in fatigue crack growth rates between R=0.1 and R=0.5 are all less than one order of magnitude for a given ΔK value.

6.5 Fractography

6.5.1 Effect of test temperature on fracture surfaces

Most specimens failed in a brittle manner, where translamellar and interlamellar crack growth were observed. Typical examples of interlamellar and translamellar fractures caused by fatigue loading are shown in Figure 6.31. The fracture surfaces generated at R=0.1, 0.5 and 0.8 at different test temperatures are presented in Figure 6.32 to Figure 6.34, respectively. Beside the fracture surfaces of specimens tested at 750 °C, the fracture surfaces are similar for the same R ratio at all test temperatures in these low magnification SEM images. The fracture surfaces generated at 750 °C seems slightly rougher than the fracture surfaces of the other test temperatures.

Comparisons of fracture surfaces near fatigue threshold regimes at different temperatures for R ratio of 0.1 and 0.5 are shown in Figure 6.35 and Figure 6.36 respectively. As seen in both images, at both R ratios the fracture surfaces of specimens tested at RT contains several interlamellar fractures, while just few interlamellar fractures can be observed on the fracture surfaces generated at elevated temperatures. Few interlamellar fractures were also found at R=0.5 and at 700 °C, their sizes are only about 60 µm. The fracture surfaces of specimens tested at R=0.5 and at 750 °C seems rougher than other fracture surfaces. But there is still no interlamellar fracture can be found either. At R=0.8 at all temperatures, the fracture surfaces are all rough without obvious differences between them (as shown in Figure 6.34).

To investigate the effect of test temperature on translamellar and interlamellar fractures, high magnification images of these two fracture modes were taken at a constant ΔK value at different test temperatures for a fixed R ratio (shown in Figure 6.37, Figure 6.38 and Figure 6.39). There was no significant difference of these two fracture modes at different test temperatures.

For all test conditions in addition to regular features, intergranular and transgranular failure of equiaxed γ grains were occasionally observed on the fracture surfaces of some testpieces. As shown in Figure 6.40 (a) and (b), the fracture surface is mostly intergranular with a small quantity of transgranular fracture. Examples of intergranular and transgranular failures of equiaxed γ grains are given in Figure 6.40 (c) and (d), respectively. The equiaxed γ grains, when they exist in the crack path, fail predominantly in an intergranular manner but they do not deviate the crack path by a significant amount due to the small grain size. If the test piece has a large quantity of such equiaxed colonies the fracture surface usually appears flat at low magnification. The temperature does not have any obvious effect on the failure of equiaxed γ grains.

6.5.2 Effect of test temperature on fatigue crack path

In order to investigate the crack path at different temperatures, three interrupted tests were carried out by stopping the tests before the final fracture. The tests were conducted at $R=0.1$ and three different temperatures (RT, 400 °C and 650 °C). The sectioned surfaces containing cracks are shown in Figure 6.41. In general, the cracks propagate mainly in a translamellar mode.

At RT, the cracks can be easily deviated along lamellar interfaces or colony boundaries, and examples are given in Figure 6.42 (a) and (b). Hence, the crack path is more tortuous at RT. Some microcracks are found along the main crack as shown in Figure 6.42 (c).

At 400 °C, the main crack was relatively straight, and one tortuous crack deflected from the main crack of which the morphology is similar to that at RT. No microcracks can be found along the main crack.

At 650 °C, the main crack was more straight and less deflected and bifurcated compared to the crack generated at RT and 400 °C. The crack branching is different from that found at RT. It is nearly all caused by colony boundary deviation, even some colony boundaries are at high angles (about 90 ° to the loading axis) as shown in Figure 6.43. There are also no microcracks observed along the main crack at this temperature.

6.5.3 Effect of R ratio on fracture surface

The fracture surfaces of specimens tested at different R ratios are compared in Figure 6.44 for temperatures of RT, 400 °C, 650 °C and 700 °C. For the same temperature, the fracture surface observation of specimens tested at $R=0.1$ and 0.5 shows very little difference in terms of appearance at lower magnification. At all temperatures, the fracture surface of specimens tested at $R=0.8$ is rough, and similar to the fracture

surface caused by monotonic load at same temperature (see in Figure 6.6. The fracture surfaces of specimens tested under monotonic loads at different temperatures

6.5.4 Fracture surface roughness measurement

Quantitative analysis of crack path roughness were carried out to distinguish any differences between fracture surfaces obtained at $R=0.1$ and 0.5 which cannot be seen in SEM images. Table 6.5 shows the fracture surface roughness results of specimens tested at $R= 0.1, 0.5$ and at RT, 400 and 650 °C . There was a clear trend that fracture surface roughness decreases with increasing test temperatures at a given R ratio. In addition, it was also found that the fracture surface roughness values for the same temperature were higher at a higher R ratio.

6.6 Potential effects of other factors on fatigue crack growth

6.6.1 Effects of notch depth on fatigue crack growth

Tests were conducted on specimens with different notch depth to see whether notch depth has an effect on the fatigue crack threshold and growth of Ti-4522XD alloy. The notch depth varied from 0.1 mm to 0.7 mm and the actual average crack lengths calculated using the 5-point secant method are given in Table 6.6. The tests were carried out with an R ratio of 0.1 and at RT and 650 °C for all crack lengths, and ΔK_{th} values are also summarised in Table 6.6. As seen, there is no significant difference of ΔK_{th} values among specimens with different notch depth for both test conditions. All the ΔK_{th} values are within the data range of that test condition. The comparisons of FCGRs for specimens with different notch depths at RT and 650 °C are shown in Figure 6.45 and Figure 6.46, respectively. No FCGRs were generated in specimens with notch depth of 0.1 because they were used for other experimental purposes. Their ΔK_{th} values are represented by a single point in the two graphs. As seen, under each test condition, all FCGRs are consistent with each other. Therefore, the notch depth does

not have an obvious effect on both ΔK_{th} values and FCGRCs of Ti-4522XD alloy.

It is worth mentioning that specimens with shorter notch depths of 0.1 mm, 0.2 mm and 0.3 mm, all failed from the notches, even though the peak loads were much higher at the fatigue thresholds than specimens with longer notches of 0.5 mm and 0.7 mm.

6.6.2 Crack growth from a notch or from a pre-crack

The fatigue crack growth resistance curves for comparison among tests started from a notch and pre-crack are shown in Figure 6.47. The comparison was only carried out at an R ratio of 0.1 at 650 °C. Although the highest ΔK_{th} value was found in the pre-cracked specimen 1D2 (6.7 MPa.m^{1/2}), it was just slightly higher than the ΔK_{th} value of CC806 (6.5 MPa.m^{1/2}) which started from a notch. Specimen 1D2 and 2D1 were pre-cracked at an R ratio of 0.1 and at RT and 400 °C respectively. The difference of ΔK_{th} was only 0.7 MPa.m^{1/2}. These results suggest that there may be very little or no influence of pre-cracking and pre-cracking conditions on the ΔK_{th} value of a lamellar γ -TiAl alloy tested with increase-loading procedure.

6.6.3 Effects of surface condition on fatigue crack growth

Specimens were machined initially from the raw material blanks by EDM cutting to near net shape, and ground to provide a uniform and smooth surface. There were 10 specimens from IMR batch 5 failed unexpectedly away from the notches. The specimens were examined using an optical microscope and no surface cracks could be found. Then the specimens were electrochemically polished (ECM) to remove a thin layer (~200–300 μm) of material in order to release surface residual stresses caused by machining. After ECM, a large number of cracks were observed uniformly distributed on the polished surfaces, 4 examples are given in Figure 6.48. As seen, some of the cracks are even through the whole width of the parallel faces, which are nearly about 8

times longer than the notch depth. One specimen (CC706) was firstly heated at 650 °C and then tested at RT. It failed at the first applied load of only 2.8 kN. The other specimen (CC717) was test at 650 °C , and failed at 4.8 kN suddenly without any sign of increasing PD, i.e. the crack did not start from the notch. Due to oxidation induced colours at 650 °C , some surface cracks were turned up on the fracture surfaces of both specimens. As shown in Figure 6.49, the cracks are very deep and large, which are comparable or even larger than the notch.

6.6.4 Effects of equiaxed γ grain clusters on fatigue crack growth

As mentioned above, cluster of equiaxed γ grains were found in specimens. To evaluate the effects of equiaxed γ grain clusters, the FCGRC of one specimen (CC009 from TIMET batch 1), on which fracture surface large areas of equiaxed γ grains were observed (see in Figure 6.50), was compared to that of a normal specimen (CC611 from GfE batch 1) as shown in Figure 6.51. In general, these two FCGRCs are similar to each other. Even CC009 shows a slightly higher FCGR than it of CC611 when the ΔK value was greater than about $7.6 \text{ MPa}\cdot\text{m}^{1/2}$, the difference was not significant. In addition, those specimens which have high m values were not found containing large clusters of equiaxed γ grains.

6.7 High cycle fatigue (HCF) tests

In order to characterise naturally-initiated fatigue cracks in this near-fully lamellar alloy, tests were performed on specimens with a cylindrical gauge section and one CC specimen at $R=0.1$. The test conditions and results are summarised in Table 6.7. It can be seen that the highest failure load is at RT and lowest at 650 °C . There is a significant difference in failure stresses (50 MPa) between specimens tested at RT. At 650 °C , the difference between highest and lowest failure loads is only 15 MPa.

6.7.1 HCF at RT

The fracture surfaces of specimens (HF901 and HF902) tested at RT with R=0.1 are shown in Figure 6.52. At RT, once the specimen failed, the whole fractures are exposed to air, thus heat-tint is not applicable, and no colour difference can be used to identify the crack initiation. Indeed, it is also difficult to distinguish any fatigue crack initiation sites from low-magnification SEM images. In general, the fracture surfaces of specimens tested at RT are similar to a monotonic fracture. On the fracture surface of HF901, some radial patterns can be observed starting from some small areas. By examining high-magnification SEM images, two possible fatigue crack initiation sites were found as shown in Figure 6.53. One site contains some conjoined similar-oriented interlamellar fractures at the surface of the specimen. The other site has three large interlamellar fractures within a small area. The site A in Figure 6.53 is more likely to be the crack initiation site because its overall size is about 3-4 times larger than any interlamellar fractures in the site B. If site A is regarded as a semicircular surface crack, the ΔK_{th} value can be estimated using the following stress intensity factor range for a semicircular surface crack in a circular cross section:

$$\Delta K = 0.5\sigma\sqrt{\pi a} \quad \dots 6.1$$

The area (A_1) of site A measured by AxioVision software is about $4.1 \times 10^4 \mu m^2$. Hence the area of semicircular crack (A_2)

$$A_2 = 2A_1 = \pi\left(\frac{a}{2}\right)^2 \quad \dots 6.2$$

$$\rightarrow a = \sqrt{\frac{4A_2}{\pi}} = \sqrt{\frac{8A_1}{\pi}} = \sqrt{\frac{8 \times 5.6 \times 10^4}{\pi}} = 323 \mu m = 3.23 \times 10^{-4} m \quad \dots 6.3$$

where a is the diameter of that semicircular fracture, i.e. crack length. The testpiece failed under a maximum stress of 425 MPa (see in Table 6.7) which gives stress range of 382.5 MPa. Hence:

$$K_{max, HF901} = 0.5\sigma\sqrt{\pi a} = 0.5 \times 425 \times \sqrt{\pi \times 3.23 \times 10^{-4}} = 6.8 MPa.\sqrt{m} \quad \dots 6.4$$

$$\Delta K_{th, HF901} = K_{max} - K_{min} = K_{max} - 0.1K_{max} = 0.9 \times 6.8 = 6.1 MPa.\sqrt{m} \quad \dots 6.5$$

Therefore, the crack can be deduced to have grown at a ΔK value of $6.1 \text{ MPa.m}^{1/2}$, which is consistent with threshold values of CC specimens tested at RT with an R ratio of 0.1 (see in Table 6.2(a), R=0.1 and RT).

In HF902, there are no conjoined interlamellar fractures with areas of large interlamellar fracture facets. The maximum stress at failure was 475 MPa. As shown in Figure 6.52 (b), the failure of HF902 is probably caused by several small fatigue crack initiation sites and those small cracks linked up leading to the final failure. It is likely to be the reason why the maximum stress to caused failure of HF902 was 50MPa higher than that of HF901.

In addition, no more than 4 conjoined linked interlamellar fractures can be found on the fracture surfaces of both specimens.

6.7.2 HCF at 650 ℃

The optical images of facture surfaces obtained at 650 ℃ are shown in Figure 6.54. Unlike the RT tests, at 650 ℃ the fatigue initiation sites are relatively easy to be determined either by in-situ heat tinting colours or SEM images. The initiation sites are pointed out by arrows in the images.

The whole fracture surface of HF904 is presented in Figure 6.55 (a). The SEM image shows consistent observation with optical image about the location and size of the fatigue initiation site as shown in Figure 6.55 (b). The ‘river pattern’ was found to radiate from the initiation site. Figure 6.55 (c) shows more details about this fatigue crack initiation site in which some particles were found in the middle. The largest particle was about $20 \mu\text{m} \times 40 \mu\text{m}$ in dimension. The EDS result showed the major composition of these particles was Yttrium as shown in Figure 6.56. As indicated by the EDS results, the Yttrium is mainly concentrated in the particles rather than the

matrix, and the morphology of these particles is different from any microstructures in the Ti4522XD alloy, thus the particles are likely to be inclusions caused by mixing of unexpected element during material manufacture. If regarding these inclusions together as a single crack initiation site, its approximate area (A) can be outlined as shown in Figure 6.27(c) which is about $3 \times 10^4 \mu\text{m}^2$. By assuming this crack as an embedded circular crack, the crack length a ($\phi=2a$) can be calculated as [17]:

$$A = \pi a^2 \rightarrow a = \sqrt{\frac{A}{\pi}} = \sqrt{\frac{3 \times 10^4}{\pi}} = 97.7 \mu\text{m} = 9.8 \times 10^{-5} \text{ mm} \quad \dots 6.6$$

For a single crack in an infinite plate subjected to a tension load which is 415 MPa (see in Table 6.7) in specimen HF904, the maximum stress intensity factor at fatigue threshold can be approximately estimated by the following equation:

$$K_{max, HF904} = \sigma \sqrt{\pi a} = 415 \times \sqrt{\pi \times 9.8 \times 10^{-5}} = 7.3 \text{ MPa} \cdot \sqrt{\text{m}} \quad \dots 6.7$$

and the ΔK_{th} value of HF904 is:

$$\Delta K_{th, HF905} = K_{max} - K_{min} = K_{max} - 0.1 K_{max} = 0.9 \times 7.3 = 6.6 \text{ MPa} \cdot \sqrt{\text{m}} \quad \dots 6.8$$

The fatigue crack initiation site in HF905 is shown in Figure 6.57 (a). Similar to HF904, this fatigue crack origin was surrounded by a radial ‘river pattern’. In Figure 6.57 (b) at high magnification, three large conjoined interlamellar fractures were found in the middle of the fatigue crack initiation site. Two of these interlamellar fractures were larger than 100 μm in diameter. The area (A) was also measured by AxioVision software which is about $2.7 \times 10^4 \mu\text{m}^2$ in two-dimensions. If regarding this site as an embedded circular crack as well, the crack length a ($\phi=2a$) can be calculated as:

$$A = \pi a^2 \rightarrow a = \sqrt{\frac{A}{\pi}} = \sqrt{\frac{2.7 \times 10^4}{\pi}} = 92.7 \mu\text{m} = 9.3 \times 10^{-5} \text{ mm} \quad \dots 6.9$$

The maximum failure stress of HF905 was 415 MPa. Similar estimation of the maximum stress intensity factor at fatigue threshold can be approximately estimated using the same equation for HF904, hence:

$$K_{max, HF905} = \sigma \sqrt{\pi a} = 415 \times \sqrt{\pi \times 9.3 \times 10^{-5}} = 7.1 \text{ MPa} \cdot \sqrt{\text{m}} \quad \dots 6.10$$

and the ΔK_{th} value of HF905 is:

$$\Delta K_{th, HF905} = K_{max} - K_{min} = K_{max} - 0.1K_{max} = 0.9 \times 7.1 = 6.4 \text{ MPa} \cdot \sqrt{\text{m}} \dots 6.11$$

The difference of ΔK_{th} values between specimen HF904 and HF905 is only $0.2 \text{ MPa} \cdot \text{m}^{1/2}$, and ΔK_{th} values of both specimens are also consistent with the average ΔK_{th} value of CC specimens tested under the same condition (see in Table 6.2 (a), $R=0.1$ and $650 \text{ }^{\circ}\text{C}$).

The fatigue crack initiation site of 5C2 is shown in Figure 6.58 (a). Similar to the observations on the fracture surfaces of HF904 and HF905, there is also a radial ‘river pattern’ starting from the initiation site. As seen in Figure 6.58 (b), 3 separate interlamellar fractures were also found in the crack initiation sites which are all larger than $100 \text{ }\mu\text{m}$ in diameter. However, there is no clear knowledge of how the three separated interlamellar fractures could interact with each other in this alloy, and the calculation of ΔK_{th} value is difficult to be carried out.

6.8 Creep crack growth

6.8.1 Specimens failing in creep manner

One specimen (CC009-T) from TIMET 3rd batch was planned for a test with an R ratio of 0.8 at $750 \text{ }^{\circ}\text{C}$. This specimen was pre-cracked with an $R=0.1$ at $T=400 \text{ }^{\circ}\text{C}$. Unlike other tests at 0.8, the crack showed signs of growth at the first applied peak load ($P_{max}=5\text{kN}$ and $\Delta K \approx 1.33 \text{ MPa} \cdot \text{m}^{1/2}$) which was much lower than the average ΔK_{th} value for the fatigue threshold at $R=0.8$. It was observed that the crack growth rate was very slow (between 10^{-8} and 10^{-7} mm/cycle) after crack initiation. This test lasted more than one month and the growth in PD was more than $1400 \text{ }\mu\text{V}$ until unstable crack propagation occurred. After cooling down the furnace to RT, the specimen was taken out from the machine without breaking open, and then observed using an optical microscope. The notched crack was widely opened and severe deformation around the crack could be seen even with the naked eye as shown in Figure 6.59.

The other specimen from the same batch, CC008-T, was tested with a stress ratio of 0.8 at 700 °C. The same procedure and conditions were applied for pre-cracking as CC009-T. Similar to CC009-T, the sign of crack initiation revealed by PD was also noticed at the very first load cycle (5.2 kN) which was also far below the load for the average threshold level of this test condition. The crack growth rate was also very slow. The crack was allowed to grow by about 27 μV (~ 0.09 mm in terms of crack length) under these conditions, which took nearly 4 days and the corresponding FCGR was about 2.8×10^{-8} mm/cycle. Then the load was increased by 0.2 kN every step to let the crack propagate faster until the crack growth rate was above 10^{-7} mm/cycle. Although slow crack growth was also found in specimens CC006-T and CC007-T (see in Figure 6.22) under the same tests conditions, the lowest FCGRs of these two tests were still above 10^{-7} mm/cycle. The maximum loads (P_{max}) of CC006-T and CC007-T at fatigue threshold were 7.8 kN and 7.5 kN, respectively. These two values are similar to the P_{max} value (7.7 kN) that allow CC008-T to propagate with FCGRs of more than 10^{-7} mm/cycle. Comparing the crack growth behaviour in CC008-T with CC006-T and CC007-T, there are probably different crack growth mechanisms at low and high fatigue loadings at $R=0.8$ and at 700 °C. The two different mechanisms will be discussed in Chapter 7.

6.8.2 Fractography of specimen failed in creep manner

The SEM image showing the widely opened crack in specimen CC009-T is presented in Figure 6.60. There is a clear boundary between the severely deformed zone and less damaged area. Ahead of the crack tip, there are several cracks attached to the notch which are about 45 ° to the loading direction (as shown in Figure 6.61 (a)) and a large number of small cracks in the severely deformed area (as shown in Figure 6.61 (b)) are found. Details of the fracture surface and side surface are given in Figure 6.62. Unlike fatigue and static fracture surfaces, there were no clear features of translamellar, interlamellar and intralamellar fractures, and even no distinct colony boundaries or

grain boundaries and lamellar characteristics can be identified (see Figure 6.62 (a)). In Figure 6.62 (b), some relatively flat areas were found near the notch. By tilting the specimen, these step-like flat cleavage features are similar to the morphology of interlamellar fracture caused by fatigue or static fracture as shown in Figure 6.62 (c). However, the edges of these cleavage features were more torturous, and the surface of a single lamella was also not as flat as interlamellar fracture. An SEM image of $\times 8000$ was taken to examine the side surface. As seen in Figure 6.62 (d), the surface was fully covered with pine-needle-like oxidation particles and cracks. Additionally, in the region close to the boundaries of the severe deformed area, clusters of needle-like precipitates protrude on the surface as shown in Figure 6.62 (e).

Table 6.1. Summary of test conditions and results for fracture toughness tests

sample ID	T (°C)	Original fatigue pre-crack length (mm)	P _{max} at failure (kN)	K _C (MPa.m ^{1/2})	average K _C (MPa.m ^{1/2})
CC003	RT	1.75	8.51	19.8	17.8
CC006		1.78	7.51	17.7	
CC802		1.86	7.06	17.9	
CC803		2.09	5.55	15.2	
2D2		2.12	6.67	18.3	
CC002	400	1.95	7.98	20.4	20.3
CC007		2.00	8.28	21.7	
CC811		1.76	8.55	20.1	
CC812		1.48	9.34	19.1	
CC013		1.96	7.97	20.3	
CC005	650	1.6	8.34	18.2	18.2
CC009		1.79	7.88	18.7	
CC809		2.10	6.54	17.9	
CC810		2.33	6.68	20.2	
5A1		1.70	8.49	19.1	
CC001	700	1.83	8.13	19.7	18.2
CC011		1.62	7.81	17.1	
CC012		1.48	8.71	17.8	
5A2	750	1.77	7.64	17.8	17.8

Table 6.2. A summary of fatigue threshold values according to different stress ratios: (a) R=0.1, (b) R=0.5 and (c) R=0.8. For each test condition, the highest and lowest ΔK_{th} values are highlight by red and blue colours, respectively.

(a) R=0.1

T (°C)	Sample ID	ΔK_{th} (MPa.m ^{1/2})	Average ΔK_{th} (MPa.m ^{1/2})	$K_{max,th}$ (MPa.m ^{1/2})	Average $K_{max,th}$ (MPa.m ^{1/2})
RT	CC002*	6.9	6.5	7.7	7.1
	CC003*	7.8		8.6	
	CC602	7.2		8.0	
	CC801	6.4		7.1	
	CC802	5.8		6.4	
	CC002	7.0		7.7	
	5A2	5.5		6.1	
	11-6-4	5.2		5.7	
	2D1	6.3		7.0	
400	CC603	5.0	5.1	5.6	5.7
	CC604	5.1		5.7	
	CC703	4.2		4.7	
	CC715	4.1		4.6	
	CC803	5.3		5.9	
	CC814	5.1		5.7	
	CC816	5.7		6.3	
	CC011-T	5.5		6.1	
	CC003	6.3		7.0	
650	CC605	5.4	5.8	6.0	6.5
	CC615	6.0		6.7	
	CC806	6.5		7.2	
	CC817	4.4		4.9	
	CC818	4.8		5.3	
	CC005	6.0		6.7	
	1D1	6.5		7.2	
	1D2	6.7		7.4	
	5A1	5.2		5.8	
	2D1	6.0		6.7	
700	CC006	6.5	6.5	7.2	7.3
	CC011	6.1		6.8	
	CC012	7.0		7.8	
750	CC714	6.6	6.8	7.3	7.5
	CC718	6.5		7.2	
	CC001-T	7.2		8.0	

*specimens from CC assessment trials

(b) R=0.5

T (°C)	Sample ID	ΔK_{th} (MPa.m ^{1/2})	Average ΔK_{th} (MPa.m ^{1/2})	$K_{max,th}$ (MPa.m ^{1/2})	Average $K_{max,th}$ (MPa.m ^{1/2})
RT	CC608	4.7	4.2	9.4	8.4
	CC807	3.6		7.2	
	CC808	4.1		8.2	
	CC008	4.3		8.6	
400	CC609	4.3	3.9	8.6	7.9
	CC610	4.1		8.2	
	CC710	3.7		7.4	
	CC809	3.8		7.6	
	CC810	3.8		7.6	
	CC007	3.9		7.9	
650 °C	CC611	4.6	4.4	9.2	8.7
	CC612	4.1		8.2	
	CC711	4.0		8.0	
	CC811	4.3		8.6	
	CC812	4.7		9.4	
	CC009	4.4		8.8	
700 °C	CC617	4.6	4.6	9.2	9.2
	CC002-T	4.5		9.1	
	CC001	4.6		9.2	
750 °C	CC003-T	5.1	5.1	10.2	10.2
	CC004-T	5.3		10.6	
	CC005-T	4.9		9.8	

(c) R=0.8

T (°C)	Sample ID	ΔK_{th} (MPa.m ^{1/2})	Average ΔK_{th} (MPa.m ^{1/2})	$\Delta K_{max,th}$ (MPa.m ^{1/2})	Average $\Delta K_{max,th}$ (MPa.m ^{1/2})
RT	CC610	3.4	3.3	17.0	16.5
	CC612	3.5		17.5	
	CC814	3.0		15.0	
400	CC604	3.3	3.3	16.3	16.2
	CC715	3.2		16.0	
	CC816	3.2		16.0	
	CC011	3.3		16.3	
650	CC817	3.6	3.3	18.0	16.5
	CC818	3.0		15.0	
700	CC006-T	2.8	2.9	13.8	14.1
	CC007-T	2.9		14.3	

Table 6.3. Statistical analysis of effect of test temperature on ΔK_{th}

R ratio	T (°C)	Number of individual tests	Standard Deviation	Standard Deviation of all tests	Average ΔK_{th} of all tests (MPa.m^{1/2})	Average ΔK_{th} (MPa.m^{1/2})	Min ΔK_{th} (MPa.m^{1/2})	Max ΔK_{th} (MPa.m^{1/2})
0.1	RT	9	0.82	0.87	6.1	6.5	5.2	7.8
	400	9	0.70			5.1	4.1	6.3
	650	12	0.70			5.8	4.4	6.7
	700	3	0.45			6.5	6.1	7
	750	3	0.4			6.8	6.5	7.2
0.5	RT	4	0.46	0.48	4.5	4.2	3.6	4.7
	400	6	0.22			3.9	3.7	4.3
	650	8	0.40			4.4	4	5.1
	700	3	0.06			4.6	4.5	4.6
	750	3	0.20			5.1	4.9	5.1
0.8	RT	3	0.26	0.25	3.3	3.3	3	3.5
	400	4	0.10			3.3	3.2	3.3
	650	2	0.42			3.3	3	3.6
	700	2	0.07			2.9	2.8	2.9

Table 6.4. A summary of Paris Law exponent (m) and Paris coefficient values for all test conditions (a) R=0.1, (b) R=0.5 and (c) R=0.8

(a) R=0.1

R	T (°C)	Specimen ID	Paris exponent (m)	Average m value	Paris coefficient (C) (mm/cycle)	Average C value
0.1	RT	CC602	7	7.2	3.00E-12	2.69E-11
		CC801	6		2.80E-11	
		CC802	5.3		1.28E-10	
		1A2	7.1		2.00E-12	
		11-6-4	7.7		5.00E-13	
		CC002	9.8		2.00E-15	
	400	CC603	2.7	3.6	9.60E-08	1.34E-7
		CC703	2		3.80E-07	
		CC715	2.3		3.20E-07	
		CC803	4.5		1.40E-09	
		CC814	4.6		2.00E-09	
		CC003	4.3		2.00E-09	
	650	CC605	3.2	3.7	3.90E-09	9.42E-8
		CC615	3		2.50E-07	
		11-9-3	3.3		1.00E-07	
		11-6-11	3.1		2.00E-07	
		2D2	3.2		1.00E-07	
		2D1	3.5		5.00E-08	
		CC806	4.8		6.00E-09	
		CC818	3		2.00E-07	
		CC817	5.7		2.00E-09	
		CC005	3.9		3.00E-08	
	700	CC006	3.5	4.4	7.00E-8	3.29E-08
		CC011	5.4		9.65E-10	
		CC012	3.9		2.76E-08	
	750	CC001-T	4.9	6.0	1.97E-09	8.05E-10
		CC714	7.1		3.12E-11	
		CC718	5.9		4.13E-10	

(b) R=0.5

R	T (°C)	Specimen ID	Paris exponent (m)	Average m value	Paris coefficient (C) (mm/cycle)	Average C value
0.5	RT	CC608	8.4	8.6	1.20E-12	8.52E-08
		CC808	5.4		3.50E-08	
		CC807	9.2		9.10E-08	
		CC808	5.4		3.00E-07	
		CC008	14.5		8.00E-16	
	400	CC609	3.3	3.0	1.90E-06	4.16E-07
		CC610	2.8		1.20E-08	
		CC710	2.7		1.00E-07	
		CC810	2.9		4.60E-08	
		CC007	3.5		2.00E-08	
	650	CC611	3.4	3.8	9.70E-10	4.73E-08
		CC612	2.4		2.00E-07	
		CC711	4.2		9.00E-08	
		CC809	2.4		1.00E-08	
		CC811	4.9		1.00E-08	
		CC812	4.9		2.00E-12	
		CC009	4.3		2.00E-08	
	700	CC617	4.8	4.8	1.00E-09	1.17E-08
		CC002-T	5.3		5.00E-09	
		CC001	4.3		2.90E-08	
	750	CC003-T	5.3	5.8	3.00E-09	1.47E-09
		CC004-T	5.6		1.00E-09	
		CC005-T	6.5		4.00E-10	

(c) R=0.8

R	T (°C)	Specimen ID	Paris exponent (m)	Average m value	Paris coefficient (C) (mm/cycle)	Average C value
0.8	RT	CC610	20.9	26.2	1.20E-18	1.74E-17
		CC612	36.9		3.20E-17	
		CC814	20.9		1.90E-17	
	400	CC604	N/A	13.5	N/A	1.11E-13
		CC816	13.5		1.11E-13	
		CC715	N/A		N/A	
	650	CC818	N/A	15	N/A	15
		CC817	15		1.00E-06	
	700	CC006-T	N/A	N/A	N/A	N/A
		CC007-T	N/A		N/A	

Table 6.5. Results of fracture surface roughness measurement

R	T (°C)	SRa* (mm)
0.1	RT	8.2
0.1	400	6.4
0.1	650	5.8
0.5	RT	14.9
0.5	400	9.6
0.5	650	6.9

* SRa is the arithmetic average roughness-height of the absolute values

Table 6.6. Summary of ΔK_{th} values of specimens with different crack length tested at R ratio of 0.1 and at (a) RT and (b) 650°C

(a) At R=0.1 and RT

Notch depth (mm)	Average crack length (mm)	Specimen ID	P _{max} at threshold (kN)	Threshold ΔK_{th} (MPa.m ^{1/2})	Threshold K _{max} (MPa.m ^{1/2})
0.7	0.85	CC602	5.5	7.2	8.0
0.5	0.70	CC002*	5.9	6.9	7.7
0.5	0.68	CC801	5	6.4	7.1
0.5	0.53	CC802	5.4	5.8	6.4
0.5	0.63	CC002**	5.8	7.0	7.7
0.3	0.38	1A2	7	6.0	6.7
0.2	0.27	11-6-4	7.2	5.2	5.7
0.1	0.18	5A2	9.4	5.5	6.1

*specimens from trial batch

**specimen from Timet second batch

(b) At R=0.1 and 650 °C

Notch depth (mm)	Average crack length (mm)	Specimen ID	P _{max} at threshold (kN)	Threshold ΔK_{th} (MPa.m ^{1/2})	Threshold K _{max} (MPa.m ^{1/2})
0.7	0.81	CC605	4.6	5.4	6.0
0.7	0.85	1D1	5	6.5	7.2
0.5	0.58	CC615	5.4	6.0	6.7
0.5	0.59	CC806	5.8	6.5	7.2
0.5	0.60	CC817	4	4.4	4.9
0.5	0.60	CC818	4.4	4.8	5.3
0.5	0.6	CC005	5.4	6.0	6.7
0.3	0.38	11-6-11	6.2	5.6	6.3
0.2	0.27	11-9-3	8.2	5.9	6.5
0.1	0.16	5A1	9.4	5.2	5.8

Table 6.7. A Summary of testing conditions, applied stresses and duration of each test on smooth specimens

SP ID	R ratio	T (°C)	Geometry	Maximum Stress (MPa)	Peak load (kN)	Number of cycles
HF901	0.1	RT	cylindrical	300	4.84	10^7
				350	5.64	10^7
				400	6.45	10^7
				425 *	6.85 **	6.6×10^6 ***
HF902	0.1	RT	cylindrical	400	6.45	10^7
				450	7.25	10^7
				475 *	7.66 **	3.7×10^6 ***
HF904	0.1	650	cylindrical	355	5.72	1.3×10^7
				370	5.96	10^7
				385	6.21	1.3×10^7
				400	6.45	1.3×10^7
				415 *	6.69 **	9.5×10^6 ***
HF905	0.1	650	cylindrical	355	5.72	1.4×10^7
				370	5.96	10^7
				385	6.21	1.2×10^7
				400	6.45	2.2×10^7
				415 *	6.69 **	1.7×10^7 ***
5C2	0.1	650	square	385	9.63	1.5×10^7
				400 *	10 **	4×10^5 ***

* The final stress causing failure of specimens

** The final Peak load causing failure of specimens

*** The number of cycles the specimens lasted at the final failure load

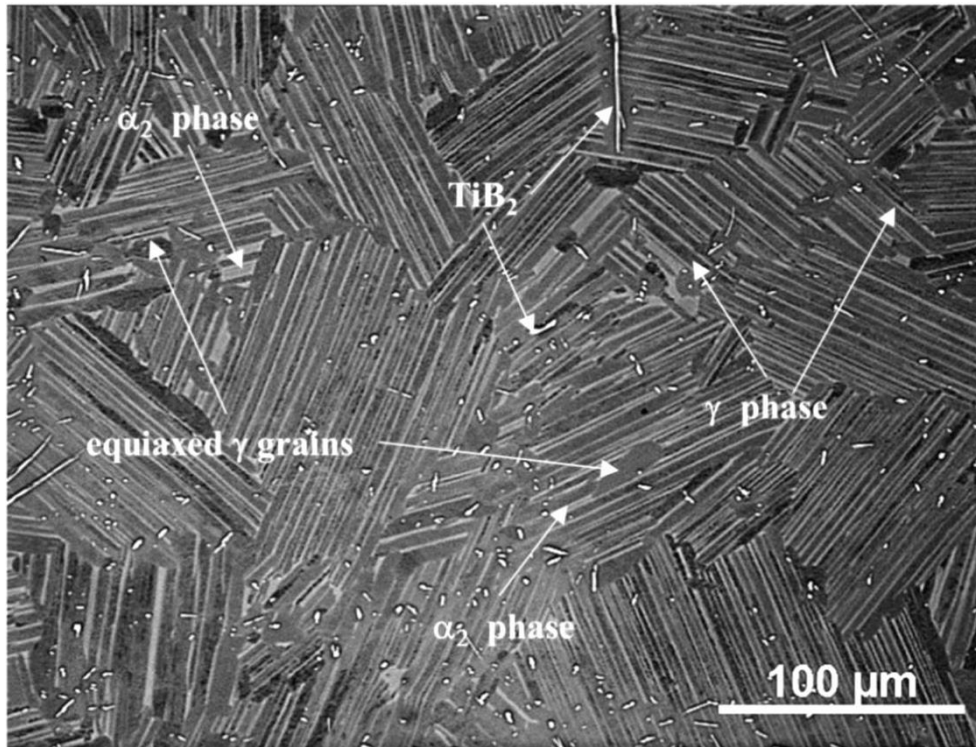


Figure 6.1 General microstructure of Ti-4522XD alloy

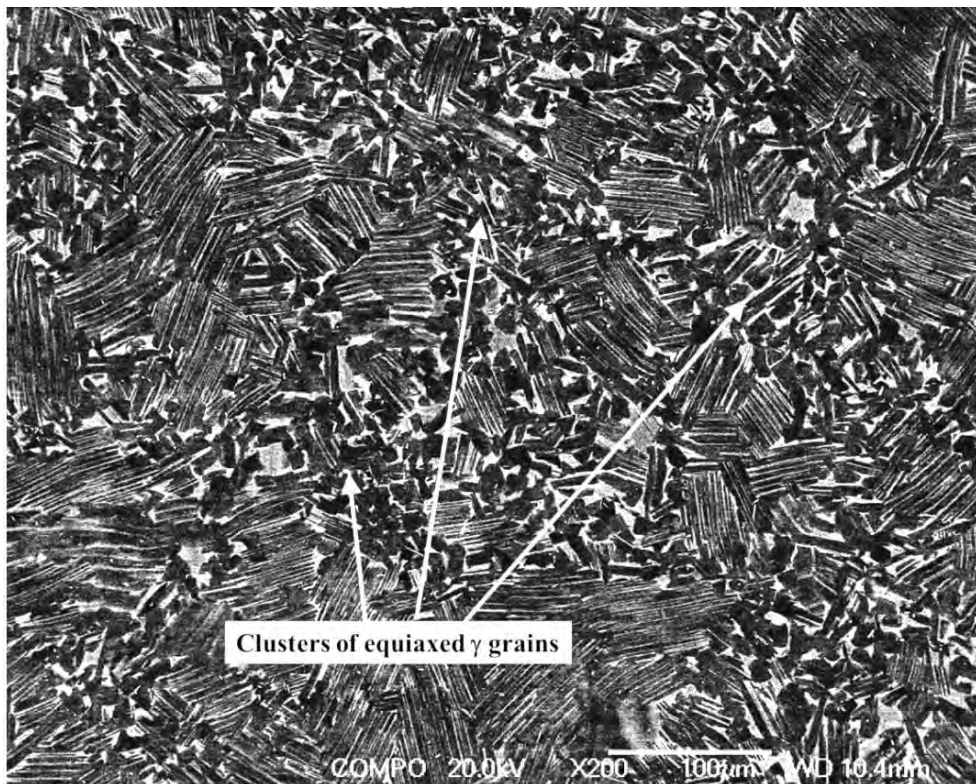


Figure 6.2. An example of clustered equiaxed γ grains found occasionally close to surfaces

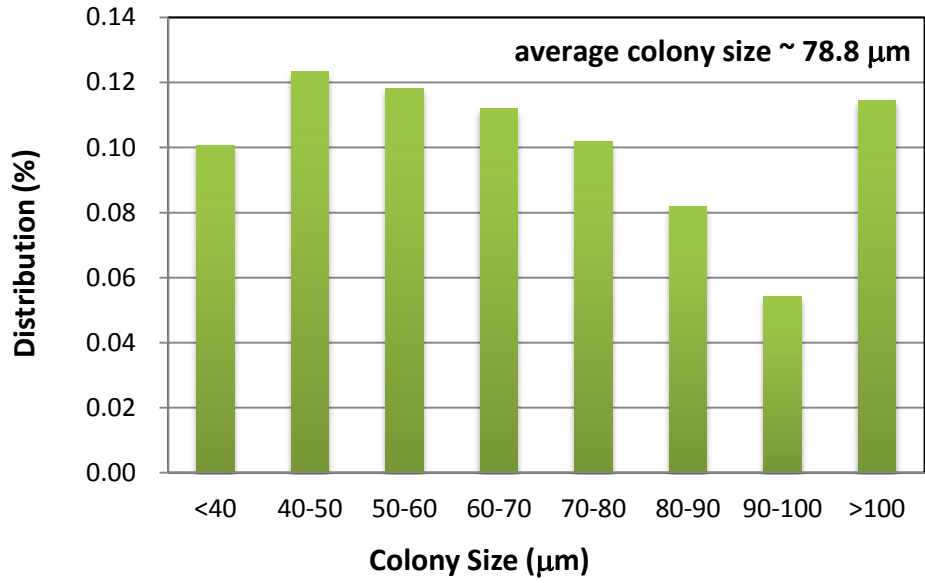


Figure 6.3. Average distribution of colony size of material in three batches (GfE batch1, GfE batch 2 and IMR batch 5)

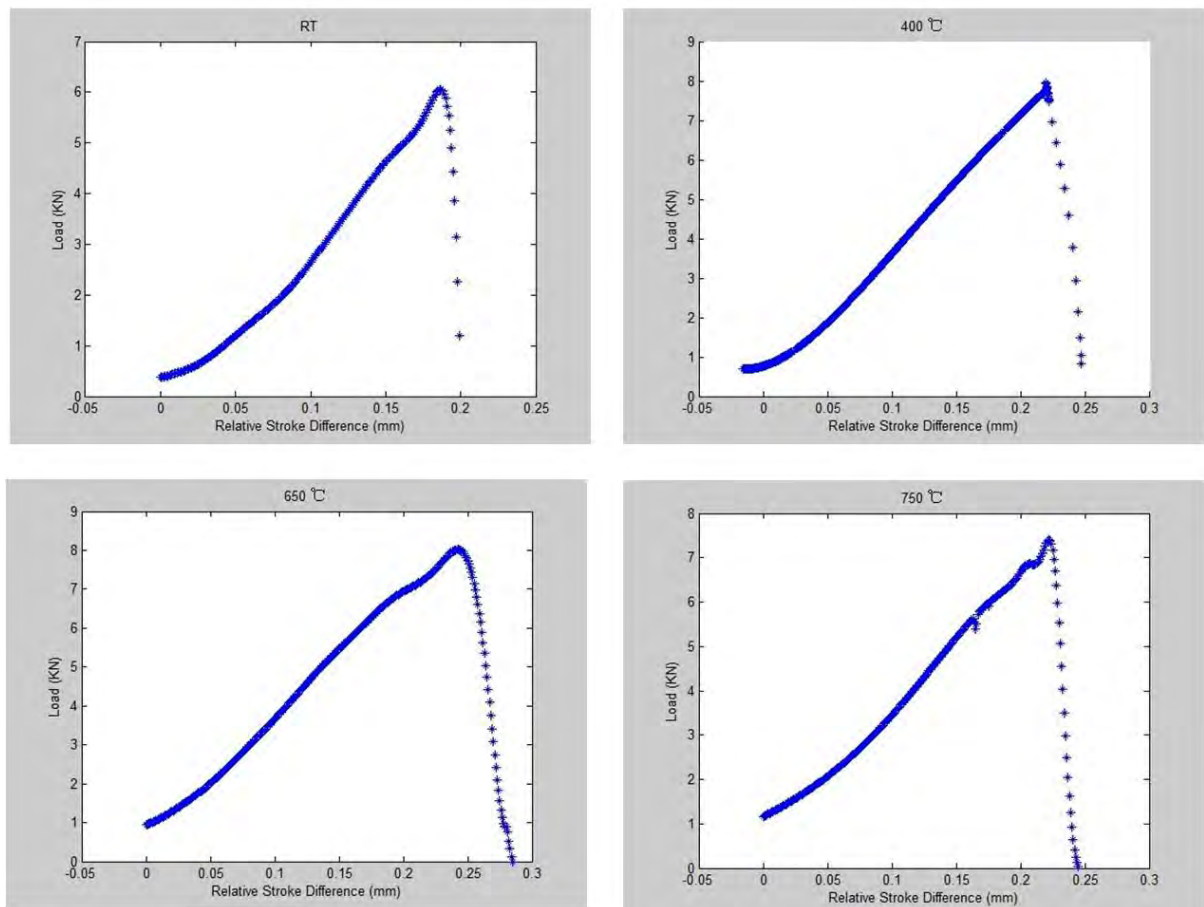


Figure 6.4. Load-stroke curves of Ti4522XD under monotonic loading at different temperatures (RT, 400, 650 and 750 °C)

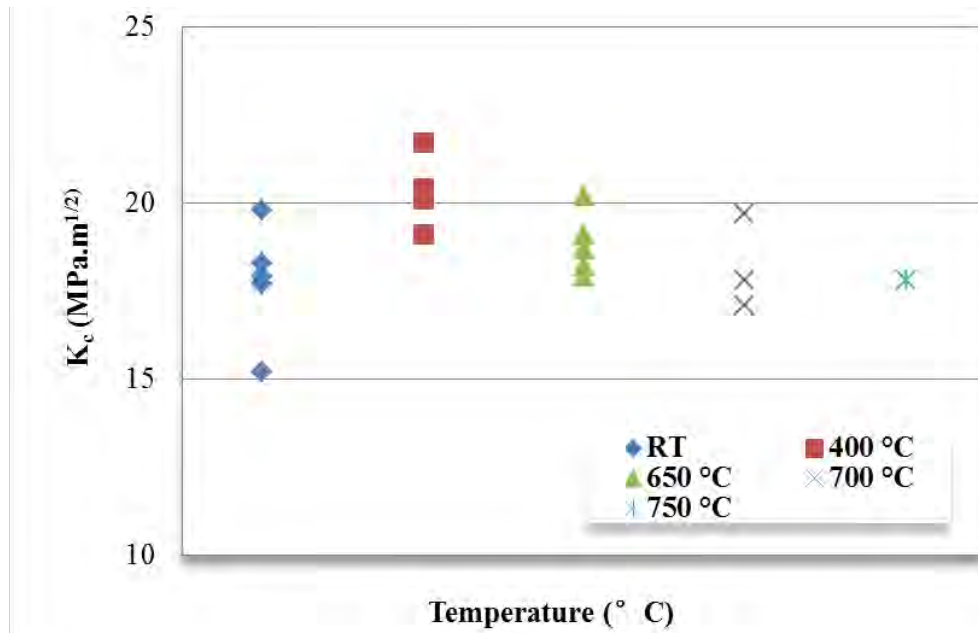


Figure 6.5. Fracture toughness (K_C) values obtained at five different temperatures: RT, 400 °C, 650 °C, 700 °C and 750 °C.

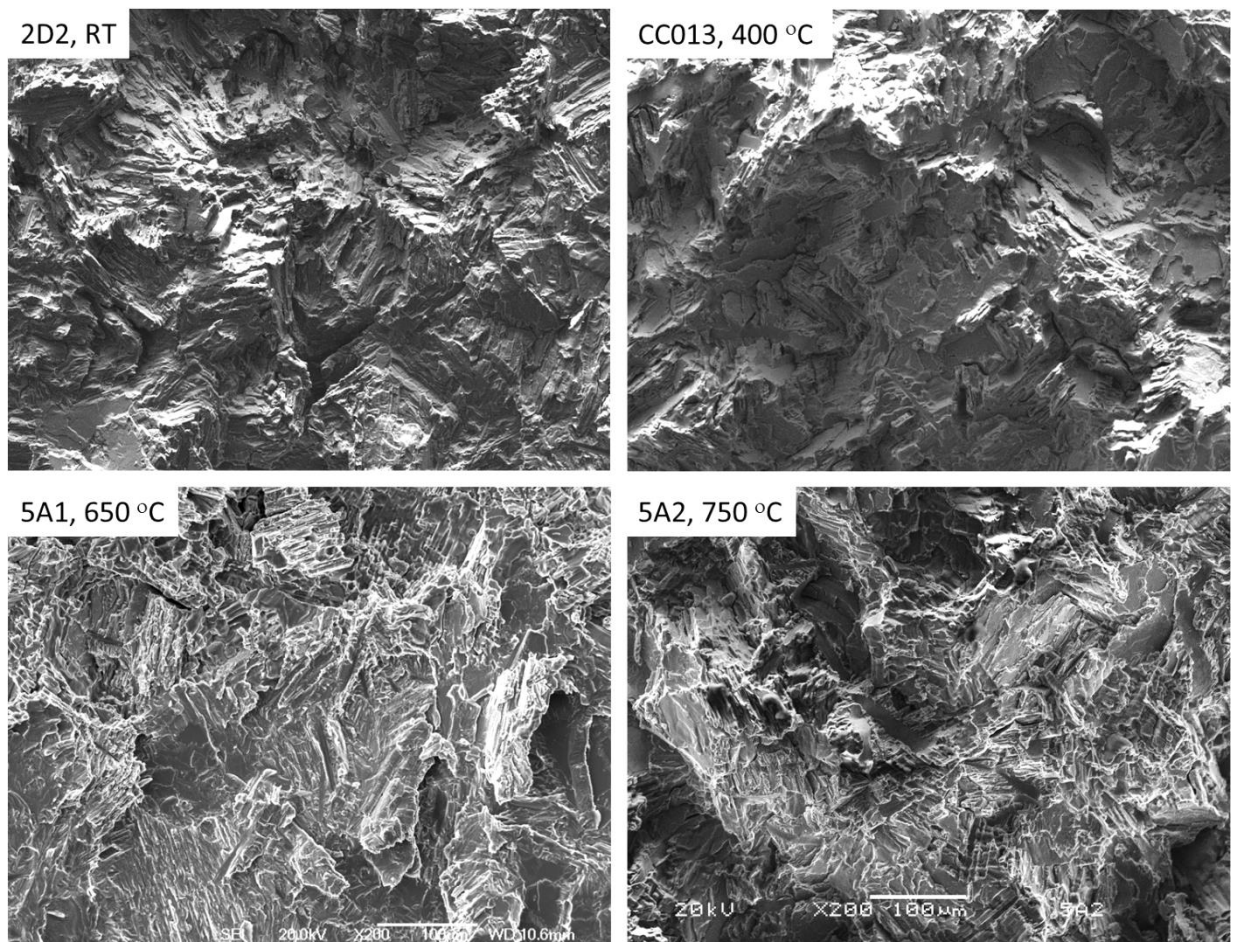


Figure 6.6. The fracture surfaces of specimens tested under monotonic loads at different temperatures

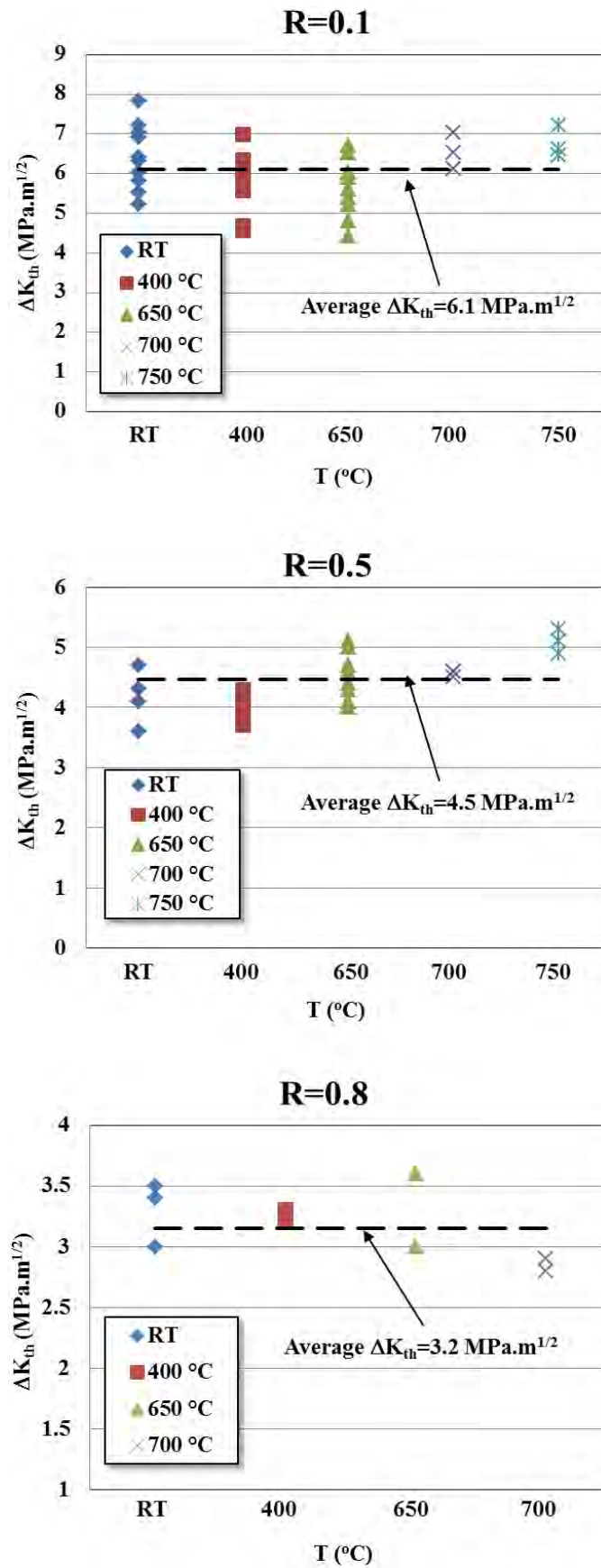


Figure 6.7. Comparison of fatigue threshold values at different test temperatures for a fixed R ratio

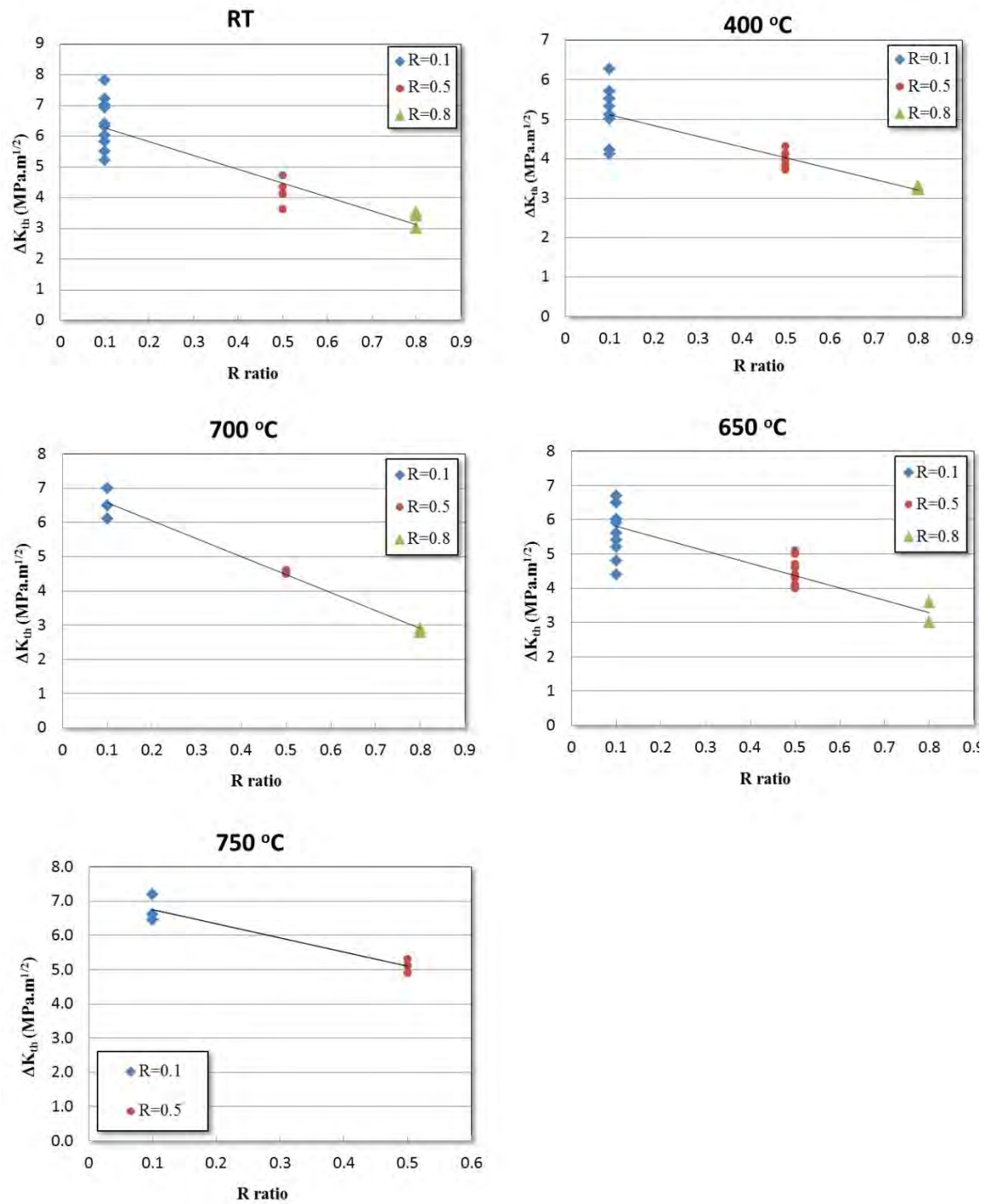


Figure 6.8. Comparison of fatigue threshold values at different R ratios for a fixed test temperature

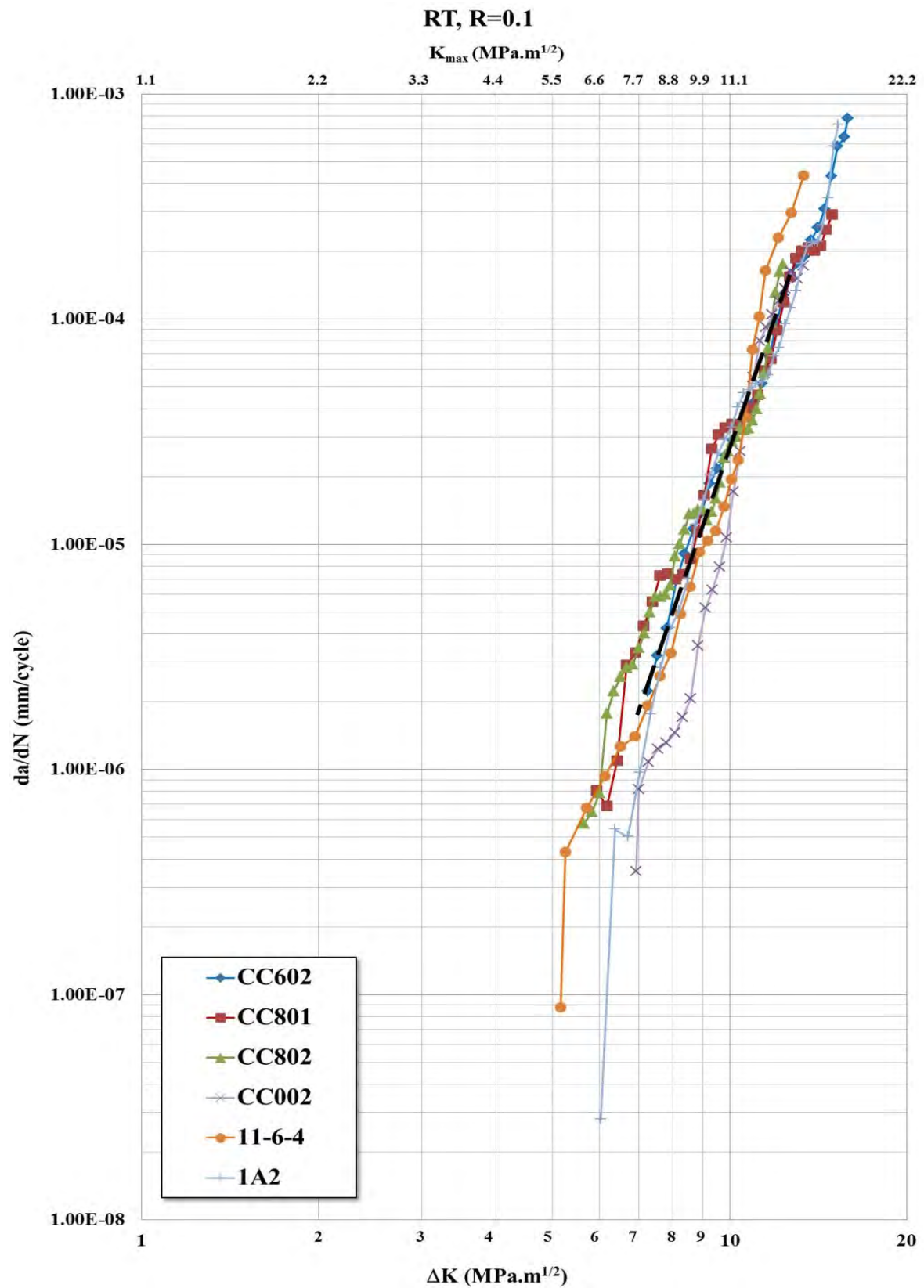


Figure 6.9. Fatigue crack growth resistance curves of Ti-4522XD alloy tested at RT with an R ratio of 0.1. The dotted lines is taken as representative of this set of tests.

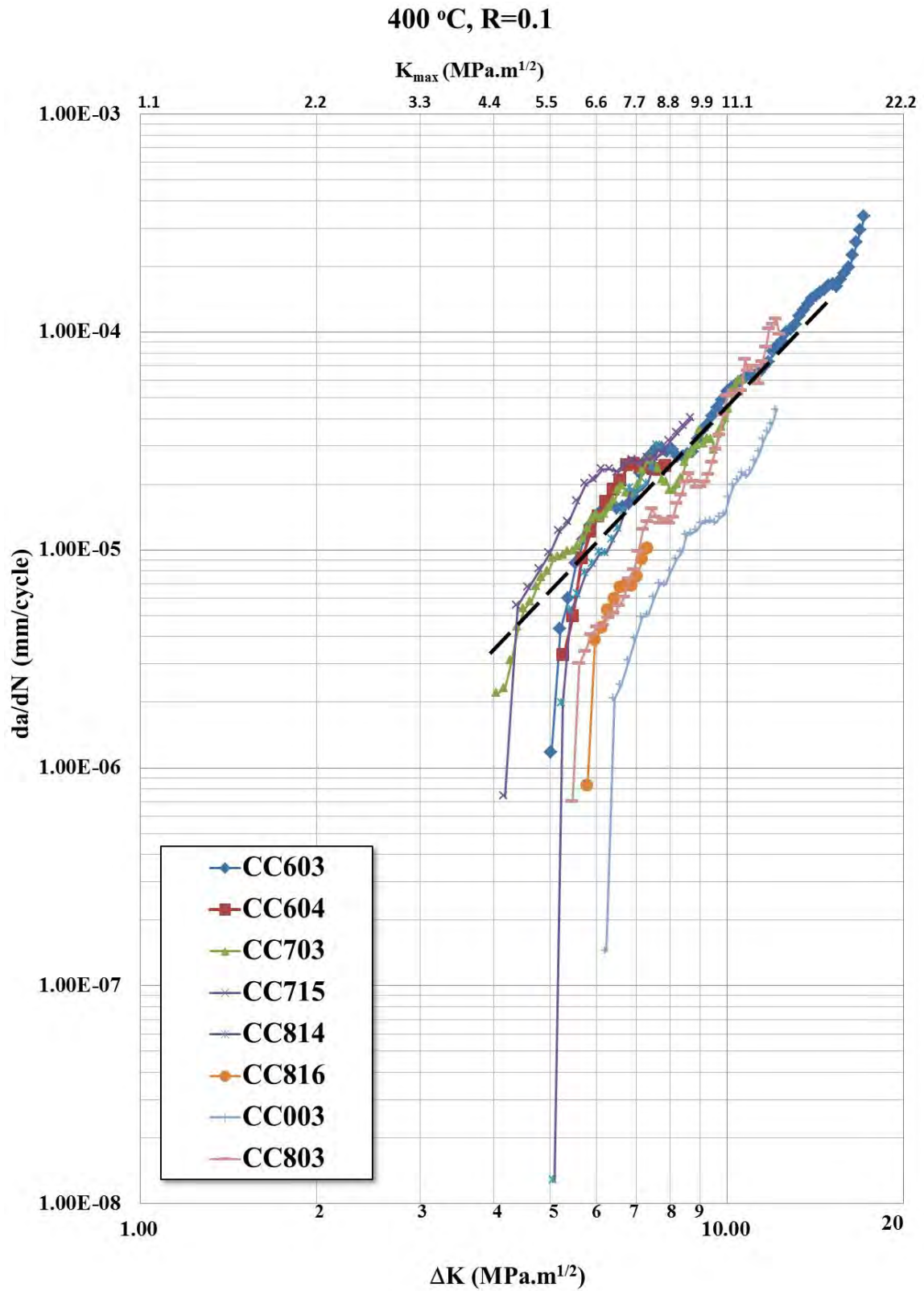


Figure 6.10. Fatigue crack growth resistance curves of Ti-4522XD alloy tested at 400 °C with an R ratio of 0.1. The dotted lines is taken as representative of this set of tests.

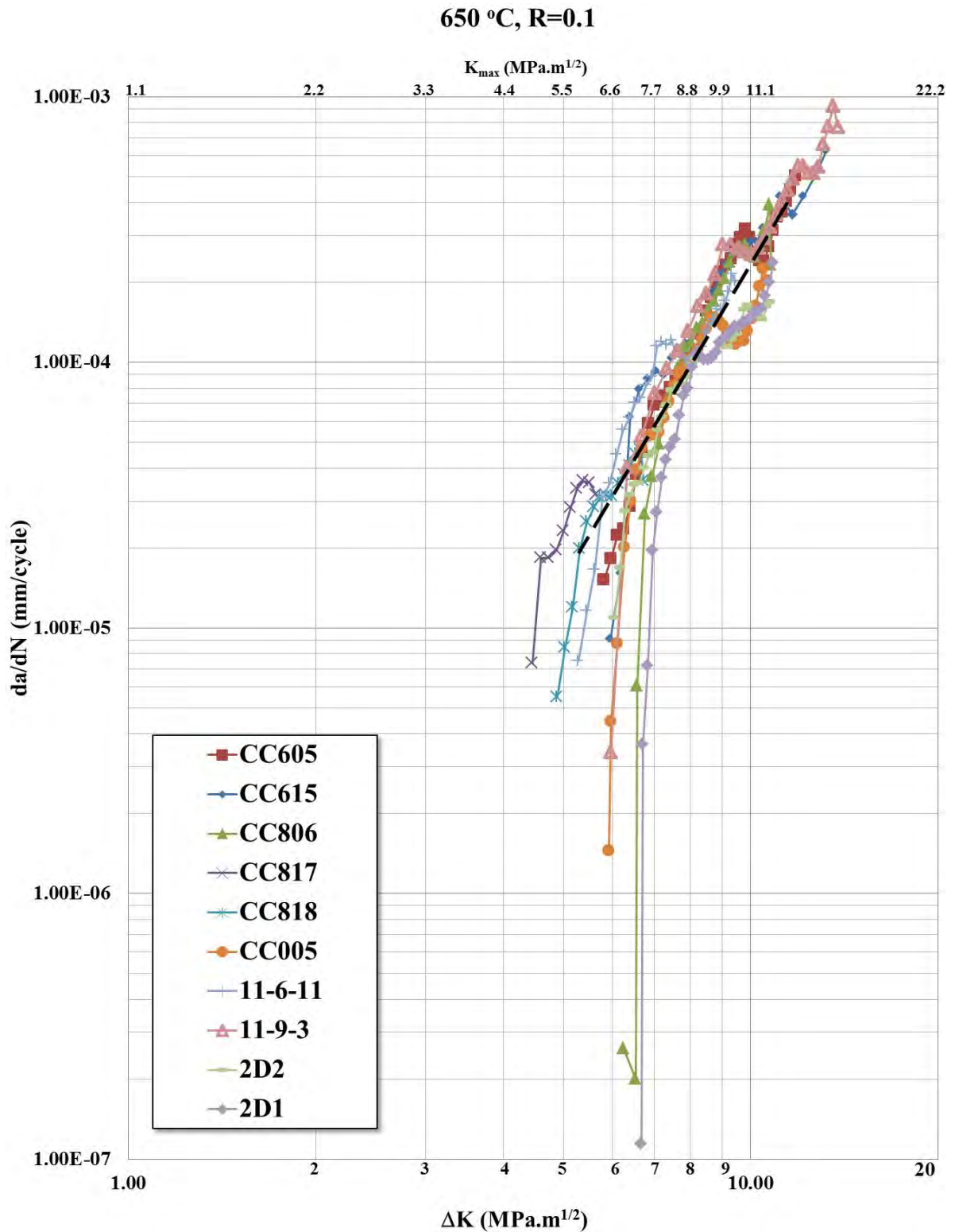


Figure 6.11. Fatigue crack growth resistance curves of Ti-4522XD alloy tested at 650°C with an R ratio of 0.1. The dotted lines is taken as representative of this set of tests.

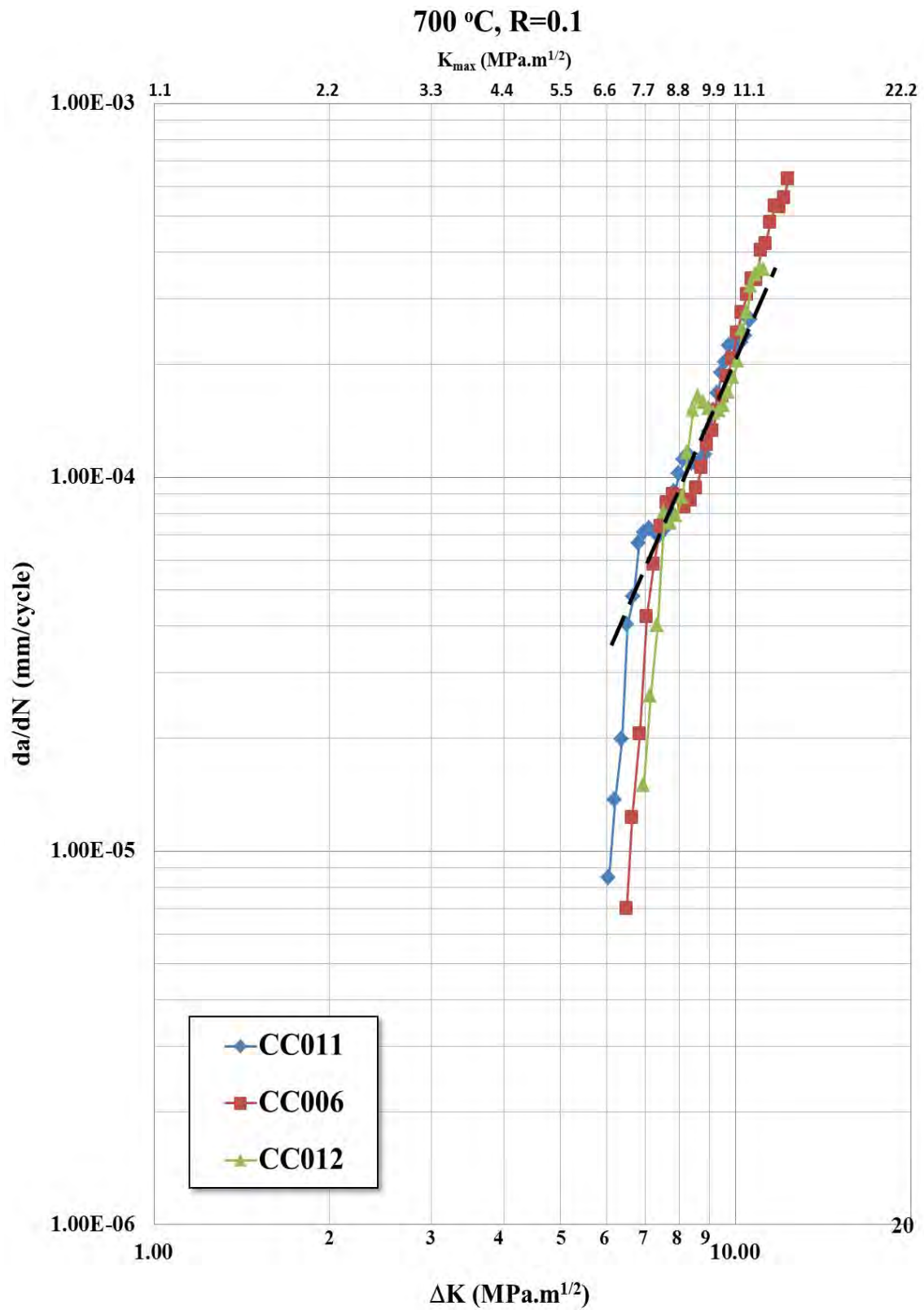


Figure 6.12. Fatigue crack growth resistance curves of Ti-4522XD alloy tested at 700°C with an R ratio of 0.1. The dotted lines is taken as representative of this set of tests.

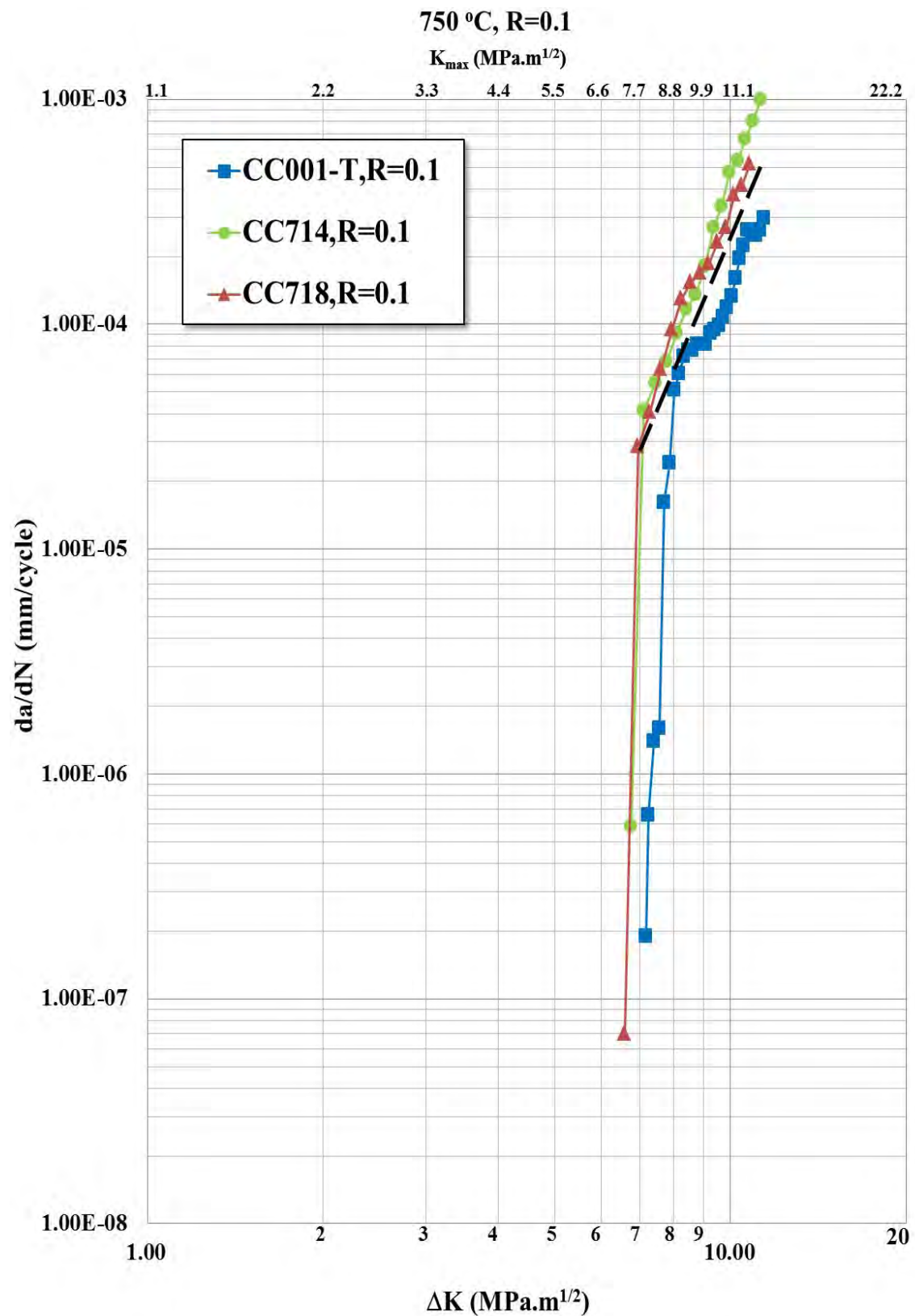


Figure 6.13. Fatigue crack growth resistance curves of Ti-4522XD alloy tested at 750°C with an R ratio of 0.1. The dotted lines is taken as representative of this set of tests.

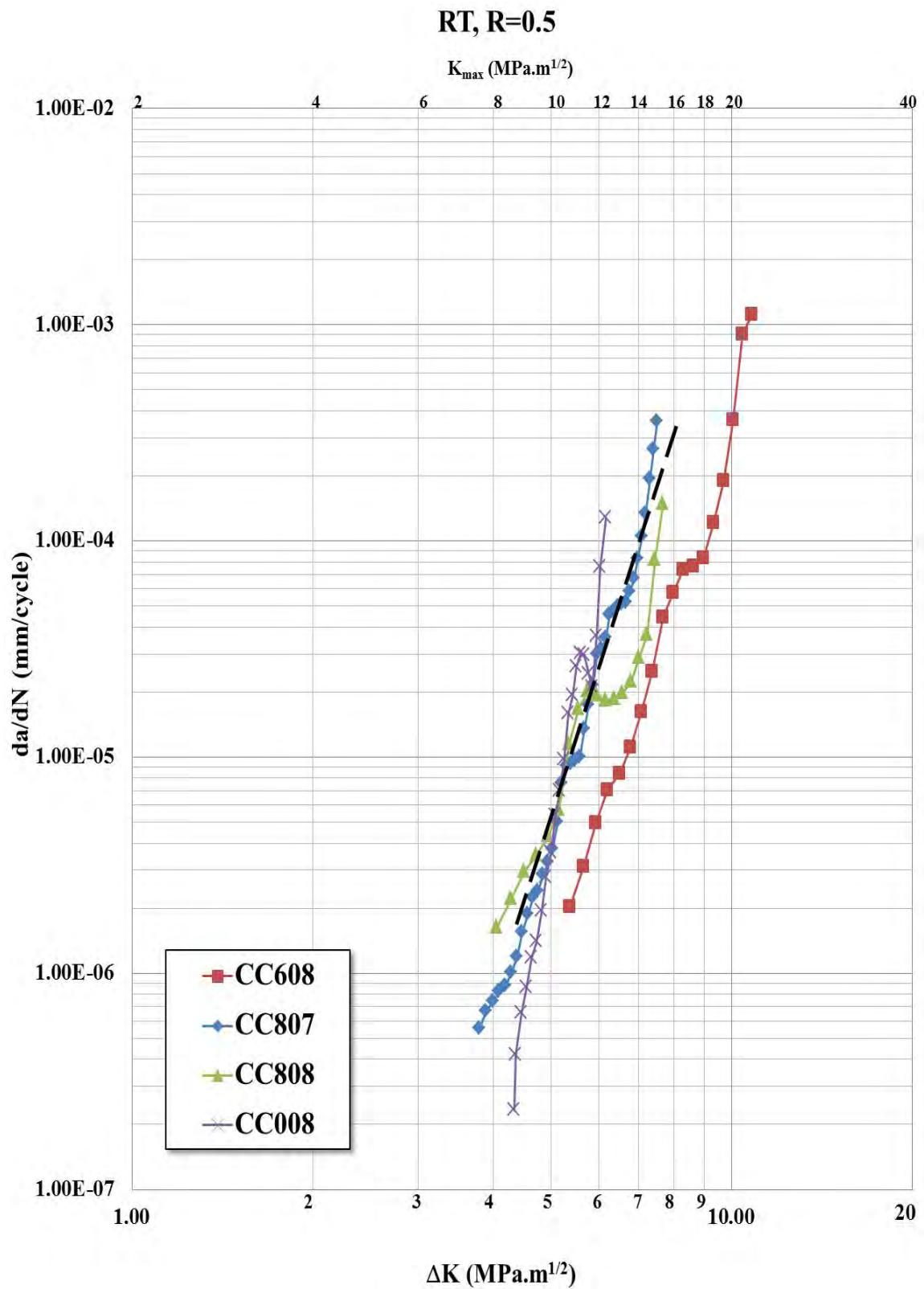


Figure 6.14. Fatigue crack growth resistance curves of Ti-4522XD alloy tested at RT with an R ratio of 0.5. The dotted lines is taken as representative of this set of tests.

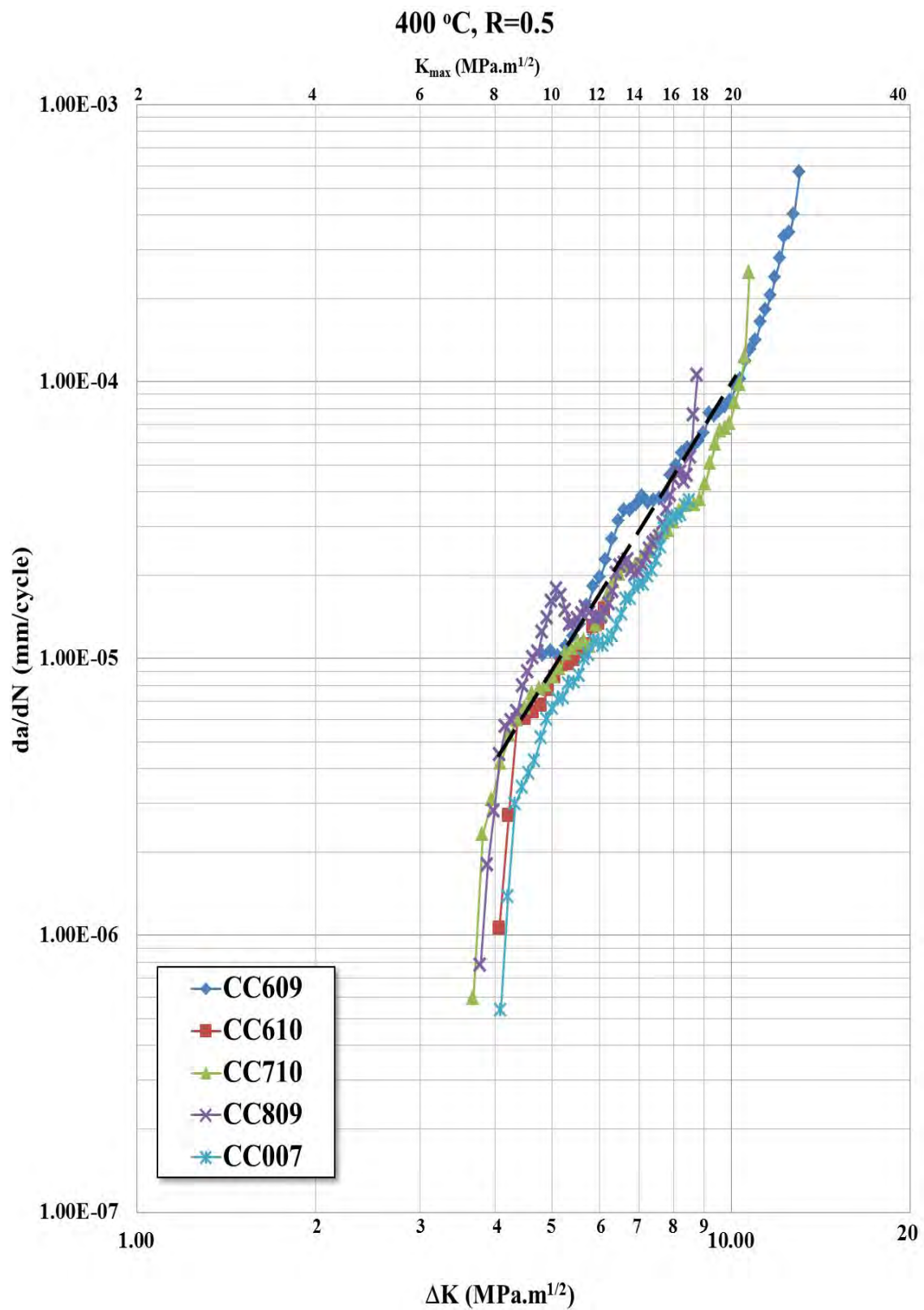


Figure 6.15. Fatigue crack growth resistance curves of Ti-4522XD alloy tested at 400°C with an R ratio of 0.5. The dotted lines is taken as representative of this set of tests.

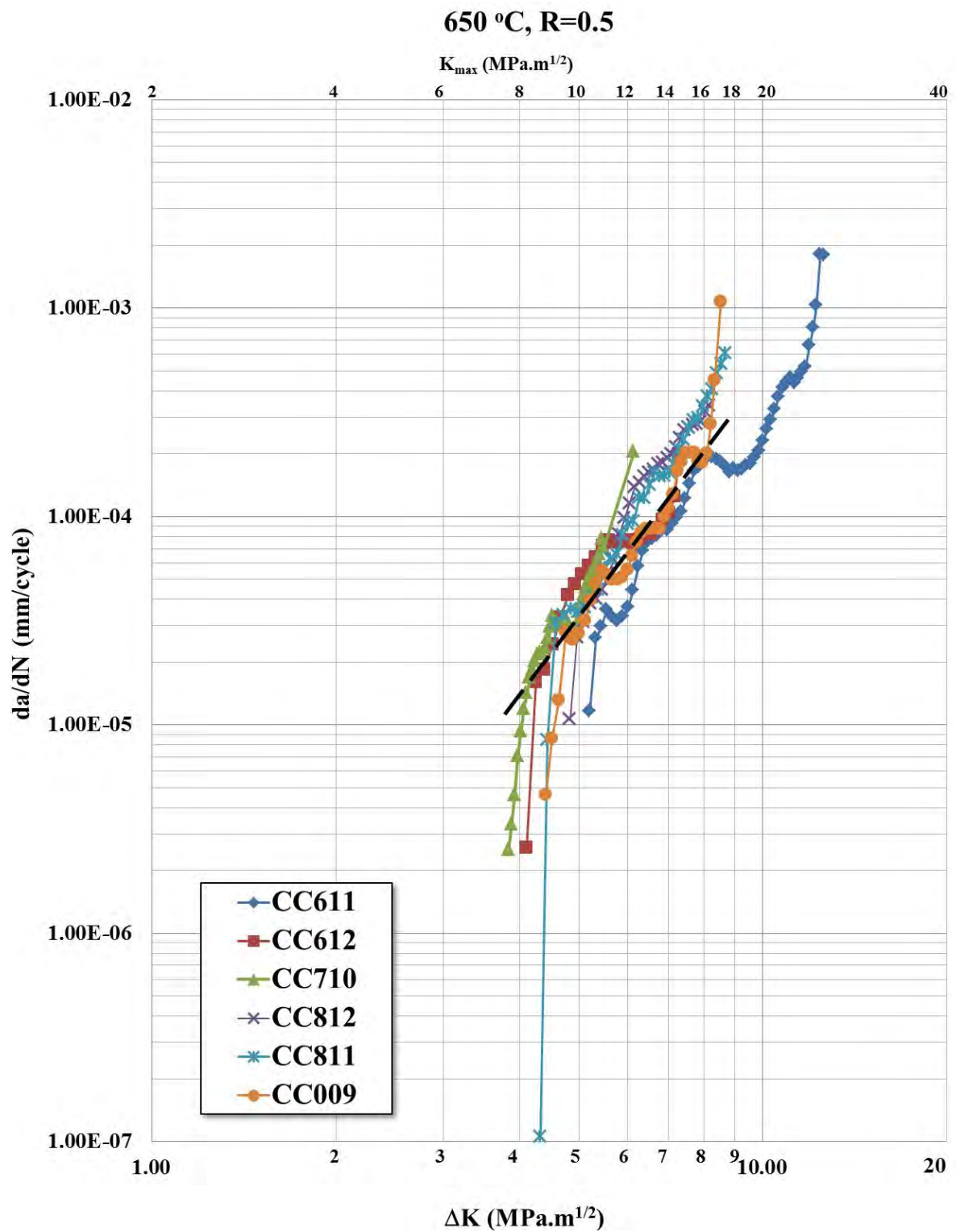


Figure 6.16. Fatigue crack growth resistance curves of Ti-4522XD alloy tested at 650°C with an R ratio of 0.5. The dotted lines is taken as representative of this set of tests.

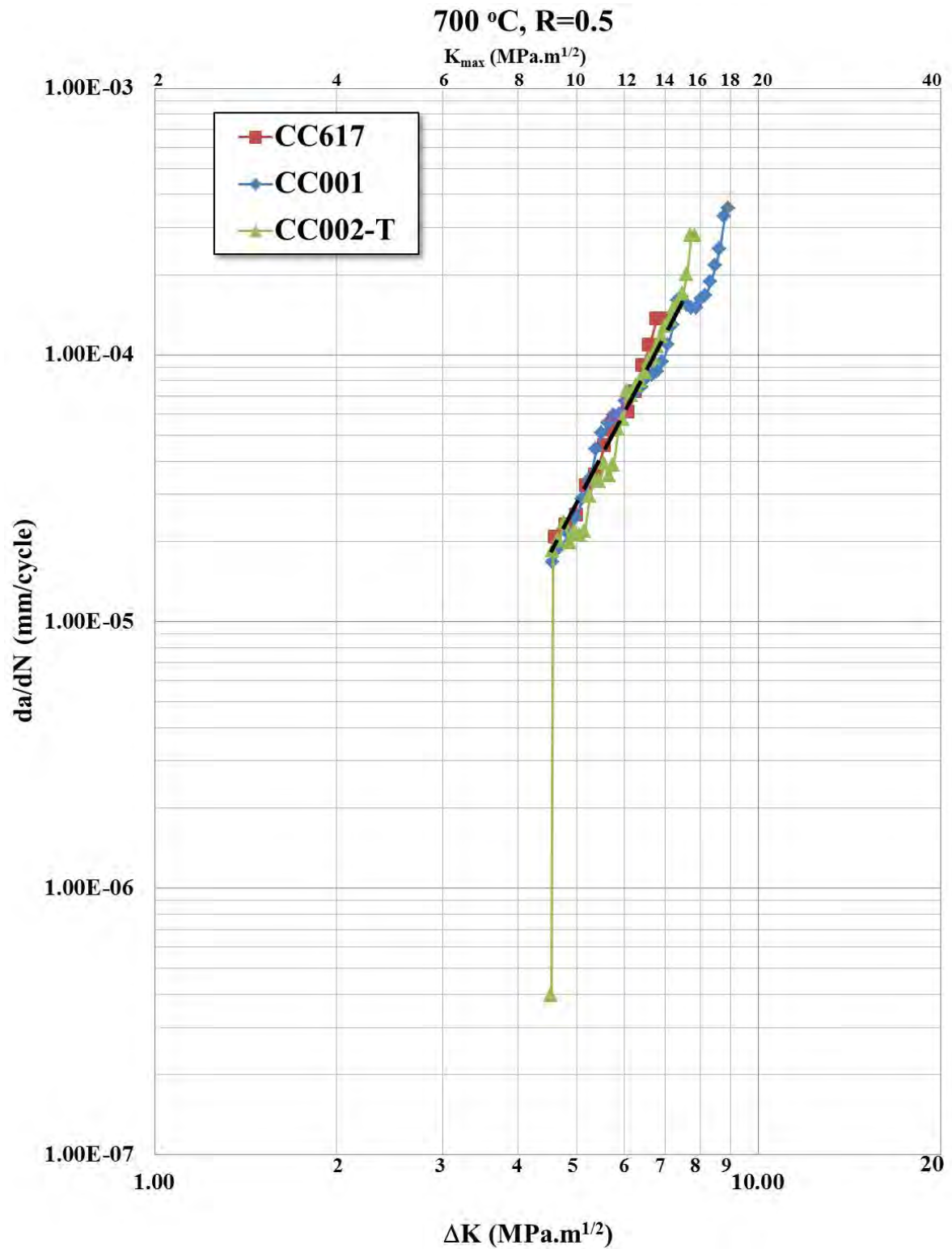


Figure 6.17. Fatigue crack growth resistance curves of Ti-4522XD alloy tested at 700°C with an R ratio of 0.5. The dotted lines is taken as representative of this set of tests.

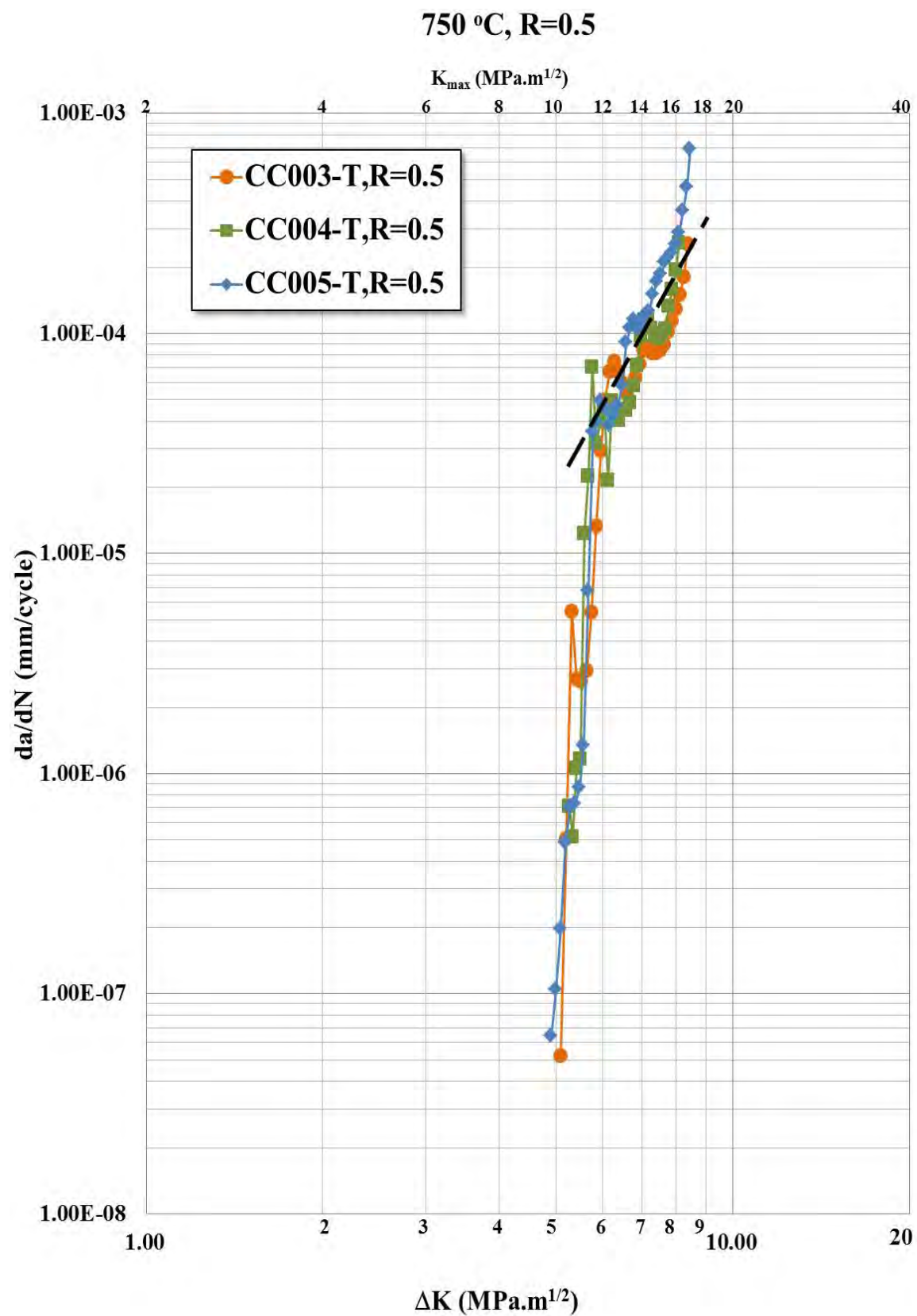


Figure 6.18. Fatigue crack growth resistance curves of Ti-4522XD alloy tested at 750°C with an R ratio of 0.5. The dotted lines is taken as representative of this set of tests.

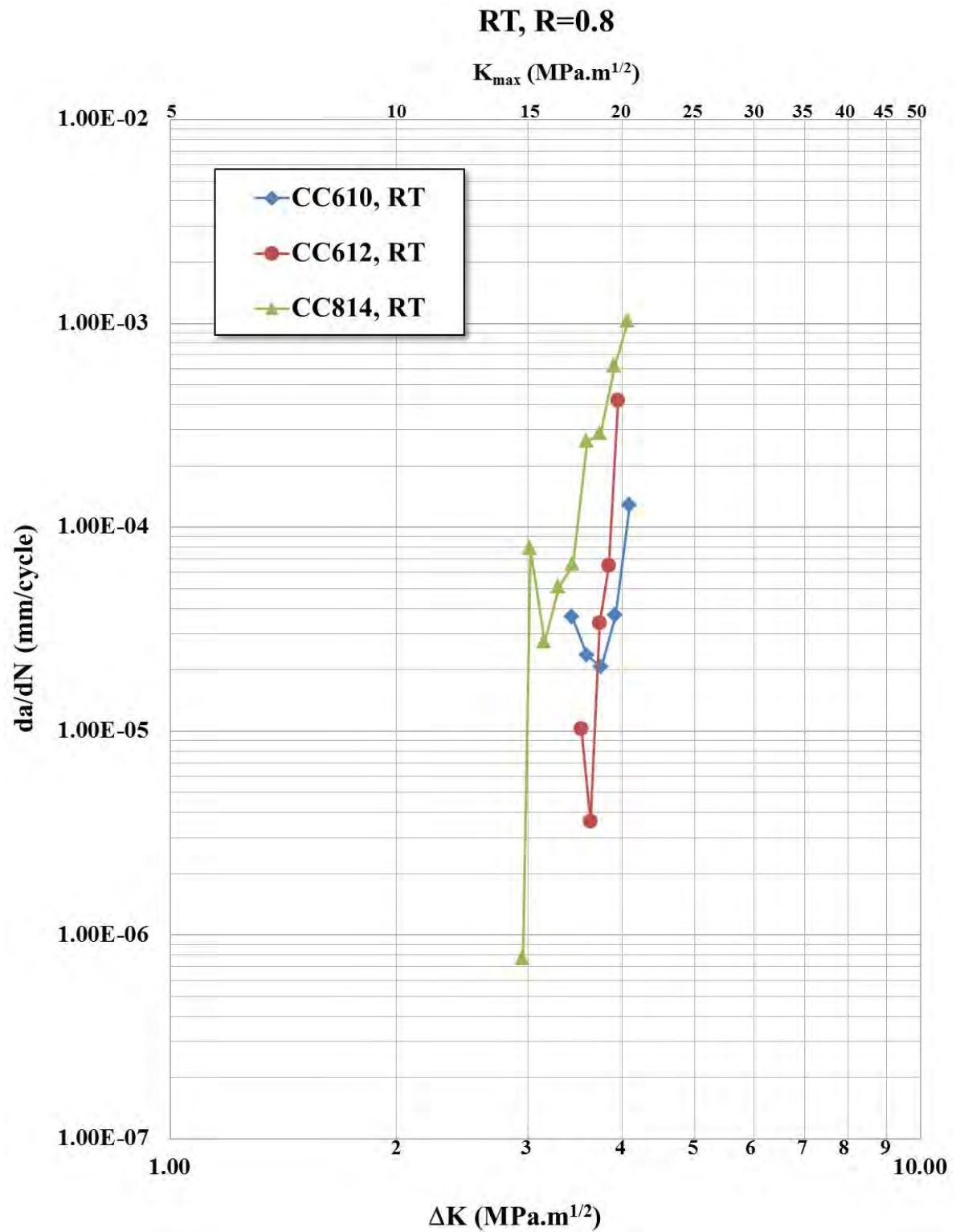


Figure 6.19. Fatigue crack growth resistance curves of Ti-4522XD alloy tested at RT with an R ratio of 0.8.

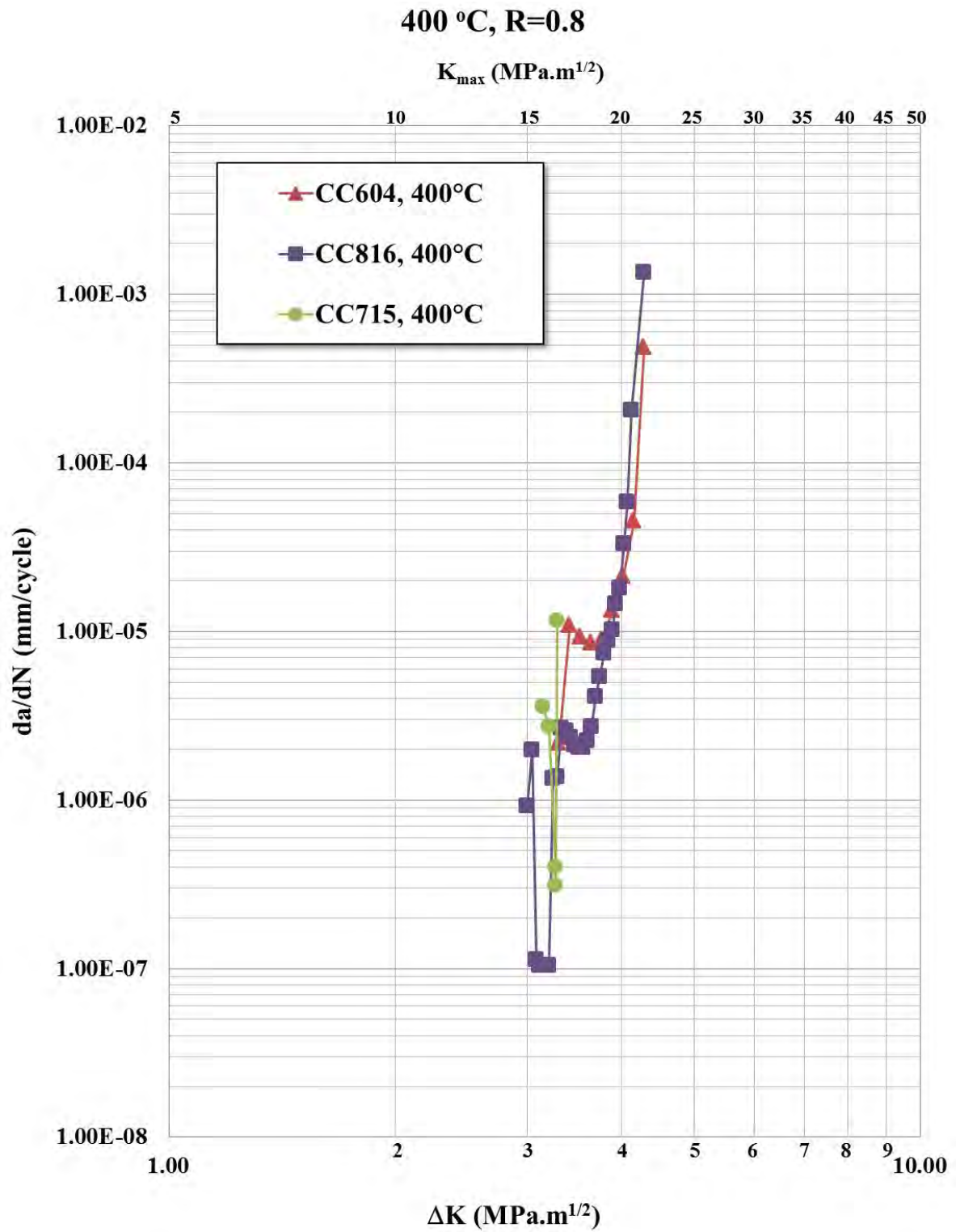


Figure 6.20. Fatigue crack growth resistance curves of Ti-4522XD alloy tested at 400°C with an R ratio of 0.8.

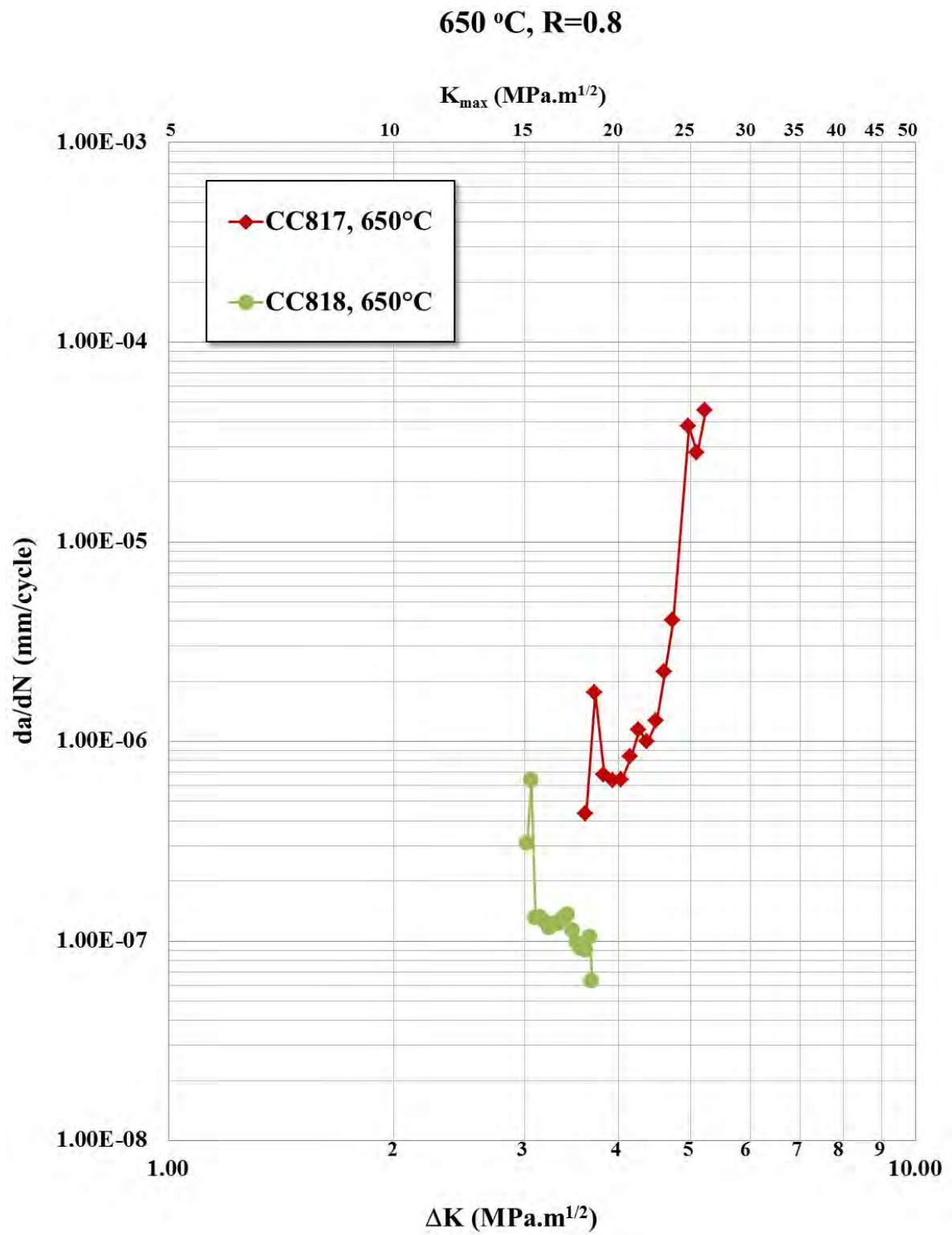


Figure 6.21. Fatigue crack growth resistance curves of Ti-4522XD alloy tested at 650°C with an R ratio of 0.8

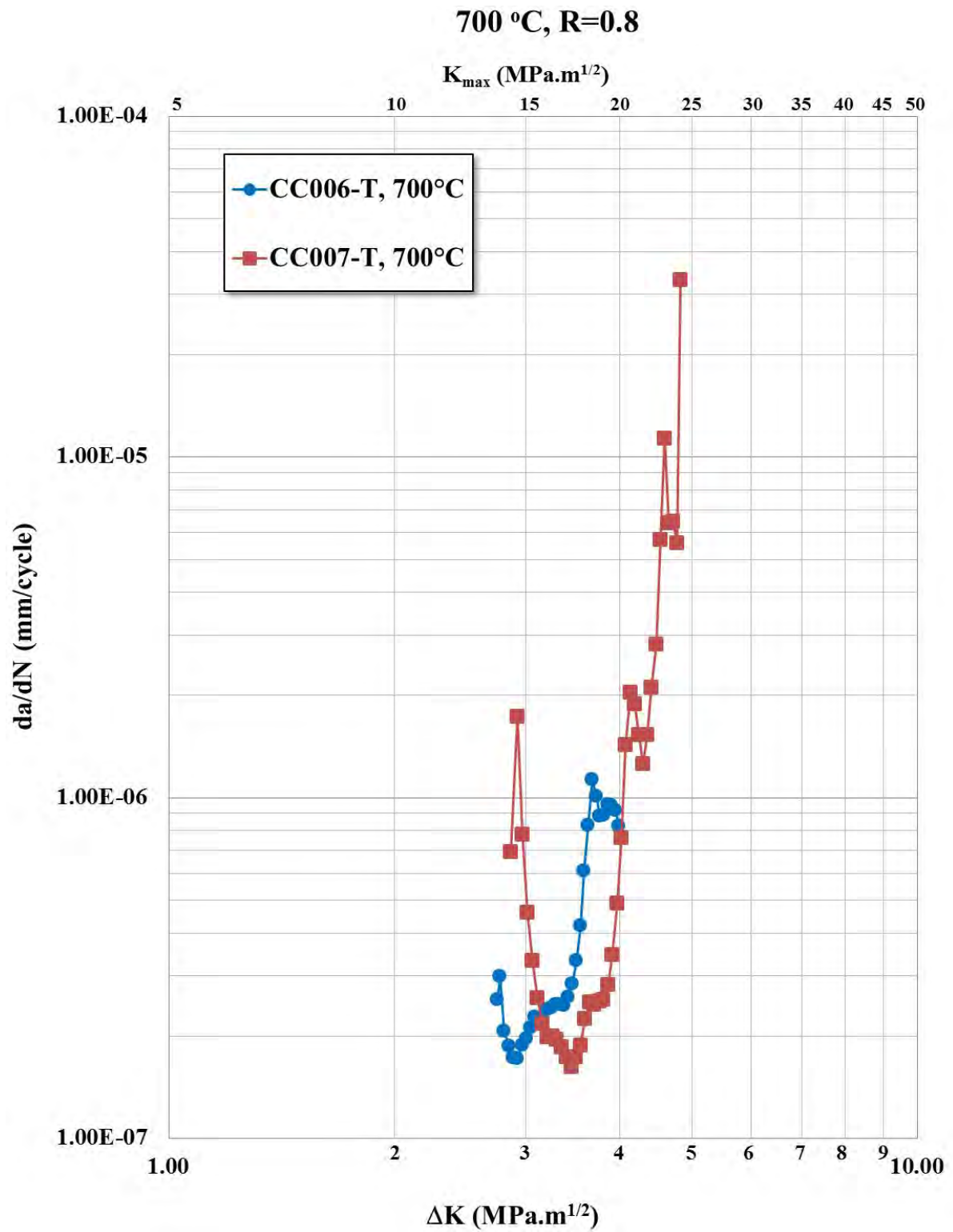


Figure 6.22. Fatigue crack growth resistance curves of Ti-4522XD alloy tested at 700°C with an R ratio of 0.8

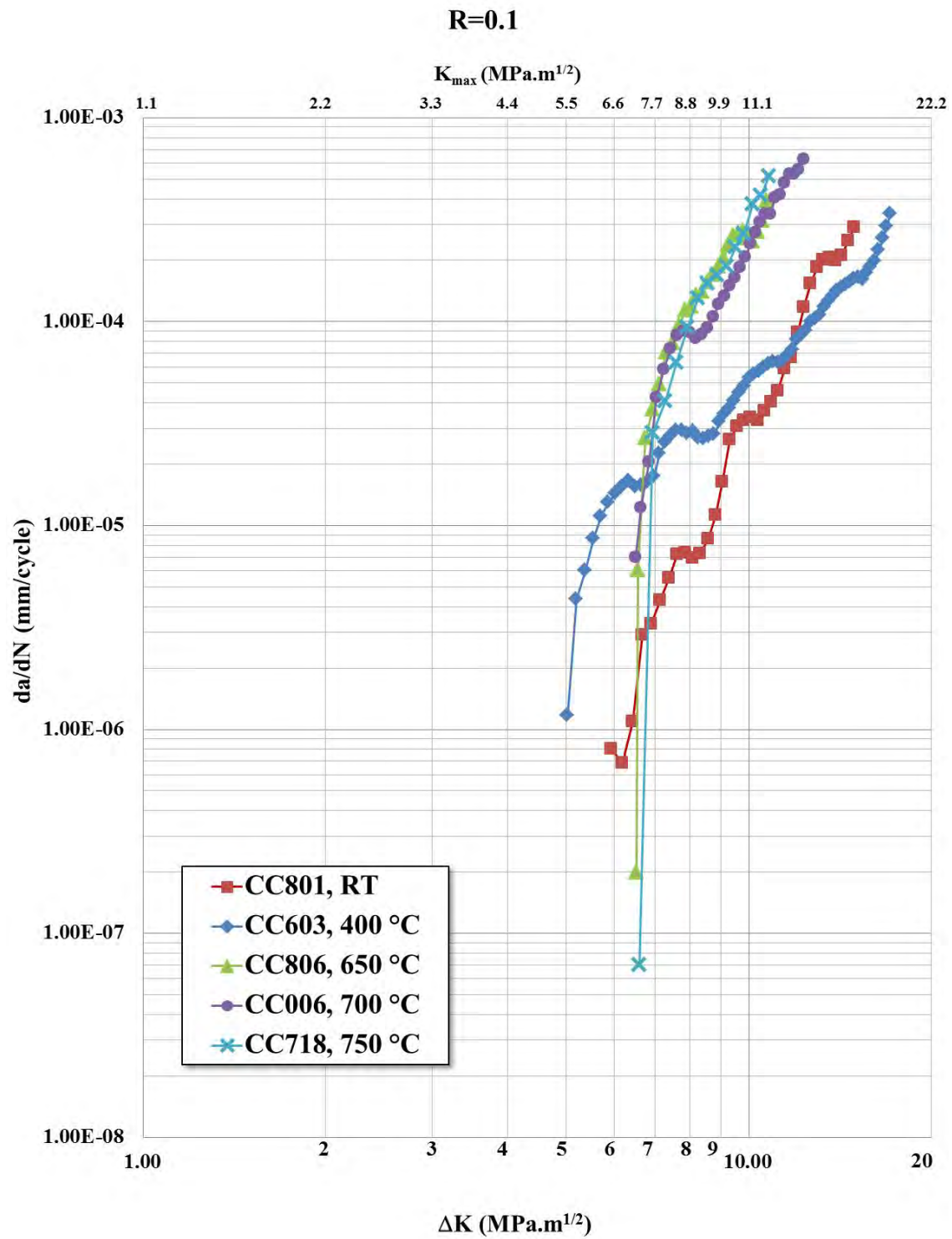


Figure 6.23. Fatigue crack growth resistance curves of Ti-4522XD alloy tested at an R ratio of 0.1 and at temperatures of RT, 400, 650, 700 and 750 °C

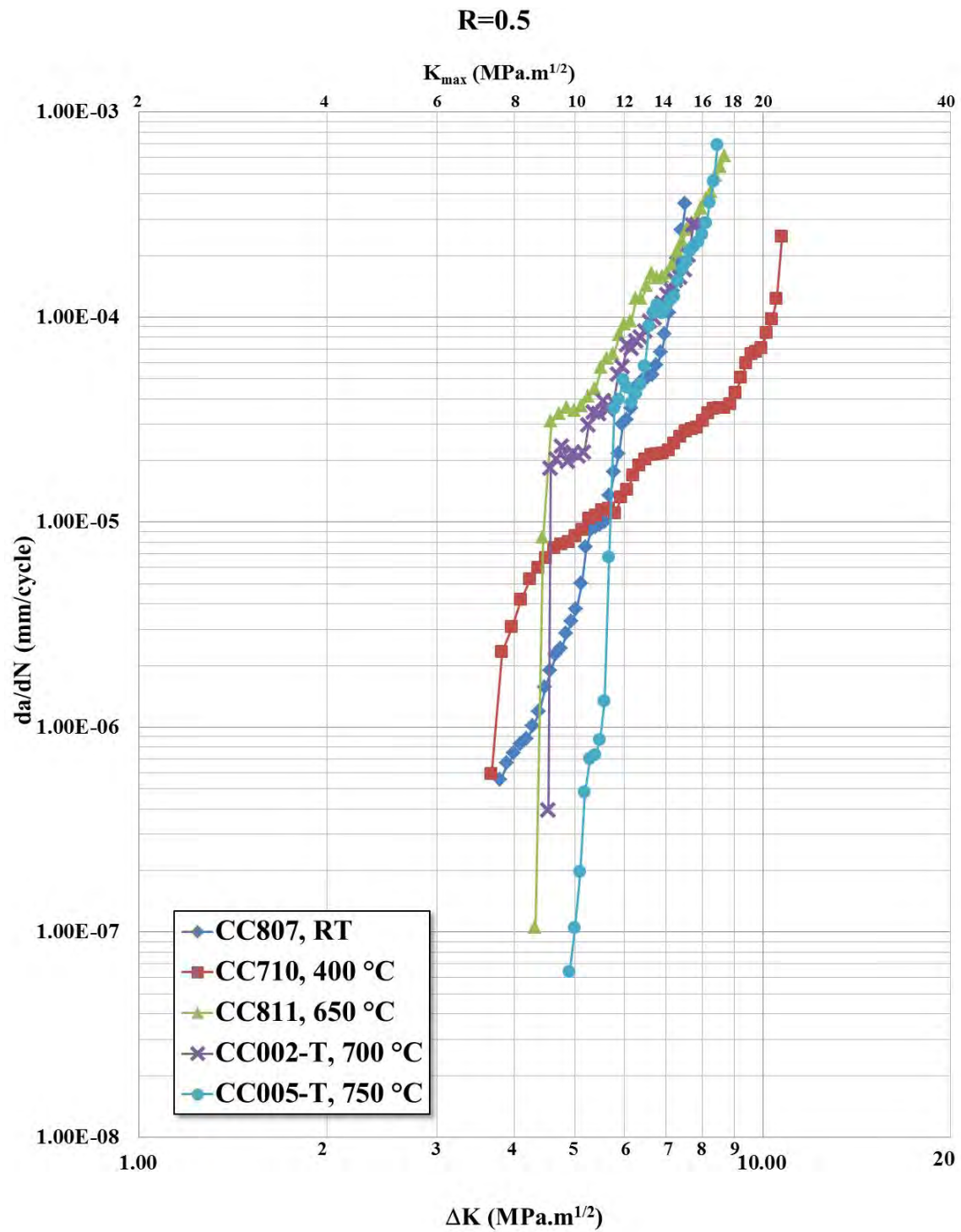


Figure 6.24. Fatigue crack growth resistance curves of Ti-4522XD alloy tested at an R ratio of 0.5 and at temperatures of RT, 400, 650, 700 and 750 °C

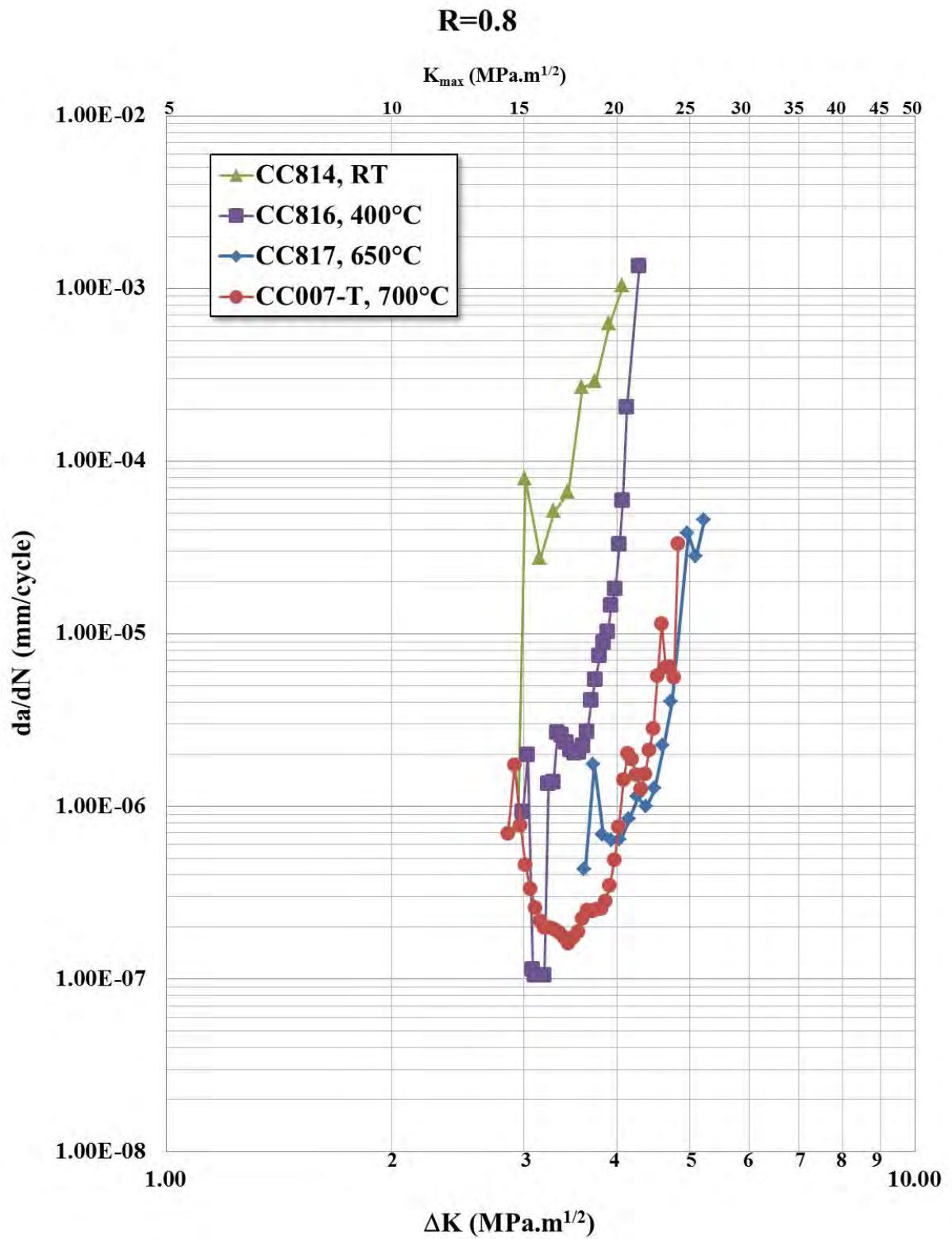


Figure 6.25. Fatigue crack growth resistance curves of Ti-4522XD alloy tested at an R ratio of 0.8 and at temperatures of RT, 400, 650, 700 and 750 °C

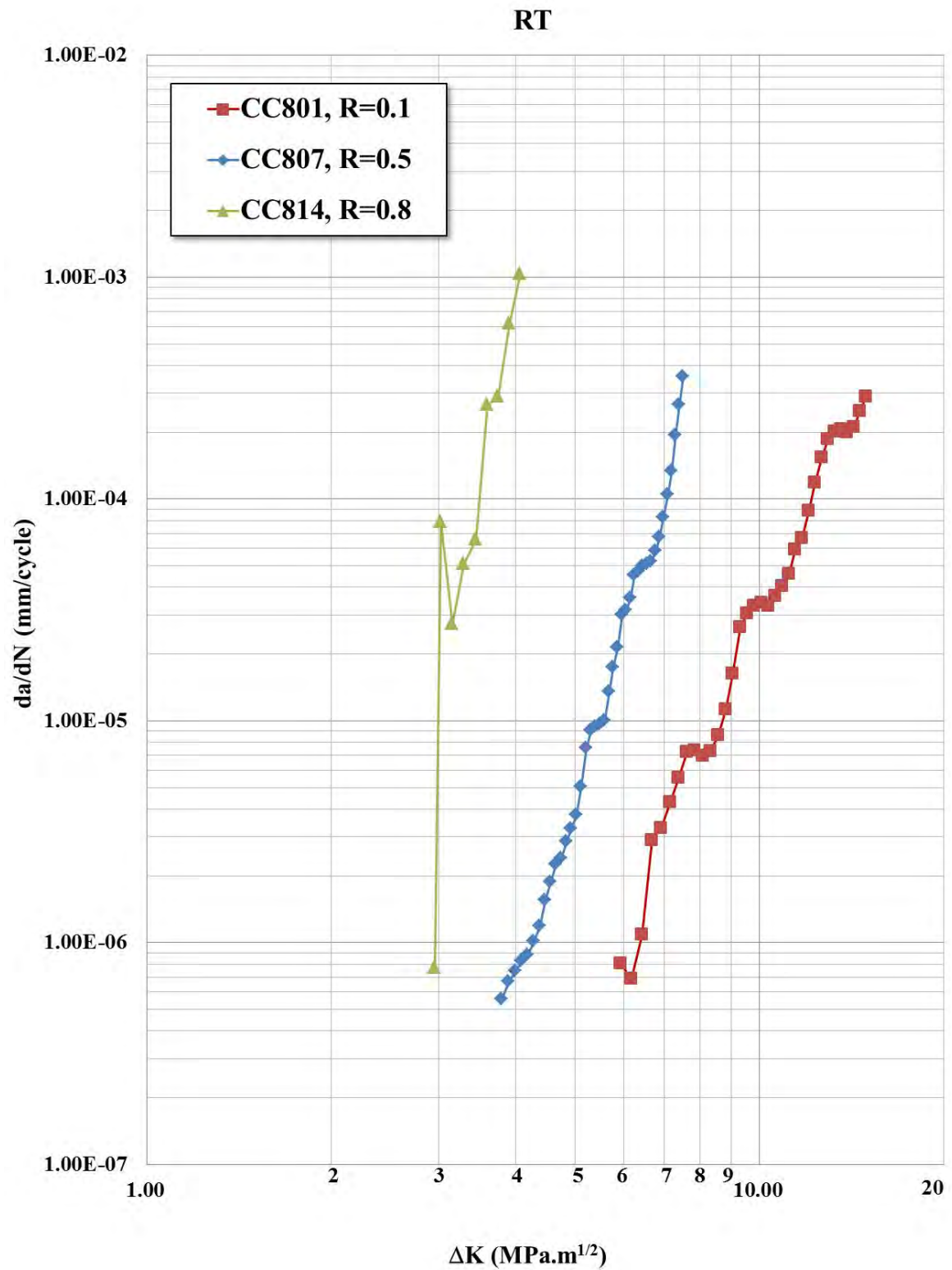


Figure 6.26. Fatigue crack growth resistance curves of Ti-4522XD alloy tested at RT and at R=0.1, 0.5 and 0.8

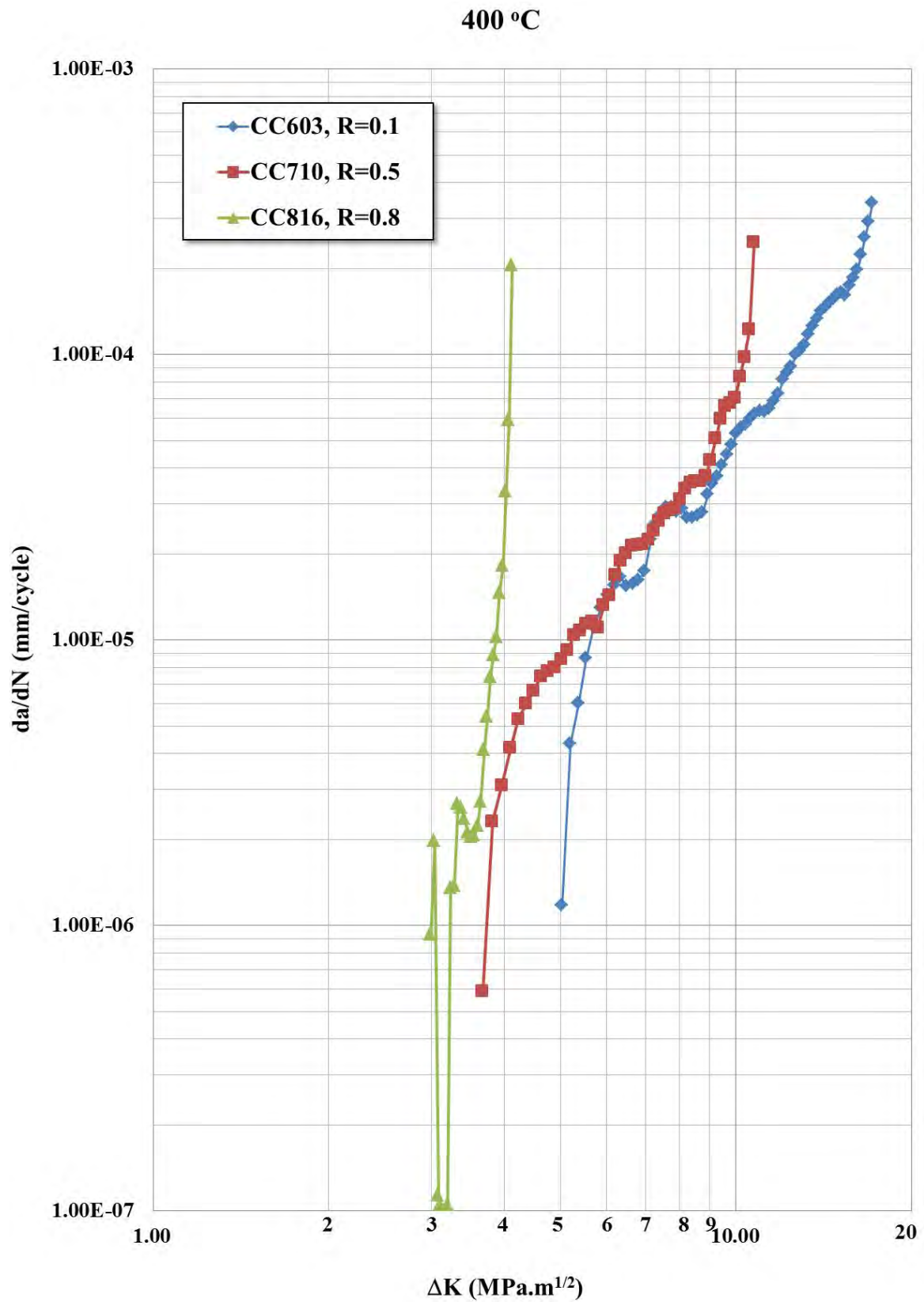


Figure 6.27. Fatigue crack growth resistance curves of Ti-4522XD alloy tested at 400°C and at R=0.1, 0.5 and 0.8

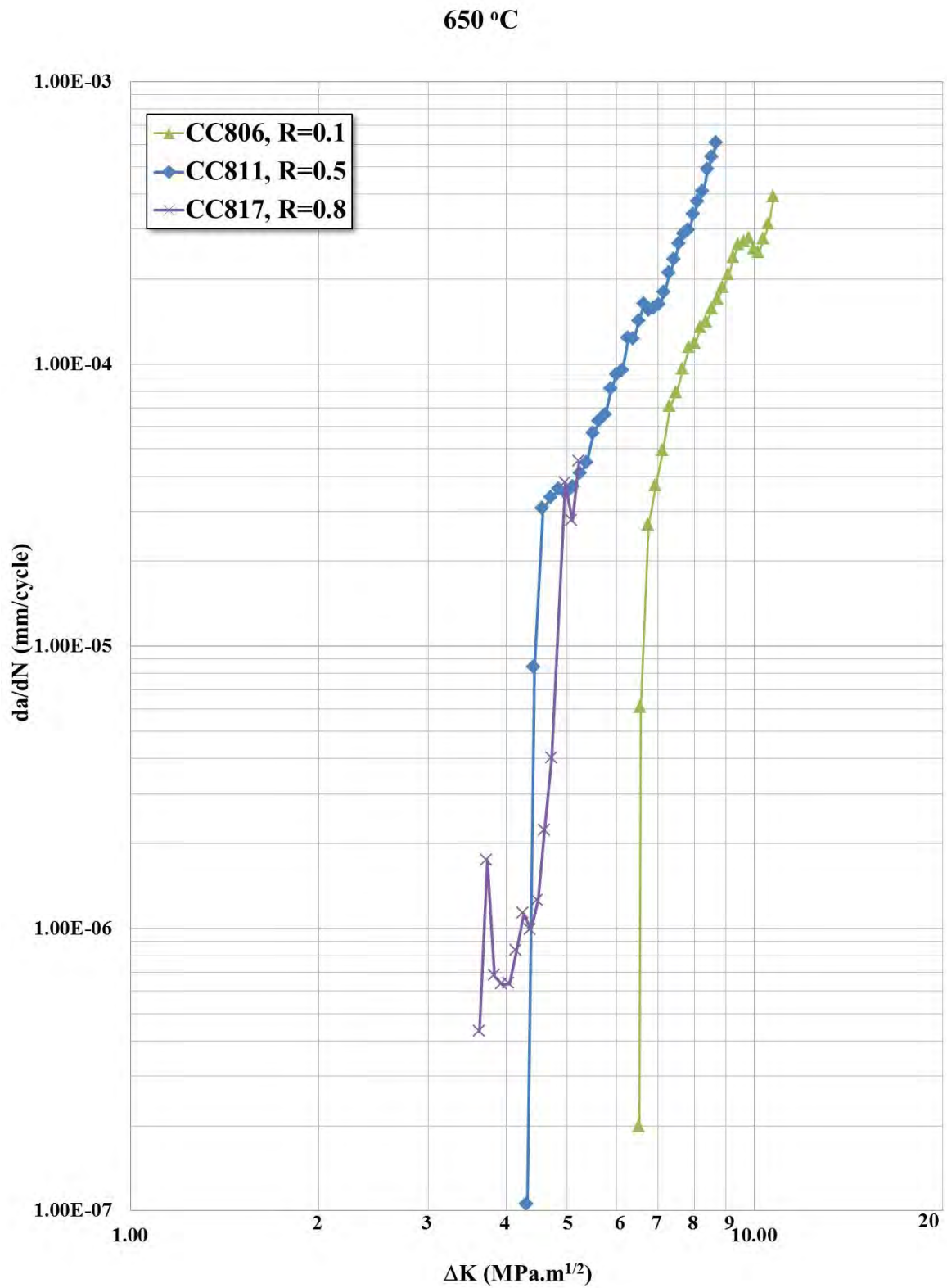


Figure 6.28. Fatigue crack growth resistance curves of Ti-4522XD alloy tested at 650°C and at R=0.1, 0.5 and 0.8

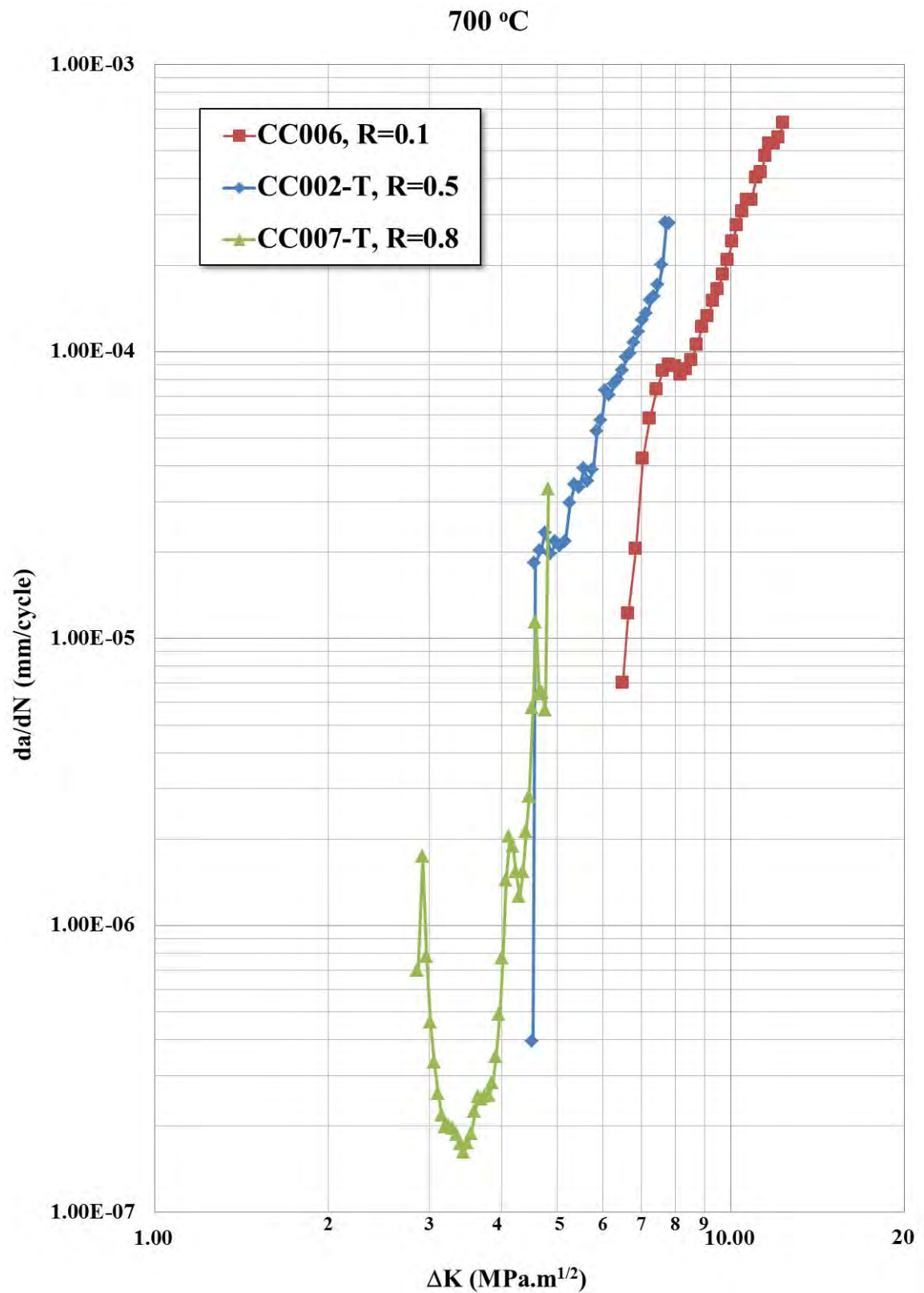


Figure 6.29. Fatigue crack growth resistance curves of Ti-4522XD alloy tested at 700°C and at R=0.1, 0.5 and 0.8

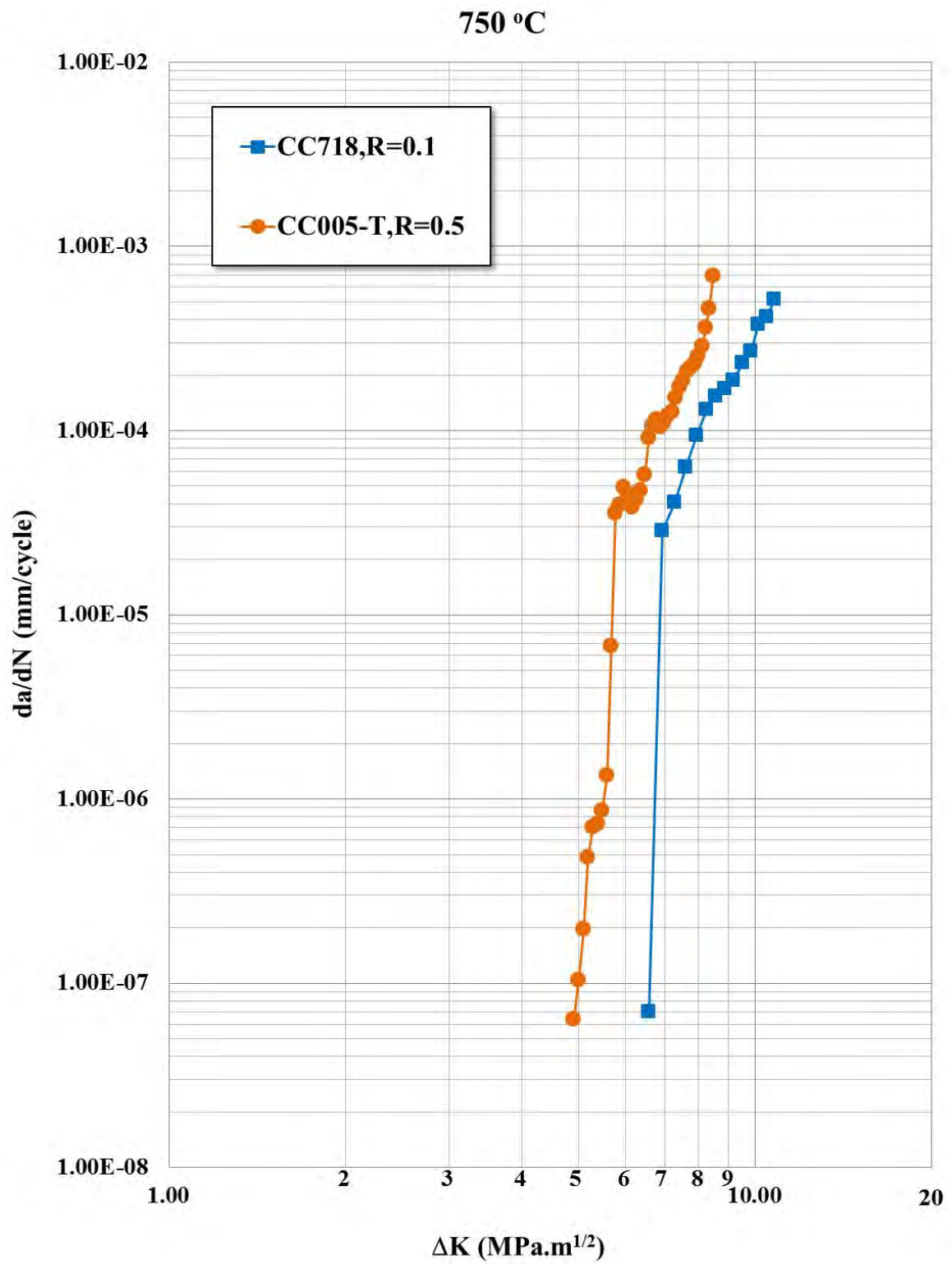


Figure 6.30. Fatigue crack growth resistance curves of Ti-4522XD alloy tested at 750°C and at R=0.1, 0.5 and 0.8

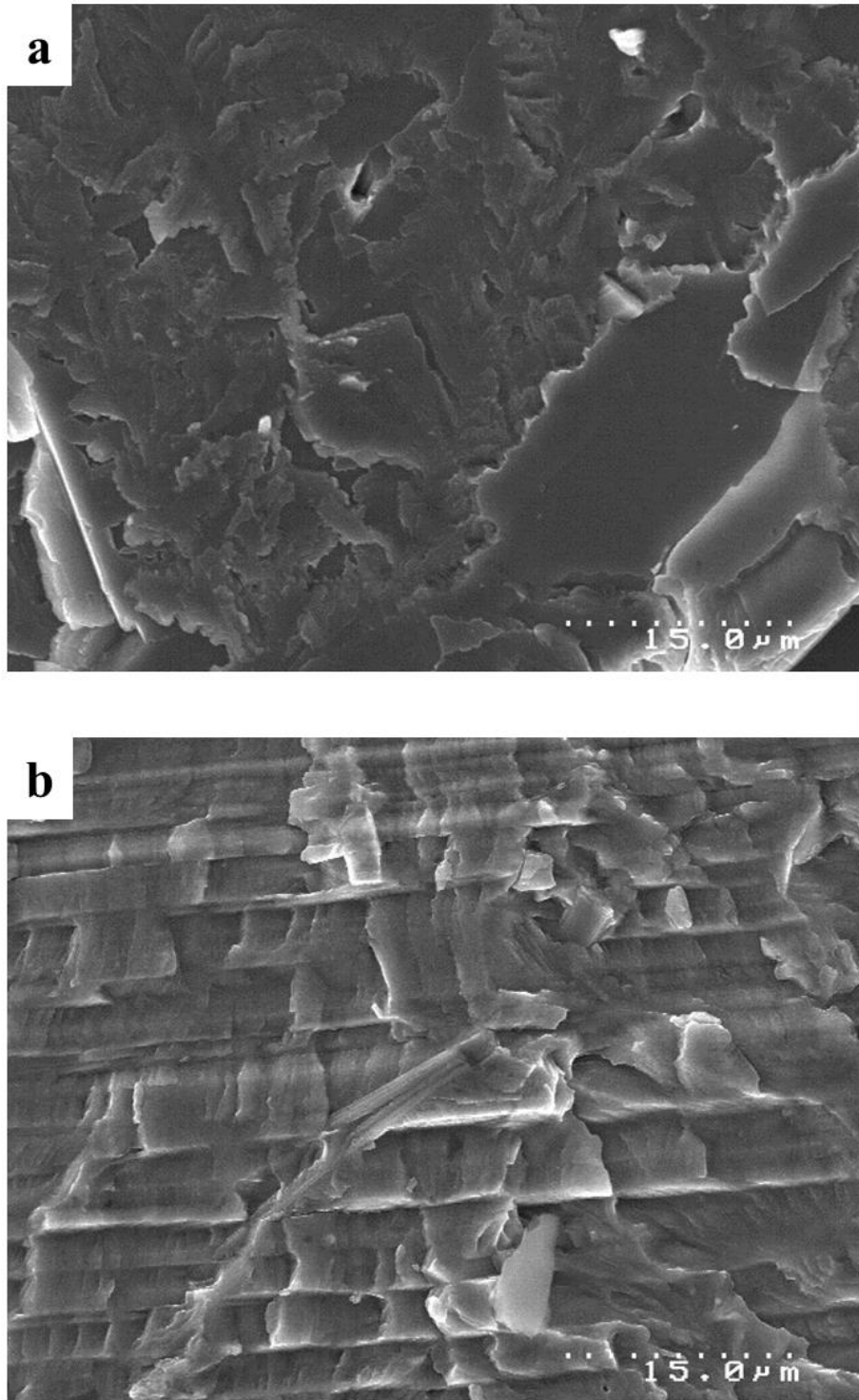


Figure 6.31. Two main fracture modes caused by fatigue loading in lamellar Ti-4522XD alloy: (a) interlamellar fracture and (b) translamellar fracture

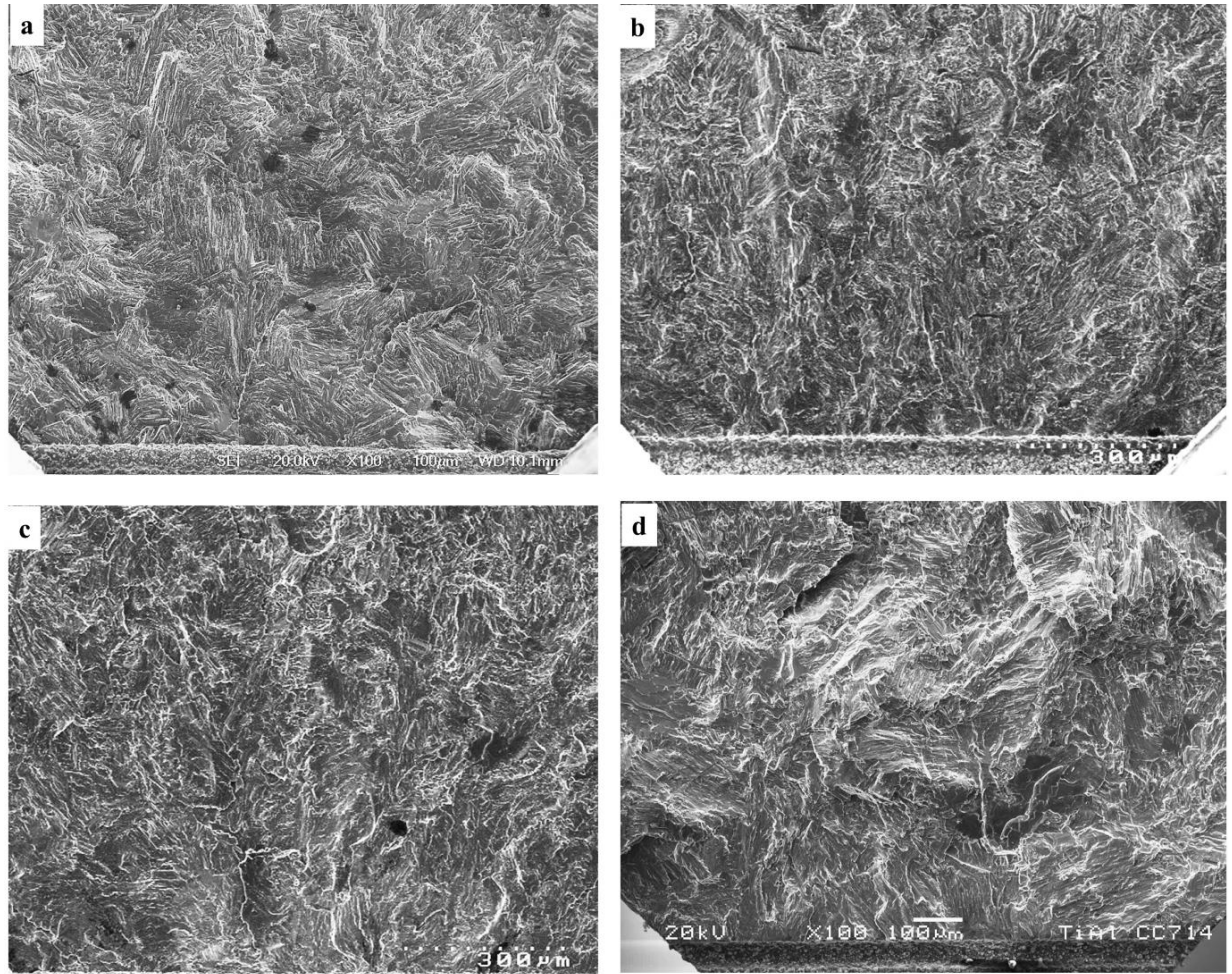


Figure 6.32. The fracture surfaces images of specimens tested at an R ratio of 0.1 at (a) RT, (b) 400 °C, (c) 650 °C and (d) 750 °C

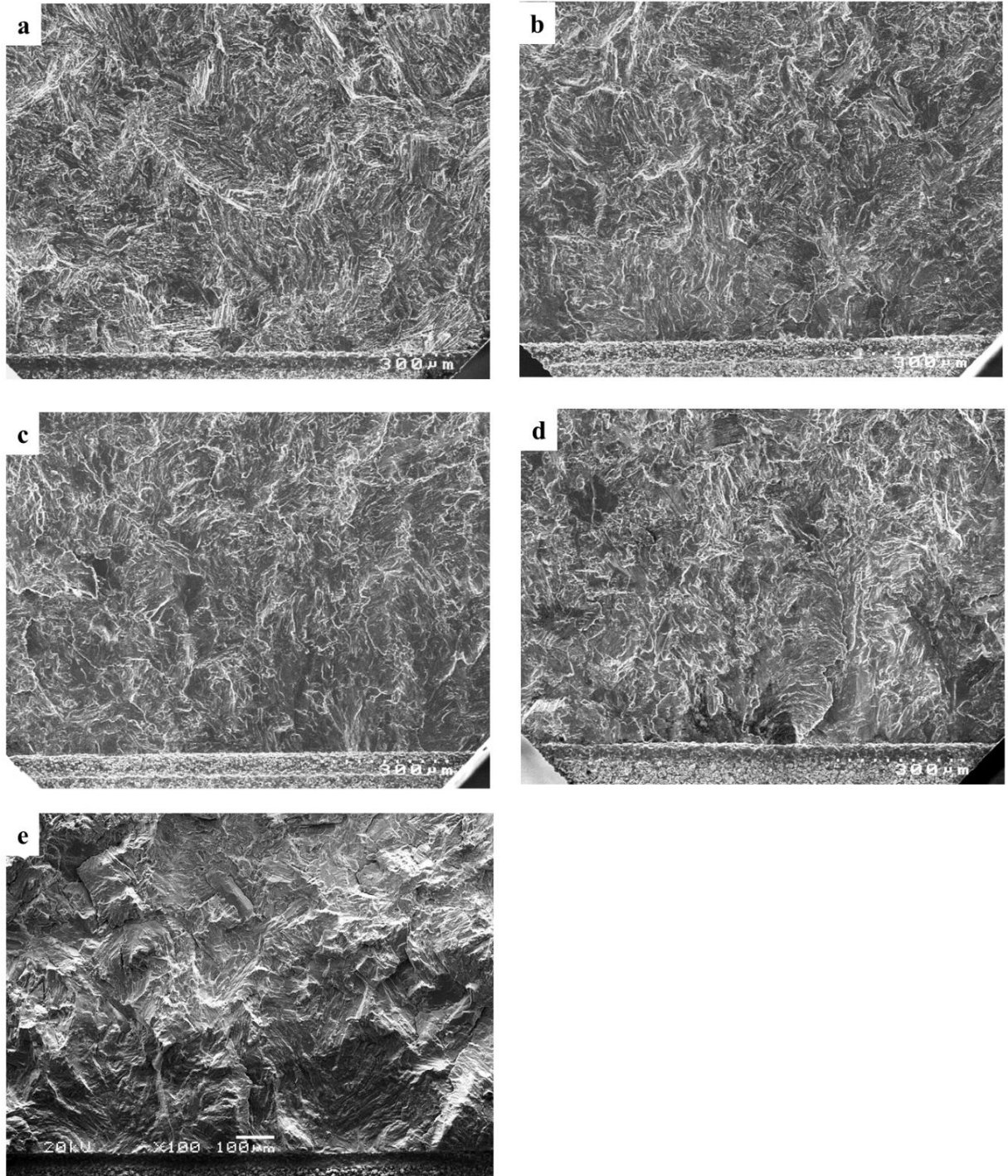


Figure 6.33. The fracture surfaces images of specimens tested at an R ratio of 0.5 at (a) RT, (b) 400 °C, (c) 650 °C, (d) 700 °C and (e) 750 °C

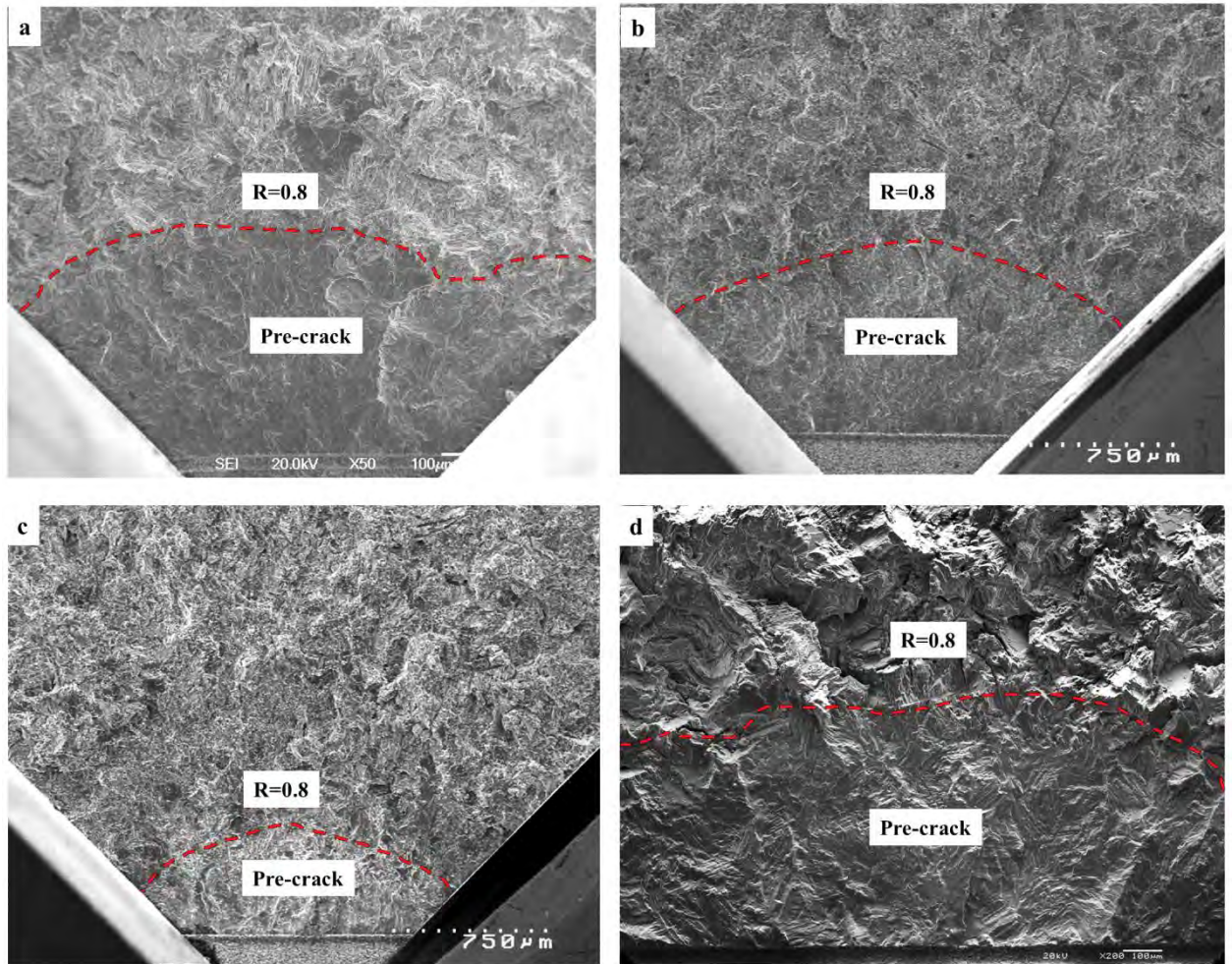


Figure 6.34. The fracture surfaces images of specimens tested at an R ratio of 0.8 at (a) RT, (b) 400 °C, (c) 650 °C and (d) 700 °C. The pre-crack regions and fatigue region obtained at R=0.8 are divided by the black dotted line.

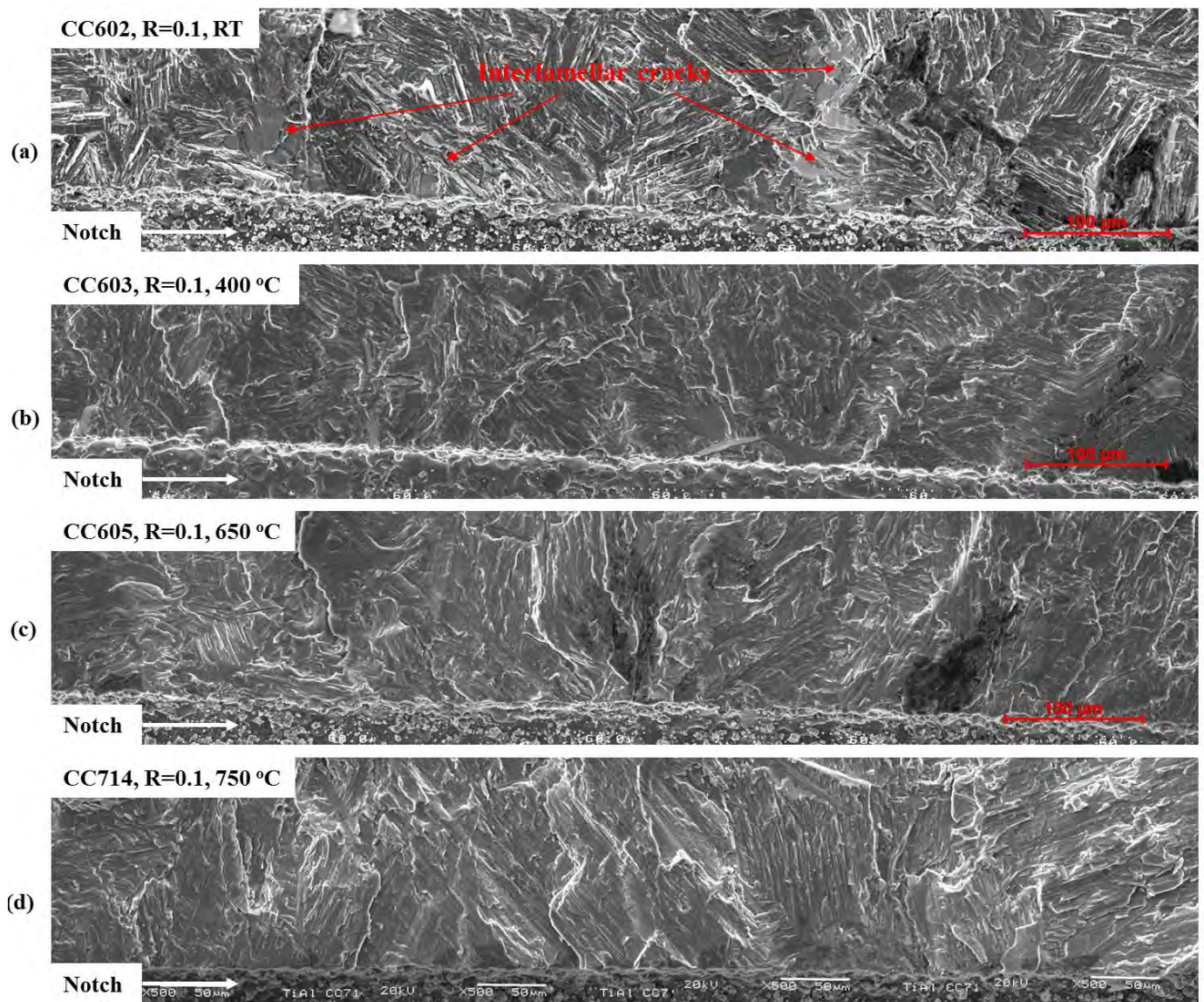


Figure 6.35. Comparison of fracture surfaces which are taken behind notch front at a depth of about 0.1 mm. The specimens were tested with an R ratio of 0.1 and at (a) RT, (b) 400°C, (c) 650 °C and (d) 750 °C

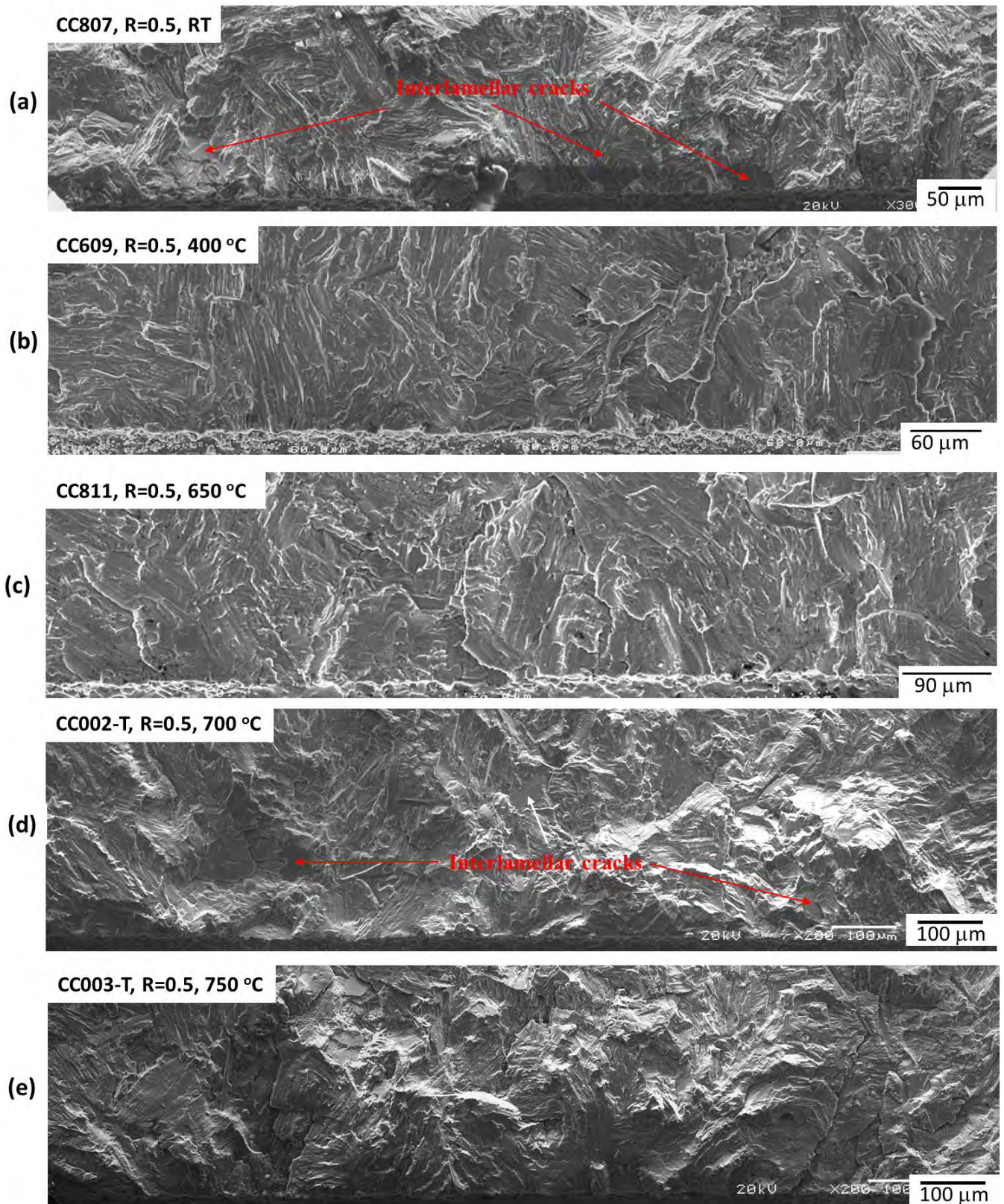
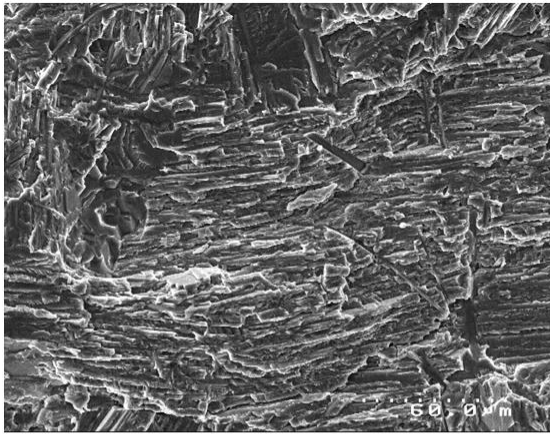


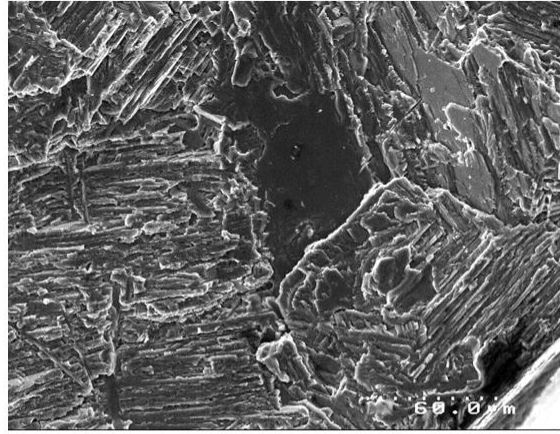
Figure 6.36. Comparison of fracture surfaces which are taken behind notch front at a depth of about 0.1 mm. The specimens were tested with an R ratio of 0.1 and at (a) RT, (b) 400 $^{\circ}\text{C}$, (c) 650 $^{\circ}\text{C}$, (d) 700 $^{\circ}\text{C}$ and (e) 750 $^{\circ}\text{C}$

Translamellar fracture

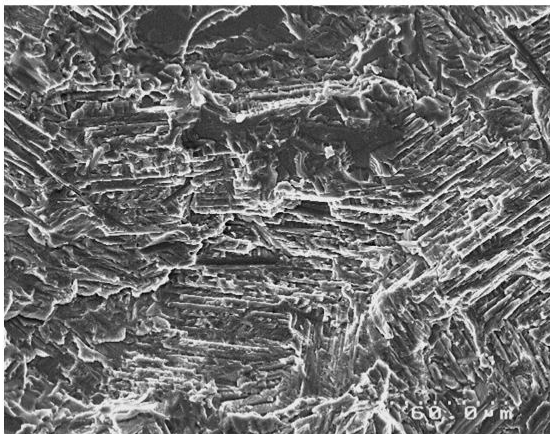


(a) RT, a=1.2mm

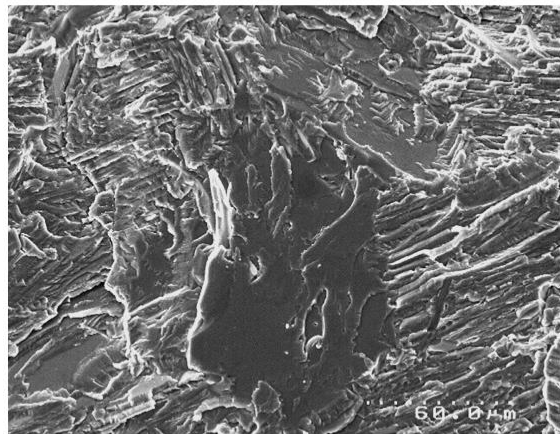
interlamellar fracture



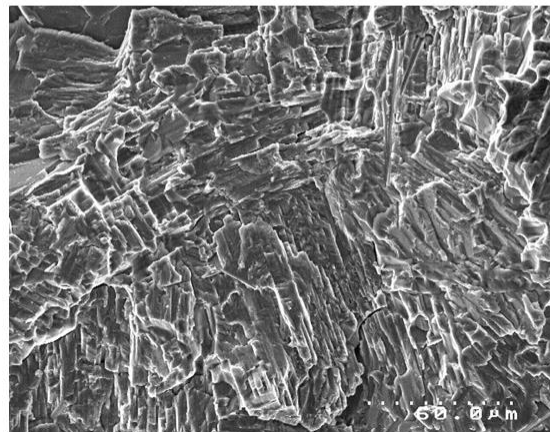
(b) RT, a=1.2 mm



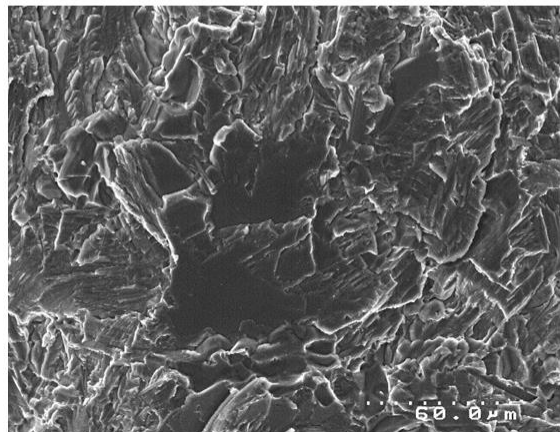
(c) 400 °C, a=1.6 mm



(d) 400 °C, a=1.6 mm



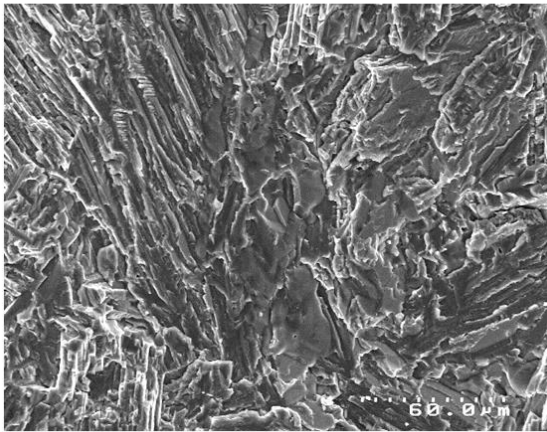
(e) 650 °C, a=1.6 mm



(f) 650 °C, a=1.6 mm

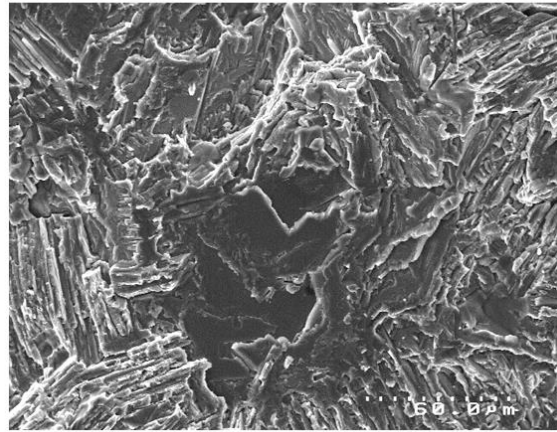
Figure 6.37. Fracture surface images taken at various temperatures at $R=0.1$ for a constant ΔK value $\approx 9 \text{ MPa.m}^{1/2}$

Translamellar fracture

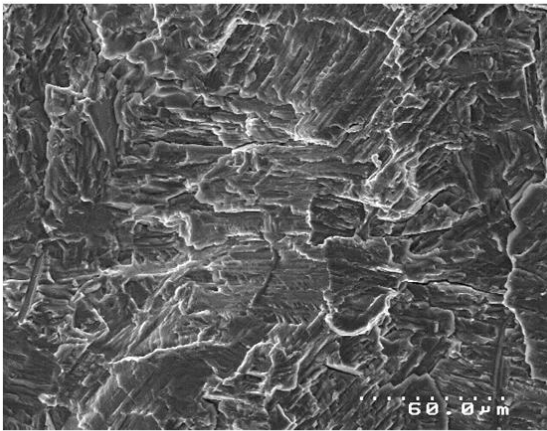


(a) RT, a=1.3mm

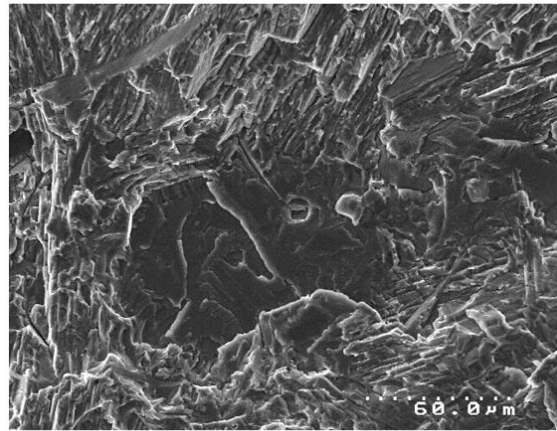
interlamellar fracture



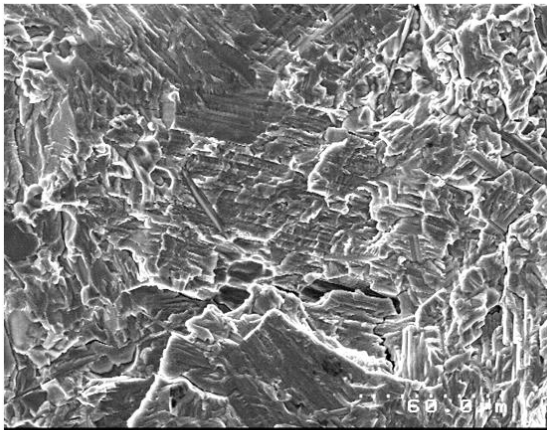
(b) RT, a=1.3 mm



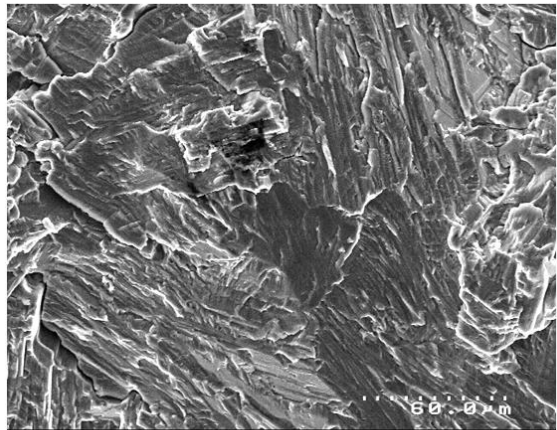
(c) 400 °C, a=1.4 mm



(d) 400 °C, a=1.4 mm



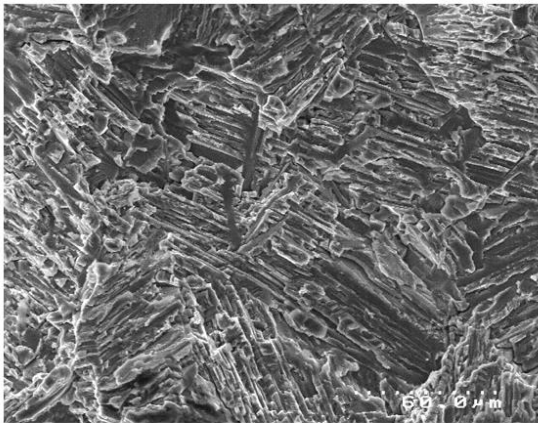
(e) 650 °C, a=1.4 mm



(f) 650 °C, a=1.4 mm

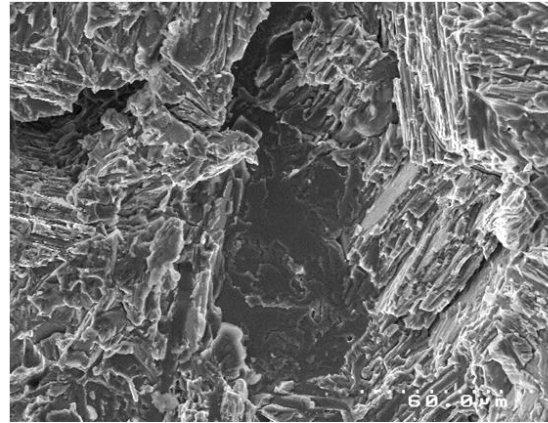
Figure 6.38. Fracture surface images taken at various temperatures at $R=0.5$ for a constant ΔK value $\approx 6.5 \text{ MPa}\cdot\text{m}^{1/2}$

Translamellar fracture

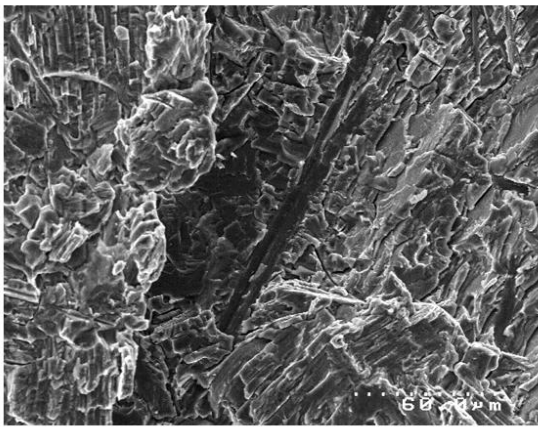


(a) RT, a=1.5 mm

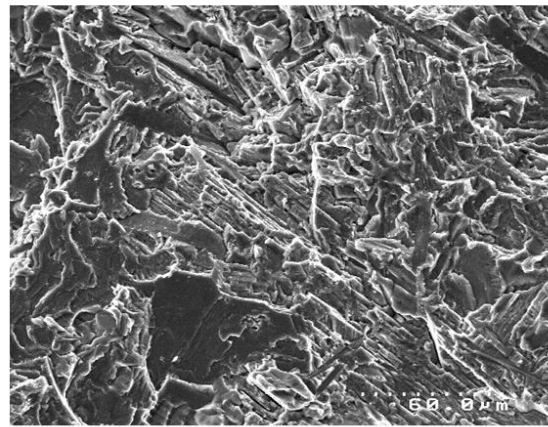
interlamellar fracture



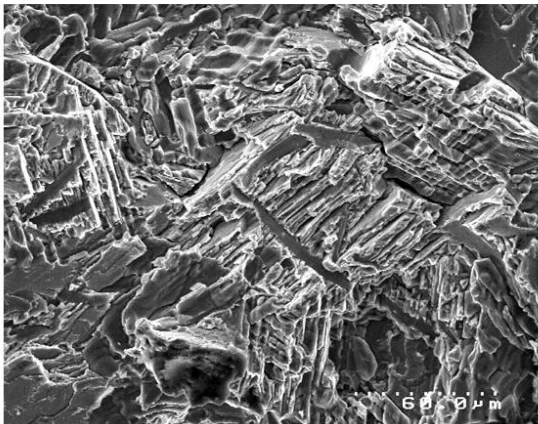
(b) RT, a=1.5 mm



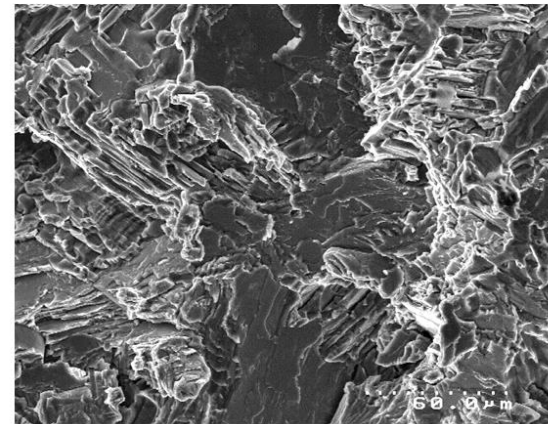
(c) 400 °C, a=1.8 mm



(d) 400 °C, a=1.8 mm



(e) 650 °C, a=1.3 mm



(f) 650 °C, a=1.3 mm

Figure 6.39. Fracture surface images taken at various temperatures at $R=0.8$ for a constant ΔK value $\approx 3.6 \text{ MPa}\cdot\text{m}^{1/2}$

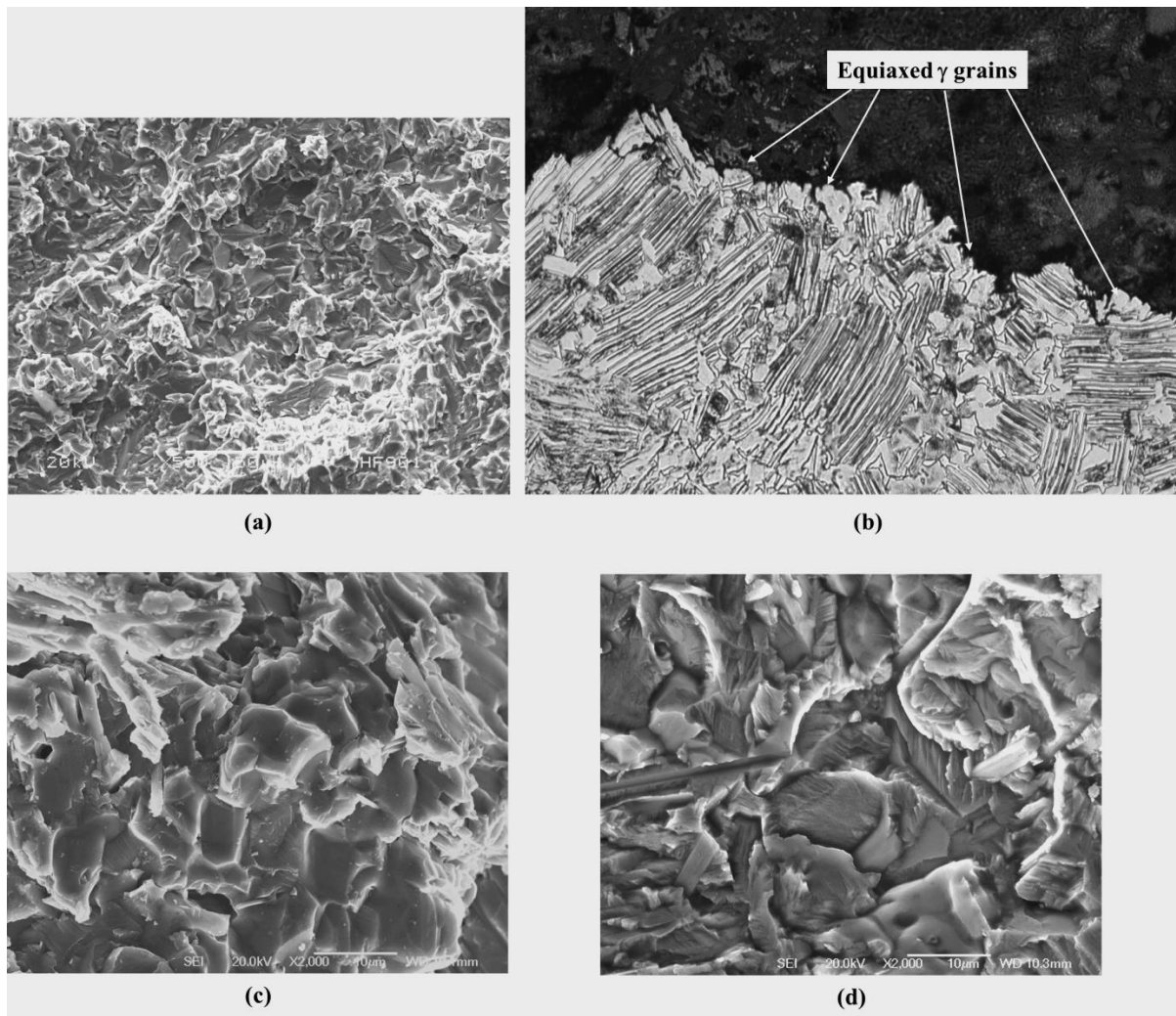


Figure 6.40. Failure of equiaxed γ grains found on fracture surfaces in the fatigue region: (a) cluster of equiaxed γ grains; (b) section of specimen tested at R=0.5 and 650 °C to show the crack path through equiaxed γ grains; (c) equiaxed γ grains failed intergranularly and (d) equiaxed γ grains failed transgranularly

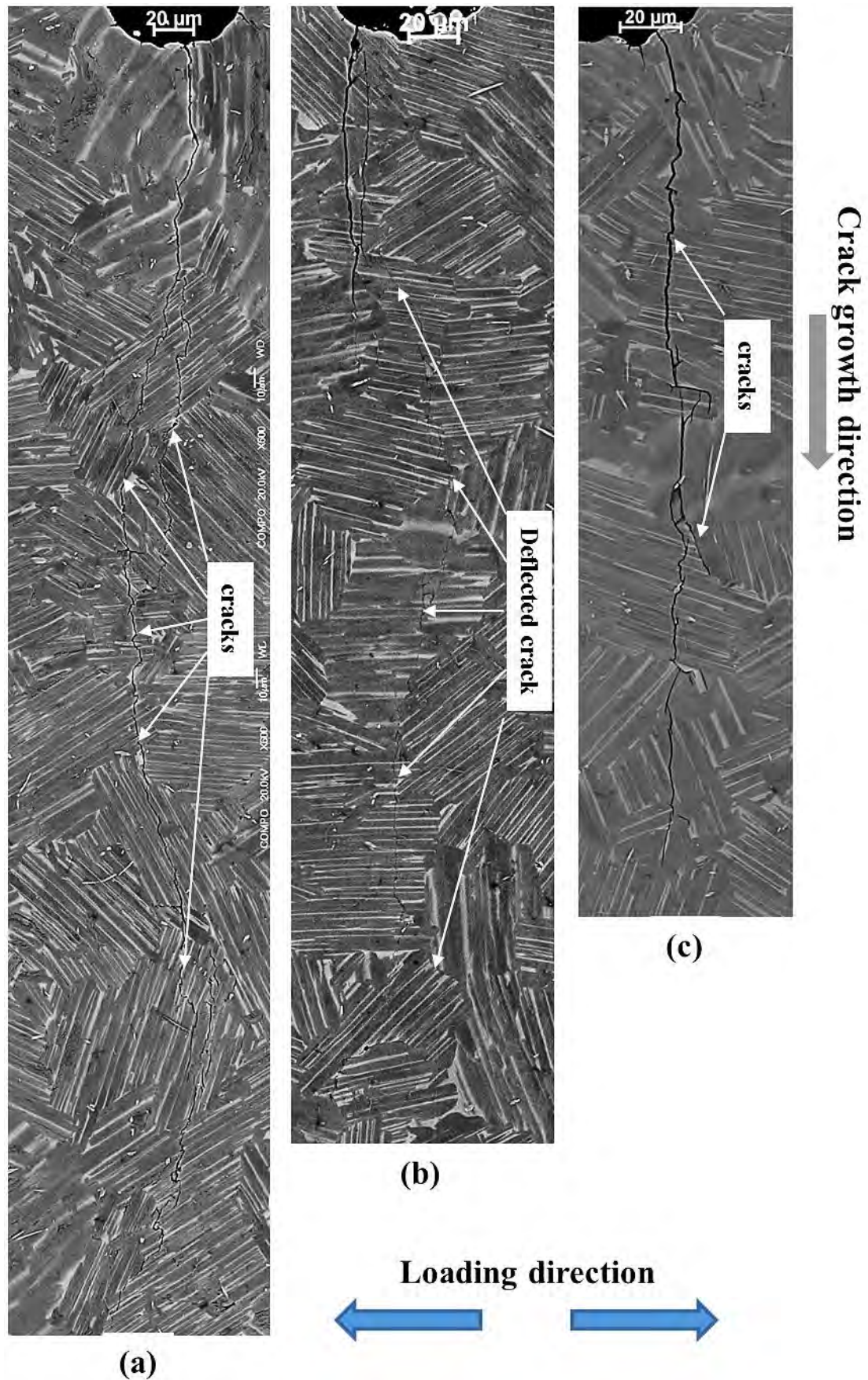


Figure 6.41. Sections showing fatigue crack propagation paths in specimens tested at a stress ratio of 0.1 at (a) RT, (b) 400 °C and (c) 650 °C

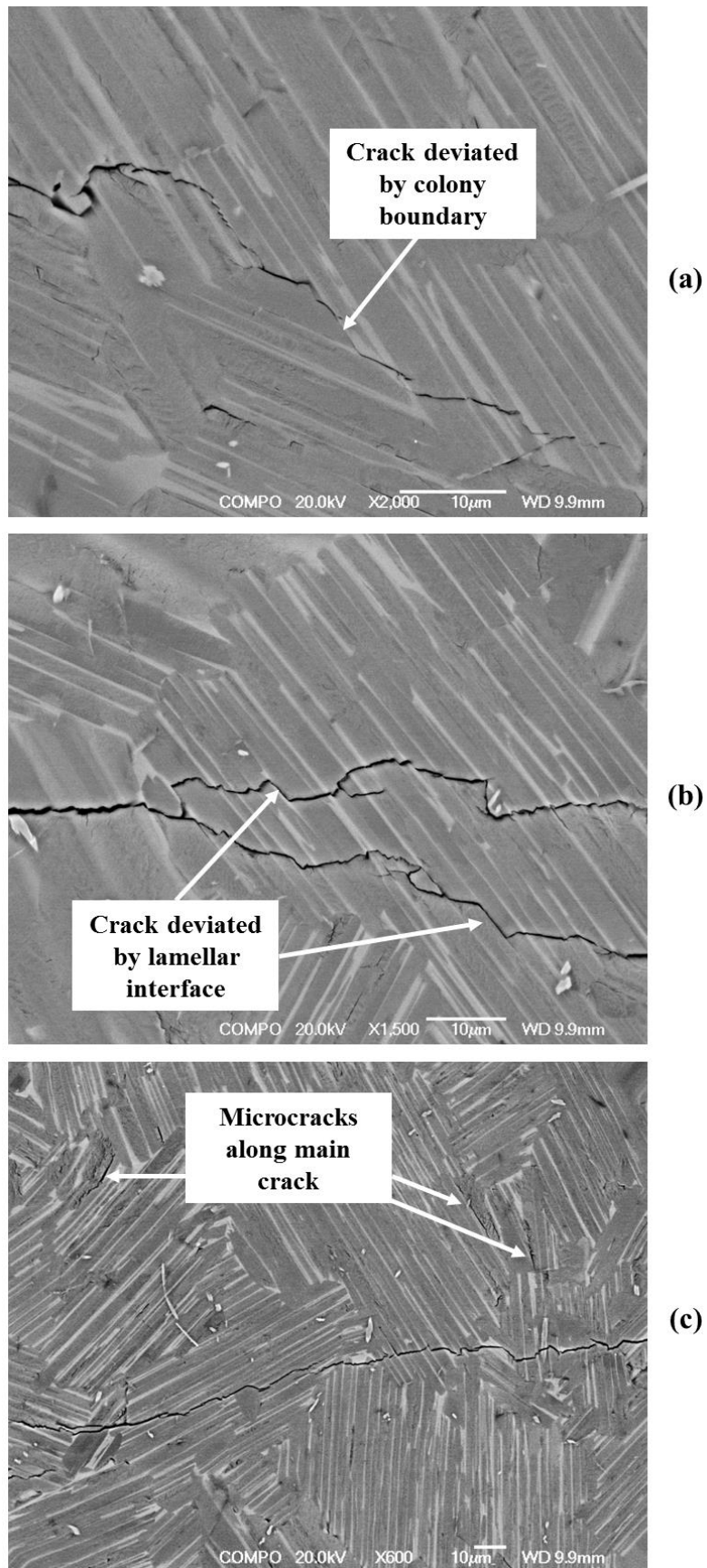


Figure 6.42. High magnification SEM images showing crack deviation by (a) colony boundary and (b) lamellar interface as well as (c) some microcracks found along the main crack

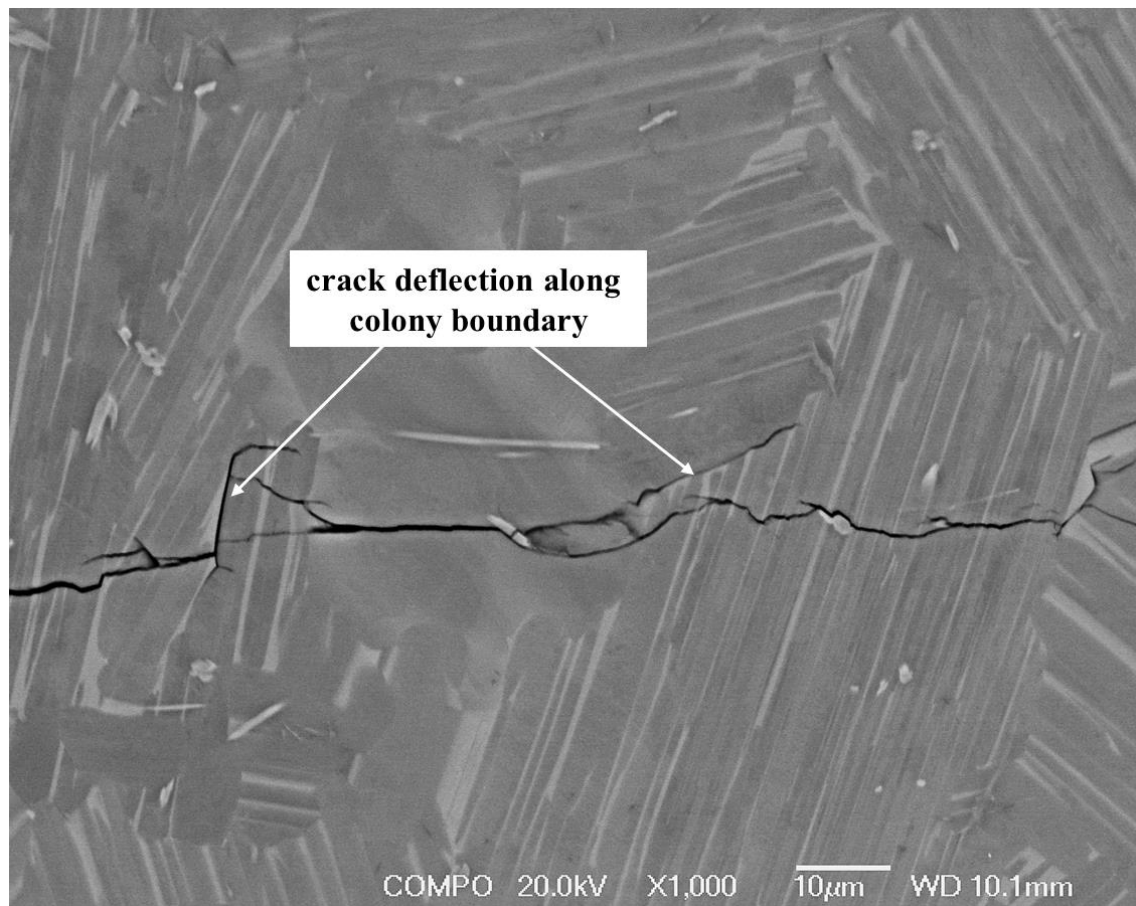


Figure 6.43. A high magnification SEM image showing the crack branching observed in sectioned surface of a specimen tested at an R ratio of 0.1 at 650 °C

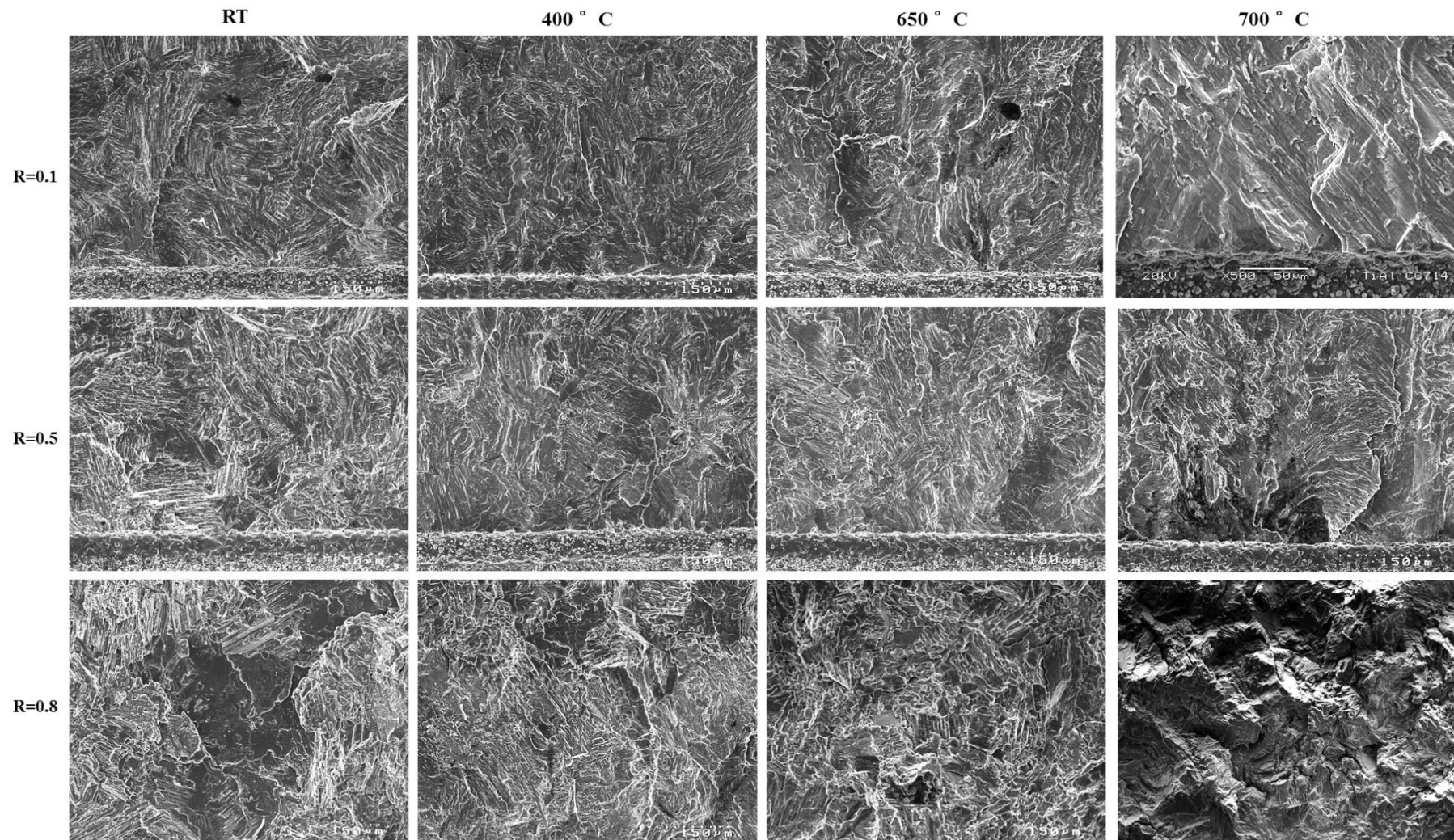


Figure 6.44. Fracture surface of crack initiation areas of specimens tested at different R ratios and temperatures.

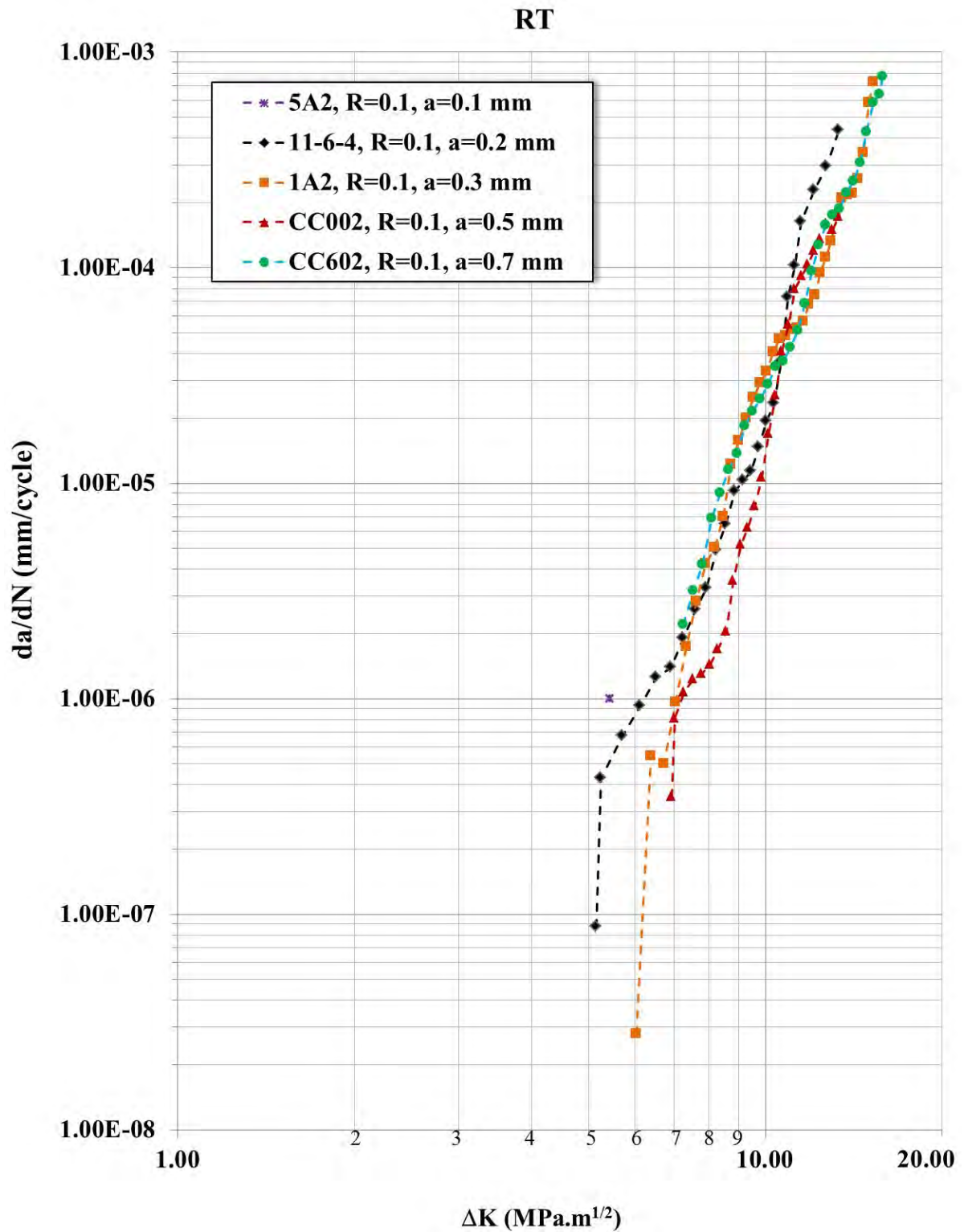


Figure 6.45. Comparison of fatigue crack growth resistance curves of specimens with different notch depths (0.1 mm, 0.2 mm, 0.3 mm, 0.5 mm and 0.7 mm) tested at RT and R = 0.1. There is no FCGRC for the specimen with a notch depth of 0.1 mm, thus the ΔK_{th} value is indicated by single point on the graph.

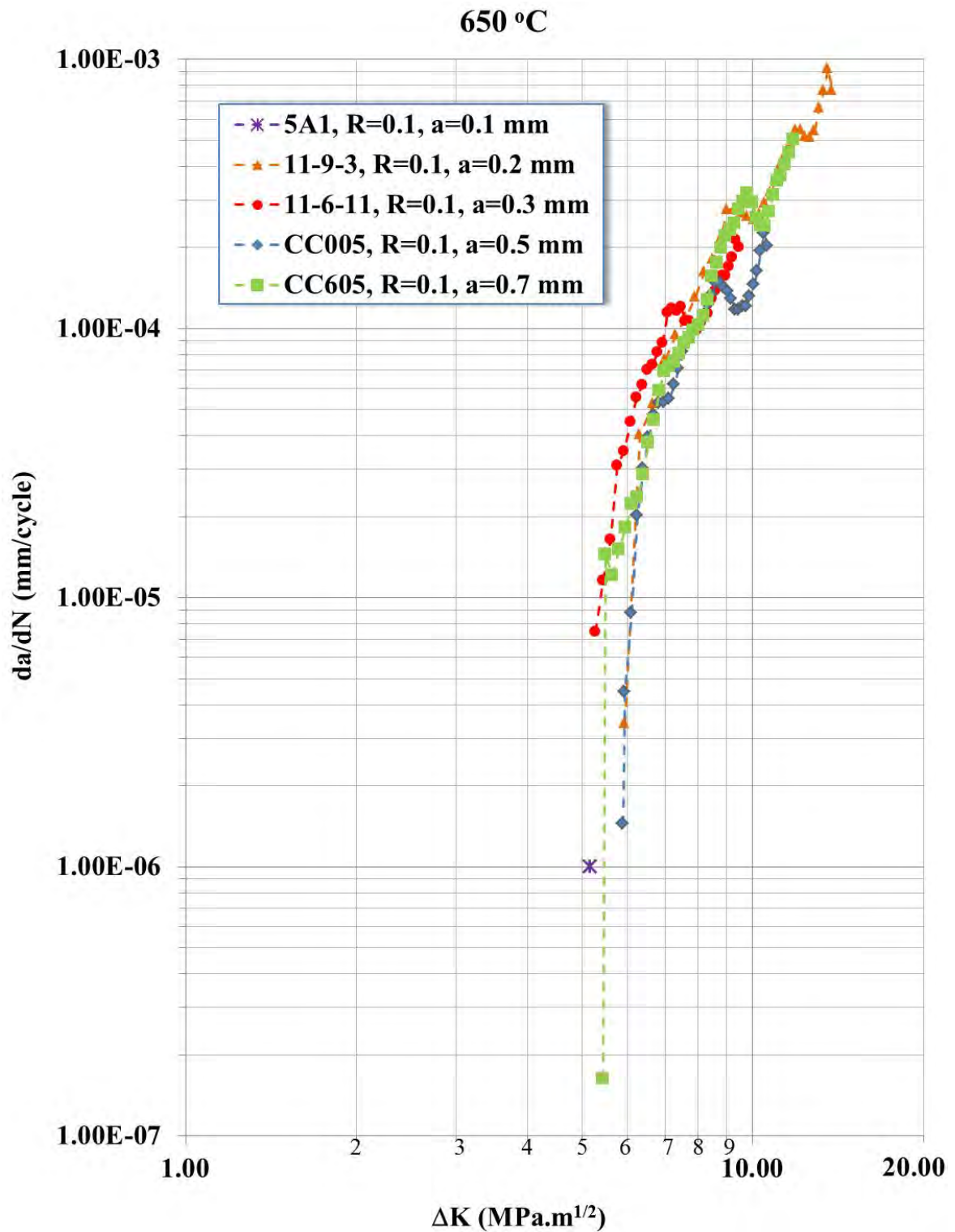


Figure 6.46. Comparison of fatigue crack growth resistance curves of specimens with different notch depths (0.1 mm, 0.2 mm, 0.3 mm, 0.5 mm and 0.7 mm) tested at 650 °C and $R = 0.1$. There is no FCGRC for the specimen with a notch depth of 0.1mm, thus the ΔK_{th} value is indicated by single point on the graph.

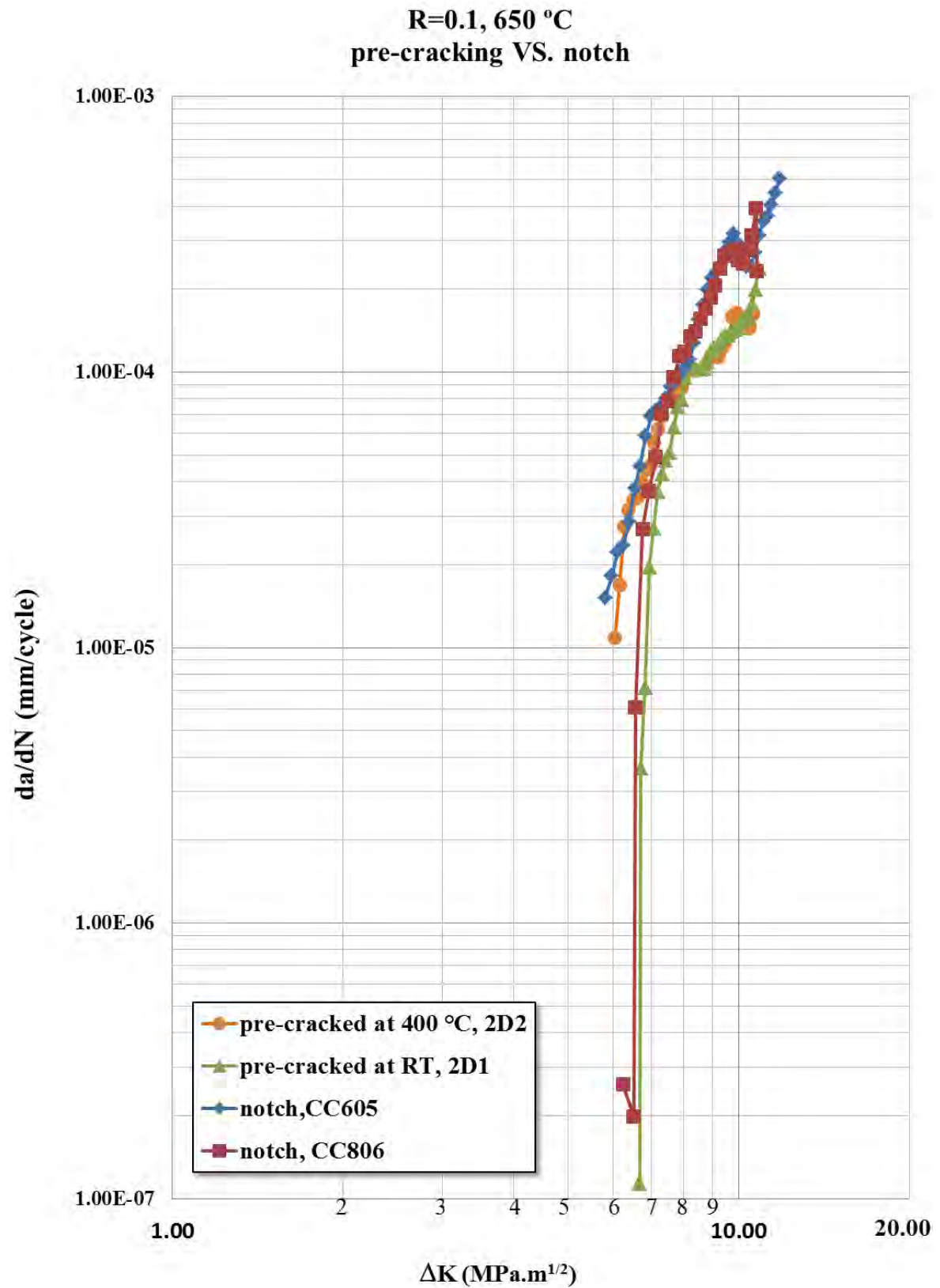


Figure 6.47. Fatigue crack growth resistance curves showing a comparison of tests starting from notches and from pre-cracks at an R ratio of 0.1 and at 650 °C

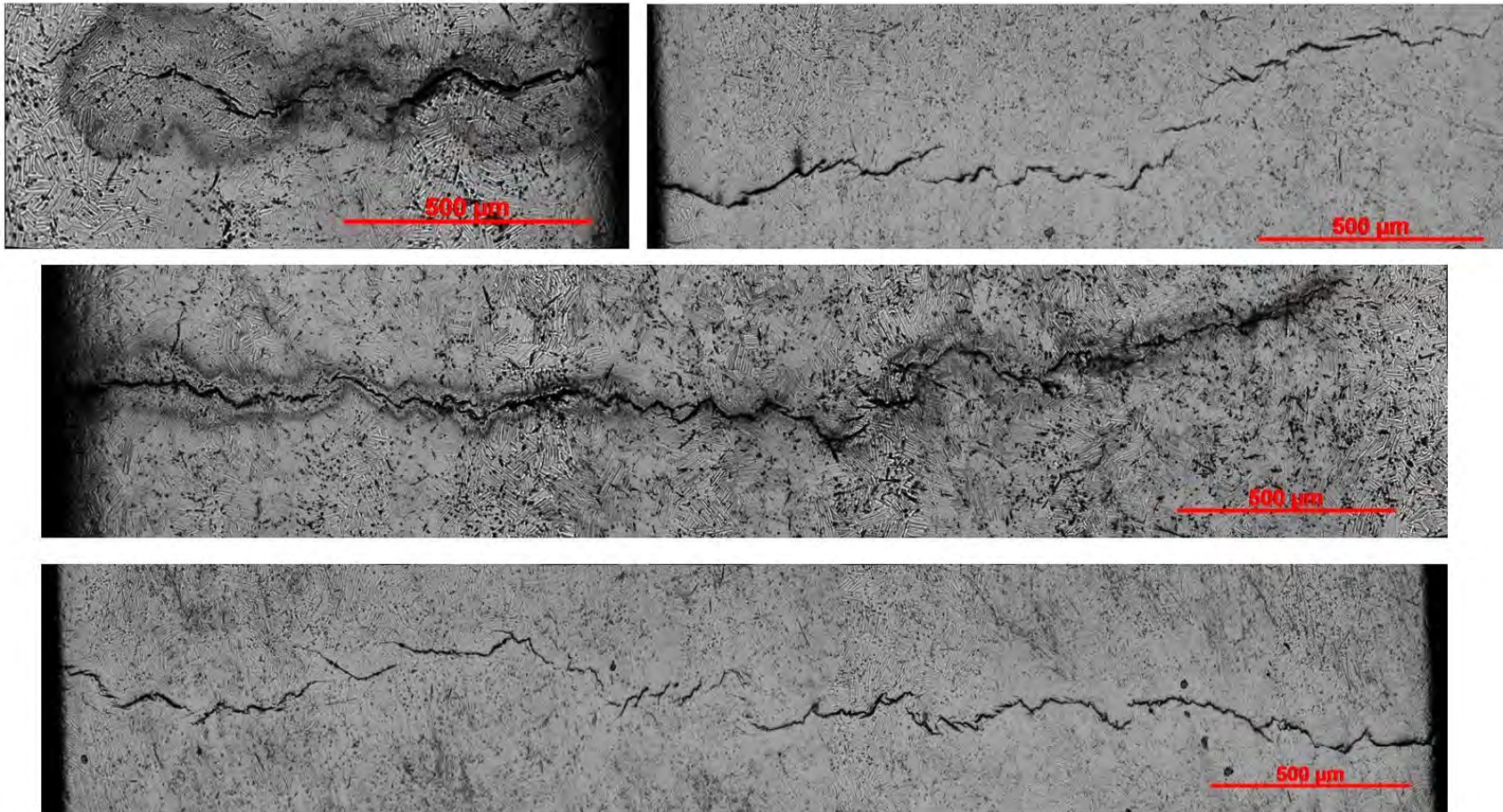


Figure 6.48. Surface cracks found after electrochemically polishing the specimens from IMR batch 5

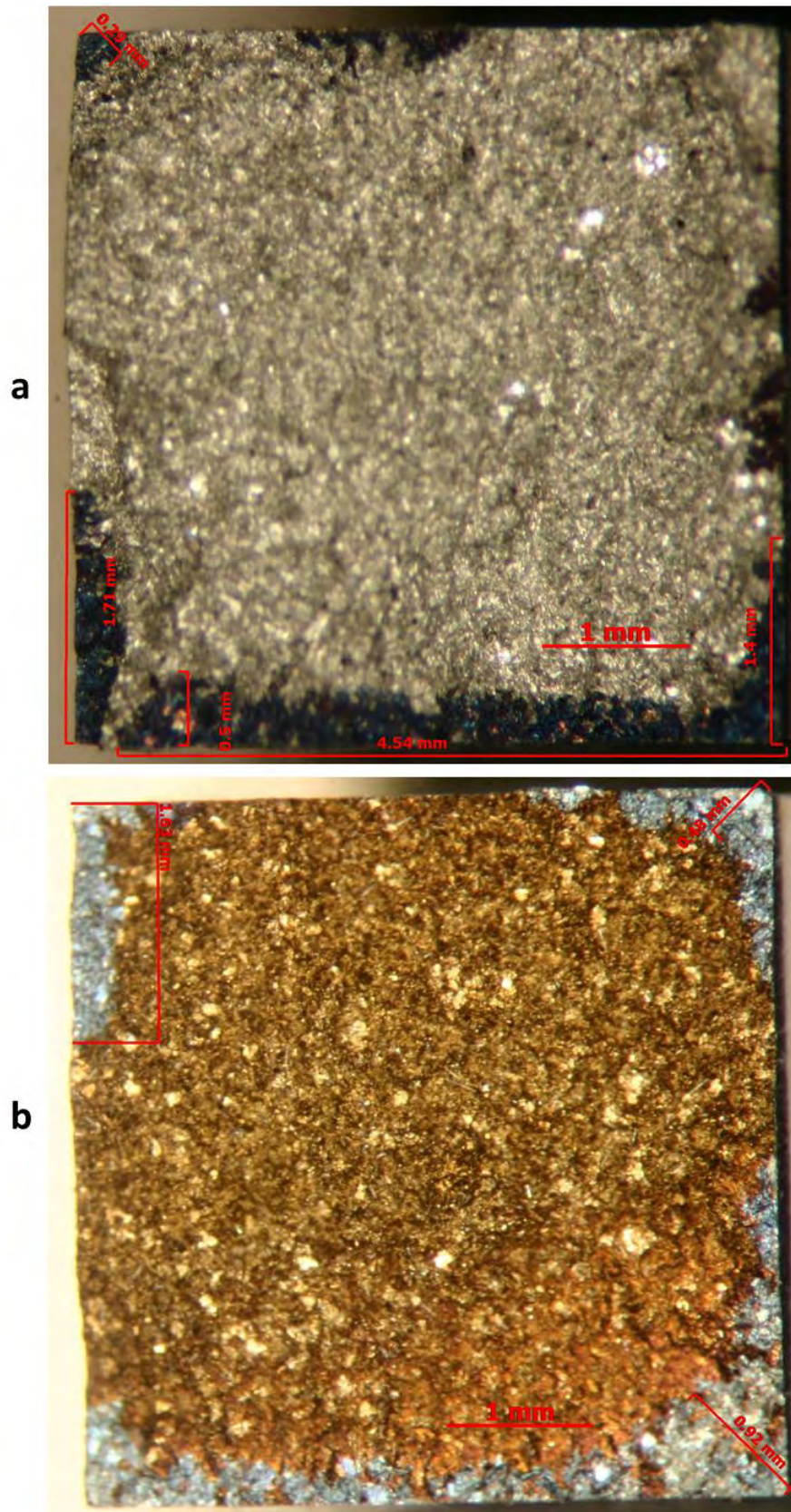


Figure 6.49. Surface cracks found in specimens after heat tinting: (a) CC706 and (b) CC717

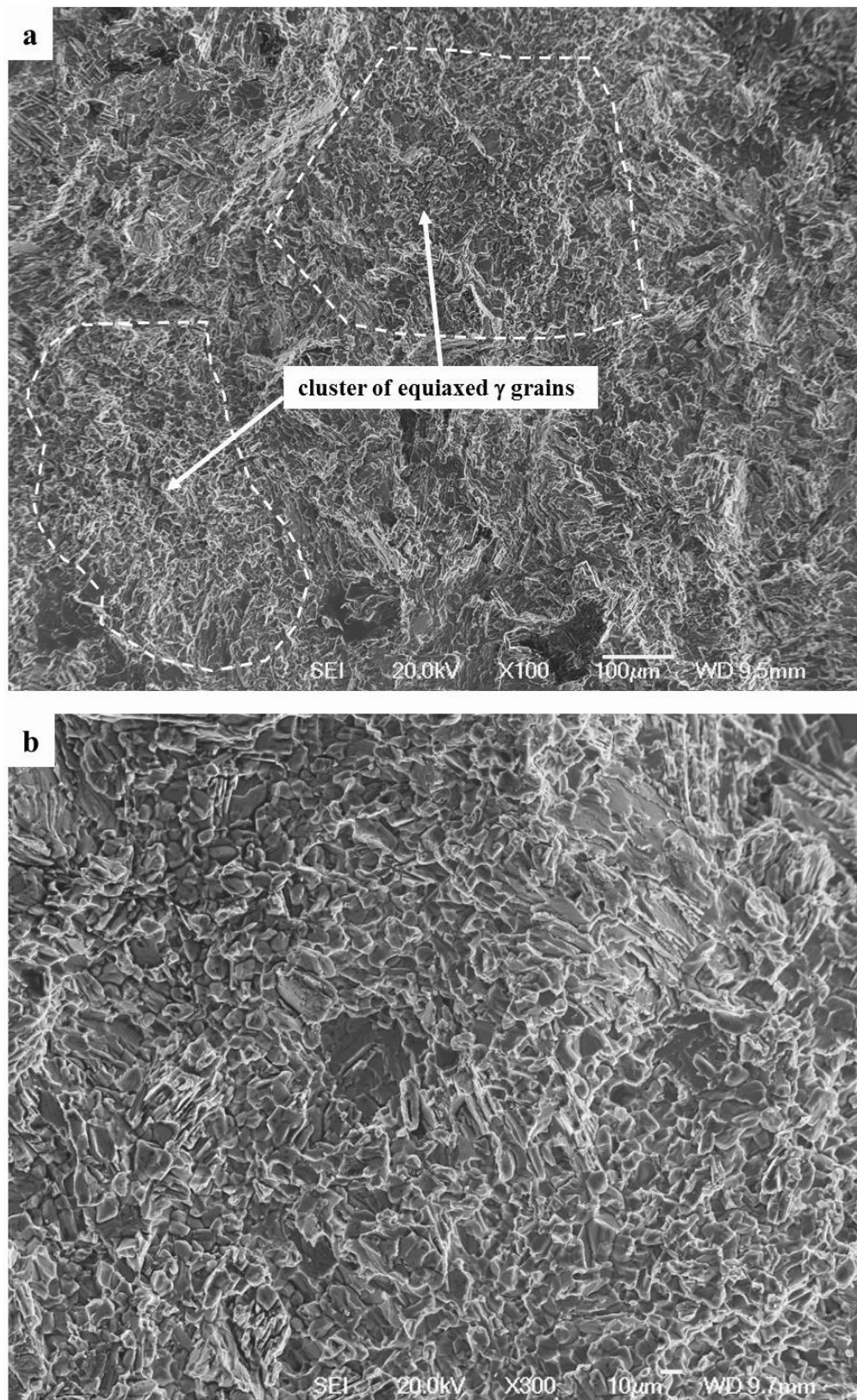


Figure 6.50. SEM images showing clusters of equiaxed γ grains found in specimen CC009 which were tested at $R=0.5$ and $650\text{ }^{\circ}\text{C}$, at (a) low magnification and (b) higher magnification

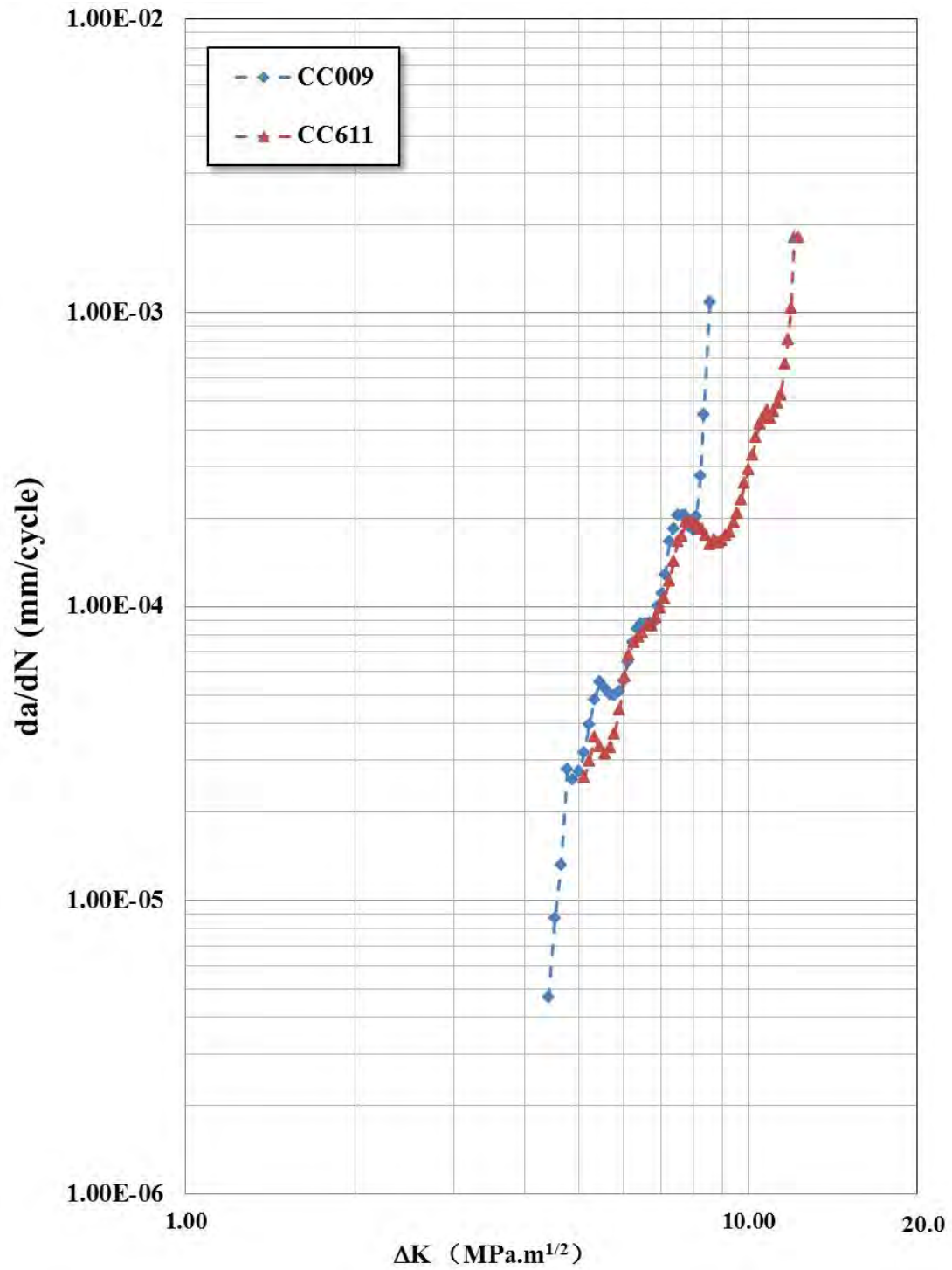


Figure 6.51. Fatigue crack growth resistance curves of specimen CC009 and specimen CC611 which were both tested at $R=0.5$ and $650\text{ }^{\circ}\text{C}$. The specimen CC009 contains large area of equiaxed γ grain, while CC611 has a normal microstructure.

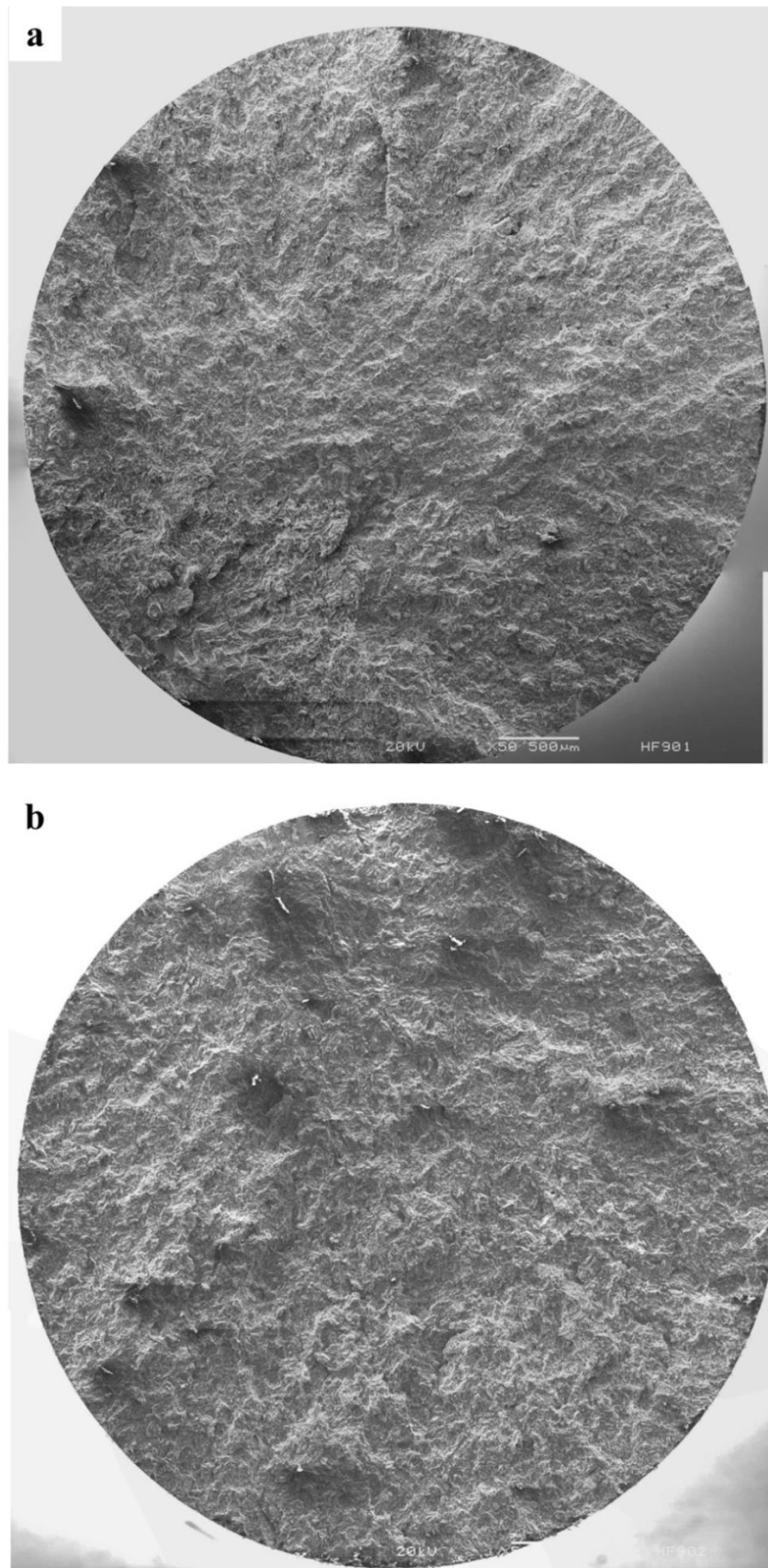
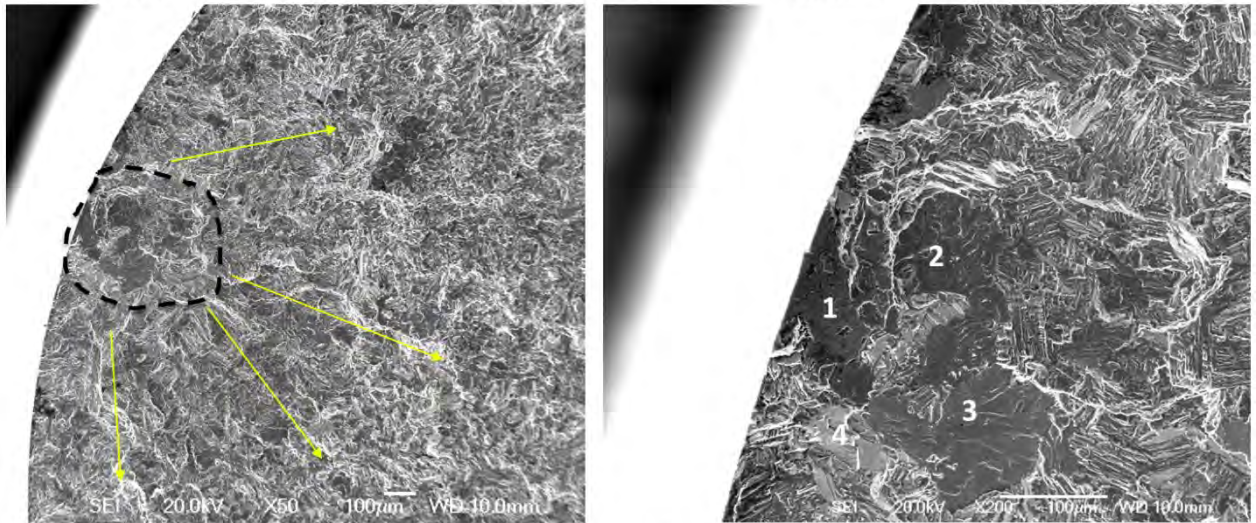


Figure 6.52. Low-magnification SEM images showing the whole fracture surface of (a) HF901 and (b) HF902 which were both tested with $R=0.1$ and at RT

A: Possible crack initiation site 1 – conjoint large interlamellar colonies at favour orientations



B: Possible crack initiation site 2 – several large interlamellar colonies in a same area

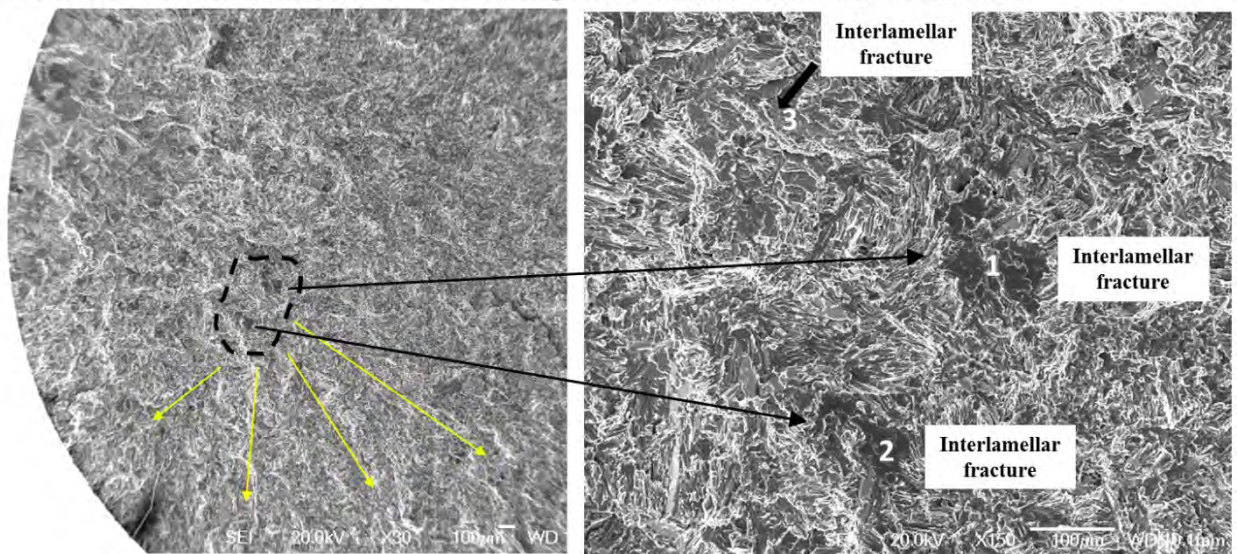


Figure 6.53. Possible fatigue crack initiation sites A and B found on the fracture surface of specimen HF901 indicated by the radial pattern as shown by the yellow arrows. The common feature of these sites is several larger interlamellar fractures within a small area.

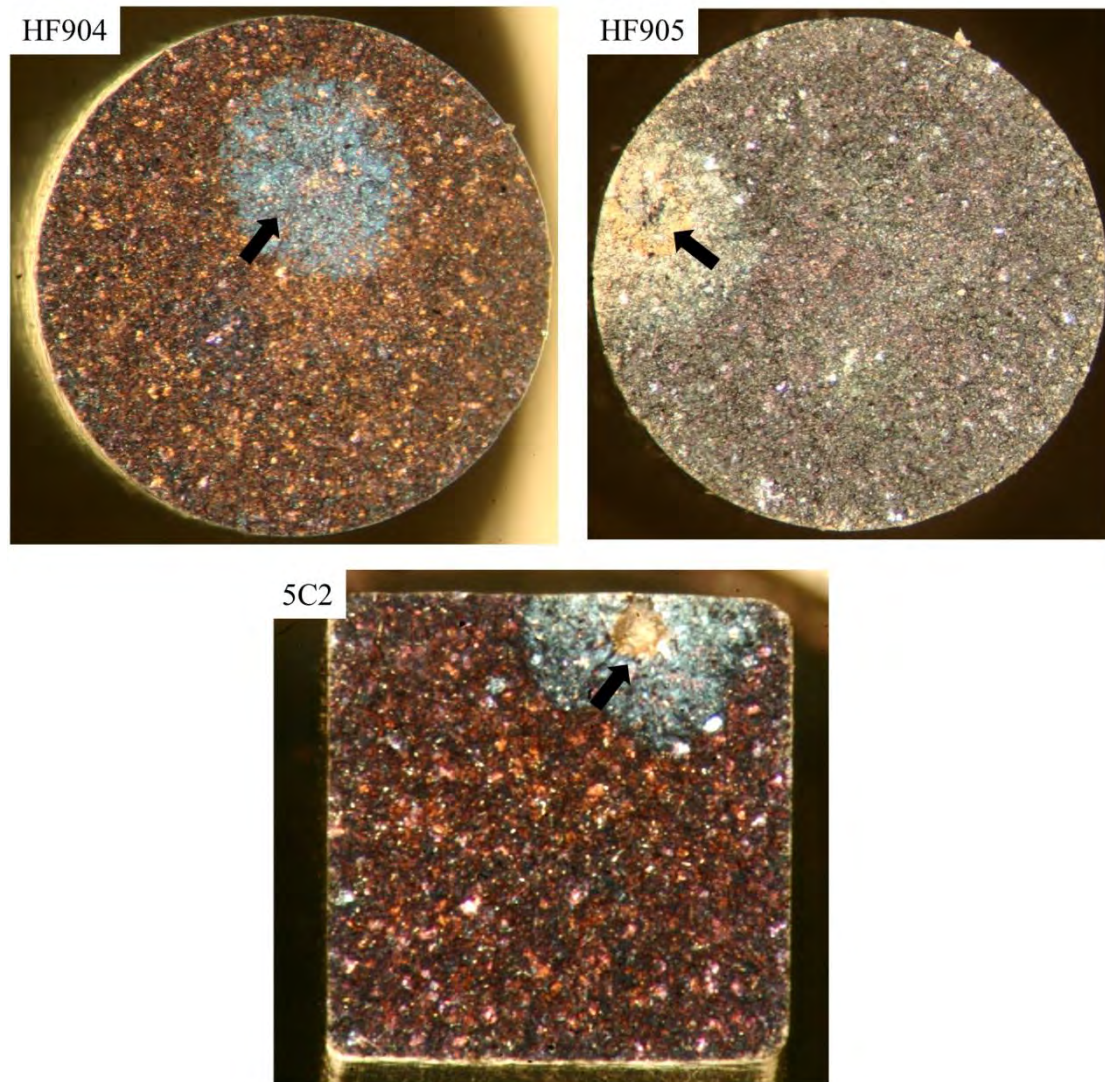


Figure 6.54. Optical images of HF904, HF905 and 5C2 which were tested at $R=0.1$ and $T=650\text{ }^{\circ}\text{C}$. The fatigue crack initiation sites are indicated by black arrows.

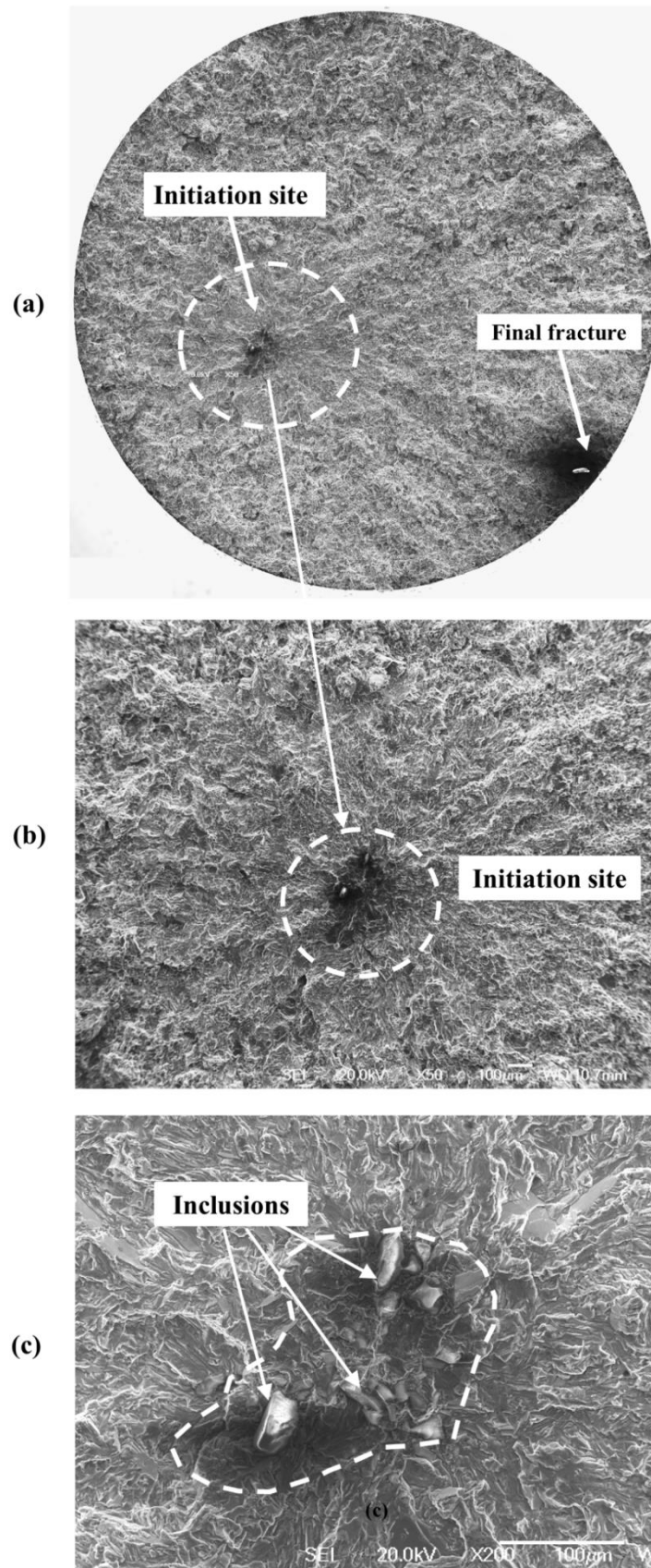
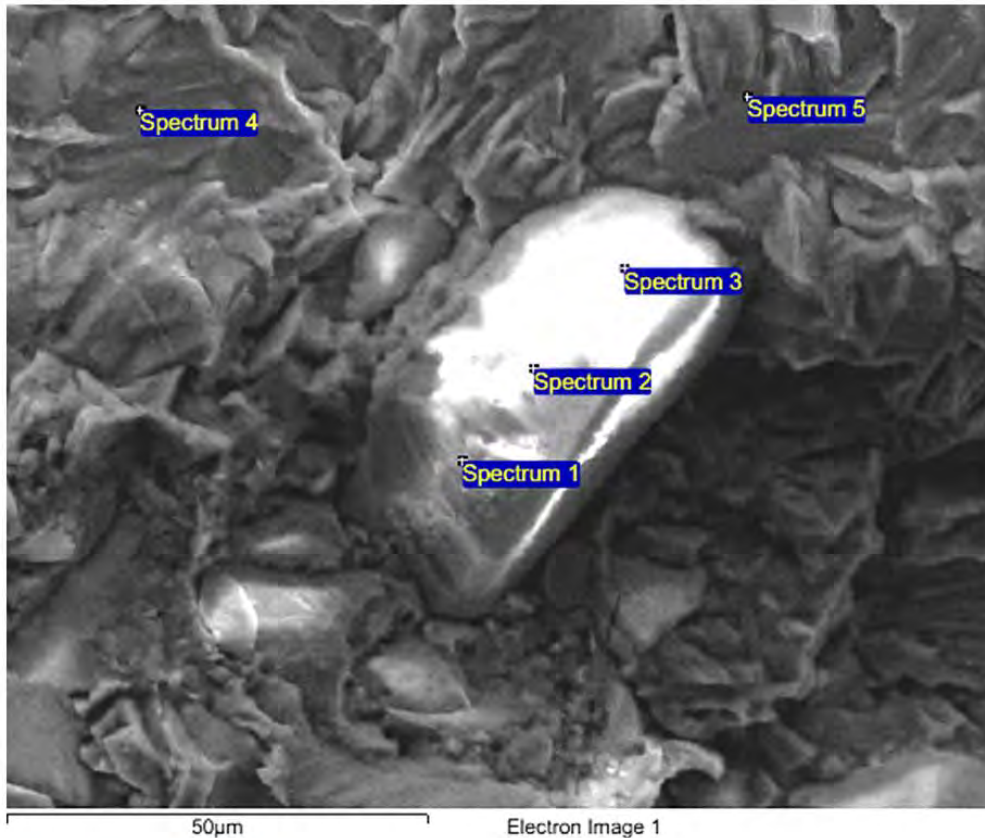


Figure 6.55. SEM images showing (a) the whole fracture surface of HF904, (b) the crack initiation site and (c) inclusions found in the initiation site



All results in atomic %

Processing option : All elements analysed (Normalised)

Spectrum	In stats.	O	Al	Ti	Mn	Y	Nb
Spectrum 1	Yes	60.89	9.99	10.71		18.42	
Spectrum 2	Yes	66.18	1.67	2.61		29.55	
Spectrum 3	Yes	73.97	2.41	4.44		19.17	
Spectrum 4	Yes	30.74	25.17	41.35	1.24		1.49
Spectrum 5	Yes	32.32	11.83	52.13	1.62	1.33	0.77
Max.		73.97	25.17	52.13	1.62	29.55	1.49
Min.		30.74	1.67	2.61	1.24	1.33	0.77

All results in weight %

Processing option : All elements analysed (Normalised)

Spectrum	In stats.	O	Al	Ti	Mn	Y	Nb	Total
Spectrum 1	Yes	28.70	7.94	15.11		48.24		100.00
Spectrum 2	Yes	27.46	1.17	3.24		68.13		100.00
Spectrum 3	Yes	37.38	2.06	6.72		53.84		100.00
Spectrum 4	Yes	14.64	20.22	58.97	2.03		4.13	100.00
Spectrum 5	Yes	14.31	8.84	69.12	2.46	3.27	1.99	100.00
Max.		37.38	20.22	69.12	2.46	68.13	4.13	
Min.		14.31	1.17	3.24	2.03	3.27	1.99	

Figure 6.56. EDS results in atomic% and weight% showing the compositions of the largest inclusion (spectrum 1, spectrum 2 and spectrum 3) and matrix (spectrum 4 and spectrum 5) around the inclusion

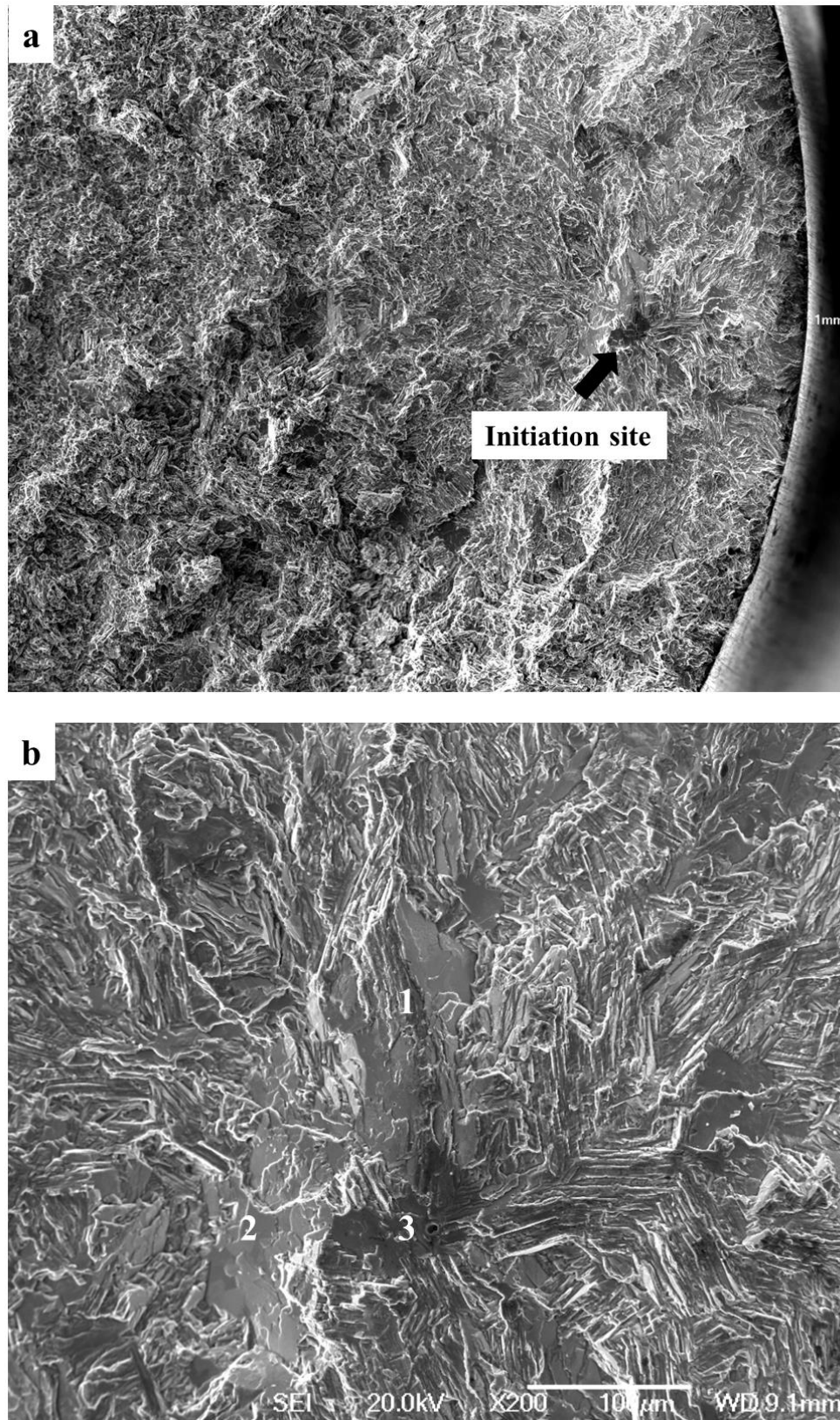


Figure 6.57. SEM images of the fatigue initiation site found on the fracture surface of HF905: (a) low magnification image shows the position and size of the crack initiation site and (b) higher magnification image shows 3 conjoined interlamellar fractures in the middle of the crack initiation site

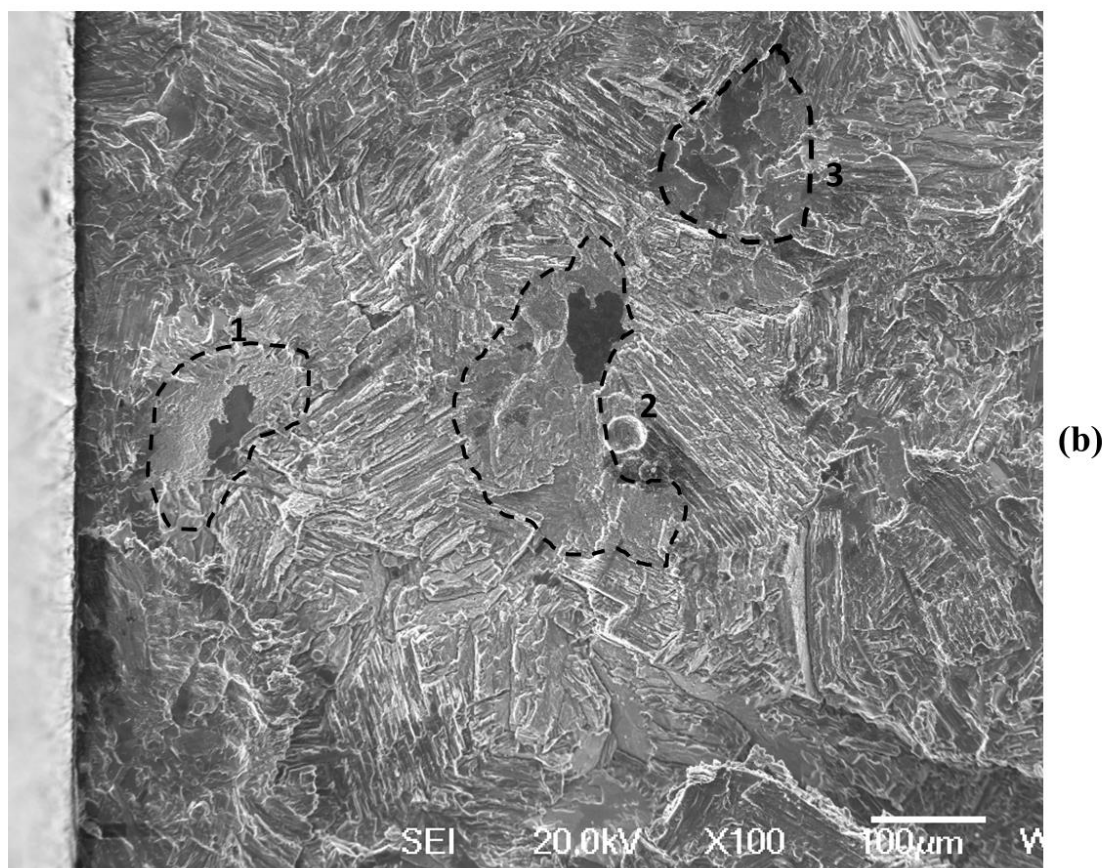
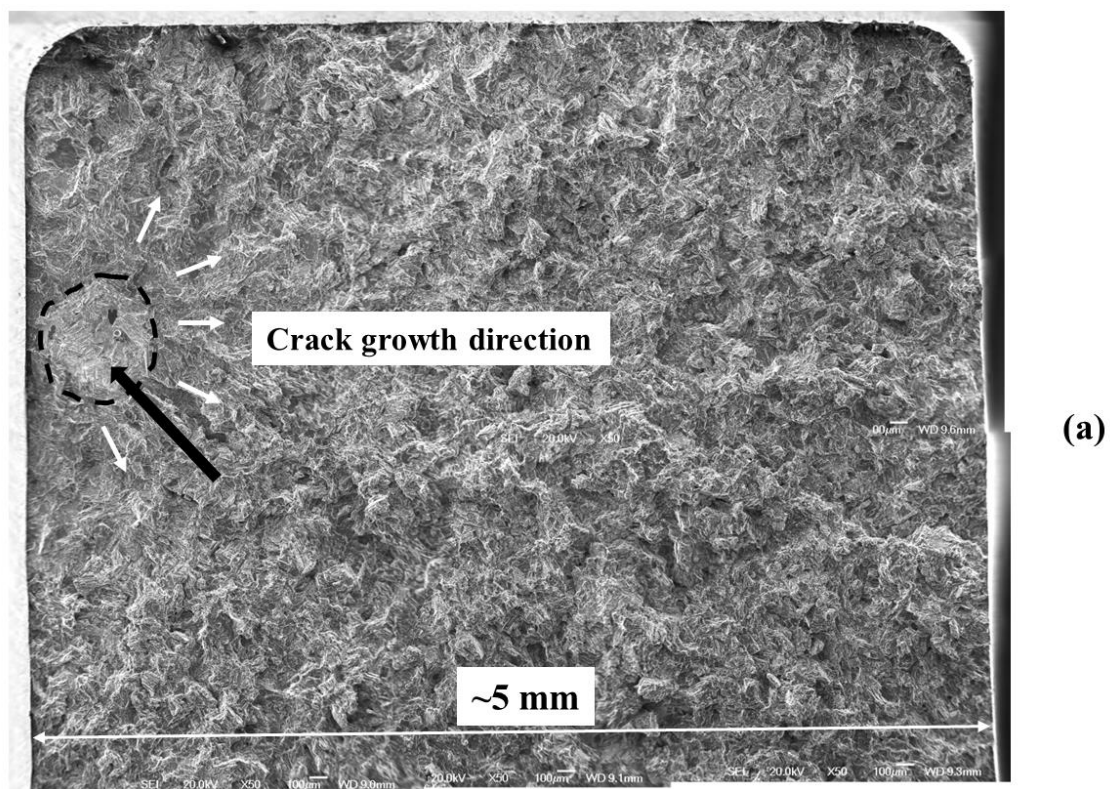


Figure 6.58. SEM images showing (a) fatigue crack initiation site in specimen 5C2 and (b) three large interlamellar fractures found within the crack initiation site



Figure 6.59. Specimen CC009 from TIMET 3rd batch failed due to creep, severe deformation can be observed around the widely opened crack

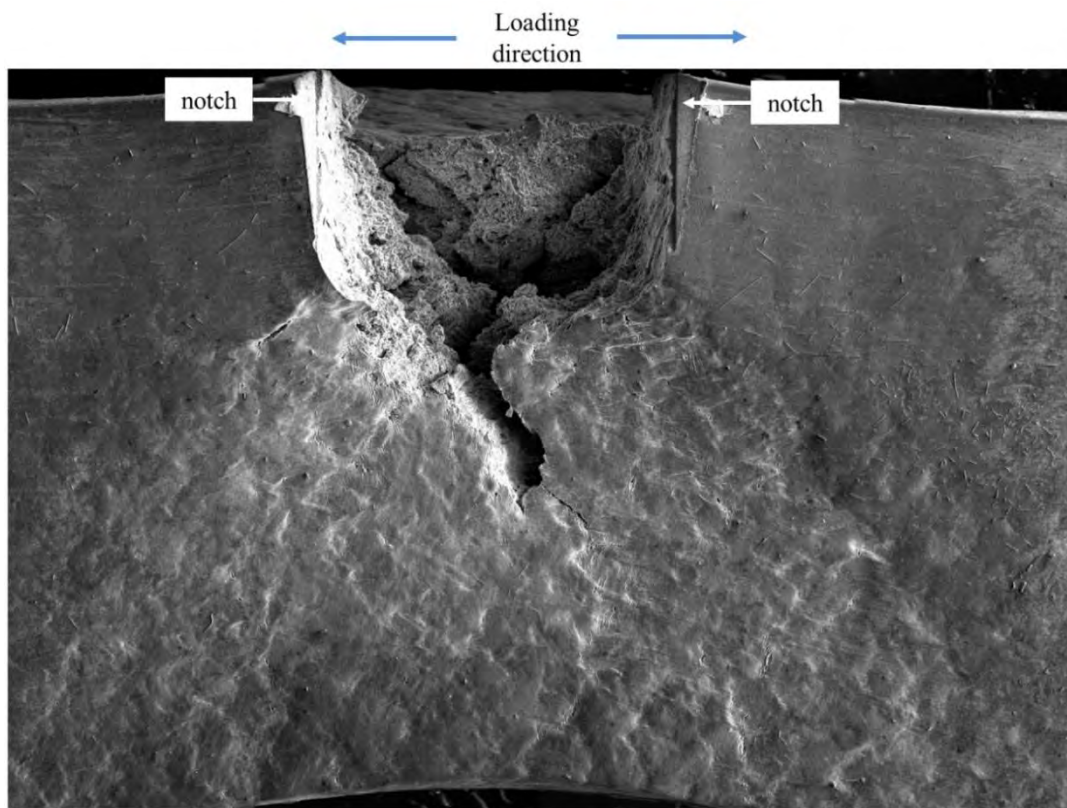


Figure 6.60. SEM image showing the side surface and crack of CC009 (TIMET 3rd batch) which failed due to creep

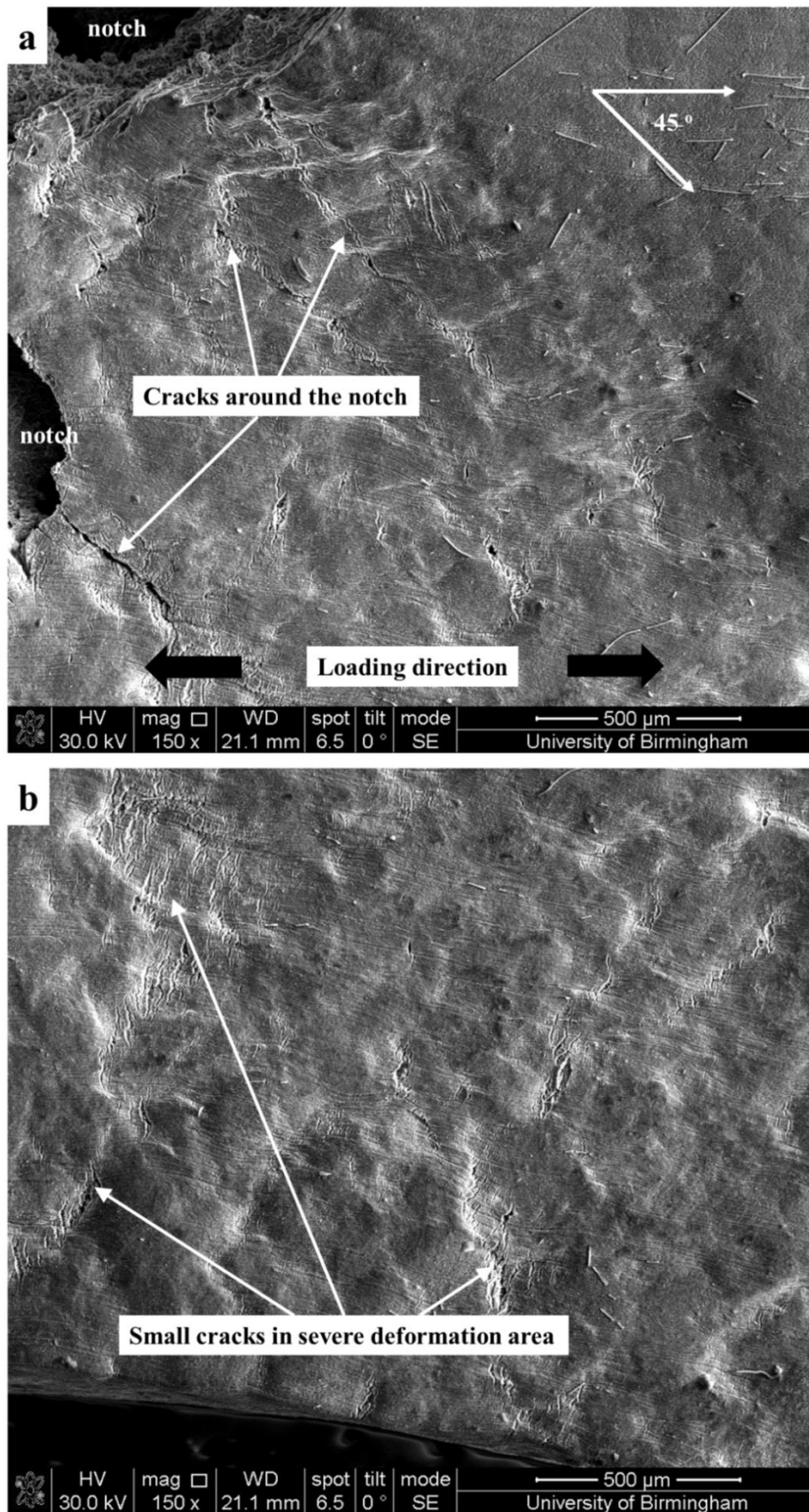


Figure 6.61. SEM image showing (a) cracks attached to the notch at an angle around 45° to the loading direction, and (b) small cracks in the serverly deformed area

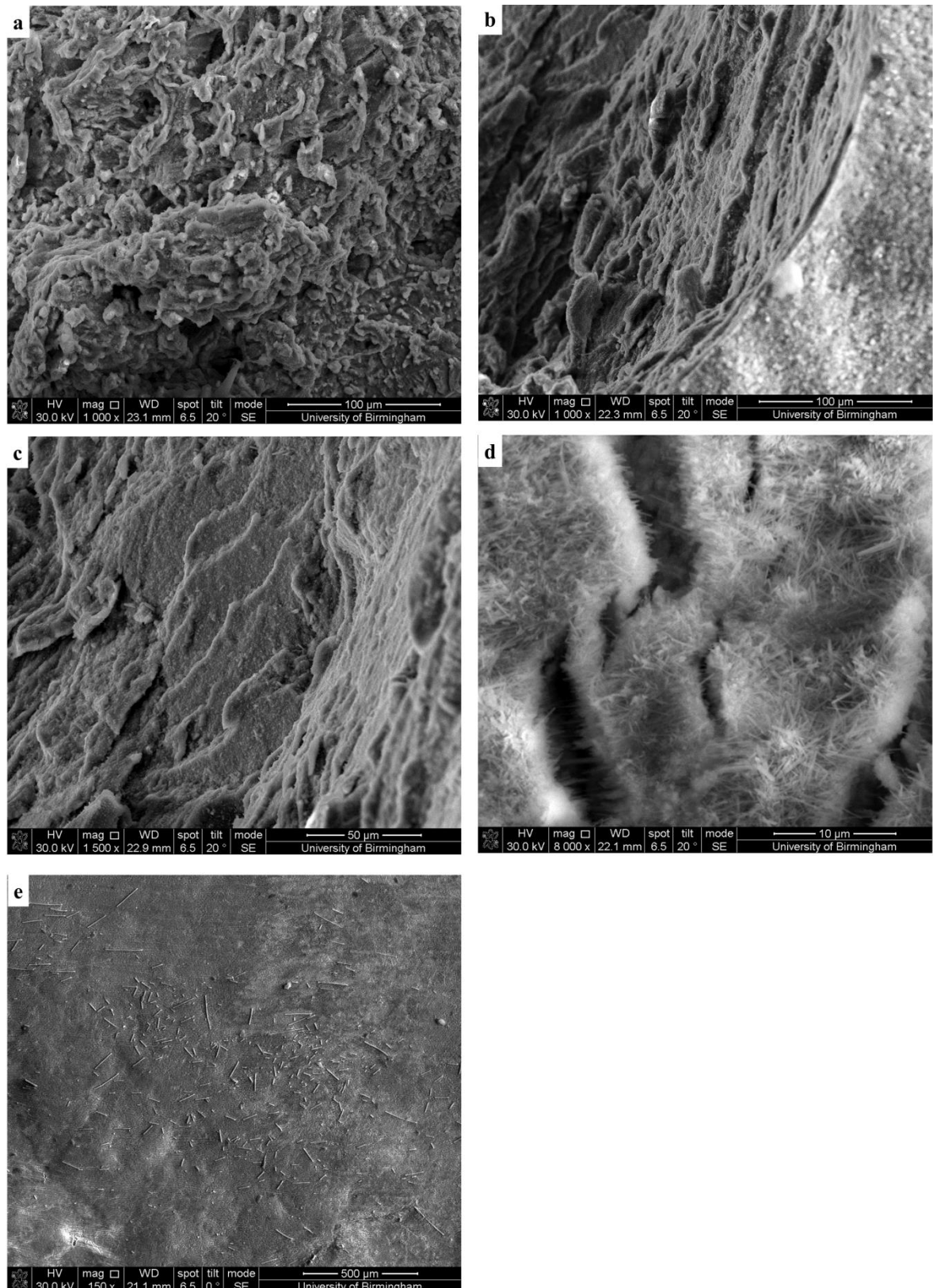


Figure 6.62. Fractographic observation of specimen CC009-T showing (a) fracture surface with no microstructural features of lamellar γ -TiAl, (b) flat area near notch, (c) feature similar to interlamellar fracture, (d) oxidation particles on the fracture surface, and (e) precipitates found in the side surface

7. Discussion

7.1 Introduction

It was shown in early work that TiAl based alloys normally show steep fatigue crack growth resistance curves as indicated by high m values (usually $\sim 9-22$) at low and intermediate temperatures [53, 56, 84], extreme values can be nearly 5 to 10 times higher than the average values for metallic systems [56]. A lamellar microstructure and colony size refinement can offer significant improvements by producing lower Paris exponents and higher ΔK_{th} values. However, the fatigue crack path depends highly on the colony orientation. Translamellar cracks require relatively higher ΔK levels for propagation than interlamellar cracks [126]. However, interlamellar fracture is not always related to low fatigue crack growth resistance. Only colonies where interlamellar fracture can contribute to mode I cracking cause significant reductions in fatigue crack growth resistance. Although in lamellar γ -TiAl alloys the colonies are often randomly oriented, 3-4 conjoined colonies in the mode I orientation were still found in the alloys studied here. All these characteristics can lead to significant anisotropy in the fatigue crack threshold and growth behaviour [56, 126]. Besides, both the fatigue crack initiation and growth exhibit complicated trends with other factors, such as test temperature, environment and R ratio. Since different fatigue crack growth regimes have different dominant mechanisms, how these factors affect fatigue properties of a near fully-lamellar γ -TiAl is discussed here in terms of the three different fatigue crack growth regimes.

7.2 Fatigue crack threshold and near threshold behaviour

A crack-arrest phenomenon was found under some test conditions which is caused by microstructural barriers, such as colony boundaries and lamellar interfaces. To achieve a continuous change of PD, cracks are required to break out from interlamellar fracture to general translamellar crack growth. A higher peak load is required when the crack-arrest phenomenon occurs to provide a higher driving force for the ‘breaking out’

of cracks. Therefore, the fatigue threshold is defined as the minimum stress intensity factor range that allows continuous fatigue crack growth. Moreover, in order to avoid crack wake effects, both a ΔK - increasing loading method together with growth from a notch (and/or a very short, less than 100 μm fatigue pre-crack) were applied throughout the tests in this study.

7.2.1 Effects of microstructure and test temperature on ΔK_{th} values

In fatigue regime I, i.e. fatigue threshold regime, crack initiation is mostly controlled by localized microstructural units. Microstructural barriers in lamellar γ -TiAl alloys can restrict fatigue crack initiation and propagation, and thereby result in higher ΔK_{th} values compared to other microstructures [7]. In this study, most tests were carried out directly from a notch, the ΔK_{th} values are only affected by intrinsic properties since there were no pre-crack induced loading history and ‘extrinsic’ toughening within the pre-crack wake. Therefore, the microstructure ahead of the notch plays a decisive role on ΔK_{th} values. In the current study, the microstructure is clearly controlled to give a consistent near-fully lamellar microstructure of colony size 80-100 μm . This has enabled the current study to allow definitive trends of ΔK_{th} and FCGR to be established as a feature of R ratio and test temperatures.

The anisotropic fracture toughness tests at RT in a cast lamellar alloy with colony size of 1 mm showed that the K_{C} value for crack propagation along preferred lamellae orientation was about $12.5 \text{ MPa}\cdot\text{m}^{1/2}$, which is about $8 \text{ MPa}\cdot\text{m}^{1/2}$ lower than for crack propagation in the transverse lamellar orientation and resulted in more interlamellar cracks [127]. In this study, the length of the crack front is about 1.0-1.4 mm which covers approximately 12-18 colonies. In the fatigue threshold regime, the possibility of colonies approximately at the mode I orientation among the total number of colonies is likely to vary the ΔK_{th} values. In a specimen, if there are more colonies at an orientation that is close to the mode I direction at the notch front, its ΔK_{th} value could

be lower compared those have fewer weak-orientated colonies. Currently, no study has been done to evaluate the relationship between the number of colonies at the mode I direction and ΔK_{th} values. It is of interesting to have relevant statistics.

Table 6.1, Table 6.3, Figure 6.7 and Figure 6.8 show the importance of repeat tests to establish the range of ΔK_{th} values at a given test temperature and R ratio. Here, it is argued that this variation is not directly associated with test temperature since for a given R ratio the average ΔK_{th} values at each temperature are all close to the average ΔK_{th} value of all the tests. In addition, at R=0.1 and 0.5, three temperatures (RT, 400 and 650 °C) at which the ΔK_{th} values are scattered show similar standard deviation values, i.e. similar dispersion.

From the discussion above, it can be deduced that for a given R ratio, the variation of ΔK_{th} value in this near fully lamellar γ -TiAl alloy is more likely to be caused by the microstructure along the notch front, and test temperature does not have a remarkable influence on the ΔK_{th} values.

In addition, although most authors [70, 97, 121, 128] found that equiaxed γ grain or duplex microstructure has lower crack growth resistance because of lack ligament bridging toughening, no significant influence of equiaxed γ grain clusters on the FCGR was found. If the clusters of equiaxed γ grain appear around the middle and end of the crack, where ΔK values are medium and high, the driving force could be high enough to reduce or counteract the enhancement of lamellar ligaments, especially at high R ratios.

7.2.2 Effect of temperature on fatigue crack growth in the near-threshold region

As mentioned above, a crack-arrest phenomenon was sometimes found during the tests. This phenomenon is mostly found in tests performed at RT or at R=0.8, and barely

observed in tests carried out at elevated temperatures with an R ratio of 0.1 and 0.5. Such a difference at $R=0.1$ and 0.5 can be explained by Figure 6.35 and Figure 6.36. At RT, the fatigue fracture surfaces near the notches contain several interlamellar fractures at multiple angles and are relatively rougher than the fatigue fracture surfaces of specimens tested at elevated temperatures (as shown in Table 6.5). These observations have already been reported in a previous study [72]. In lamellar alloys the highly tortuous fracture surfaces with more serrated and faceted surface morphologies observed at RT have been found to lead to roughness-induced crack closure [56, 85]. The roughness-induced crack closure can reduce the stress intensity driving force and thereby reduce the effective driving force for FCGR. Relatively smooth fatigue fracture surfaces are found in the near fatigue threshold region at elevated temperatures presumably with reduced extrinsic toughening and increased FCGR. In addition, small amounts of interlamellar fracture which deviate the crack growth direction away from a mode I direction could still benefit the fatigue crack growth resistance and result in reduction of FCGR as found on the fracture surfaces of specimens tested at RT.

As seen in Figure 6.34 and Figure 6.44, the fracture surfaces of specimens tested at $R=0.8$ are all visibly rough with features similar to those of monotonic load caused fractures. These features are uneven translamellar fractures, more large interlamellar fractures and jagged colony boundary fractures.

All fracture surfaces of specimens tested either at RT or with an R ratio of 0.8 show static fracture related features. In lamellar microstructures, the cracks always prefer to initiate at lamellar interfaces which are approximately at mode I direction, and are obstructed by surrounding colonies away from the mode I directions. To overcome these barriers, higher driving forces are required to grow cracks into general intralamellar fractures and thus achieve continuous crack growth. Therefore, this ‘start-and-stop’ phenomenon was observed during tests below the loading level of the threshold for continuous growth.

7.2.3 Effect of R ratio on ΔK_{th} values

In general, for all test temperatures ΔK_{th} values decrease with increasing R ratio as shown in Figure 6.8 and Table 6.2. However, the average K_{max} values at fatigue threshold increase as R ratio increases. Many authors have proposed that such behaviour is associated with the reduction in extrinsic crack shielding effects at higher R ratios [27, 124, 129]. However, as mentioned above, for cracks started directly from notches the fatigue threshold behaviour is only dominated by intrinsic properties ahead of the notches. At higher R ratios, increasing static driving force, K_{max} , at fatigue threshold promotes damage ahead of the notch front, such as microcrack growth by forcing additional dislocations to accumulate at microstructural barriers. Hence, the fracture surfaces around fatigue crack initiation regions get rougher as R ratio increases.

At an R ratio of 0.8, the K_{max} values (see in Table 6.2 (c)) are only 2.8 MPa.m^{1/2} lower than the K_C values (shown in Table 6.3) at the same temperature. The results of fracture toughness tests indicate that the fracture behaviour in this near fully-lamellar γ -TiAl alloy does not vary significantly with temperature. Such a high static driving force (K_{max}) at fatigue threshold can conquer most microstructural barriers, such as colony boundaries, interlamellar interfaces. Therefore, for tests performed at R=0.8, the microstructural influence can be negligible as the driving forces at fatigue threshold are high enough to fracture those microstructural barriers, for instance unbroken lamellar ligaments. In addition, it has been observed that no crack closure effect could be found at R ratios above 0.5 even in a near-fully lamellar microstructure [92].

7.3 Fatigue crack growth behaviour in near-lamellar TiAls

In the fatigue regime II, i.e. Paris Law regime, stable crack growth is assumed, and Paris Law exponent (m) and coefficient (C) are usually applied to describe the fatigue crack growth in this regime. As a consequence of crack growth, the stress intensity

becomes higher, the plastic zone also grows larger to cover more slip planes and more extrinsic shielding effects are involved in fatigue crack growth. In addition, environmental effects are able to have interactions with temperatures on formed crack wakes.

7.3.1 Effect of temperature and environment at $R=0.1$ and 0.5 :

At RT, the fatigue crack growth resistance curves (FCGRCs) at all R ratios show similar characteristics to brittle materials (see in Figure 6.9 for $R=0.1$ and Figure 6.14 for $R=0.5$). The three fatigue crack growth regimes are not distinctive and m values (see Table 6.4) are highest among test temperatures. The m values can be interpreted as high sensitivity to applied stress intensity factor range. In contrast to the FCGRCs of tests at RT, three fatigue crack growth regimes are identifiable at intermediate temperatures ($400\text{ }^{\circ}\text{C}$) and high temperatures ($650\text{--}750\text{ }^{\circ}\text{C}$) as usually seen in ductile materials, even though the ΔK ranges are still small. In addition, as shown in Table 6.4 (a) and (b) the average m values of tests at intermediate and elevated temperatures are also apparently lower than those at RT for a same R ratio. All the findings on FCGRCs indicate an involvement of increased plasticity at elevated temperatures.

Although the Figure 6.23 and Figure 6.24 may give the impression that the slopes of FCGRCs at $400\text{ }^{\circ}\text{C}$ are slightly flatter than those at high temperatures, actually, the average m values of tests at 400 and $650\text{ }^{\circ}\text{C}$ are similar, and are slightly lower than those at $700\text{ }^{\circ}\text{C}$ (see Table 6.4), because a single FCGRC usually cannot fully represents every situation for a test condition. Hence, repeated tests are necessary for characterising the fatigue behaviour of γ -TiAl alloys.

Generally, at high temperature the highest average m values are found at $750\text{ }^{\circ}\text{C}$ (6.0 for $R=0.1$ and 5.8 for $R=0.5$). The increase of m values at higher temperatures is associated with increasing environmental influence. Liu et al. reported that the degree of oxidation

increases with increasing temperature in TiAl alloys [130]. Early studies [131] show that significant penetration of oxygen can result in interstitial embrittlement and thereby degrades the mechanical properties of γ -TiAl alloys. An order of magnitude higher FCGR was found in air as compared to the results in vacuum for gamma alloys (K-5 and Ti-47Al-1.5Cr-2Nb) [113, 132]. Similar results were also observed from the in-house tests carried out by Pardhi as shown in Figure 7.1. However, the mechanisms of the environmental effects behind the higher FCGR in air are not clear for this alloy.

Another in-house investigation carried out by Ding shows the existence of oxides on the fracture surface of a specimen tested at 700 °C in this study, as shown in Figure 7.2. There are two oxidation mechanisms distinguished according to the depth of damage ahead of the crack tip, which are short-range diffusion oxidation and long-range diffusion oxidation [133]. The short-range diffusion is associated with the oxides at the crack tip and may result in grain boundary embrittlement. The long-range diffusion of oxygen ahead of the crack tip could cause localise damage [133]. As shown in Figure 6.32, Figure 6.33 and Figure 6.36, the slightly rougher fracture surfaces found at 750 °C at both R=0.1 and 0.5 may be caused by the oxidation related embrittlement and more severe damage ahead of the crack tip at such a high temperature.

7.3.2 Effect of temperature on extrinsic mechanisms

The fracture surfaces generated at RT are slightly rougher with more multiple-angled interlamellar fractures and the crack path is also more torturous at RT (at R=0.1) than for those tests at higher temperatures. As observed in Figure 6.42, the crack path at RT can be more easily deviated by either lamellar interfaces or colony boundaries, and the numbers of microcracks observed around the main crack. Crack branching, deflection and meandering caused by microcracking at weak-oriented colonies are common extrinsic shielding effects in intermetallics [4]. These extrinsic shielding mechanisms can impede the fatigue crack propagation and subsequently reduce the crack growth

rate. At 400 °C, crack branching and deflection can still be discovered, whereas microcracks are no longer visible around the main crack. At 650 °C, neither microcracks nor obvious crack branching and deflection can be observed along and around the main crack. The crack morphologies at different temperatures imply that any extrinsic shielding effects are reduced as the temperature increases. Hence, for an R ratio of 0.1 and 0.5, the FCGRs are lowest at RT in low and intermediate ΔK range. However, as K_{max} increases with increasing crack length, the extrinsic shielding becomes less comparable to the high static driving force. Due to the lack of ductility at RT, the FCGRs surpass the curves at 400 °C and get close to the curves of high-temperature tests at high ΔK range.

7.3.3 Effect of temperature at R=0.8

The FCGRs at an R ratio of 0.8 show different behaviour compared to the FCGRs at an R ratio of 0.1 and 0.5. For a given ΔK value, the FCGRs become getting lower as test temperature increases. All tests at R=0.8 show a ‘valley’ of FCGR in FCGRs. This kind of reduction is more significant at 650 °C and 700 °C. It has been confirmed that crack closure effects do not exist at this high R ratio [103]. Based on the observations above, there must be retardation mechanisms at high temperatures which are high- K_{max} level associated and also increase with increasing temperature.

Several features found in the test of specimen CC009-T which was carried out at 750°C with an R ratio of 0.8, such as extremely slow deformation rate (as mentioned in section 6.8.1), degradation of lamellar microstructure and precipitates on the side surface (see in Figure 6.61), indicated that it failed in a creep manner. Moreover, the result of specimen CC008-T tested at 700 °C indicates that a certain degree of creep is also available at 700 °C with an R ratio of 0.8. McKelvey [101] reported ‘anomalous behaviour’ found in a near fully lamellar XD alloy at 800 °C with lower R ratios (0.1, 0.3 and 0.5). According to the comparison between calculated value and experimental

data of transition time, it was revealed that creep was significant at 800°C which resulted in crack-tip blunting and the subsequent reduction in the near-tip stress field. Zhu et al. [105] also pointed out the K_{\max} dependent crack growth is creep-fatigue related at elevated temperatures. Creep deformation ahead of the crack tip tends to relax the stress concentration. The reasons for crack growth in a creep manner even under a fatigue loading condition are: (1) at $R=0.8$ the static driving forces (K_{\max}) are high, about $2.8 \text{ MPa}\cdot\text{m}^{1/2}$ lower than the K_C values on average, and even the K_{\min} values are all above $11.0 \text{ MPa}\cdot\text{m}^{1/2}$; (2) Previous studies found the temperature range above which creep deformation becomes significant for two-phase ($\gamma+\alpha_2$) TiAl alloys was 650-700°C [134]. At 750 °C the highly increased plastic flow can result in large creep deformation as seen in specimen CC009-T.

Generally, the brittle-ductile transition temperature (DBTT) in γ -TiAl alloys ranges between 600 and 800 °C [7, 101, 113]. Although no exact values of DBTT have been obtained for this Ti-4522XD alloy, specimens tested at both 650 °C and 750 °C with an R ratio of 0.8 all show different levels of crack-tip blunting and FCGR retardation (see in Figure 6.21 and Figure 6.22). Based on the observations above, it can be deduced that, at $R=0.8$, near the DBTT the fatigue crack growth behaviour is mainly dominated by fatigue mechanisms while creep is also available in certain degrees. At or above the DBTT creep becomes the predominant mechanism on fatigue crack growth as a consequence of increasing temperature.

7.3.4 Effect of R ratio on stable fatigue crack growth

The comparisons of FCGRs at RT-750 °C for different R ratios are shown from Figure 6.26 to Figure 6.30. At all test temperatures, for the same ΔK value, the FCGRs of tests at $R=0.5$ are nearly always higher than the FCGRs of tests at $R=0.1$. This difference is highlighted particularly at RT and reduced at the higher test temperatures. For the tests at $R=0.8$, the FCGRs are highest among the tests at RT and 400 °C, while

lowest at 650 °C and 700 °C. Thus fatigue crack growth appears to be dependent on both ΔK and K_{\max} . However, FCGRs do not collapse when plotted versus K_{\max} at the same test temperature (see Figure 7.3 - Figure 7.7). Below 650 °C, for an equivalent ΔK value, a higher R ratio means a higher K_{\max} value which leads to higher FCGRs. As temperature increases, the mobility of dislocations also increases because the thermal-assisted movement of dislocation cross-slip and climb are raised [135]. This has been evidenced at R=0.1 and 0.5 by reduction in FCGRs differences at intermediate temperature and high temperatures. The different fatigue crack growth behaviours at R=0.8 have been explained above as static fracture related mechanisms at low and intermediate temperature (RT and 400 °C) and fatigue-creep interaction resulted crack blunting and retardation at high temperatures (≥ 650 °C).

7.4 Fracture toughness

In this study, the K_{IC} values at different temperatures do not exhibit significant differences between each other. This temperature independence of fracture toughness was explained by Appel [56]. In lamellar alloys, the major toughening mechanisms, such as ligament bridging, crack deflection, surface-roughness induced contact, involve a process zone containing several colonies, are microstructure related, can be barely affected by temperature. Additionally, the lamellar morphology cannot be significantly changed on a mesoscopic scale. In spite of higher interface-related plasticity ahead of the crack tip which may be achieved at high temperatures due to an increase of thermal activation related dislocation mobility, this toughening is not comparable to the inherent high toughening level in lamellar alloys at RT. Thus, the fracture toughness is weakly dependent on temperature. No obvious distinctions on the fracture surfaces which were generated under monotonic loads at different temperatures further prove that fracture toughness is weakly dependent on temperature in this alloy.

7.5 Small fatigue crack considerations in near fully lamellar γ -TiAl alloys

Two tests at RT and three tests at 650 °C were carried out with an R ratio of 0.1 in smooth specimens to investigate naturally-initiated fatigue cracks in this lamellar TiAl alloy. This gives opportunities to see if the procedure of interlamellar fracture growing into general translamellar from naturally-initiated cracks is consistent with the previous description and assessment of ΔK_{th} .

7.5.1 Natural-initiated small fatigue cracks

It has been reported by several authors that fatigue cracks usually initiate from a lamellar interface at orientations along the maximum loading axis in lamellar TiAl alloys [76, 77]. Apart from such weak-oriented colonies, early crack growth will be affected by the crystallographic orientation of the neighbouring colonies. These surrounding colonies could either accelerate (poor oriented) or retard crack progress (translamellar with interlamellar failure perpendicular to the fracture plane). The specimen HF901 failed at a maximum stress of 425 MPa which was 50 MPa lower than specimen HF902 tested under a same condition (R=0.1 and RT). In specimen HF901, 3-4 conjoined colonies at favourable angles were observed on the edge of the fracture surface as shown in Figure 6.53. The approximate ΔK_{th} value of specimen HF901 was $6.1 \text{ MPa.m}^{1/2}$ which is similar to the average ΔK_{th} value ($6.5 \text{ MPa.m}^{1/2}$) of CC specimens under the same test conditions.

In HF902, the crack probably initiated at multiple single large weak-oriented colonies and failed by translamellar cracks joining up with main cracks. Although no conjoined weak-oriented colonies were observed in specimen 5C2 (R=0.1 and 650 °C), three interlamellar cracks were found at the crack initiation site. Jha [76] found that the crack was likely to nucleate in the γ/α_2 interface, which is consistent with an earlier study carried out by Huang [136]. The possible reasons were proposed as the γ - α_2 interface

has a higher chemical energy for changes and more of an obstacle to slip than γ - γ interface. Thus dislocations are more difficult to cross the γ - α_2 interface leading to pile-up at lamellar interfaces.

Similar embedded fatigue crack initiation site as seen in specimen HF901 was also found in specimen HF905 tested at 650 °C. The calculated ΔK_{th} value for this specimen is 6.4 MPa.m^{1/2} which is again closely similar (0.6 MPa.m^{1/2} higher) to the average ΔK_{th} value of CC specimens (see in Table 6.2 (a)).

Beside of several conjoined and close-located large weak-oriented colonies, clusters of inclusions is the other possible cause for the naturally-initiated fatigue cracks as found in the specimen HF904 tested at 650 °C (see in Figure 6.55). The estimation of ΔK_{th} value was also made by considering the inclusions acting cooperatively as a single crack initiation site, which gives a ΔK_{th} value of 6.6 MPa.m^{1/2}. This value is once more similar to the result of specimen HF905 and also falls into the ΔK_{th} range of CC specimens (see in Table 6.2 (a))

The ΔK_{th} values of tests in smooth specimens as shown above indicate that the crack growth of naturally-initiated small fatigue cracks probably follow similar fatigue crack growth behaviour to that seen in CC specimens. The ΔK_{th} value is the minimum stress intensity factor range that allows interlamellar fractures or cooperative inclusion cluster to grow into general translamellar fractures.

In addition, several gathered large inclusions as found in specimen 5C2 (show in Figure 6.57 (b)) could significant raise localised stress concentrations and so cause crack initiation.

7.5.2 Small fatigue cracks behaviour

Many authors have addressed the small fatigue crack issues in γ -TiAl alloys [39, 40, 53, 97, 105]. All these investigations show that small fatigue cracks behave different from long fatigue cracks in lamellar γ -TiAl alloys, such as lower fatigue threshold values and higher FCGRs, which are explained as lack of crack wake associated extrinsic toughening effects.

In this study, there was no obvious influence of notch size on both ΔK_{th} values and FCGRs at RT and 650 °C as shown in Figure 6.45 and Figure 6.46. These indistinctive results are all due to intrinsic properties dependence as mentioned above. Therefore, if the microstructures are similar around the notches in these specimens, there should be no significant differences of fatigue properties, and this is confirmed in present study. Although, at fatigue threshold, higher loads are required to grow a crack for specimens with short notches (0.1-0.2 mm in depth) (as shown in Table 6.6), the cracks all start growing from the notches. In addition, FCGRs of these specimens all show similar behaviour as specimens with long notches exhibit no rapid rupture. It worth noting that short notch fronts can cover fewer colonies than long notches, thus the ΔK_{th} value of specimens with short notches should be more sensitive to the colony orientation ahead of the notch. It can be deduced that in the absence of colonies at mode I orientation in front of the notch, the notch depth does not have obvious effect on ΔK_{th} values and FCGRs in near-fully lamellar TiAl alloys.

The naturally-initiated small cracks are more representative for the actual small cracks in components. As mentioned above, these results are consistent with the range of ΔK_{th} values measured from CC specimens tested at same conditions.

Actually, when referring to small cracks, there are several standards to define small cracks as mentioned in section 3.6. However, these definitions all focus on the length or size of cracks, none of them stress the difference of morphology between the ‘small’

and ‘long’ crack. As for CC specimens, even the notches can be regarded as cracks in a component, the actual length of crack wake which can remain closed after removing the fatigue load barely exists. The differences of fatigue crack threshold and growth between ‘small’ and ‘long’ cracks in a lamellar TiAl alloy are mainly caused by extrinsic toughening mechanisms in the crack wake, such as roughness-induced crack closure, unbroken ligaments induced bridging effect, crack deflection and branching [53, 97, 105]. However, the total crack size is not equivalent to the crack wake size as defined in Figure 7.8. The difference between total crack length and crack wake length is whether the crack surfaces can have interactions during a fatigue loading. In fact, the ‘small crack’ effects addressed in previous studies are referred to the length/size of crack wake rather than total crack length. Therefore, for a fatigue crack starts directly from a notch in any geometry (such as CC and SENB), even the notches are long enough to be called ‘long crack’, the fatigue properties should be regarded as for ‘small crack’ instead of ‘long crack’.

7.5.3 Practical concerns of small cracks in near fully-lamellar γ -TiAl alloys

For γ -TiAl alloys which exhibit relative steep FCGRCs as a function of ΔK compared to conventional ductile materials, the fatigue threshold has been widely acknowledged as the most important aspect for engineering designs [73, 87, 137]. In practice, engineering components are always well manufactured to avoid large defects, thus failures usually start with small cracks or defects which may be induced by external impacts, manufacturing defects or naturally-initiated fatigue cracks. For the reasons above, the characterisation for the fatigue threshold of small cracks are necessary for deciding the magnitude of tolerable cyclic-stress levels in damage-tolerance approach.

In this study, the largest naturally-initiated fatigue crack is about 4 conjoined colonies which are large enough to result in a fatigue failure. Several adjacent colonies at near mode I direction within a small area have a chance to cause unexpected fatigue failure

in lamellar TiAl alloy. For the fatigue critical applications such as aero engines, increased attention should be paid to the control of microstructure in order to avoid such kind of weak microstructural units in lamellar TiAl alloys. Furthermore, the estimation of ΔK_{th} values for the engineering design purposes must take this kind of small cracks (about 3-4 colonies) as lower limit of crack length instead of those crack size calculated using the ΔK_{th} values of long cracks.

7.6 General discussion

In this study, a consistent increasing- ΔK procedure was applied to minimise crack wake effects. Most of the tests were started directly from notch. Limited number of tests was carried out from pre-cracks which were less than 100 μm of growth ahead of notch before tests, and these pre-cracks have proved to have no obvious influence on the ΔK_{th} values.

This Ti-4522XD alloy exhibits clear and consistent trends of fatigue crack threshold and growth behaviour under different fatigue conditions as presented. This is a consequence of consistent microstructure and the testing method. Such repeatability of results is vital for the prediction of critical crack length and applied stress based on the damage-tolerance approach. The relatively fine lamellar structure does have an improvement over the fatigue properties compared to coarse-grain lamellar TiAl alloys studied previously [123], higher ΔK_{th} values and lower m values. Although the FCGRs are steep and the extent in ΔK is small which lead to difficulties for the implements of this alloy in practice, an accurate prediction of ΔK_{th} values could still enable the working stresses well controlled below the fatigue threshold level, thus allows this alloy to be used in adaptive applications.

Creep predominant crack growth and creep-fatigue interaction affected crack growth were found at elevated temperature (≥ 650 °C), especially at R ratio of 0.8. More effort should be made to improve the creep resistance for γ -TiAl based alloys as they are

considered to be used in applications with service temperatures in the range of 650-750°C [56].

Interlamellar fractures play an important role on determining fatigue crack initiation. Colony orientations along mode I direction can easily generate interlamellar fractures at $\Delta K \leq \Delta K_{th}$. At both RT and elevated temperature, such interlamellar cracks can act as fatigue crack initiation sites and have chance leading to final failure if driving force is high enough to enable them propagate into general translamellar fractures, especially when 3-4 of these interlamellar cracks are linked (examples: HF901 and HF905). However, some questions about can they act jointly if close together (example: 5C2) need to be answered by future work. In addition, attentions should be paid on controlling cleanliness of TiAl based alloys since cluster of inclusions can result in similar effect on fatigue crack initiation as conjoined interlamellar fractures (example: HF904).

Above all, the engineering design should take ΔK_{th} of small fatigue cracks as lower limited for calculating the critical crack length in lamellar γ -TiAl based alloys. In this way, any significant crack wake effects can be avoided.

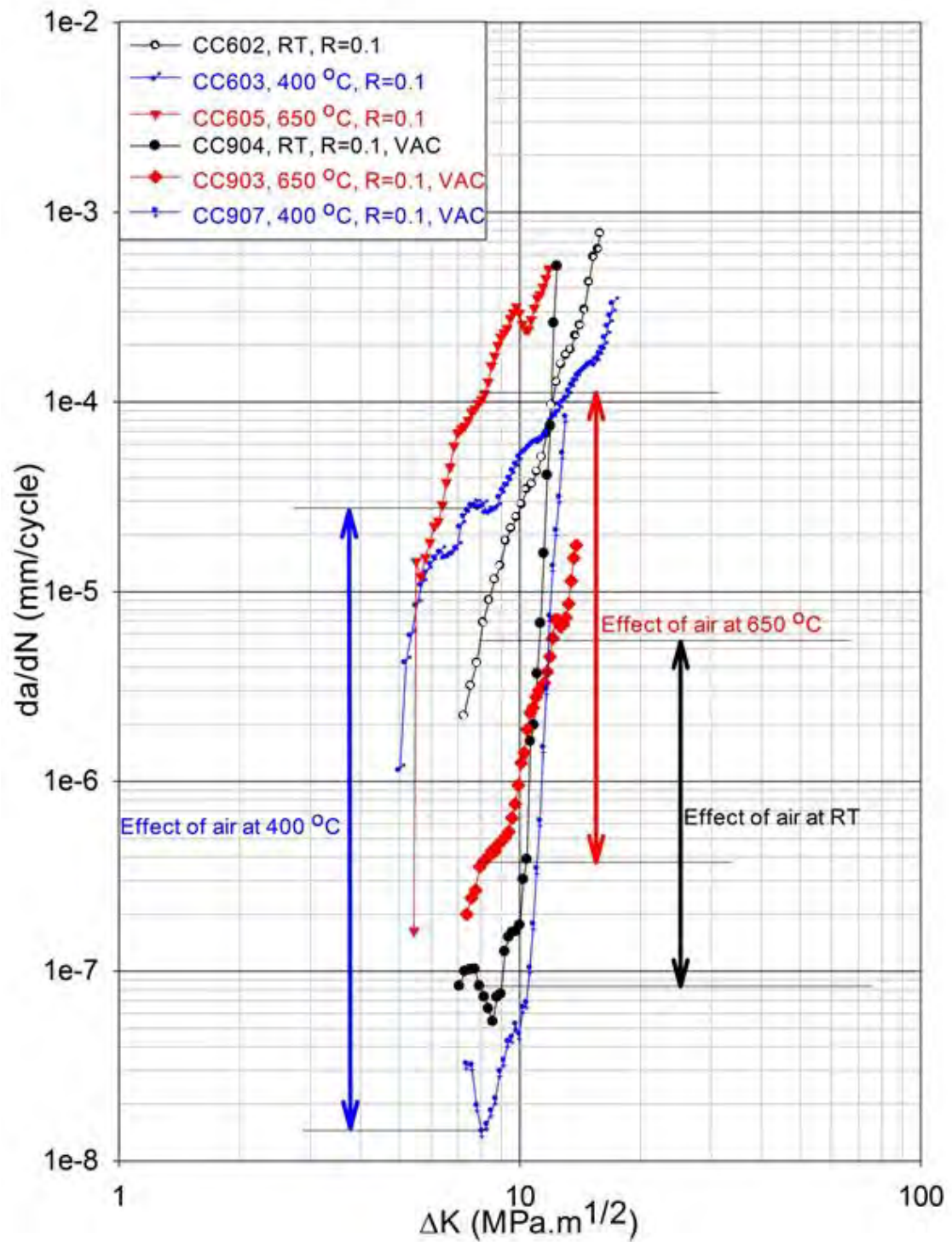
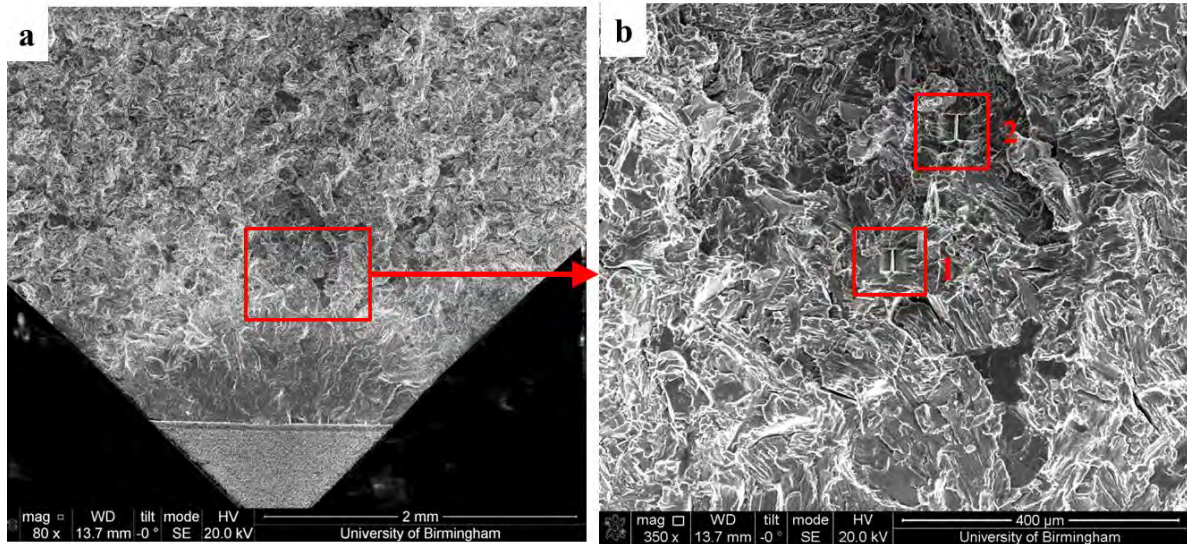


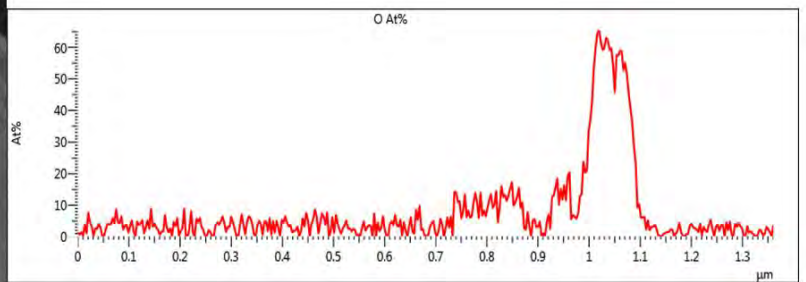
Figure 7.1. Fatigue crack growth resistance curves of specimens tested in vacuum at RT, 400 and 650 °C with an R ratio of 0.1, are compared to results obtained in air under the same test conditions.



Electron Image 1



Oxidation analysis of site 1



Electron Image 2



Oxidation analysis of site 2

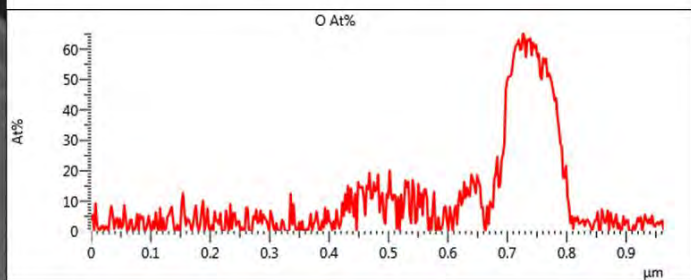


Figure 7.2. TEM foils taken from the fracture surface of specimenS tested at 700 °C with an R ratio of 0.8: (a) the fracture surface taken along crack growth direction, (b) two sites where the TEM foils were taken, and results of oxidation analysis of site 1 and 2

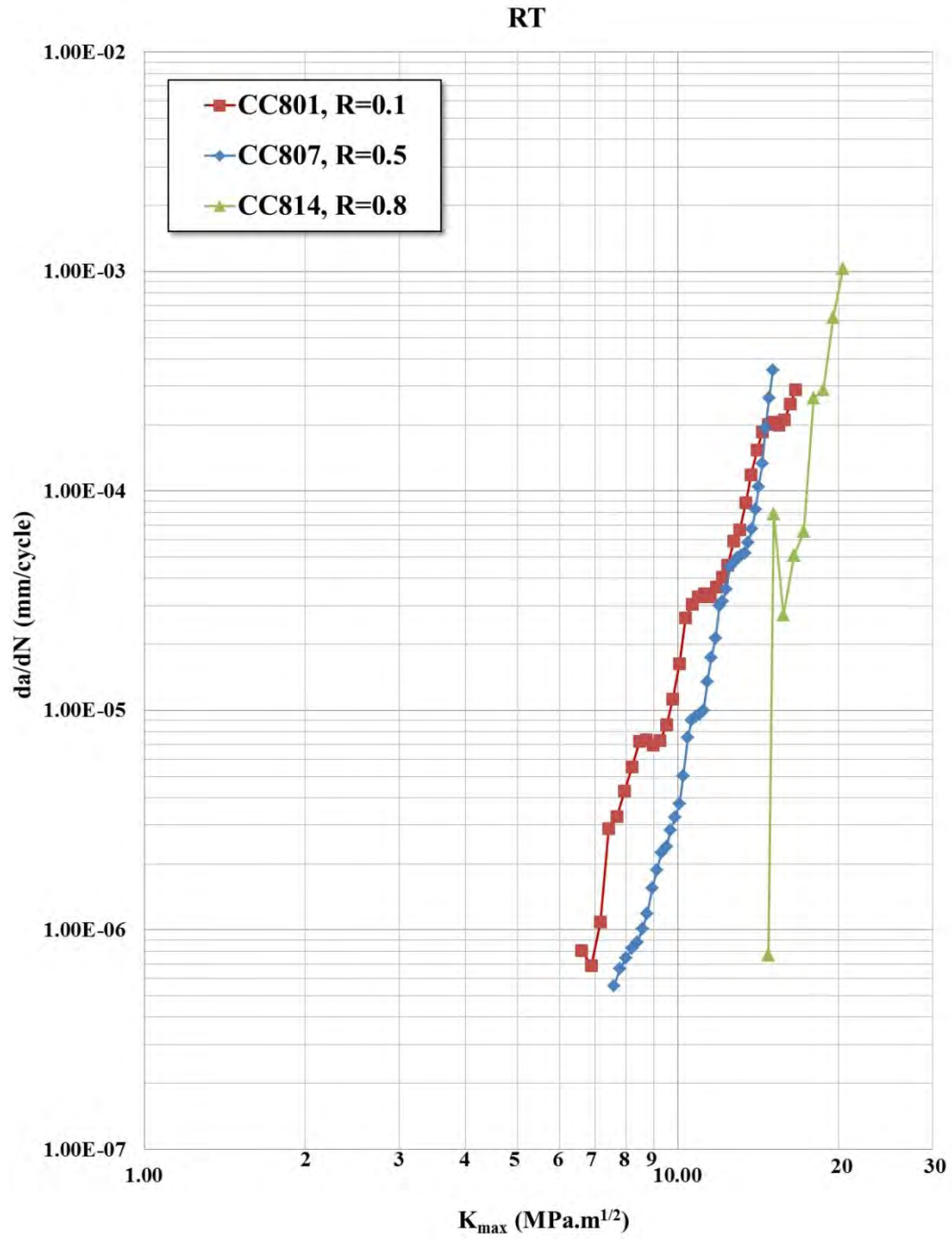


Figure 7.3. Fatigue crack growth resistance curves plotted as a function of K_{\max} for different R ratios (0.1, 0.5 and 0.8) and at RT

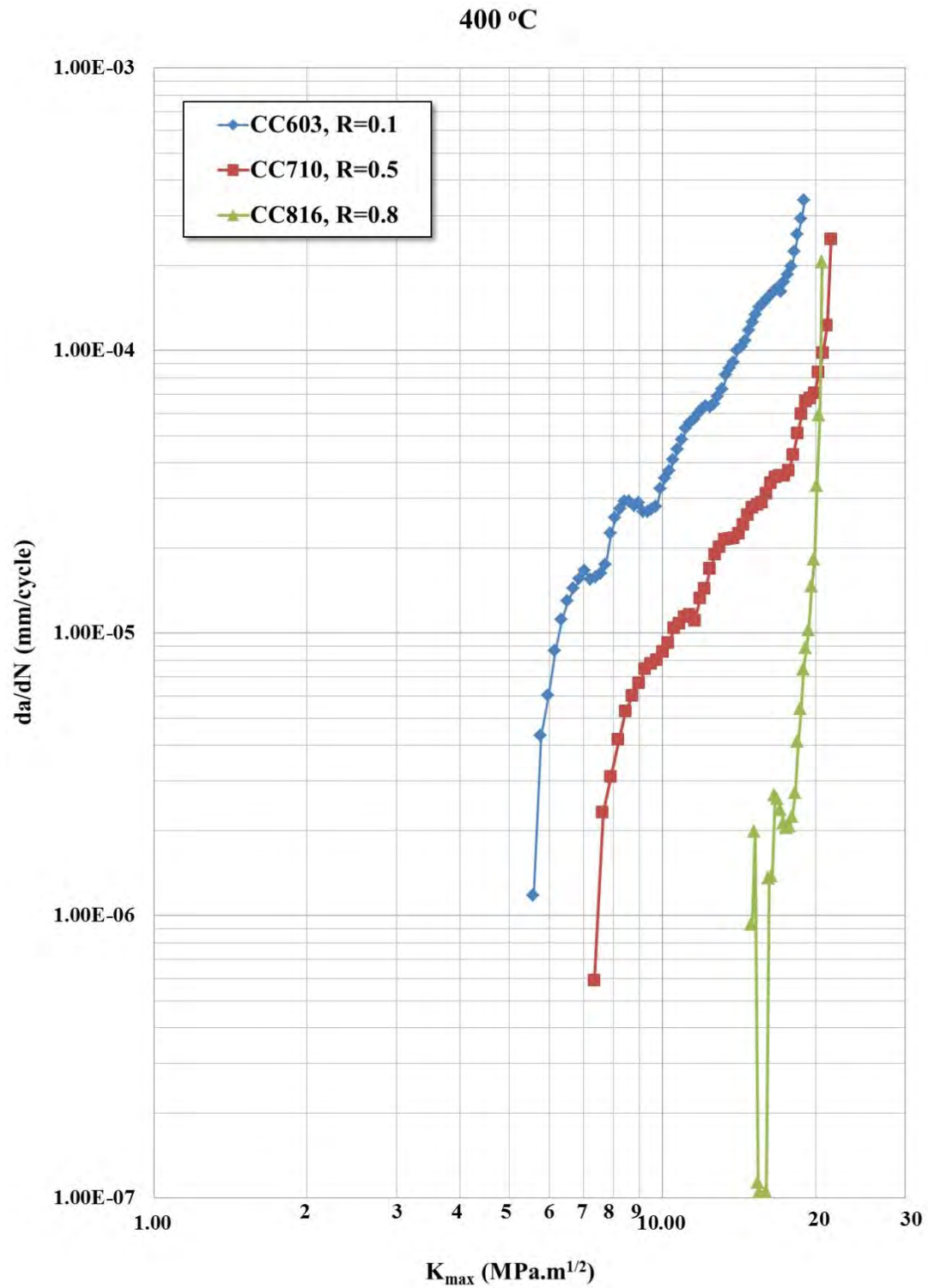


Figure 7.4. Fatigue crack growth resistance curves plotted as a function of K_{max} for different R ratios (0.1, 0.5 and 0.8) and at 400 °C

650 °C

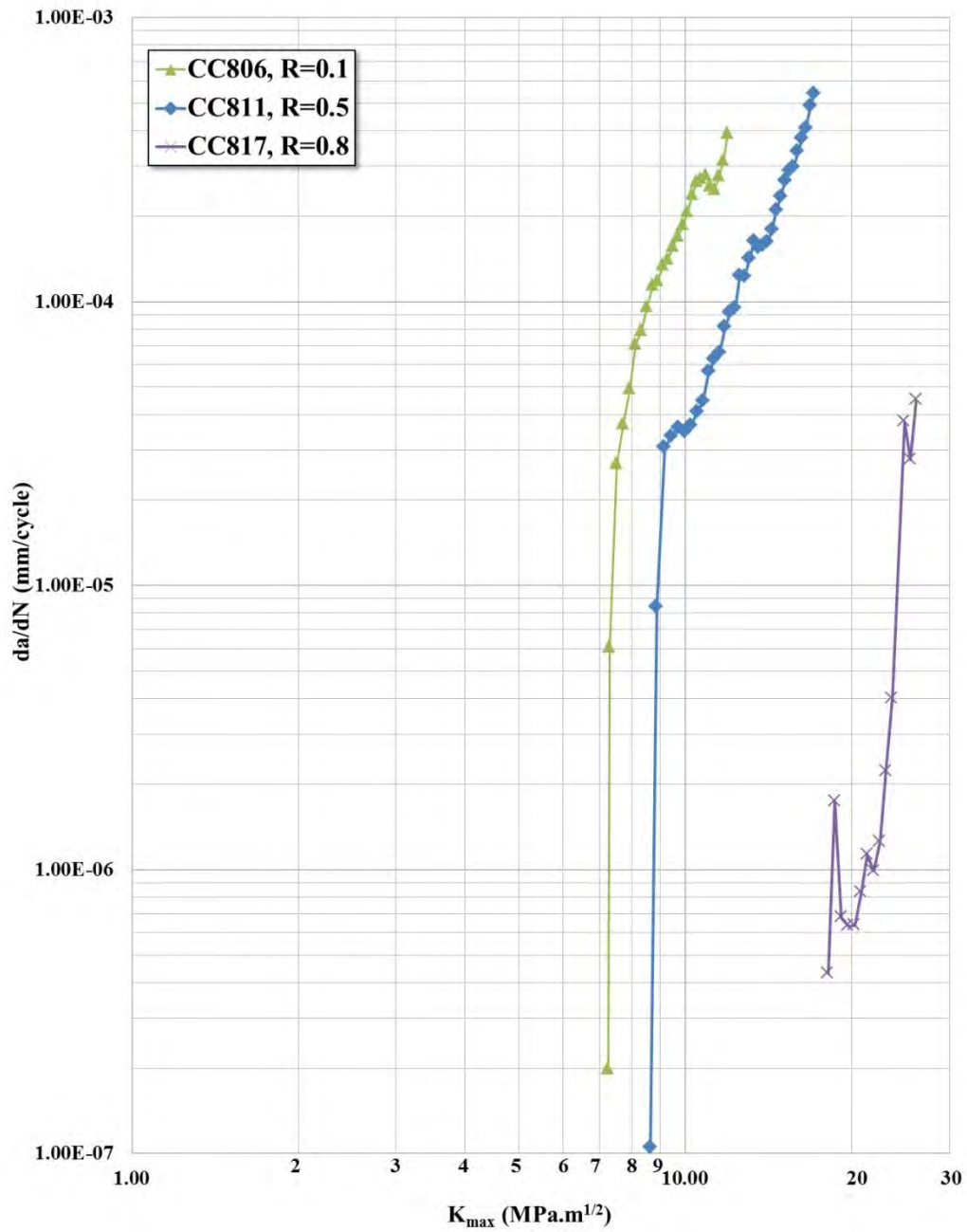


Figure 7.5. Fatigue crack growth resistance curves plotted as a function of K_{\max} for different R ratios (0.1, 0.5 and 0.8) and at 650 °C

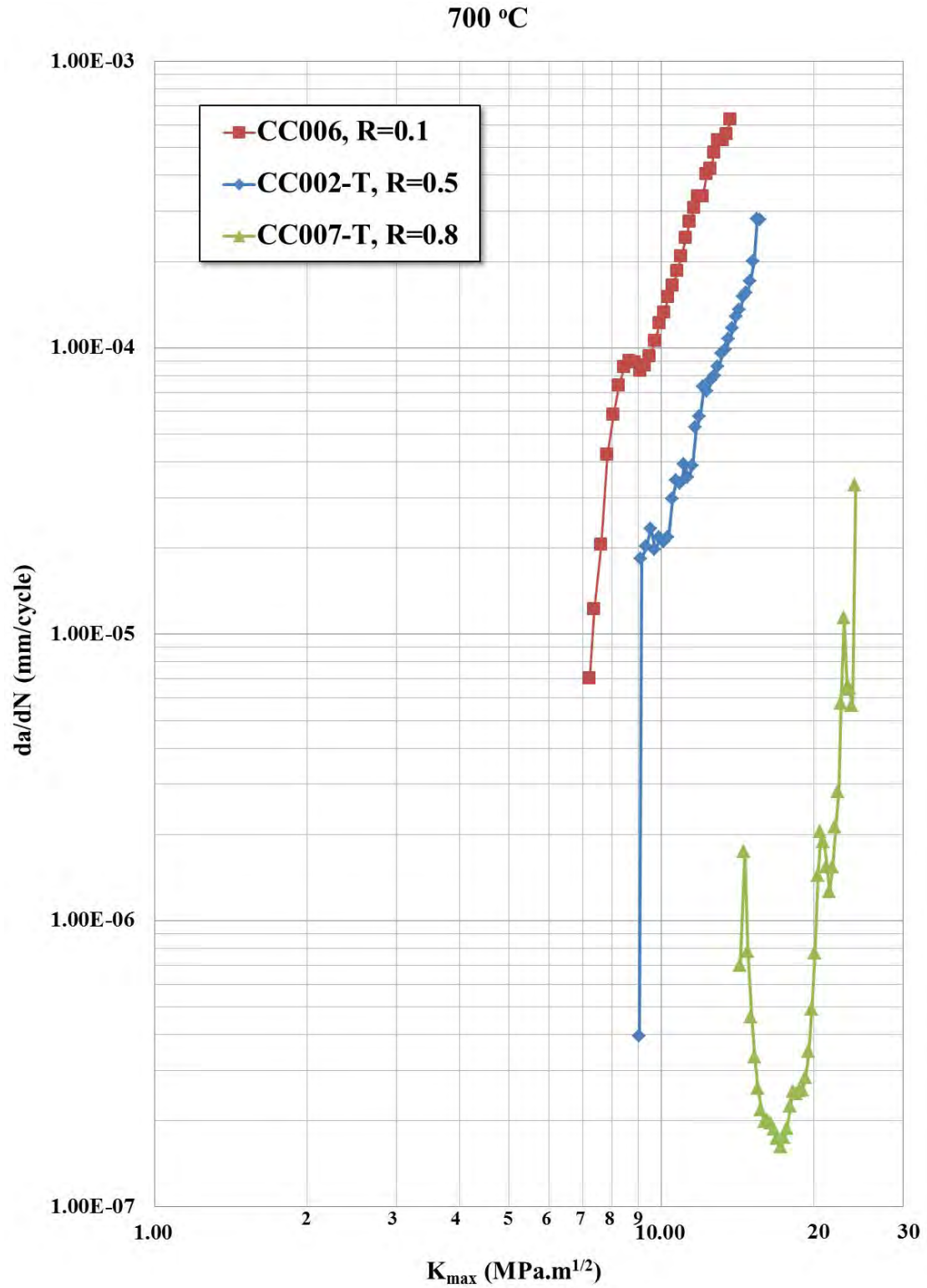


Figure 7.6. Fatigue crack growth resistance curves plotted as a function of K_{max} for different R ratios (0.1, 0.5 and 0.8) and at 700 °C

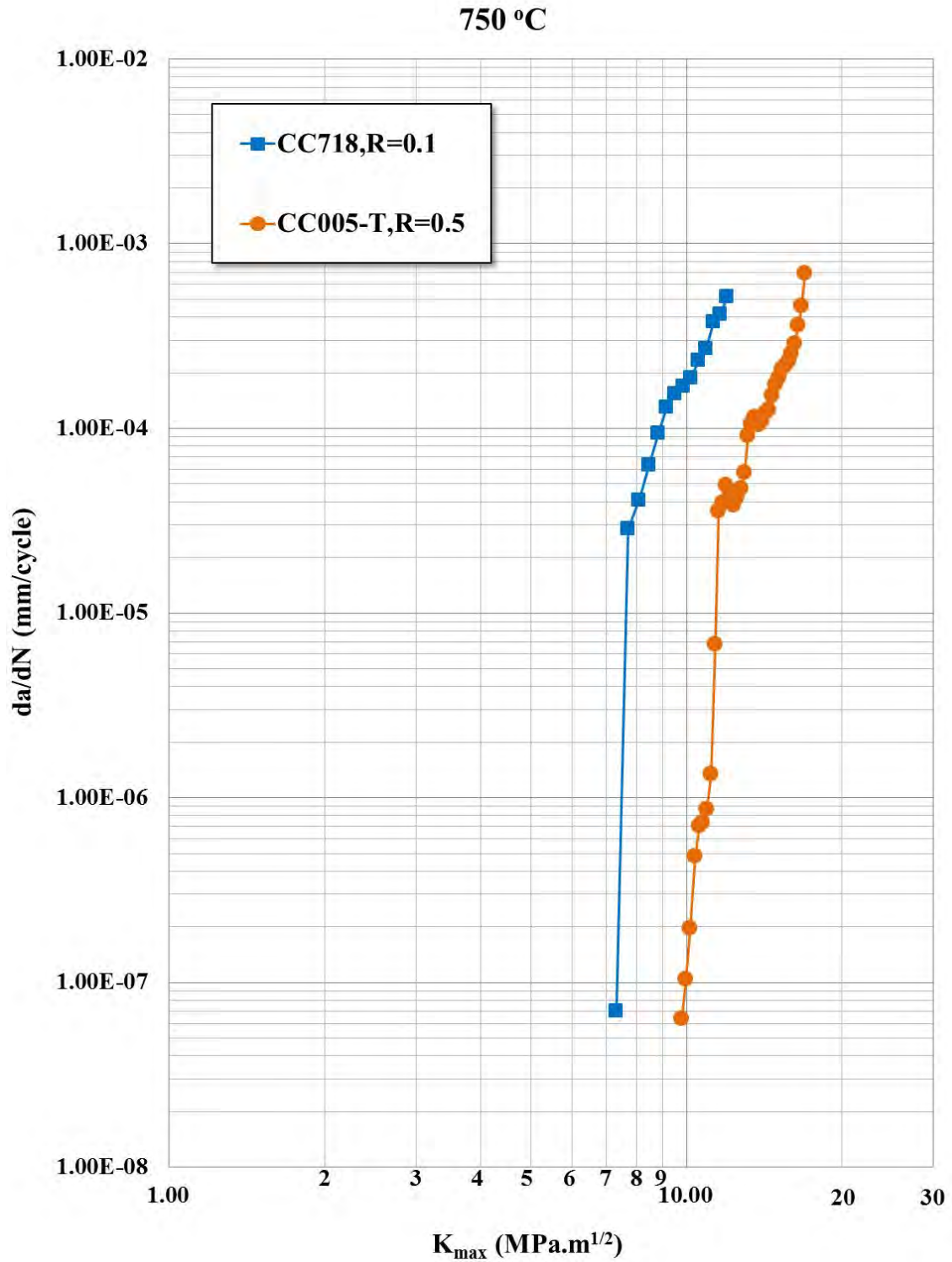


Figure 7.7. Fatigue crack growth resistance curves plotted as a function of K_{max} for different R ratios (0.1, 0.5 and 0.8) and at 750 °C

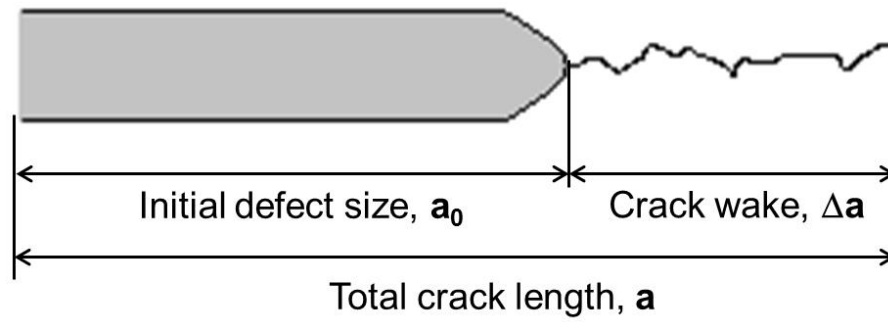


Figure 7.8. Schematic definitions of different parts in a crack (Note that fatigue pre-cracks prior to ΔK_{th} assessment were always less than 100 μm)

8. Conclusions

The fatigue crack threshold and growth behaviour of a near fully-lamellar γ -TiAl alloy (Ti-4522XD alloy) with an average colony size of 78 μm has been investigated in air at five temperatures (room temperature, 400, 650, 700 and 750 $^{\circ}\text{C}$) and at three R ratios (0.1, 0.5 and 0.8) in this study. The fatigue crack growth behaviour of both corner-cracked specimens and from naturally-initiated cracks in smooth specimens are considered.

1. A consistent material microstructure, use of a standardised ΔK - increasing loading method and sufficient numbers of tests make the trends in fatigue threshold and crack growth behaviour consistent and repeatable. Thus for the first time the trends have been established in a comprehensive study on a 'single' microstructure in TiAl.
2. For a given R ratio, there is little effect of test temperature on ΔK_{th} values. Average values, obtained across the temperature range of up to 750 $^{\circ}\text{C}$, are 6.1, 4.5 and 3.3 $\text{MPa}\cdot\text{m}^{1/2}$ at R ratios of 0.1, 0.5 and 0.8, respectively.
3. The 'start-and-stop' phenomenon observed routinely for near threshold crack growth at room temperature is deduced to be because cracks are arrested at colonies with orientations away from the mode I crack propagation direction. Such cracks are forced to progress across (translamellar) colonies. Continuous crack growth requires such translamellar progression.
4. Average ΔK_{th} values decrease with increasing R ratio up to 750 $^{\circ}\text{C}$. Average values, are 6.1, 4.5 and 3.3 $\text{MPa}\cdot\text{m}^{1/2}$ at R ratios of 0.1, 0.5 and 0.8, respectively. In the current study, this is interpreted as demonstrating that fatigue crack growth can have a dependency both on the cyclic stress range and on the maximum stress applied over the cycle.

5. In terms of the fatigue crack growth resistance curve, the steepest Paris exponent (m) values, 7.2 and 8.6 for $R=0.1$ and 0.5 respectively, are found at room temperature. At this test temperature a conventional three-region resistance curve is not easily seen and there is a strong dependence of crack growth rates on K_{\max} values.
6. A three-region resistance curve is seen at elevated test temperatures up to 750°C. Over much of the temperature range from 400 to 700 °C, lower Paris exponent (m) values are now obtained: typically 3.6, 3.7 and 4.4 for tests at 400, 650 and 700 °C at $R=0.1$, respectively; 3.0, 3.8 and 4.8 for 400, 650 and 700 °C at $R=0.5$, respectively. This observation is considered to be consistent with an increased amount of plasticity available to contribute to the fatigue crack growth resistance at elevated temperature. At these temperatures a reduced dependence on K_{\max} values is observed. At the higher test temperature of 750 °C, values of the Paris exponent (m) increase, 6.0 and 5.8 for $R=0.1$ and 0.5 respectively. This observation is considered to be consistent with an increased contribution of oxidation induced damage ahead of the crack tip.
7. In all tests at $R=0.8$, K_{\max} approaches the critical value of K for catastrophic failure under monotonic loading. This leads to high values of the Paris exponent (m) value where they can be measured reliably. For example, m values of 26 and 14 are obtained at room temperature and 400 °C respectively. This is deduced to emphasise the role of static failure modes even under fatigue loading. At still higher temperatures (650 and 700 °C) crack tip blunting occurred and at the highest test temperature (750 °C) creep crack growth became the predominant failure mechanisms.
8. Consistent with the similar brittle fracture mechanism observed at all test temperatures, ‘fracture toughness’ values (17.8 – 20.3 MPa.m^{1/2}) were independent of test temperature in this study. Similar fracture mechanisms (interlamellar and

translamellar fracture) are thus observed under both catastrophic failure and fatigue crack growth conditions.

9. Although there is no marked difference in microstructure on any fracture surfaces, evidence of critical sites of interlamellar failure can be seen in the initiation of small cracks and they can subsequently propagate to cause failure. However, these interlamellar cracks need to grow out across the colonies (translamellar growth) to cause failure. The values of ΔK at which such interlamellar cracks grow to failure are consistent with ΔK_{th} values measured for corner-cracked specimens.
10. The largest size of conjoined interlamellar fractures found in this alloy is from 3-4 colonies. These can be large enough to grow eventually to cause failure. Thus defects of the order of 400 μm must be assumed to be present in testpieces. Cleanliness is also important for the performance of this alloy since clusters of inclusions can also initiate fatigue cracks.
11. This near fully-lamellar γ -TiAl alloy is possible to be used at modest stresses as defined by a combination of design stress range and defect size through ΔK_{th} values. For example, a surface breaking defect of size 320 μm is likely to propagate only at an applied stress range of 260, 230 and 180 MPa for R ratios of 0.1, 0.5 and 0.8 respectively.

9. Future works

Mechanical tests

- A number of tensile tests is required at different temperatures (RT, 400 °C, 650 °C, 700 °C and 750 °C, or even higher temperatures). This may help to obtain more accurate fracture toughness values at each temperature, and determine the DBTT for this Ti5422XD alloy.
- It may be helpful to perform some vacuum tests under test conditions which are consistent with this study. By comparing fatigue behaviour in air and vacuum the environmental influence could be revealed.
- Fatigue tests on smooth cylindrical specimens at three different temperatures (RT, 400 °C and 650 °C) with an R ratio of 0.5 could be carried out to find out whether naturally-initiated cracks still show the same features as those observed at R=0.1.
- Although the comparison has already been done between load-increasing and load-shedding procedures for the single-edge bend specimens by Po-Sri [124], some tests using a load-shedding procedure on CC specimens could also be necessary to investigate the effect of loading method for this geometry.

Mathematical analysis

- As large quantity of data have been generated for ΔK_{th} values under various test conditions. Mathematical methods can be introduced to establish mathematical relationships between influential factors, such as R ratio and temperature, and ΔK_{th} values.
- Statistics on how colony orientation along the notch tip affects the ΔK_{th} values, can be carried out to help understand the divergence of ΔK_{th} values.

References

1. Backman, D.G. and J.C. Williams, *Advanced Materials for Aircraft Engine Applications*. Science, 1992. **255**(5048): p. 1082-1087.
2. Lasalmonie, A., *Intermetallics: Why is it so difficult to introduce them in gas turbine engines?* Intermetallics, 2006. **14**(10–11): p. 1123-1129.
3. Sauthoff, G., *Intermetallics*. 1995: John Wiley and Sons.
4. Ritchie, R.O., *Mechanisms of fatigue-crack propagation in ductile and brittle solids*. International Journal of Fracture, 1999. **100**(1): p. 55-83.
5. Yamaguchi, M., H. Inui, and K. Ito, *High-temperature structural intermetallics*. Acta Materialia, 2000. **48**(1): p. 307-322.
6. Loria, E.A., *Gamma titanium aluminides as prospective structural materials*. Intermetallics, 2000. **8**(9–11): p. 1339-1345.
7. Campbell, J.P., K.T.V. Rao, and R.O. Ritchie, *The effect of microstructure on fracture toughness and fatigue crack growth behavior in gamma-titanium aluminide based intermetallics*. Metallurgical and Materials Transactions a-Physical Metallurgy and Materials Science, 1999. **30**(3): p. 563-577.
8. Kothari, K., R. Radhakrishnan, and N.M. Wereley, *Advances in gamma titanium aluminides and their manufacturing techniques*. Progress in Aerospace Sciences, 2012. **55**(0): p. 1-16.
9. Voice, W., *The future use of gamma titanium aluminides by Rolls-Royce*. Aircraft Engineering and Aerospace Technology, 1999. **71**(4): p. 337-340.
10. Griffith, A.A., *The phenomena of rupture and flow in solids*. Philosophical transactions of the royal society of london. Series A, containing papers of a mathematical or physical character, 1921: p. 163-198.
11. Roylance, D., *Introduction to fracture mechanics*. Department of Materials Science and Engineering, Massachusetts Institute of Technology , Cambridge, 2001.
12. *Front Matter*, in *Fracture Mechanics*, C.T.S.H. Jin, Editor. 2012, Academic Press: Boston. p. i-ii.
13. Erdogan, F., *Fracture mechanics*. International Journal of Solids and Structures, 2000. **37**(1–2): p. 171-183.
14. Perez, N., *Fracture Mechanics*. 2004: Springer.

15. Hills, D.A., et al., *Solution of Crack Problems: The Distributed Dislocation Technique*. 2013: Springer Netherlands.
16. Janssen, M., J. Zuidema, and R. Wanhill, *Fracture Mechanics, Second Edition: Fundamentals and Applications*. 2004: Taylor & Francis.
17. Sun, C.T. and Z.H. Jin, *Fracture Mechanics*. 2012: Academic Press.
18. Suresh, S., *Fatigue of Materials*. 1998: Cambridge University Press.
19. Anderson, T.L., *Fracture Mechanics: Fundamentals and Applications, Third Edition*. 2005: Taylor & Francis.
20. Saxena, A., et al., *Nonlinear Fracture Mechanics: Elastic-plastic fracture*. 1988: ASTM.
21. A.A.Wells, *application of fracture mechanics at and beyond general yielding*. application of fracture mechanics at and beyond general yielding, 1963. **10**: p. 563-570.
22. John, H.B.I., *Developments in Elastic-Plastic Fracture Mechanics and Analysis using R- Curve*. European Journal of Scientific Research, 2012. **75**(1450-216X): p. 346-360.
23. Schijve, J., *Fatigue of Structures and Materials*. 2008: Springer.
24. Campbell, F.C., *Elements of Metallurgy and Engineering Alloys*. 2008: ASM International.
25. Chang, J.B., J.L. Rudd, and A.C.E.-o.F. Testing, *Damage Tolerance of Metallic Structures: Analysis Methods and Applications : a Symposium*. 1984: American Society for Testing and Materials.
26. Totten, G., *Fatigue crack propagation*. Advanced Materials and Processes, 2008. **166**(5): p. 39.
27. McEvily, A. and R. Ritchie, *Crack closure and the fatigue-crack propagation threshold as a function of load ratio*. Fatigue and Fracture of Engineering Materials and Structures, 1998. **21**: p. 847-856.
28. R.G.Forman, V.E.K., R.M.Engle, J. Basic Eng. Trans. ASME, 1967. **89**: p. 459.
29. Hertzberg, R.W., *Deformation and fracture mechanics of engineering materials*. Vol. 89. 1996: Wiley.
30. *Front-matter*, in *Modern Physical Metallurgy (Eighth Edition)*, R.E. Smallman and A.H.W. Ngan, Editors. 2014, Butterworth-Heinemann: Oxford. p. i-iii.

31. Tien, J.K., *Superalloys, Supercomposites and Superceramics*. 2012: Elsevier Science.
32. Halford, G.R., *Fatigue and Durability of Structural Materials*. 2006: ASM International.
33. Mateo, A., et al., *Anisotropy effects on the fatigue behaviour of rolled duplex stainless steels*. International Journal of Fatigue, 2003. **25**(6): p. 481-488.
34. Newman, J.C., et al., *Mechanics of Fatigue Crack Closure*. 1988: ASTM.
35. Shih, T. and R.P.-y. Wei, *A study of crack closure in fatigue*. Engineering Fracture Mechanics, 1974. **6**(1): p. 19-32.
36. Kemp, R.M.J. and G.B.M.o.D.P. Executive, *Fatigue Crack Closure: A Review*. 1990: H.M. Stationery Office.
37. Gray, G.T., Williams, J. C., and Thompson, A. W., Metallurgical Transactions 1983. **14A**: p. 421.
38. Suresh, S., G.F. Zamiski, and D.O. Ritchie, *Oxide-Induced Crack Closure: An Explanation for Near-Threshold Corrosion Fatigue Crack Growth Behavior*. Metallurgical Transactions A, 1981. **12**(8): p. 1435-1443.
39. Ritchie, R. and J. Peters, *Small fatigue cracks: mechanics, mechanisms and engineering applications*. Materials Transactions(Japan), 2001. **42**(1): p. 58-67.
40. Lankford, J., *The influence of microstructure on the growth of small fatigue cracks*. Fatigue & Fracture of Engineering Materials & Structures, 1985. **8**(2): p. 161-175.
41. Ellyin, F., *Fatigue Damage, Crack Growth and Life Prediction*. 1997: Springer.
42. Ritchie, R.O., *Mechanisms of fatigue crack propagation in metals, ceramics and composites: Role of crack tip shielding*. Materials Science and Engineering: A, 1988. **103**(1): p. 15-28.
43. Ravichandran, K.S. and J.M. Larsen, *Influence of mode of initiation on the growth of small surface cracks in titanium aluminides*. International Journal of Fatigue, 1996. **18**(1): p. 9-16.
44. Peralta, P., et al., *Effects of Local Grain Orientation on Fatigue Crack Growth in Multicrystalline fcc Metallic Materials*. Journal of Engineering Materials and Technology, 2005. **127**(1): p. 23-32.
45. Hussain, K., *Short fatigue crack behaviour and analytical models: a review*. Engineering Fracture Mechanics, 1997. **58**(4): p. 327-354.

46. Kim, Y.-W., *Intermetallic alloys based on gamma titanium aluminide*. Jom, 1989. **41**(7): p. 24-30.
47. Mercer, C., J. Lou, and W.O. Soboyejo, *An investigation of fatigue crack growth in a cast lamellar Ti-48Al-2Cr-2Nb alloy*. Materials Science and Engineering a-Structural Materials Properties Microstructure and Processing, 2000. **284**(1-2): p. 235-245.
48. Sawai, T. and A. Hishinuma, *Twin intersection in tensile deformed gamma-TiAl intermetallic compounds*. Journal of Physics and Chemistry of Solids, 2005. **66**(2-4): p. 335-338.
49. Nakano, T., et al., *Classification of gamma-gamma and gamma-alpha(2) lamellar boundaries on the basis of continuity of strains and slip-twinning planes in fatigued TiAl polysynthetically twinned crystals*. Philosophical Magazine a-Physics of Condensed Matter Structure Defects and Mechanical Properties, 2001. **81**(6): p. 1447-1471.
50. Ng, B.C., et al., *The role of mechanical twinning on microcrack nucleation and crack propagation in a near-[gamma] TiAl alloy*. Intermetallics, 2004. **12**(12): p. 1317-1323.
51. Appel, F., et al., *Physical aspects of hot-working gamma-based titanium aluminides*. Intermetallics, 2004. **12**(7-9): p. 791-802.
52. Kim, Y.-W., *Ordered intermetallic alloys, part III: Gamma titanium aluminides*. JOM, 1994. **46**(7): p. 30-39.
53. Kruzic, J.J., J.P. Campbell, and R.O. Ritchie, *On the fatigue behavior of gamma-based titanium aluminides: Role of small cracks*. Acta Materialia, 1999. **47**(3): p. 801-816.
54. Kim, Y.-W., *Effects of microstructure on the deformation and fracture of γ -TiAl alloys*. Materials Science and Engineering: A, 1995. **192-193**, Part 2(0): p. 519-533.
55. Tsuyama, S., S. Mitao, and K.-n. Minakawa, *Alloy modification of γ -base titanium aluminide for improved oxidation resistance, creep strength and fracture toughness*. Materials Science and Engineering: A, 1992. **153**(1-2): p. 451-456.
56. Appel, F., J.D.H. Paul, and M. Oehring, *Gamma Titanium Aluminide Alloys: Science and Technology*. 2011: Wiley.
57. Hanamura, T., R. Uemori, and M. Tanino, *Mechanism of plastic deformation of Mn-added TiAl L 1 (0)-type intermetallic compound*. Journal of Materials Research, 1988. **3**: p. 656-664.

58. Soboyejo, W., et al., *An investigation of the fatigue and fracture behavior of mn-containing gamma titanium aluminides*. Metallurgical and Materials Transactions A, 1995. **26**(9): p. 2275-2291.
59. McKee, D.W. and S.C. Huang, *The oxidation behavior of gamma-titanium aluminide alloys under thermal cycling conditions*. Corrosion Science, 1992. **33**(12): p. 1899-1914.
60. Hu, D., *Effect of composition on grain refinement in TiAl-based alloys*. Intermetallics, 2001. **9**(12): p. 1037-1043.
61. Hu, D., *Effect of boron addition on tensile ductility in lamellar TiAl alloys*. Intermetallics, 2002. **10**(9): p. 851-858.
62. Sadler, P., K.S. Kumar, and J.A. Green, *Applicability and Performance Benefits of XD (Tradename) Titanium Aluminides to Expendable Gas Turbine Engines*. 1993, DTIC Document.
63. Larsen, D.E. and L. Christodoulou. *Effect of XD™ TiB2 Volume Fraction on the Microstructure of a Cast Near-gamma titanium aluminide alloy*. in *MRS Proceedings*. 1990. Cambridge Univ Press.
64. Kishida, K., et al., *Character—istics, benefits and applications of PST TiAl crystal*. Kim Y W. Gamma Titanium Aluminide, 1995. **229**.
65. Jenkins, N.B., *Fracture and Fatigue of Gamma Based Titanium Aluminide Intermetallic alloy*, in *School of Metallurgy and Materials*. 1999, Univeristy of Birmingham: University of Birmingham, Interdisciplinary Research Centre in Materials for High Performance Applications, School of Metallurgy and Materials, Faculty of Engineering, 2000. p. 106.
66. Kim, Y.-W., *Strength and ductility in TiAl alloys*. Intermetallics, 1998. **6**(7–8): p. 623-628.
67. Appel, F. and R. Wagner, *Microstructure and deformation of two-phase γ -titanium aluminides*. Materials Science and Engineering: R: Reports, 1998. **22**(5): p. 187-268.
68. CHAN, K. and Y.-. KIM, *Fracture processes in a two-phase gamma titanium aluminide alloy*. Microstructure/property relationships in titanium aluminides and alloys, 1991: p. 179-196.
69. Chan, K.S. and Y.W. Kim, *Effects of lamellae spacing and colony size on the fracture resistance of a fully-lamellar TiAl alloy*. Acta Metallurgica et Materialia, 1995. **43**(2): p. 439-451.
70. Larsen, J., et al., *Assuring reliability of gamma titanium aluminides in*

long-term service. Minerals, Metals and Materials Society/AIME, Gamma Titanium Aluminides 1999(USA), 1999: p. 463-472.

71. Balsone, S.J., et al., *EFFECTS OF MICROSTRUCTURE AND TEMPERATURE ON FATIGUE-CRACK GROWTH IN THE TIAL ALLOY TI-46.5AL-3NB-2CR-0.2W*. Materials Science and Engineering a-Structural Materials Properties Microstructure and Processing, 1995. **192**: p. 457-464.
72. Balsone, S.J., et al., *FRACTOGRAPHIC STUDY OF FATIGUE-CRACK GROWTH-PROCESSES IN A FULLY LAMELLAR GAMMA-TIAL ALLOY*. Scripta Metallurgica Et Materialia, 1995. **32**(10): p. 1653-1658.
73. D.M, D., *Gamma titanium aluminide alloys—an assessment within the competition of aerospace structural materials*. Materials Science and Engineering: A, 1999. **263**(2): p. 281-288.
74. Sastry, S.M.L. and H.A. Lipsitt, *FATIGUE DEFORMATION OF TIAL BASE ALLOYS*. Metallurgical Transactions a-Physical Metallurgy and Materials Science, 1977. **8**(2): p. 299-308.
75. Sharman, A.R.C., et al., *The effects of machined workpiece surface integrity on the fatigue life of γ -titanium aluminide*. International Journal of Machine Tools and Manufacture, 2001. **41**(11): p. 1681-1685.
76. Jha, S.K., J.M. Larsen, and A.H. Rosenberger, *The role of competing mechanisms in the fatigue life variability of a nearly fully-lamellar γ -TiAl based alloy*. Acta Materialia, 2005. **53**(5): p. 1293-1304.
77. Zhou, Y., et al., *High-temperature fatigue property of Ti46Al8Nb alloy with the fully lamellar microstructure*. Intermetallics, 2012. **24**(0): p. 7-14.
78. Henaff, G. and A.L. Gloanec, *Fatigue properties of TiAl alloys*. Intermetallics, 2005. **13**(5): p. 543-558.
79. Aspinwall, D.K., R.C. Dewes, and A.L. Mantle, *The machining of gamma-TiAl intermetallic alloys*. Cirp Annals-Manufacturing Technology, 2005. **54**(1): p. 99-104.
80. Nazmy, M., et al., *Surface defect tolerance of a cast TiAl alloy in fatigue*. Scripta Materialia, 2001. **45**(7): p. 787-792.
81. Bentley, S.A., A.L. Mantle, and D.K. Aspinwall, *The effect of machining on the fatigue strength of a gamma titanium aluminide intermetallic alloy*. Intermetallics, 1999. **7**(8): p. 967-969.
82. Vaidya WV, S.K.-H., Wagner R, *Understanding the fatigue resistance of gamma titanium aluminide*, Gamma Titanium Aluminides. TMS, 1995: p.

867-874.

83. Trail, S.J., *Fatigue of gamma based titanium aluminide alloys*, in *University of Birmingham, IRC in Materials for High Performance Applications*. 1996, University of Birmingham: University of Birmingham, IRC in Materials for High Performance Applications. p. 118.
84. Campbell, J.P., Venkateswara Rao, K. T. and Ritchie, R. O., *Metall. Mater. Trans. A*, 1998. **30A**.
85. Hénaff, G., et al., *Fatigue crack propagation resistance of a Ti48Al2Mn2Nb alloy in the as-cast condition*. *Materials Science and Engineering: A*, 1996. **219**(1-2): p. 212-220.
86. Chan, K.S., et al., *Intrinsic and extrinsic fracture resistance in lamellar TiAl alloys*. *Acta Materialia*, 2004. **52**(15): p. 4601-4614.
87. Pippan, R., et al., *Fatigue threshold and crack propagation in gamma-TiAl sheets*. *Intermetallics*, 2001. **9**(1): p. 89-96.
88. Venkateswara Rao, K., G. Odette, and R. Ritchie, *Ductile-reinforcement toughening in γ -TiAl intermetallic-matrix composites: Effects on fracture toughness and fatigue-crack propagation resistance*. *Acta metallurgica et materialia*, 1994. **42**(3): p. 893-911.
89. Yokoshima S, Y.M., *Acta Materialia*, 1996. **44**: p. 873.
90. Elbert, W. *The significance of fatigue crack closure*. in *Damage Tolerance in Aircraft Structures: A Symposium Presented at the Seventy-third Annual Meeting American Society for Testing and Materials, Toronto, Ontario, Canada, 21-26 June 1970*. 1971. ASTM International.
91. Sadananda, K. and A. Vasudevan, *Fatigue crack growth behaviour in titanium aluminides*. *Materials Science and Engineering: A*, 1995. **192**: p. 490-501.
92. Gloanec, A.L., et al., *Fatigue crack growth behaviour of a gamma-titanium-aluminide alloy prepared by casting and powder metallurgy*. *Scripta Materialia*, 2003. **49**(9): p. 825-830.
93. García, A.M. and H. Sehitoglu, *Contact of crack surfaces during fatigue: Part I. Formulation of the model*. *Metallurgical and Materials Transactions A*, 1997. **28**(11): p. 2263-2275.
94. Gnanamoorthy, R., Y. Mutoh, and Y. Mizuhara, *Fatigue crack growth behavior of equiaxed, duplex and lamellar microstructure γ -base titanium aluminides*. *Intermetallics*, 1996. **4**(7): p. 525-532.

95. Mine, Y., K. Takashima, and P. Bowen, *Effect of lamellar spacing on fatigue crack growth behaviour of a TiAl-based aluminide with lamellar microstructure*. Materials Science and Engineering: A, 2012. **532**(0): p. 13-20.
96. Peng, L., H. Li, and J. Wang, *Processing and mechanical behavior of laminated titanium–titanium tri-aluminide ($Ti-Al_{3/2}Ti$) composites*. Materials Science and Engineering: A, 2005. **406**(1): p. 309-318.
97. Campbell, J.P., et al., *On the growth of small fatigue cracks in γ -based titanium aluminides*. Scripta Materialia, 1997. **37**(5): p. 707-712.
98. Filippini, M., et al., *Defect tolerance of a gamma titanium aluminide alloy*. Procedia Engineering, 2011. **10**(0): p. 3677-3682.
99. Chan, K.S. and D.S. Shih, *Fatigue and fracture behavior of a fine-grained lamellar TiAl alloy*. Metallurgical and Materials Transactions a-Physical Metallurgy and Materials Science, 1997. **28**(1): p. 79-90.
100. Soboyejo, W.O., F. Ye, and T.S. Srivatsan, *The fatigue and fracture behavior of a gamma-titanium aluminide intermetallic: Influence of ductile phase reinforcement*. Engineering Fracture Mechanics, 1997. **56**(3): p. 379-395.
101. McKelvey, A.L., K.T.V. Rao, and R.O. Ritchie, *High-temperature fracture and fatigue-crack growth behavior of an XD gamma-based titanium aluminide intermetallic alloy*. Metallurgical and Materials Transactions a-Physical Metallurgy and Materials Science, 2000. **31**(5): p. 1413-1423.
102. McKelvey, A.L., K.T.V. Rao, and R.O. Ritchie, *On the anomalous temperature dependence of fatigue-crack growth in γ -based titanium aluminides*. Scripta Materialia, 1997. **37**(11): p. 1797-1803.
103. Mabru, C., et al., *Influence of temperature and environment on fatigue crack propagation in a TiAl-based alloy*. Engineering Fracture Mechanics, 1999. **64**(1): p. 23-47.
104. Umakoshi, Y., et al., *Effect of deformation temperature on fatigue and fracture behavior in TiAl polysynthetically twinned crystals*. Metallurgical and Materials Transactions A, 1998. **29**(13): p. 943-950.
105. Zhu, S.J., et al., *Materials Science and Engineering a-Structural Materials Properties Microstructure and Processing*, 2000. **290**(1-2): p. 198-206.
106. Liu, C.T. and Y.W. Kim, *ROOM-TEMPERATURE ENVIRONMENTAL EMBRITTLEMENT IN A TIAL ALLOY*. Scripta Metallurgica Et Materialia, 1992. **27**(5): p. 599-603.
107. Chan, K.S. and Y.W. Kim, *INFLUENCE OF MICROSTRUCTURE ON*

CRACK-TIP MICROMECHANICS AND FRACTURE BEHAVIORS OF A 2-PHASE TiAl ALLOY. Metallurgical Transactions a-Physical Metallurgy and Materials Science, 1992. **23**(6): p. 1663-1677.

108. Oh, M.H., et al., *ENVIRONMENTAL-EFFECTS ON THE ROOM-TEMPERATURE DUCTILITY OF POLYSYNTHETICALLY TWINNED (PST) CRYSTALS OF TiAl*. Acta Metallurgica Et Materialia, 1993. **41**(7): p. 1939-1949.
109. James, A.W. and P. Bowen, *ELEVATED-TEMPERATURE CRACK-GROWTH RESISTANCE OF TiAl UNDER MONOTONIC AND CYCLIC LOADING*. Materials Science and Engineering a-Structural Materials Properties Microstructure and Processing, 1992. **153**(1-2): p. 486-492.
110. Henaff, G., G. Odemer, and A. Tonneau-Morel, *Environmentally-assisted fatigue crack growth mechanisms in advanced materials for aerospace applications*. International Journal of Fatigue, 2007. **29**(9-11): p. 1927-1940.
111. Petit, J. and C. Sarrazin-Baudoux, *An overview on the influence of the atmosphere environment on ultra-high-cycle fatigue and ultra-slow fatigue crack propagation*. International journal of fatigue, 2006. **28**(11): p. 1471-1478.
112. Mabru, C., G. Henaff, and J. Petit, *Environmental influence on fatigue crack propagation in TiAl alloys*. Intermetallics, 1997. **5**(5): p. 355-360.
113. Rosenberger, A.H., *Effect of environment on the fatigue crack growth of gamma titanium aluminide alloys at ambient temperatures*. Scripta Materialia, 2001. **44**(11): p. 2653-2659.
114. Kim, Y.-W. and D. Dimiduk, *Progress in the understanding of gamma titanium aluminides*. JOM, 1991. **43**(8): p. 40-47.
115. Appel, F., U. Christoph, and M. Oehring, *Creep deformation in two-phase titanium aluminide alloys*. Materials Science and Engineering: A, 2002. **329**: p. 780-787.
116. Oikawa, H., *Creep in titanium aluminides*. Materials Science and Engineering: A, 1992. **153**(1-2): p. 427-432.
117. Mall, S., E. Staubs, and T. Nicholas, *Investigation of creep/fatigue interaction on crack growth in a titanium aluminide alloy*. Journal of engineering materials and technology, 1990. **112**(4): p. 435-441.
118. Cui, W.F., et al., *Thermomechanical fatigue behaviours of a third generation γ -TiAl based alloy*. Intermetallics, 2007. **15**(5-6): p. 675-678.
119. Nicholas, T., T. Weerasooriya, and N.E. Ashbaugh. *A model for creep/fatigue*

- interactions in alloy 718*. in *Fracture Mechanics: Sixteenth Symposium, ASTM STP*. 1985.
120. Chrapoński, J., et al., *Microstructure and chemical composition of phases in Ti–48Al–2Cr–2Nb intermetallic alloy*. Materials chemistry and physics, 2003. **81**(2): p. 438-442.
 121. Mitao, S., S. Tsuyama, and K. Minakawa, *Effects of microstructure on the mechanical properties and fracture of γ -base titanium aluminides*. Materials Science and Engineering: A, 1991. **143**(1): p. 51-62.
 122. Kong, M.C., D. Axinte, and W. Voice, *Aspects of material removal mechanism in plain waterjet milling on gamma titanium aluminide*. Journal of Materials Processing Technology, 2010. **210**(3): p. 573-584.
 123. James, A.W., *The fracture and fatigue of gamma based titanium aluminides*, in *School of Metallurgy and Materials*. 1995, University of Birmingham: University of Birmingham, School of Metallurgy and Materials.
 124. Po-Sri, C., *Elevates temperature crack growth in inertially welded nickel based superalloys and gamma based titanium aluminides*, in *School of Metallurgy and Materials, College of Engineering and Physical Sciences*. 2011, University of Birmingham: University of Birmingham. p. 284
 125. Pickard, A.C., *The Application of 3-Dimensional Finite Element Methods to Fracture Mechanics and Fatigue Life Prediction*. 1986: EMAS, Engineering Materials Advisory Services Limited.
 126. Gnanamoorthy, R., et al., *Influence of lamellar lath orientation on the fatigue crack growth behavior of gamma base titanium aluminides*. Scripta Metallurgica Et Materialia, 1995. **33**(6): p. 907-912.
 127. Zhang, T., *Diploma Work*. 1994, Technical University Hamburg - Harburg.
 128. Campbell, J.P., K.T. Venkateswara Rao, and R.O. Ritchie, *On the role of microstructure in fatigue-crack growth of γ -based titanium aluminides*. Materials Science and Engineering: A, 1997. **239–240**(0): p. 722-728.
 129. Pippan, R., *The growth of short cracks under cyclic compression*. Fatigue Fract. Engng Mater.Struct., 1987. **9**: p. 319-328.
 130. Li, J.C.M. and C.T. Liu, *KINETIC AND EQUILIBRIUM EFFECTS IN THE ENVIRONMENTAL EMBRITTLEMENT OF ORDERED INTERMETALLICS*. Scripta Metallurgica Et Materialia, 1995. **33**(4): p. 661-668.
 131. Brady, M., et al., *The oxidation and protection of gamma titanium aluminides*. JOM, 1996. **48**(11): p. 46-50.

132. al., S.J.B.e., Mat. Sci and Eng., 1995. **A192/193**: p. 457.
133. Knowles, D. and D. Hunt, *The influence of microstructure and environment on the crack growth behavior of powder metallurgy nickel superalloy RR1000*. Metallurgical and Materials Transactions A, 2002. **33**(10): p. 3165-3172.
134. Birks, N., G.H. Meier, and F.S. Pettit, *Introduction to the high temperature oxidation of metals*. 2006: Cambridge University Press.
135. Shih, D., et al. *The microstructural dependence of mechanical properties of Ti-48Al-2Cr-2Nb*. in *Microstructure/property relationships in titanium aluminides and alloys; Proceedings of the Symposium, Fall Meeting of the Minerals, Metals, and Materials Society, Detroit, MI, Oct. 7-11, 1990*. 1991.
136. Huang, Z.W., P. Bowen, and I.P. Jones, *Transmission electron microscopy investigation of fatigue crack tip plastic zones in a polycrystalline γ -TiAl-based alloy*. Philosophical Magazine A, 2001. **81**(9): p. 2183-2197.
137. Henaff, G., A. Tonneau, and C. Mabru, *Near-threshold fatigue crack growth mechanisms in TiAl alloys*. Structural Intermetallics 2001, ed. K.J. Hemker, et al. 2001. 305-314.